

**Development of Novel Multifunctional Nanocomposites for
Antimicrobial Efficiency in Water Treatment**

by

Qurban Ali

A thesis submitted to the University of Central Lancashire for the degree of Doctor
of Philosophy in Chemistry in the School of Physical Sciences and Computing.

July 2018

Declaration

Concurrent registration for two or more academic awards

I declare that while registered as a candidate for the research degree, I have not been a registered candidate or enrolled student for another award of the University or other academic or professional institution

Material submitted for another award

I declare that no material contained in the thesis has been used in any other submission for an academic award and is solely my own work

Signature of Candidate **Qurban Ali**

Type of Award **Doctor of Philosophy (PhD)**

School **School of Physical Sciences and Computing**

Abstract

Water pollution is a major concern worldwide. Bacteria, viruses and fungi present in drinking water cause various diseases as a result of poor hygienic conditions in developing countries. Similarly, presence of microorganisms in drinking water is a threat to public health in developing world due to poor hygienic condition. Numerous disinfectants and biocides are used for inhibiting the growth of pathogenic microbial contamination, producing carcinogenic by-products which are dangerous to human health.

This work involved the synthesis, characterisation and application of novel multifunctional nanocomposites by the modification of cost effective available materials for antimicrobial treatment of contaminated water and the detection of specific DNA associated with water-borne bacteria.

A series of multifunctional nanocomposites composed of commercially available carbon (activated charcoal and multi-walled carbon nanotubes), and silica-based materials such as diatomaceous earth, celatom-80 and celatom-14 were modified with silver and iron oxide nanoparticles *via* a simple one-pot synthesis protocol in order to incorporate antimicrobial and superparamagnetic properties. The resultant materials have been tested for antimicrobial efficiency using model water system containing Gram-negative *Escherichia coli* (*E. coli*) K12 and Gram-positive *Staphylococcus aureus* (*S. aureus*) microorganisms. It was found that all materials ranging from 10 to 200 $\mu\text{g/mL}$ produced excellent inhibition of *S. aureus* and *E. coli*.

All nanocomposites have been fully characterised by several physico-chemical techniques such as Transmission Electron Microscope (TEM), Scanning Electron Microscope (SEM), X-ray Fluorescence (XRF), Energy Dispersive X-ray Analysis (EDAX), Fourier Transform Infrared Spectroscopy (FT-IR), Nitrogen gas adsorption and (BET) surface area analysis. Surface area of the materials measured in range of 5 to 560 m^2/gm . XRF along with EDAX/SEM analyses have been used for the confirmation of silver and iron oxide presence in the nanocomposite materials. TEM images showed nano-sized silver particles with an average diameter of 15-17 nm and iron oxide (magnetite) nanoparticles with an average diameter of 30 nm embedded into the nanocomposites. FT-IR spectroscopy measurement confirmed the presence of Fe–O bonding of iron oxide nanoparticles due to a characteristic stretching vibration at 570 cm^{-1} . Powder X-ray Diffraction (XRD) measurements confirmed the crystalline structure of the iron oxide nanocomposite mostly magnetite (Fe_3O_4). Nitrogen gas adsorption-desorption experiments suggests the presence of average pore diameter 28 to 79 \AA , micropore volume: 0.01 to 0.16 cm^3/g , and surface area 5 to 560 m^2/g .

Gram-negative *E. coli* K12 and Gram-positive *S. aureus* bacteria were used for anti-bacterial activity study where the nutrient agar was used for the growth of the bacteria. The antimicrobial effect of the nanocomposites was quantified by counting the number of colonies (colony forming unit, CFU/mL) grown on the media compared with a blank solution. Different concentrations (0.2 $\mu\text{g/mL}$ to 300 $\mu\text{g/mL}$) of the nanocomposite materials were used for this study. MBC of QM1-3 and QM2-3 was found 10 $\mu\text{g/mL}$ for the *S. aureus* and 30 $\mu\text{g/mL}$ for *E. coli* K12, while other samples of QM3-3, QM4-3 and QM5-3 were higher such as 30 $\mu\text{g/mL}$ for the *S. aureus* and 100 to 200 $\mu\text{g/mL}$ for *E. coli*. All experiments were performed in triplicate and the data presented are the mean values of triplicate experiments \pm standard deviation.

Detection of water-borne microorganisms is the second application of the developed nanocomposites *via* surface modification with specific oligonucleotides sequences of *E. coli* gene followed by hybrid capture with complementary sequence. It was observed that multi-walled carbon nanotubes, activated charcoal and diatomaceous earth gave good and satisfactory results (0.384 to 0.400 nmol/mg) in hybrid capture of complementary oligonucleotides sequences in model assay. Surface modified optimum materials (carbon nanotubes and activated carbon) with efficient hybrid capture were also efficient in detecting amplicon of 97 base pairs (bp) of *E. coli* specific genome by PCR experiment.

Contents

Declaration	i
Abstract	ii
Contents	iv
List of Figures	xii
List of Tables.....	xxv
Acknowledgements	xxvii
List of Abbreviations.....	xxviii
List of Units	xxx
List of Publications.....	xxxi
CHAPTER ONE	1
1 Introduction and literature review	1
1.1 Nanotechnology and nanoscale.....	2
1.2 Types of nanocomposites.....	3
1.2.1 Carbon-based materials.....	3
1.2.2 Silica-based materials.....	4
1.2.3 Superparamagnetic iron oxide nanoparticles	5
1.3 Synthesis of nanomaterials.....	6
1.3.1 Synthesis of iron oxide nanoparticles	6
1.3.2 Synthesis of silver nanoparticles.....	11
1.4 Frequently found bacteria in water sources and their impact on human health.....	14

1.5	Antimicrobial features of nanomaterials	19
1.6	Challenge for the project	23
1.7	Aim and objectives of the project	24
1.7.1	Novelty of the project work	25
CHAPTER TWO		26
2	Materials, methods and characterisation techniques	26
2.1	Materials and methods	27
2.1.1	Bio-molecules	27
2.1.2	Solutions and buffers	28
2.2	Method I (Optimised from various trial and error which has been presented in appendix A-1)	29
2.2.1	Magnetite nanocomposite	29
2.2.2	Silver nanocomposite	29
2.2.3	Silver magnetite nanocomposite	30
2.2.4	Bacterial culture and growth conditions	30
2.2.5	Assaying the minimum bactericidal concentration (MBC)	30
2.2.6	Source of bacterial culture	31
2.2.7	Growth curve determination	31
2.2.8	Extraction of DNA from <i>E. coli</i> pellets	32
2.3	Characterisation techniques used.	34
2.3.1	X-ray fluorescence	35
2.3.2	Scanning electron microscopy	35
2.3.3	Transmission electron microscopy.....	36
2.3.4	Fourier transforms infrared spectroscopy	36

2.3.5	X-ray diffraction.....	36
2.3.6	Brunauer–Emmett Teller surface area measurement	37
2.4	Surface functionalisation of nanocomposites containing silver and magnetite nanoparticles.....	37
2.4.1	Silanisation of composite materials	37
2.4.2	Measurement of surface amine density	38
2.4.3	Surface amine conversion to aldehyde by reacting with glutaraldehyde solution.....	40
2.4.4	Measurement for oligonucleotide concentration (UV-visible assay).....	41
2.4.5	Grafting of the primers.....	43
2.4.6	Hybrid capture assay of complementary oligonucleotides (Model Assay)	43
2.4.7	PCR sample preparation and optimisation parameters	44
CHAPTER THREE.....		46
3	Analysis of structure, chemical composition and properties of MWCNTs and its modified composites	46
3.1	Introduction	47
3.2	Multiwall carbon nanotube-based composite (QM1 to QM1-3)	47
3.2.1	X-ray fluorescence	47
3.2.2	Energy dispersive X-ray analysis.....	49
3.2.3	Scanning electron microscopy	51
3.2.4	Transmission electron microscopy.....	52
3.2.5	Fourier transforms infrared spectroscopy	54
3.2.6	X-ray diffraction.....	56

3.2.7	Brunauer–Emmett–Teller surface area	58
CHAPTER FOUR.....		61
4	Analysis of structure, chemical composition and properties of AC based modified composites	61
4.1	Activated charcoal- based composites (QM2 to QM2-3)	62
4.1.1	X-ray fluorescence	62
4.1.2	Energy dispersive X-ray analysis.....	64
4.1.3	Scanning electron microscopy	66
4.1.4	Transmission electronic microscopy.....	67
4.1.5	Fourier transform infrared spectroscopy.....	70
4.1.6	X-ray diffraction.....	71
4.1.7	Brunauer–Emmett–Teller surface area measurement	73
CHAPTER FIVE.....		75
5	Analysis of structure, chemical composition and properties of DAE based modified composites	75
5.1	Diatomaceous earth-based composite (QM3 to QM3-3).....	76
5.1.1	X-ray fluorescence	76
5.1.2	Energy dispersive X-ray analysis.....	78
5.1.3	Scanning electron microscopy	80
5.1.4	Transmission electron microscopy.....	82
5.1.5	Fourier transform infrared analysis.....	86
5.1.6	X-ray diffraction.....	88
CHAPTER SIX.....		92
6	Analysis of structure, chemical composition and properties of Celatom-14 and	

Celatom-80 based modified composites	92
6.1 Celatom-14-based composite (QM4 to QM4-3)	93
6.1.1 X-ray fluorescence	93
6.1.2 Energy dispersive X-ray analysis.....	95
6.1.3 Scanning electron microscopy	97
6.1.4 Transmission electron microscopy.....	98
6.1.5 Fourier transform infrared spectroscopy	101
6.1.6 X-ray diffraction.....	102
6.1.7 Brunauer–Emmett–Teller surface area	103
6.2 Celatom-80-based composite (QM5 to QM5-3).....	106
6.2.1 X-ray fluorescence	106
6.2.2 Energy dispersive X-ray analysis.....	108
6.2.3 Scanning electron microscopy	110
6.2.4 Transmission electron microscopy.....	112
6.2.5 Fourier transform infrared spectroscopy	115
6.2.6 X-ray diffraction.....	117
6.2.7 Brunauer–Emmett–Teller surface area	118
6.3 Comparison of different nanocomposites with respects to their physicochemical properties	120
6.4 Conclusions	121
CHAPTER SEVEN.....	123
7 Antimicrobial applications	123
7.1 Introduction	124
7.2 Antibacterial activity of the nanocomposite materials.....	125

7.3	Antimicrobial applications of synthesised nanocomposites containing silver and iron oxide nanoparticles on Gram-positive and Gram-negative bacteria	126
7.3.1	Control plates of <i>E. coli</i>	127
7.3.2	Control plates of <i>S. aureus</i>	128
7.3.3	QM1-3-based nanocomposite (MWCNTs-modified with iron-silver nanoparticles) against <i>E. coli</i> K12 and <i>S. aureus</i>	130
7.3.4	Summary of QM1-3-based composite	134
7.3.5	QM2-3 nanocomposites (AC-modified with iron and silver nanoparticles) against <i>E. coli</i> and <i>S. aureus</i>	135
7.3.6	Summary of QM2-3-based composite	139
7.3.7	QM3-3 nanocomposite (DAE-modified with iron and silver nanoparticles) against <i>E. coli</i> and <i>S. aureus</i>	140
7.3.8	Summary of QM3-3-based composite	144
7.3.9	QM4-3-based composite (CPW-14-modified with iron and silver nanoparticles) against <i>E. coli</i> K12 and <i>S. aureus</i>	145
7.3.10	Summary of QM4-3-based composite	148
7.3.11	QM5-3-based nanocomposite (CPW-80-modified with iron and silver nanoparticles) against <i>E. coli</i> and <i>S. aureus</i>	149
7.3.12	Summary of QM5-3-based nanocomposite	152
7.4	Antimicrobial efficiency of synthesised materials against Gram-negative bacteria by SP method	153
7.5	Recycling of the modified nanocomposites	154
7.6	Comparison of antimicrobial applications of all modified (QM1-3, QM2-3, QM3-3, QM4-3 and QM5-3) nanocomposites	161

7.7	Conclusions	163
7.8	Introduction	165
7.9	Surface amine density	166
7.10	Grafting of the oligonucleotides on the surface of the nanocomposite materials produced	170
7.11	Hybrid capture assay of complementary oligonucleotide	173
7.12	Dehybridisation of complementary oligonucleotide	177
7.13	Optimisation of the extracted DNA	180
7.13.1	Determining the capturing efficiency and sensitivity for the detection of <i>E. coli</i> DNA from water sample.	181
7.13.2	PCR results of grafted and modified material with oligonucleotides	181
7.14	Comparison properties of all modified (QM1-3, QM2-3, QM3-3, QM4-3 and QM5-3) nanocomposites for hybrid capture efficiency	184
7.14.1	Surface amine density	184
7.14.2	Grafting of oligonucleotides	185
7.14.3	Hybridisation	186
7.14.4	Dehybridisation	187
7.15	Conclusions	188
CHAPTER EIGHT		190
8	Conclusions and future work	190
8.1	Conclusions	191
8.2	Future work	196

References	198
Appendices	215

List of Figures

Figure 1-1 Diatomaceous earth (Schatzlein, 2015).....	5
Figure 1-2 Types of magnetic particles.....	9
Figure 2-1 Growth curves of (a) <i>S. aureus</i> and (b) <i>E. coli</i>	32
Figure 2-2 Silanisation (molecular modelling) of the nanocomposites with (a) APTS and (b) APDS	38
Figure 2-3 Calibration curve for 4-NBA (a) coupling and (b) hydrolysis solution ...	39
Figure 2-4 Molecular modelling of 4-NBA colorimetric surface assay	39
Figure 2-5 Schematic presentation using molecular modelling for the conversion of surface amine to aldehyde.....	41
Figure 2-6 Standardisation curves for complementary oligonucleotides specific to <i>E.</i> <i>coli</i> (a) forward sequence and (b) reverse. Values are mean (\pm SD, No=3).	42
Figure 2-7 Standard curves for oligonucleotides-specific to <i>E. coli</i> (a) with spacer C12 forward (b) with spacer C12 reverse, while specific sequence with (c) spacer C6 forward and (d) with spacer C6 reverse. Results are mean (\pm SD, No=3).	42
Figure 2-8 Complete illustration using molecular modelling (a) grafting of oligonucleotides (b) Hybrid capture (c) Dehybridisation of the complementary sequence.	44
Figure 3-1 XRF of QM1-based composite (a) QM1 (unmodified MWCNTs) (b) QM1-1 (MWCNTs modified with only iron oxide nanoparticles) (c) QM1-2 (MWCNTs modified with only silver nanoparticles) and (d) QM1-3 (MWCNTs modified with silver coating iron oxide nanoparticles).....	48
Figure 3-2 EDAX spectrum of QM1-based composite (a) QM1 (unmodified MWCNTs) (b) QM1-1 (MWCNTs modified with only iron oxide nanoparticles)	

(c) QM1-2 (MWCNTs modified with only silver nanoparticles) and (d) QM1-3 (MWCNTs modified with silver coating iron oxide nanoparticles)50

Figure 3-3 SEM shows images of QM1-based composite (a) QM1 (unmodified MWCNTs) (b) QM1-1 (MWCNTs modified with only iron oxide nanoparticles) (c) QM1-2 (MWCNTs modified with only silver nanoparticles) and (d) QM1-3 (MWCNTs modified with silver coating iron oxide nanoparticles)51

Figure 3-4 TEM images of QM1-based composite (a and b) QM1 (unmodified MWCNTs) (c) QM1-1 (MWCNTs modified with only iron oxide nanoparticles) (d) QM1-2 (MWCNTs modified with only silver nanoparticles) and (e) QM1-3 (MWCNTs modified with silver coating iron oxide nanoparticles)53

Figure 3-5 FT-IR spectrum of QM1-based composite (a) QM1 (unmodified MWCNTs) (b) QM1-1 (MWCNTs modified with only iron oxide nanoparticles) (c) QM1-2 (MWCNTs modified with only silver nanoparticles) and (d) QM1-3 (MWCNTs modified with silver and iron oxide nanoparticles).....55

Figure 3-6 XRD pattern of QM1-based composite (a) QM1 (unmodified MWCNTs) (b) QM1-1 (MWCNTs modified with only iron oxide nanoparticles) (c) QM1-2 (MWCNTs modified with only silver nanoparticles) and (d) QM1-3 (MWCNTs modified with silver and iron oxide nanoparticles).....57

Figure 3-7 Adsorption-desorption isotherm of QM1-based composite (a) QM1 (unmodified MWCNTs) (b) QM1-1 (MWCNTs modified with only iron oxide nanoparticles) (c) QM1-2 (MWCNTs modified with only silver nanoparticles) and (d) QM1-3 (MWCNTs modified with silver coating iron oxide nanoparticles).59

Figure 4-1 XRF of QM2-based composite (a) QM2 (AC-unmodified) (b) QM2-1 (AC- modified with only iron oxide nanoparticles) (c) QM2-2 (AC- modified

with only silver nanoparticles) and (d) QM2-3 (AC- modified with silver coating iron oxide nanoparticles)	63
Figure 4-2 EDAX Spectrum of QM2-based composite (a) QM2 (AC-unmodified) (b) QM2-1 (AC- modified with only iron oxide nanoparticles) (c) QM2-2 (AC- modified with only silver nanoparticles) and (d) QM2-3 (AC- modified with silver coating iron oxide nanoparticles)	65
Figure 4-3 SEM of QM2 based composite (a) QM2 (AC-unmodified) (b) QM2-1 (AC- modified with only iron oxide nanoparticles) (c) QM2-2 (AC- modified with only silver nanoparticles) and (d) QM2-3 (AC- modified with silver and iron oxide nanoparticles).....	67
Figure 4-4 TEM images of QM2-based composite (a) QM2 (AC-unmodified) (b) QM2-1 (AC- modified with only iron oxide nanoparticles) (c) QM2-2 (AC- modified with only silver nanoparticles) and (d) QM2-3 (AC- modified with silver coating iron oxide nanoparticles)	68
Figure 4-5 High resolution STEM images of QM2-3-based composite (a,b and c) QM2-3 (AC -modified with silver coating iron oxide) (b) QM2-3 (AC- modified with silver and iron oxide) shows the nano-size of silver nanoparticle and (c) presence of well crystalline iron oxide nanoparticles in QM2-3.	69
Figure 4-6 (a and b) QM2-3-based composite, modified with iron and silver nanoparticles.	70
Figure 4-7 FT-IR spectra of QM2-based composite (a) QM2 (AC-unmodified) (b) QM2-1 (AC- modified with only iron oxide nanoparticles) (c) QM2-2 (AC- modified with only silver nanoparticles) and (d) QM2-3 (AC- modified with silver coating iron oxide nanoparticles)	70
Figure 4-8 XRD of QM2-based composite (a) QM2 (AC-unmodified) (b) QM2-1	

(AC- modified with only iron oxide nanoparticles) (c) QM2-2 (AC- modified with only silver nanoparticles) and (d) QM2-3 (AC- modified with silver and iron oxide nanoparticles).....72

Figure 4-9 N₂ gas adsorption isotherm of QM2-based composite (a) QM2 (AC-unmodified) (b) QM2-1 (AC- modified with only iron oxide nanoparticles) (c) QM2-2 (AC- modified with only silver nanoparticles) and (d) QM2-3 (AC- modified with silver coating iron oxide nanoparticles).....73

Figure 5-1 X-ray fluorescence of QM3-based composite (a) QM3 (DAE-unmodified) (b) QM3-1 (DAE- modified with only iron oxide nanoparticles) (c) QM3-2 (DAE- modified with only silver nanoparticles) and (d) QM3-3 (DAE- modified with silver and iron oxide77

Figure 5-2 EDAX spectrum of QM3-based composite (a) QM3 (DAE-unmodified) (b) QM3-1 (DAE- modified with only iron oxide nanoparticles) (c) QM3-2 (DAE- modified with only silver nanoparticles) and (d) QM3-3 (DAE- modified with silver coating iron oxide nanoparticles).....79

Figure 5-3 Surface morphology of QM3-based composite (a) QM3 (DAE-unmodified) (b) QM3-1 (DAE- modified with only iron oxide nanoparticles) (c) QM3-2 (DAE- modified with only silver nanoparticles) and (d) QM3-3 (DAE- modified with silver coating iron oxide nanoparticles).....81

Figure 5-4 TEM images of QM3-based composite (a) QM3 (DAE-unmodified) (b) QM3-1 (DAE- modified with only iron oxide nanoparticles) (c) QM3-2 (DAE- modified with only silver nanoparticles) and (d) QM3-3 (DAE- modified with silver coating iron oxide nanoparticles83

Figure 5-5 High resolution HTEM images of QM3-3 materials (a, b, c and d) (DAE- modified with silver coating iron oxide nanoparticles).....85

Figure 5-6 FT-IR analysis of all samples of QM3-based composite (a) QM3 (DAE-unmodified) (b) QM3-1 (DAE- modified with only iron oxide nanoparticles) (c) QM3-2 (DAE- modified with only silver nanoparticles) and (d) QM3-3 (DAE-modified with silver and iron oxide nanoparticles).....87

Figure 5-7 XRD of QM3-based composite (a) QM3 (DAE-unmodified) (b) QM3-1 (DAE- modified with only iron oxide nanoparticles) (c) QM3-2 (DAE-modified with only silver nanoparticles) and (d) QM3-3 (DAE- modified with silver coating iron oxide nanoparticles)88

Figure 5-8 N₂ gas adsorption-desorption isotherm of QM3-based composite (a) QM3 (DAE-unmodified) (b) QM3-1 (DAE- modified with only iron oxide nanoparticles) (c) QM3-2 (DAE- modified with only silver nanoparticles) and (d) QM3-3 (DAE- modified with silver coating iron oxide nanoparticles).90

Figure 6-1 X-ray fluorescence of QM4-based composite (a) QM4 (CPW-14-unmodified) (b) QM4-1 (CPW-14- modified with only iron oxide nanoparticles) (c) QM4-2 (CPW-14- modified with only silver nanoparticles) and (d) QM4-3 (CPW-14- modified with silver coating magnetite nanoparticles).....94

Figure 6-2 EDAX spectrum of QM4-based composite (a) QM4 (CPW-14-unmodified) (b) QM4-1 (CPW-14-modified with only iron oxide nanoparticles) (c) QM4-2 (CPW-14- modified with only silver nanoparticles) and (d) QM4-3 (CPW-14-modified with silver coating iron oxide nanoparticles96

Figure 6-3 Surface morphology of QM4-based composite (a) QM4 (CPW-14-unmodified) (b) QM4-1 (CPW-14-modified with only iron oxide nanoparticles) (c) QM4-2 (CPW-14- modified with only silver nanoparticles) and (d) QM4-3 (CPW-14-modified with silver coating iron oxide nanoparticles97

Figure 6-4 TEM images of QM4-based composite (a) QM5 (CPW-14-unmodified)

(b) QM4-1 (CPW-80-modified with only iron oxide nanoparticles) (c) QM4-2 (CPW-80- modified with only silver nanoparticles) and (d) QM4-3 (CPW-14- modified with silver coating iron oxide nanoparticles only silver nanoparticles) and (d) QM5-3 (CPW-80-modified with silver coating iron oxide nanoparticles99

Figure 6-5 HTEM image (a), and electron diffraction pattern (b) of QM4-3 (CPW-14-modified with iron and silver nanoparticles 100

Figure 6-6 FT-IR spectrum of QM4-based composite (a) QM4 (CPW-14- unmodified) (b) QM4-1 (CPW-14-modified with only iron oxide nanoparticles) (c) QM4-2 (CPW-14- modified with only silver nanoparticles) and (d) QM4-3 (CPW-14-modified with silver coating iron oxide nanoparticles)..... 101

Figure 6-7 XRD pattern of of QM4-based composite (a) QM4 (CPW-14- unmodified) (b) QM4-1 (CPW-14-modified with only iron oxide nanoparticles) (c) QM4-2 (CPW-14- modified with only silver nanoparticles) and (d) QM4-3 (CPW-14-modified with silver and iron oxide nanoparticles)..... 102

Figure 6-8 N2 gas adsorption-desorption isotherm of QM4-based composite (a) QM4 (CPW-14-unmodified) (b) QM4-1 (CPW-14-modified with only iron oxide nanoparticles) (c) QM4-2 (CPW-14- modified with only silver nanoparticles) and (d) QM4-3 (CPW-14-modified with silver coating iron oxide nanoparticles). 104

Figure 6-9 XRF of QM5-based composite (a) QM5 (CPW-80-unmodified) (b) QM5-1 (CPW-80-modified with only iron oxide nanoparticles) (c) QM5-2 (CPW-80- modified with only silver nanoparticles) and (d) QM5-3 (CPW-80-modified with silver coating iron oxide nanoparticles 107

Figure 6-10 EDAX spectrum of QM5-based composite (a) QM5 (CPW-80-

unmodified) (b) QM5-1 (CPW-80-modified with only iron oxide nanoparticles)
(c) QM5-2 (CPW-80- modified with only silver nanoparticles) and (d) QM5-3
(CPW-80-modified with silver coating iron oxide..... 109

Figure 6-11 Surface morphology of QM5-based composite (a) QM5 (CPW-80-
unmodified) (b) QM5-1 (CPW-80-modified with only iron oxide nanoparticles)
(c) QM5-2 (CPW-80- modified with only silver nanoparticles) and (d) QM5-3
(CPW-80-modified with silver coating iron oxide nanoparticles)..... 111

Figure 6-12 TEM images of QM5-based composite (a) QM5 (CPW-80-unmodified)
(b) QM5-1 (CPW-80-modified with only iron oxide nanoparticles) (c) QM5-2
(CPW-80- modified with only silver nanoparticles) and (d) QM5-3 (CPW-80-
modified with silver coating iron oxide nanoparticles..... 112

Figure 6-13 High resolution HTEM images of (a, b, c and d) QM5-3-based
composite (CPW-80-modified with iron oxide and silver nanoparticles) 114

Figure 6-14 HTEM image (a), QM5-3(CPW-80-modified with iron and silver
nanoparticles) and electron diffraction pattern (b) of QM5-3 nanocomposite 115

Figure 6-15 FT-IR spectrum of QM5-based composite (a) QM5 (CPW-80-
unmodified) (b) QM5-1 (CPW-80-modified with only iron oxide nanoparticles)
(c) QM5-2 (CPW-80- modified with only silver nanoparticles) and (d) QM5-3
(CPW-80-modified with silver coating iron oxide nanoparticles)..... 116

Figure 6-16 XRD pattern of QM5-based composite (a) QM5 (CPW-80-unmodified)
(b) QM5-1 (CPW-80-modified with only iron oxide nanoparticles) (c) QM5-2
(CPW-80- modified with only silver nanoparticles) and (d) QM5-3 (CPW-80-
modified with silver and iron oxide nanoparticles)..... 117

Figure 6-17 N₂ gas adsorption -desorption isotherm of QM5-based composite (a)
QM5 (CPW-80-unmodified) (b) QM5-1 (CPW-80-modified with only iron

oxide nanoparticles) (c) QM5-2 (CPW-80- modified with only silver nanoparticles) and (d) QM5-3 (CPW-80-modified with silver coating iron oxide nanoparticles)	119
Figure 6-18 A comparasion of BET surface area of all developed materials.	121
Figure 7-1 schematic illustration for the composition of the composite and their functions.....	125
Figure 7-2 Control plates of <i>E. coli</i> K12 (a) upper half 10^0 dilution and lower half 10^{-1} bacterial dilution, (b) upper half 10^{-2} dilution and lower half 10^{-3} bacterial dilution, (c) upper half 10^{-4} dilution and lower half 10^{-5} bacterial dilution and (d) upper half 10^{-6} lower half 10^{-7} bacterial dilution.....	127
Figure 7-3 Control plates <i>S. aureus</i> (a) upper half 10^0 dilution and lower half 10^{-1} bacterial dilution, (b) upper half 10^{-2} dilution and lower half 10^{-3} bacterial dilution and (c) upper half 10^{-4} dilution and lower half 10^{-5} bacterial dilution	128
Figure 7-4 Qunatitative Growth assay of control of <i>E. coli</i> and <i>S. aureus</i>	129
Figure 7-5 Antimicrobial efficiency of QM1-3(MWCNTs-modified with silver coating iron oxide nanoparticles) at various concentrations i.e. (a) 10 and 20 $\mu\text{g/mL}$ (b) 30 $\mu\text{g/mL}$ (c) 50 and 100 $\mu\text{g/mL}$ and (d) 200 and 300 $\mu\text{g/mL}$ against <i>E. coli</i> K12.	130
Figure 7-6 (a) Minimum bactericidal concentration assay against <i>E. coli</i> , (b) Time-Kill assay using 50 $\mu\text{g/mL}$ nanocomposite	131
Figure 7-7 QM1-3 nanocomposite (MWCNTs-modified with silver coating iron oxide nanoparticles) against <i>S.aureus</i> with (a) 2 $\mu\text{g/mL}$, (b) 4 $\mu\text{g/mL}$, (c) 6 $\mu\text{g/mL}$, (d) 8 $\mu\text{g/mL}$, (e) (upper half 10 $\mu\text{g/mL}$ and lower half 20 $\mu\text{g/mL}$)...	132
Figure 7-8 (a) Minimum bactericidal concentration assay against <i>S. aureus</i> (b) Time-kill assay using 10 $\mu\text{g/mL}$ nanocomposite	133

Figure 7-9 Quantitative growth assay of QM1-based composite: QM1 (unmodified MWCNTs), QM1-1 (MWCNTs modified with only iron oxide nanoparticles), QM1-2 (MWCNTs modified with only silver nanoparticles) and QM1-3 (MWCNTs modified with silver coating iron oxide nanoparticles) against <i>E. coli</i> (blue bar) and <i>S. aureus</i> (orange bar) at various concentrations of nanocomposites.	134
Figure 7-10 QM2-3 nanocomposite (AC-modified with silver coating iron oxide nanoparticles) against <i>E. coli</i> K12: (a) 10 µg/mL, (b) 20 µg/mL, (c) , 30 µg/mL and (d) 50 µg/mL	135
Figure 7-11 (a) Minimum bactericidal concentration assay against <i>E. coli</i> , (b) Time-kill assay using 50 µg/mL of nanocomposite.....	136
Figure 7-12 QM2-3 nanocomposite (AC-modified silver coating iron oxide nanoparticles) against <i>S.aureus</i> : (a) 2 µg/mL, (b) 4 µg/mL, (c) 6 µg/mL, (d) 8 µg/mL, (e) (upper half 10 µg/mL and lower half 20 µg/mL).	137
Figure 7-13 (a) Minimum bactericidal concentration assay against <i>S. aureus</i> , (b) Time-kill assay using 10 µg/mL.	138
Figure 7-14 Quantitative growth assay of QM2-based composite: QM2 (unmodified AC), QM2-1 (AC modified with only iron oxide nanoparticles), QM2-2 (AC modified with only silver nanoparticles) and QM2-3 (AC modified with silver coating iron oxide nanoparticles) against <i>E. coli</i> (blue bar) and <i>S. aureus</i> (orange bar).	138
Figure 7-15 QM3-3 nanocomposite (DAE-silver coating iron oxide nanoparticles) against <i>E. coli</i> : (a) (upper half 10 µg/mL and lower half 20 µg/mL), (b) 30 µg/mL and (c) (upper half 50 µg/mL and lower half 100 µg/mL)	140
Figure 7-16 Antimicrobial activity of QM3-3 against <i>E. coli</i> (a) Minimum	

bactericidal concentration assay, (b) Time-kill assay at 100 $\mu\text{g/mL}$	141
Figure 7-17 QM3-3 nanocomposite (DAE-modified with iron and silver nanoparticles) against <i>S. aureus</i> : (a) (upper half 10 $\mu\text{g/mL}$ and lower half 20 $\mu\text{g/mL}$) and (b) 30 $\mu\text{g/mL}$	141
Figure 7-18 Antimicrobial activity of QM3-3 against <i>S. aureus</i> (a) Minimum bactericidal concentration assay, (b) Time-kill assay at 30 $\mu\text{g/mL}$	143
Figure 7-19 Quantitative growth assay of QM3-based composite QM3 (unmodified DAE), QM3-1 (DAE modified with only iron oxide nanoparticles), QM3-2 (DAE modified with only silver nanoparticles) and QM3-3 (DAE modified with silver coating iron oxide) against <i>E. coli</i> (blue bar) and <i>S. aureus</i> (orange bar).	143
Figure 7-20 QM4-3 nanocomposite (CPW-14-modified with iron and silver nanoparticles) against <i>E. coli</i> with (a) 30 $\mu\text{g/mL}$, (b) 50 and 100 $\mu\text{g/mL}$ (upper half 100 $\mu\text{g/mL}$ and lower half 50 $\mu\text{g/mL}$).....	145
Figure 7-21 Antimicrobial activity of QM4-3 against <i>E. coli</i> (a) Minimum bactericidal concentration assay, (b) Time-kill assay at 100 $\mu\text{g/mL}$ concentration.....	146
Figure 7-22 QM4-3 nanocomposite (CPW-14-modified with silver coating iron oxide nanoparticles) against <i>S. aureus</i> at various concentrations (a) (upper half 10 $\mu\text{g/mL}$ and lower half 20 $\mu\text{g/mL}$) and (b) 30 $\mu\text{g/mL}$	146
Figure 7-23 Antimicrobial activity of QM4-3 against <i>S. aureus</i> (a) Minimum bactericidal concentration assay, (b) Time-kill assay at 30 $\mu\text{g/mL}$	147
Figure 7-24 Quantitative growth assay of QM4-based composite: QM4 (unmodified CPW-14), QM4-1 (CPW-14 modified with only iron oxide nanoparticles), QM4-2 (CPW-14-modified with only silver nanoparticles) and QM4-3 (CPW-	

14 modified with silver coating iron oxide) against <i>E. coli</i> (blue bar) and <i>S. aureus</i> (orange bar)	147
Figure 7-25 QM5-3 nanocomposite (CPW-80-modified with silver coating iron oxide nanoparticles) against <i>E. coli</i> (a) (upper half 10 µg/mL concentration and lower half 20 µg/mL concentration), (b) 50 µg/mL, (c) 100 µg/mL and (d) (upper half 200 µg/mL and lower half 300 µg/mL).....	149
Figure 7-26 Antimicrobial activity of QM5-3 against <i>E. coli</i> (a) Minimum bactericidal concentration assay, (b) Time-kill assay at 200 µg/mL	150
Figure 7-27 QM5-3 nanocomposite (CPW-80-modified with silver coating iron oxide nanoparticles) against <i>S. aureus</i> with various concentrations, (a) (upper half 10 µg/mL concentration and lower half 20 µg/mL concentration) and (b) 30 µg/mL.....	151
Figure 7-28 (a) Antimicrobial activity of QM5-3 against <i>S. aureus</i> Minimum bactericidal concentration assay, (b) Time-kill assay at 30 µg/mL concentration	151
Figure 7-29 Quantitative growth assay of QM5-based composite QM5 (unmodified CPW-80), QM5-1 (CPW-80 modified with only iron oxide nanoparticles), QM5-2 (CPW-80-modified with only silver nanoparticles) and QM5-3 (CPW-80 modified with silver coating iron oxide) against <i>E. coli</i> (blue bar) and <i>S. aureus</i> (orange bar)	152
Figure 7-30 Schematic representation of recycling of the developed nanocomposite	155
Figure 7-31 (a,b and c) control plates of <i>E. coli</i> in triplicate.....	157
Figure 7-32 Recycling of QM1-3 composite against <i>E. coli</i> in triplicate three times: (a-1,a-2 and a-3) are the first use of the QM1-3 composite against <i>E. coli</i> , (b-	

1,b-2 and b-3) are the re-use of composite for the second time, (c-1,c-2 and c-3)	
are the re-use of the composite for the third time against <i>E. coli</i>	157
Figure 7-33 Harvesting of QM1-3 against <i>E. coli</i>	158
Figure 7-34 (a,b and c) control plates of <i>E. coli</i> in triplicate for QM2-3	
nanocomposite.....	158
Figure 7-35 Harvesting of QM2-3 composite against <i>E. coli</i> in triplicate three times:	
(a-1,a-2 and a-3) are the first use of the QM2-3 composite against <i>E. coli</i> , (b-	
1,b-2 and b-3) are re-use of composite second time and (c-1,c-2 and c-3) are the	
re-use of the composite third time.....	159
Figure 7-36 Harvesting of QM2-3 against <i>E. coli</i>	160
Figure 7-37 (a) shows the recycling of QM1-3 (blue) and QM 2-3 (orange) against <i>E.</i>	
<i>coli</i> respectively	161
Figure 7-38 MBC of all developed composites. (\pm SD, No=3)	162
Figure 7-39 Time-kill assay of all developed composites. (\pm SD, No=3)	163
Figure 7-40 Surface amine densities of nanocomposite (a) APTS functionalised	
measuring in coupling solution (b) APDS functionalised measuring in coupling	
solution (\pm SD, No=3).....	167
Figure 7-41 Surface amine density of five modified commercial nanomaterials	
(QM1-3 to QM5-3), (a) APTS functionalised measuring in hydrolysis solution,	
(b) APDS functionalised in hydrolysis solution. (\pm SD, No=3)	168
Figure 7-42 (a) Oligonucleotide-grafted composite of QM1-3, QM2-3, QM3-3, QM4-	
3 and QM5-3 on APTS surface functionalised materials, (b) Oligonucleotide-	
grafted composites of QM1-3, QM2-3, QM3-3, QM4-3 and QM5-3 on APDS	
surface functionalised material. (\pm SD, No=3)	170
Figure 7-43 (a) Hybrid capture assay of complementary sequence of all APTS	

functionalised oligonucleotide-grafted nanocomposites (b) Hybrid capture assay with complementary sequence of all APDS functionalised oligonucleotide-grafted nanocomposites composites. (\pm SD, No=3)	173
Figure 7-44 Dehybridisations of captured <i>E. coli</i> specific oligonucleotides via APTS functionalisation route (b) Dehybridisations of captured <i>E. coli</i> specific oligonucleotides via APDS functionalisation route. (\pm SD, No=3).....	177
Figure 7-45 Optimisation of extracted <i>E. coli</i> DNA	180
Figure 7-46 PCR results: of samples (a) Oligonucleotide grafted QM1-3 with APTS and APDS along with oligonucleotide QM3-3 with APTS and control, (b) Oligonucleotide grafted QM2-3 with APTS and APDS along with control. (c) Oligonucleotide grafted QM4-3 QM5-3 with APTS and APDS along with control, (d) QM1-3 and QM3-3 with APTS, APDS (without grafted oligonucleotides), ladders 100pb, (e) QM2-3 with APTS, APDS (without grafted oligonucleotides) along with control and (f) QM5-3 and QM4-3 with APTS and APDS (without grafted oligonucleotides), with control.....	182
Figure 7-47 Surface amine density of five commercial nanomaterials (QM1-3 to QM5-3), (a) APTS and APDS functionalised measuring in hydrolysis solution . (\pm SD, No=3).....	185
Figure 7-48 Oligonucleotide-grafted composite of QM1-3, QM2-3, QM3-3, QM4-3 and QM5-3 on APTS and APDS. . (\pm SD, No=3)	186
Figure 7-49 Hybrid capture assay of complementary sequence of all APTS and APDS functionalised oligonucleotide-grafted composites. (\pm SD, No=3).	187
Figure 7-50 Dehybridisations of captured <i>E. coli</i> specific oligonucleotides of all APTS and APDS functionalised material . (\pm SD, No=3).	188

List of Tables

Table 1-1. Important preparation methods of SPIONs	8
Table 2-1. Complete table of buffers and chemical solutions.....	28
Table 2-2. Amino modified oligonucleotides of <i>E. coli</i> , along with the corresponding complementary sequences.....	28
Table 2-3. Host–guest matrices with characterisation	34
Table 3-1. BET analysis of unmodified QM1 and modified QM1-based magnetite silver nanocomposite.....	60
Table 4-1. BET analysis of unmodified QM2 and modified QM2-based magnetite silver nanocomposite.....	74
Table 5-1. BET analysis of unmodified QM3 and modified QM3-based magnetite silver nanocomposite.....	91
Table 6-1. BET analysis of unmodified QM4 and modified QM4-based magnetite silver.....	105
Table 6-2. BET analysis of unmodified QM5 series nanocomposites.....	120
Table 7-1. Applied nanocomposites (QM1-3, QM2-3, QM3-3, QM4-3 and QM5-3 (MWCNTs, AC, DAE, CPW-14 and CPW-80-based nanocomposites respectively, modified with iron and silver nanoparticles) and bacterial strains	126
Table 7-2. Tested bacterial strains	126
Table 7-3. Summary for the silanisation of the modified materials in APTS and APDS. (\pm SD, No=3)	169
Table 7-4. Conjugation of oligonucleotides on APTS and APDS surface functionalised material. (\pm SD, No=3).....	172

Table 7-5. Summary for the capture efficiency of complementary sequences of all the surface functionalised materials. (\pm SD, No=3).....	175
Table 7-6. Summary for the dehybridisation of complementary sequences of all the surface functionalised materials. (\pm SD, No=3).....	179

Acknowledgements

I would like to extend a special thanks to Dr Tapas Sen for the opportunity to work with him on this project. I am extremely grateful for all the help, guidance and continued support he has provided throughout my PhD project at UCLan. I would like to thank Prof: Waqar Ahmed, for his guidance and continued support he has provided throughout my PhD work at UCLan. I would like to acknowledge Mr Gary Hogben, technical manager, feed water Ltd, UK for giving me the access to work in their research laboratory and his valuable time and feedback.

I extended my thanks to Shah Abdul Latif University Khairpur Mir's for financial support and providing me with the opportunity to pursue my higher studies to abroad. I also sincerely acknowledge UK-India Education and Research Initiative (Grant Ref. IND/Cont (E) 14-15/055) for giving me the opportunity to work in that project and partial financial support. I am indebted to the following people for their help with analysis of my samples and general advice Dr Runjie Mao (UCLan, UK) for his help with BET surface area, Dr Sibte Hadi (UCLan UK) for his help with PCR, and all of the technicians and staff from the analytical unit at UCLan, I am also thankful to Dr Karl Dawson University of Liverpool for providing TEM facility.

I would thank my parents, family and friends for their continued support and encouragement. Finally, I would like to give special thanks to my wife and children for their continued love and support during my work.

List of Abbreviations

AC	Activated Charcoal
Ag	Silver
AgNPs	Silver nanoparticles
APDS	3-aminopropyl di-ethoxymethylsilane
APTS	3-aminopropyl tri-ethoxysilane
ATP	Adenosine triphosphate
BET	Brunauer–Emmett–Teller
BSA	Bovine serum albumin
CPW-80	Celatom powder-80
CPW-14	Celatom powder-14
CNT	Carbon nanotube
DAE	Diatomeous earth
DNA	Deoxyribonucleic acid
dNTP	Deoxyribonucleotide triphosphate
DP	Drop Plate method
EC	<i>Escherichia coli</i>
EDAX	Energy dispersive X-Ray analysis
FT-IR	Fourier transforms infrared spectroscopy
Fe ₃ O ₄	Magnetite
<i>K. Pneumoniae</i>	<i>Klebsiella pneumoniae</i>
MWCNTs	Multi-wall carbon nanotubes

4-NBA	4-nitrobenzaldehyde
NaBH_4	Sodium borohydride
<i>P. aeruginosa</i>	<i>Pseudomonas aeruginosa</i>
PBS	Phosphate buffered saline
PCR	Polymerase chain reaction
PVA	Polyvinyl alcohol
PVP	Poly vinyl pyrrolidone
QM1	Carbon nanotube
QM2	Activated charcoal
QM3	Diatomeous earth
QM4	Celatom -14
QM5	Celatom -80
SEM	Scanning Electron Microscopy
SP	Spread plate method
SPIONs	Superparamagnetic iron oxide nanoparticles
SSC	Buffer consisting of sodium chloride, sodium citrate and water
TEM	Transmission electron microscopy
XRD	X-Ray diffraction
XRF	X-Ray fluorescence

List of Units

Å	angstrom = 1×10^{-10} m	mins	minutes
°C	degree Celsius	mL	millilitre (1×10^{-3} L)
CFU	colony forming units	mm	millimetre (1×10^{-3} m)
emu	electromagnetic units	mmol	millimoles (1×10^{-3} moles)
fg	femtogram (1×10^{-15} g)	µg	microgram (1×10^{-6} g)
g	gram	µL	microlitre (1×10^{-6} L)
h	hour	µm	micrometre (1×10^{-6} m)
K	degree Kelvin	µmol	Micromoles (1×10^{-6} moles)
kOe	kilooersted (1×10^3 Oe)	nm	nanometre (1×10^{-9} m)
Km	kilometre (1×10^3 m)	nmol	nanomoles (1×10^{-9} moles)
kV	kilovolt (1×10^3 V)	rpm	revolutions per minute
m	metre	v/v	volume per volume
M	molarity (moles per litre)	w/v	weight per volume
mg	milligram (1×10^{-3} g)		

List of Publications

Qurban Ali, Waqar Ahmed, Sham Lal and Tapas Sen (2017) Novel multifunctional carbon nanotube containing silver and iron oxide nanoparticles for antimicrobial applications in water treatment. *Materials Today: Proceedings*,4(2017), pp.57-64.

Qurban Ali, Waqar Ahmed and Tapas Sen (2018). Nanotechnology, their contribution in modern world for the purification of water. *Hand book of Nano and biomaterials*. Elsevier (submitted)

CHAPTER ONE

1 Introduction and literature review

1.1 Nanotechnology and nanoscale

Nanotechnology is generally referred as the engineering and manufacturing of the materials at the atomic and molecular scale (Farokhzad and Langer, 2009). It covers the structure ranges from 1-100 nm in at least one dimension (Farokhzad and Langer, 2009). However, it has been observed that the nanotechnology covers several hundred nanometres in size. It deals with the study of the nanoparticles or materials which exists in the nanostructure; the prefix nano stands for the billionth part of a metre: numerically it is written as 1×10^{-9} metre.

Nanocomposites are generally prepared by the incorporation of the nano-size particles such as Ag and Au into the host matrix (e.g. silica) to improve the properties of the materials; hence it could be concluded that nanocomposite matrix is the product obtained by the addition of the nanoparticles into the host material. Incorporated nanoparticles change the properties of the matrix owing to their high surface-to-volume ratio, compared to their bulk materials. Nanocomposite materials have remarkable potential due to their applications in the immobilization of proteins and enzymes (Hodgson B.J., 2013, Sen and Bruce, 2012, Sen *et al.*, 2010, Sebastianelli *et al.*, 2008, Sen *et al.*, 2006, Rudge *et al.*, 2000, Varlan *et al.*, 1996). Nanoparticles are important because of their size in nanometre length scale and an exceptionally high surface area in m^2/gm for various applications (Sotiriou and Pratsinis, 2010). Recently, a new branch “Nanomedicine” has evolved using nanomaterial for disease detection and cure. For example, surface engineered super paramagnetic iron oxide nanoparticles (SPIONs) have already been exploited in nanomedicine (Mahmoudi *et al.*, 2011) as contrasting agents for Magnetic Resonance Imaging (MRI).

1.2 Types of nanocomposites

Numerous nanocomposites have been reported and studied, and those in our research included carbon-based materials, silica based materials, and superparamagnetic iron oxide nanoparticles.

1.2.1 Carbon-based materials

There are two major types of carbon-based materials reported to be useful in various applications:

i) Activated charcoal: Activated charcoal has been used as a host matrix for the development of the nanocomposites and is administered where patient has taken a poison (Chyka *et al.*, 2005, Chyka and Seger, 1997). Activated charcoal is used as adsorbate because of its high surface area and pore sizes. It is utilised for the purification of drinking water, treatment of dyes, metal ions, and to get rid of the environmental hazards by reducing the cost of waste disposal from non-renewable resources. By the addition of copper with carbon, it can be used for the removal of the As III from liquid samples (Ioannidou and Zabaniotou, 2007). The report has shown that binary mixture of the carbon produced from almonds and pecans are very efficient for the removal of heavy metals from drinking water such as zinc (Zn^{2+}), lead (Pb^{2+}) and copper (Cu^{2+}) (Ioannidou and Zabaniotou, 2007). Some pathogenic and coliform organisms are grown on the carbon to examine their coliform organisms to the chlorine disinfection (Lechevallier *et al.*, 1984).

ii) Multi-wall carbon nanotube: Multiwall carbon nanotubes (MWCNTs) are unified cylinders of layers of single walled carbon nanotubes (Harris, 2009, Iijima, 1991). Owing to the high surface of the carbon nanotubes and their porosity, they possess high electronic conductivities and efficient chemical properties. Furthermore,

it has been reported (Kang *et al.*, 2007) that carbon nanotubes (CNTs) have potential applications as antimicrobial agent. By narrowing the diameter of the nanotubes, the antimicrobial properties have reported to be increased (Kang *et al.*, 2007). The carbon nanotube possesses the properties of adsorption of the heavy metals from the water such as Zn^{2+} (Lu and Chiu, 2006). MWCNTs have the highest adsorption capability for the removal of the biological contaminants from drinking water, which include virus, bacteria and cyanobacterial toxins from the water storage and supply system due to its structural and functional properties (Upadhyayula *et al.*, 2009).

1.2.2 Silica-based materials

i) Diatomaceous earth and its applications

It is of the high interest among the researchers because of its novel properties such as high surface area, chemical inertness, small particle size, high porosity, low thermal conductivity and high permeability (Bailey *et al.*, 1999). Diatomaceous earth is the product of fossils of aquatic and tiny organisms which are called diatoms. On the decomposition of the skeletons of marine life, they convert into the silica. Along with the passage of hundreds and thousands of years, diatoms have been deposited into rivers, lakes, oceans and streams and have made mines in water. This is sedimentary mineral rock and is obtained from fossilised remnants or marine single-celled algae which contain cell walls made up of silica (Armbrust *et al.*, 2004). Diatoms are produced from remains of algae-like plant remains in the surface of the earth. These are chalky and clay-like remains, which commonly occur in the siliceous, white and thick powder known as diatomaceous earth (Armbrust *et al.*, 2004). Silica is a component of the earth's crust, silicon a component of the silica is not found in a pure state but can occur in several forms of silica such as sand, emerald, quartz, feldspar, mica, clay, asbestos, and glass with oxygen. Silicon is mainly deposited into rivers and

sources of water hence reacts with the oxygen and water to form silicon dioxide (SiO_2). Diatomaceous earth is obtained with high purity almost as much as 85% silica SiO_2 . Hence, due to its purity, this material is odour free and non-toxic. It is a naturally occurring material in abundance, so it is also inexpensive. Some interesting properties of diatomaceous earth have been given below.

It is commonly used as toothpaste and facial exfoliator because of its robust abrasive properties, which help to remove dead skin cells and help to give freshness to new skin cells. It has been reported that diatomaceous earth has been used as a natural pesticide and provides the shield for stored agricultural yields (Korunić and Mackay, 2000) without using toxic chemicals, which are harmful for the environment as well as human health.



Figure 1-1 Diatomaceous earth (Schatzlein, 2015)

1.2.3 Superparamagnetic iron oxide nanoparticles

Superparamagnetic iron oxide nanoparticles (Fe_3O_4), have been used extensively because of its non-toxic behaviour with the advantage of one-step magnetic separation (Sen *et al.*, 2012, Lasota, 2014). Various groups (Chudasama *et al.*, 2009) have prepared $\text{Ag}/\text{Fe}_3\text{O}_4$ magnetic nanocomposites and tested their antibacterial performance. The composite of silver magnetite ($\text{Ag}/\text{Fe}_3\text{O}_4$) is prepared in two steps: in the first step magnetite (Fe_3O_4) is prepared, and in second step is coated with AgNPs by reducing the appropriate silver salts with a reducing agent. In this context, Fe_3O_4

is an important nanomaterial for the introduction of superparamagnetism in the nanocomposites. Improper coatings of AgNPs cause the oxidation of magnetite (Fe_3O_4) to maghemite (Fe_2O_3). Silica coating also saves the magnetite core and helps the immobilisation of the silver nanoparticles.

1.3 Synthesis of nanomaterials

1.3.1 Synthesis of iron oxide nanoparticles

Three main methods for the synthesis of the magnetic nanoparticles are discussed below.

- 1) Biomineralization
- 2) Physical method
- 3) Chemical method

Biomineralization: This route is used by some living organisms such as magnetotactic bacteria for the preparation of the nano sized crystals of magnetic iron oxide for their sense of direction (Krishnan, 2016) of uniform particle sizes of 20 to 45 nm (Timko *et al.*, 2013)

Physical methods: This method is divided in two sub methods “top down” and “bottom up”. Top down method is used for the conversion of macroscopic magnetic materials to the nano scale by means of milling but the required particle size and shapes cannot be achieved by these methods. Bottom up method involves the condensation of liquid or gaseous phase for the synthesis of nanoparticles. For example, laser evaporation in which metal oxide powders of small sized particles ranged in μm , are evaporated by a laser where nucleation and condensation takes place from gaseous phase and nanoparticles are prepared (Kurland *et al.*, 2009).

Chemical methods: This method is used for the development of the magnetic nanoparticles by using techniques such as, co-precipitation, thermal decompositions, micro-emulsion and hydrothermal.

- i. **Co-precipitation synthesis** This method uses the aqueous media for the development of the magnetic nanoparticles. Commonly Fe^{2+} and Fe^{3+} salt solutions are used along with base for the development of magnetic nanoparticles (Zhang *et al.*, 2011). The particle size and shape are controlled with the variation of the iron salts, temperature, pH and bases (Cornell and Schwertmann, 2003).
- ii. **Thermal decomposition:** In this method organometallic compounds are boiled in organic solvents to prepare the magnetic nanoparticles with monodisperse and narrow size distribution (Hyeon *et al.*, 2001, Park *et al.*, 2005). For example, iron acetylacetonates, iron carbonyls or cuproferronates are used as precursors in organic solvents in the presence of hexadecyl amine or oleic acids which are used as surfactants. The size and morphology of the nanoparticles is controlled with variation of solvents and surfactants.
- iii. **Micro-emulsion synthesis:** This method is also called as two-phase method in which water droplets are used in an oil phase, stabilised by surfactant molecules at the water oil interface (Zhou *et al.*, 2001) and is used to prepare the uniform particles with narrow size distribution (Okoli *et al.*, 2012).
- iv. **Hydrothermal synthesis:** This method is employed at high temperature (200 $^{\circ}\text{C}$) and high pressure at (2000 psi). In this method, metal salts are dehydrated at high temperature which causes the precipitation (Hao and Teja, 2003). Particle size and morphology are controlled by the variation of concentration, autoclaving time and temperature.

- v. **Polyol synthesis:** this method is based on the hydrolysis of oxidative alkaline of Fe^{2+} and Fe^{3+} salts in a polyol mixture such as methyl diethanol amine, diethylene glycol, poly ethylene glycol. The size and shape of the particles can be controlled with the variation of solvents or reaction factors. (Hugounenq *et al.*, 2012). Important synthesis methods for the SPIONs are summarised in Table1-1.

Table 1-1. Important preparation methods of SPIONs

Synthetic method	Advantages	Disadvantages	References
Co-precipitation	Rapid preparation with high yield	Problem of oxidation and aggregation	(Sen <i>et al.</i> , 2012, Bruce <i>et al.</i> , 2004, Bruce and Sen, 2005, Mahmoudi <i>et al.</i> , 2008, Mahmoudi <i>et al.</i> , 2010, Zhang <i>et al.</i> , 2011)
Hydrothermal reactions	Small size distribution and good control, scalable	Long reaction times	(Wang <i>et al.</i> , 2005)
High temperature decomposition	Good control of size and shape, High yield	Furthers steps needed to obtain water stable suspension	(Park <i>et al.</i> , 2004)
Microemulsion	Control of particle size	Poor yield and large amounts of solvent required, excess of surfactant to eliminate	(Narita <i>et al.</i> , 2009)

1.3.1.1 Types of magnetic particles

There are four types of magnetic materials and they are known as ferromagnetic,

antiferromagnetic, paramagnetic and antiferromagnetic. The magnetic spin alignment of each material has been presented in Figure 1-2.

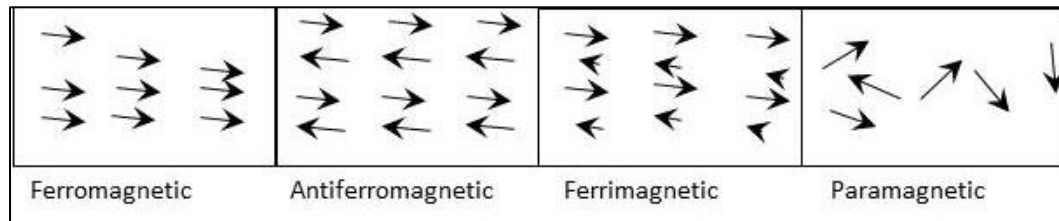


Figure 1-2 Types of magnetic particles

i) **Ferromagnetic**

The types of the magnetic materials in which movements of the magnetic vectors are aligned, show natural magnetisation due to the enduring magnetic field. These types are the most common magnetic materials (e.g. α - Fe_2O_3 or hematite)

ii) **Ferrimagnetic**

The types of the magnetic materials in which movements of the magnetic vectors are in two directions: aligned along with and anti-aligned. These types of magnetic materials include bulk magnetite (Fe_3O_4).

iii) **Paramagnetic**

These types of magnetic materials are not oriented and aligned in one direction but scattered randomly.

iv) **Antiferromagnetic**

These types of magnetic materials possess the magnetic movements aligned in regular and opposite direction, a slight ferromagnetic behaviour is observed when an external field is applied (Dzyaloshinsky, 1958).

1.3.1.2 Superparamagnetism

It has been noted that superparamagnetism is found in the ferri- or ferromagnetic nanoparticles, due to their size as these consist of one single magnetic domain. By varying the temperature, the magnetic movements change randomly in any direction along with the time. Superparamagnetic nanoparticles are easy to separate from the reaction components by applying the external magnetic field; hence these are efficient and far better particles compared to other magnetic particles. The superparamagnetic particles are dispersed and avoid aggregating without magnetic attraction to each other in the absence of magnetic field.

The preparation of core-shell magnetic nanoparticles with super paramagnetic Fe_3O_4 core and amorphous silica shell has been extensively studied, whereas similar materials with meso (Sen *et al.*, 2006) or micro-porous silica shell have been reported on account of their improved surface area and size selectivity. Mesoporous silica-magnetite materials were first reported by Wu *et al.*, 2004 but the materials were irregular in shape and sizes. Zhao *et al.*, 2005 have reported a multi-step process for the synthesis of porous magnetic silica microspheres by a one-step coating process of mesoporous silica shell on magnetite core. Nanocrystals by surfactant templating route have been reported by Sen *et al.*, 2012, due to their importance in chemical and biological applications.

Mostly, the core shell structure can be formed from magnetite or maghemite cores, and the shell can be amorphous silica (Bruce *et al.*, 2004, Philipse *et al.*, 1994) or porous silica (Sen *et al.*, 2006, Wu *et al.*, 2004). The shape and size of the core are considered to be the fundamental parameters for the morphology of such nanocomposites. The general strategy for post-synthesis dispersion of aggregated magnetite nanoparticles suspension by treatment with commercially available, cheap

dispersing agents is also reported (Sen *et al.*, 2006).

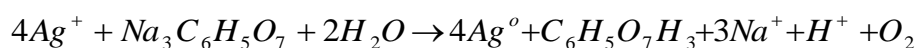
Magnetic nanocomposites of mesoporous silica shell around a magnetic core are an exciting type of nanocomposites of high surface area and magnetic properties (Sen *et al.*, 2006, Bruce *et al.*, 2004, Long *et al.*, 2004) and have been used in several applications e.g. magnetic bio-separation (Sen *et al.*, 2006) controlled drug delivery (Sen and Bruce, 2012, Sharifabad *et al.*, 2013, Sharifabad *et al.*, 2013, Rother *et al.*, 2011, Kim *et al.*, 2003) and magnetic contrasting. Sen and Bruce, 2012, Zhao *et al.*, 2005, Lee *et al.*, 2009, Deng *et al.*, 2009 have reported the fabrication of a magnetic core-shell zeolite for the immobilization of protein (trypsin). Porous materials from microporous to macroporous (pore diameter > 50 nm) have evolved as a result of extensive research during the last twenty years in order to overcome the diffusional limitation of bulkier biomolecules, i.e. protein and enzymes, through the micro/mesopores. Sen *et al.*, 2006 pioneered hierarchically ordered porous silica nanocomposites with interconnecting micro, meso and macroporosity, using a dual template-assisted synthesis protocol.

1.3.2 Synthesis of silver nanoparticles

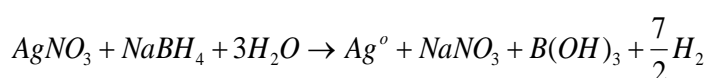
Silver nanoparticles are commonly prepared by chemical reduction and electrolysis methods. The production of stable silver nanoparticles *via* chemical reduction method depends on the suitable stabiliser and reducing agents (Song *et al.*, 2009). The size and aggregation state of synthesised silver nanoparticles through chemical reduction method is affected by several factors which include the concentration of the reducing agents and stabilisers. By using the excess amount of reducing agent (NaBH₄) causes the nanoparticles to disperse due to the formation of (BH₄⁻) which prevent the boron hydroxide layer on the surface of prepared silver nanoparticles (Song *et al.*, 2009). For the controlled size nanoparticles of silver, a two-step method is applied, Firstly, a

strong reducing agent is utilised for the preparation of nuclei particles followed by the enlargement of particles by using a weak reducing agent (Schneider *et al.*, 1994, Shirtcliffe *et al.*, 1999).

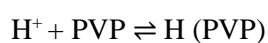
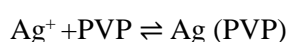
The chemical reduction mechanism for the preparation of silver nanoparticles by using silver nitrate (AgNO₃) and tri-sodium citrate Na₃C₆H₅O₇ is shown below.



The chemical reduction mechanism for the preparation of silver nanoparticles by using silver nitrate (AgNO₃) and sodium borohydride (NaBH₄) is shown below.



PVP is used as a dispersant for the preparation of silver nanoparticles of small size, which helps to avoid from the agglomeration, growing and aggregation. The silver nanoparticles of smaller size less than 50 nm are protected with the bonding of silver and N₂ while the bigger size silver nanoparticles, with the size of 500-1000nm, are protected with the co-ordination covalent bonding of silver with O₂ and N₂. PVP makes a coordinate covalent bond with Ag⁺ and H⁺, to make Ag (PVP)⁺ and H (PVP)⁺ complex compounds which make the Ag⁺ and H⁺ more stable. Furthermore, due to Ag⁺, the rate of reaction decreases but due to the stability of H⁺, rate of reaction increases.



Electrolysis method is also used for the preparation of silver nanoparticles, where Ag

/AgCl are considered as a reference electrode. The experiments performed into the electrolysis beaker connected silver sheet as an anode which is polished with fine emery paper followed by the washing with sterilised water and acetone. While platinum rod is considered as a cathode which is polished with the aluminium powder at 0.15V at a scan rate of 500 mVs⁻¹ for 5 minutes in 1.0 M H₂SO₄. Silver is prepared at inert atmosphere with vigorous and continuous stirring. Tetrabutylammonium bromide 0.1 M is used as an electrolyte into the acetonitrile and is degassed with nitrogen for about 15 minutes.

Biological method for the synthesis of silver nanoparticles: In this method, amino, proteins, vitamins and polysaccharides are extracted from bio-organisms which are used as reductant or capping agents (Eby *et al.*, 2009, Sharma *et al.*, 2009) Furthermore, a glucoside compounds, leaf extract from magnolia and pine leaf have been utilised as a reducing agent for the development of silver nanoparticles (Song *et al.*, 2009, Shankar *et al.*, 2003, Kasthuri *et al.*, 2009). It has been reported that (Kalishwaralal *et al.*, 2008, Mokhtari *et al.*, 2009, Ahmad *et al.*, 2003) numerous microbes such as *K. pneumonia*, *Bacillus licheniformis*, and fungi strains such as *Verticillium*, synthesises the silver nanoparticles.

Solvated metal atom dispersion (SMAD) method: In this method a cooled liquid nitrogen surface is used, where metal and solvent are co-vaporized in which metal atom is aggregated by the removal of liquid nitrogen (Stoeva *et al.*, 2002). Narrow sized monodispersed silver nanoparticles can be prepared by further treating them with ligands in an inert atmosphere (Smetana *et al.*, 2008).

1.4 Frequently found bacteria in water sources and their impact on human health

According to Dutil *et al.*, 2007, the opportunistic water borne pathogens such as *E. coli*, *Pseudomonas aeruginosa*, non-tuberculosis *Mycobacterium* spp and *Legionella* spp can cause respiratory diseases. It has been suggested that there are more than 25 species of bacteria which are frequently found in water and its sources. Numerous species of fungi and protozoa have also been found in water sources (Göksay *et al.*, 2008, Pankhurst and Coulter, 2007, Singh and Coogan, 2005, Szymańska, 2005). These all cause health hazards and infections for humans and especially in immunocompromised patients (Pankhurst and Coulter, 2007, O'donnell *et al.*, 2007, Singh *et al.*, 2003). Among these bacteria, Gram-negative aerobic heterotrophic are found in abundance.

Pseudomonas aeruginosa is the most commonly found bacterium in water as it needs a low level of nutrient to survive. It has been reported that *Pseudomonas aeruginosa* is highly resistant to antibiotics, disinfectants and biocides and can grow in iodophors and chlorhexidine disinfectants in diluted form (Barbeau *et al.*, 1996, Atlas *et al.*, 1995). Elderly and immuno-compromised people are affected and may, consequently, be susceptible to *pneumonia* (Pankhurst and Coulter, 2007). There are several bacteria which need to be discussed here: among this species *Legionella pneumophila* and several other species of *Legionella* are commonly found in the water sources which cause Legionnaire's disease. It has been reported that six to thirty percent of domestic hot water systems produce *Legionella* (Barbeau *et al.*, 1996) because *Legionella* grows at 20-45°C in the presence of host amoebae as a nutrient source (Wadowsky *et al.*, 1985). It causes pontiac fever, a mild flu like illness, which affects members of the

male sex, alcoholics, smokers, diabetic patients and patients with chronic respiratory or renal disease and cancer (Fields *et al.*, 2002).

A German bacteriologist, Dr Theodor Escherich, first discovered the bacteria in 1885 in the human colon and it was named bacterium *coli* but later on, it was given the name *Escherichia coli* after its discoverer (Feng *et al.*, 2002). *Escherichia coli* (*E. coli*) is the substantial widespread infecting organism in the species of Gram-negative bacteria known as Enterobacteriaceae (Eisenstein and Zaleznik, 2000). He suggested that it causes gastroenteritis and diarrhoea in infants (Feng *et al.*, 2002). There are more than 700 serotypes of *E. coli* and it is considered the most studied organism (Eisenstein and Zaleznik, 2000). It has been found that most of the strains of *E. coli* do not cause any illness or infections but a few of them cause urinary tract infections and gastrointestinal infections (Eisenstein and Zaleznik, 2000).

E. coli is commonly used in laboratories via a simple and quick growth in various media. Moreover, it can grow both in the presence and the absence of oxygen. Some strains of *E. coli* are precious and help the digestive system of humans and animals, while a few strains, such as *E. coli* O157:H7, are hazardous and cause serious diseases.

Shigella dysenteriae type 1 *E. coli*, which includes strains O157: H7, contaminates foods and beverages (Eisenstein and Zaleznik, 2000, Griffin and Tauxe, 1991), causing around 90 deaths, 3000 cases requiring treatment in hospitals and 100,000 diseases in a year in America (Gould *et al.*, 2009, Mead *et al.*, 1999). Furthermore, it was reported that \$405 million were spent on the treatment of illness caused by the *Shigella dysenteriae* type 1 *E. coli* in America in 2003 (Frenzen *et al.*, 2005).

Common symptoms of *E. coli* intestinal infection arise from day one to day five.

The following are some of the signs of *E. coli* infections: intestinal cramping,

unexpected critical watery diarrhoea may sometimes turn into bloody stools, may cause gas, lack of appetite, tiredness, vomiting and high temperatures. According to NHS recommendations, drinking water and swimming in contaminated ponds and streams can cause the *E. coli* infection if the water is not properly treated with antibacterial agents. It has been reported that 20 microorganisms of *E. coli* are fairly likely to cause infection in people and can be life-threatening for the patient (Griffin *et al.*, 1994). The serotype of *E. coli* is a threat to human life as they transfer from one patient to another and cause diseases (Griffin and Tauxe, 1991, Rangel *et al.*, 2005). The Shiga toxin-producing strains of *E. coli* cause a frightening and critical infection which is known as hemolytic uremic syndrome (HUS) (Griffin and Tauxe, 1991, Rangel *et al.*, 2005).

Children are mostly affected by this infection, which causes death and chronic injuries, and this acute infection has been found after five to ten days of diarrhoea, which results in renal failure (Garg *et al.*, 2003, Safdar *et al.*, 2002, Jay, 2000, Tauxe, 1997, Bell *et al.*, 1997, Su and Brandt, 1995). Furthermore, after HUS infection, 50% of affected children needed dialysis while the remainder suffer from several ineffective incurable complications which include critical brain damage, renal impairment and diabetes (Safdar *et al.*, 2002, Siegler, 2003, Robitaille *et al.*, 1997). After infecting the patient's blood, it creates blood clots and destroys blood cells (Garg *et al.*, 2003) and attack the patient's organs, mainly the brain, pancreas and kidneys (Su and Brandt, 1995, Siegler, 1995).

These infections caused by the *E. coli* have been known since the 1950s by medical societies and have been known by people in general since 1993 as a result of an outbreak of this infection in America. The spread of the infection was considered to be due to the consumption of contaminated hamburgers (Griffin *et al.*, 1994, Bell *et*

al., 1994). Moreover, abdominal cramping, pain, constipation and diarrhoea were the result of drinking *E. coli* contaminated water (Marshall *et al.*, 2006, Hungin *et al.*, 2005). By the consumption of *E. coli* contaminated water, 2300 people were affected, out of which 27 people were diagnosed as HUS patients, 7 patients died and 5% to 30 % of patients faced gastrointestinal infection (Marshall *et al.*, 2006).

E. coli is fecal coliform and is found in the intestine of living animals, which include pigs, deer, sheep, chickens, goats and mainly from dairy cattle, so animals are the best place for the bacteria (Eisenstein and Zaleznik, 2000, Elder *et al.*, 2000). According to the published report of America, 20 people die annually as a result of being infected by the bacteria in America (Scallan *et al.*, 2011). In 1993, the food-borne diseases were brought to the attention of the public by the presence of *E. coli* in fast food hamburger (Falkenstein, 2018).

The *Staphylococcus* is a Greek term (staphyl = bunch, Kokkos = grapes, aureus = golden), so its' meaning is a golden bunch of grapes, the name being given on the basis of their appearance and shape when seen in the microscope as round bunches about 1µm in diameter. It is a Gram-positive type of bacteria also known as Staph and was discovered in 1884 by Rosenbach. It is divided into two main types based on their capability to clot blood plasma (Levinson and Jawetz, 2000) coagulase-positive and coagulase-negative. Coagulase-positive *Staphylococcus aureus* (*S. aureus*) causes the severe infections, while negative is friendly. This bacterium causes severe infections in a body *via* a wound or respiratory tract.

There are several infections and diseases, which include skin lesions (Bhakdi and Tranum-Jensen, 1991) and deep-seated infections such as osteomyelitis and endocarditis. Furthermore, there are more serious skin infections (furunculosis),

nosocomial infection in surgical wounds, food poisoning due to the release of enterotoxins into food, toxic shock syndrome, urinary tract infections particularly in females (Prevost *et al.*, 1995, Foster and McDevitt, 1994, Foster, 1991, Lyon and Skurray, 1987, Easmon and Adlam, 1983). *S. aureus* is well known for causing boils, styes and furuncles; it may cause more severe infections such as: traumatic injury, burns and chronic illness. Furthermore, *S. aureus* causes several diseases to patients admitted into hospitals which include: osteomyelitis, pneumonia, deep abscesses, mastitis, phlebitis, endocarditis, and meningitis. Moreover, they are the source of infections of the medical devices that are jointly used for the patients such as artificial heart valves and cardiovascular devices (Levinson and Jawetz, 2000). It is found in unicellular form, pairs and in clusters like a bunch of grapes. *S. aureus* is found in the nasal passage and axillae (Levinson and Jawetz, 2000).

The bacterial endotoxin is composed of lipopolysaccharide and is delivered from cell walls of dead Gram-negative bacteria in water. It may cause high-grade fever, shocks, local inflammation, and severe asthma at high concentration of the bacteria. The presence of bacterial endotoxin in dental unit waterline severely influences the healing of dental treatment (Putnins *et al.*, 2001). The opportunistic pathogens are commonly found in municipal water systems (Pankhurst and Coulter, 2007, Rusin *et al.*, 1997) and cause systematic infections such as pneumonia and cutaneous.

For the microbial contamination of water over last few decades, numerous methods have been applied to reduce the microbial contamination of water. Among these approaches, chemical and non-chemical methods have been used by preparing the biocides and chemicals. But still, both strategies are not effective for the removal of microbes.

The properties like large surface areas of carbon and their composites are ideal adsorbent candidates for water purification (Sreeprasad *et al.*, 2011). It has been reported that MWCNTs are the best materials for the removal of chemical contaminants from drinking water due to the large surface area and mesoporous nature (Hemraj-Benny *et al.*, 2008). Four different classes of nanoscale materials are being considered to be important for water purification: metal-containing nanoparticles, carbon-containing nanoparticles, zeolites and dendrimers, carbon nanotubes and carbon nanofibers (Tiwari *et al.*, 2008). In order to obtain the bacteriostatic water filters for household use or for the purification of swimming pools algacides (Wang *et al.*, 2013), AgNPs have been used with the organic biocides and inorganic active reagents (Sharma *et al.*, 2009).

1.5 Antimicrobial features of nanomaterials

Nanoparticles have attracted the attention in the world as an antimicrobial material due to the ineffectiveness of the traditional antimicrobial substances (Seil and Webster, 2012). Researchers have found in *in-vitro* studies that antimicrobial effect depends on concentration and size of the nanoparticles along with the type of the materials, for example, copper, silver, zinc etc. (Seil and Webster, 2012). ZnO was used to reduce the growth of bacteria, and in particular it was used for the gram positive without adding any antibiotic substance (Yamamoto, 2001). The researchers performed this experiment on microscale and nanoscale particles of ZnO on the Gram-positive bacteria and found that nanoscale particles are more effective than the microscale particles due to a high surface area (Yamamoto, 2001, Zhang *et al.*, 2007). In another study on the nanoparticles of the aluminium oxide on *E. coli*, it was found that a smaller size of particle was more effective than a larger size (Simon-Deckers *et*

al., 2009). Furthermore, same type of experiment was performed on the nanoparticles of titanium dioxide (TiO₂) with an average size of 12 to 707nm and it was found that smaller particles were more effective as an antimicrobial agent while larger ones failed to inhibit the growth of the bacteria on the agar plate (Simon-Deckers *et al.*, 2009). Furthermore, now scientists are more interested to prepare the magnetic biosensors for their bio sensing performance and have developed the bioreporter cells with efficiency of 99.96 ±0.01% for the functionalisation of bacterial cell walls with the magnetic nanoparticles (Zhang *et al.*, 2011).

There are many antimicrobial composites but in recent years' silver-based nanocomposites have been given distinct attention by virtue of some brilliant properties, which makes the silver-based material distinct from other antimicrobial additives. For antimicrobial purposes, silver nanoparticles and their composites have a significant role (Rai *et al.*, 2009, Nersisyan *et al.*, 2003, Jeong *et al.*, 2005, Howard, 2011, Ali *et al.*, 2017). Silver has been used as a dental resin component (Herrera *et al.*, 2001). Silver nanoparticles showed antibacterial properties (Feng *et al.*, 2000) by weakening the DNA replication and deactivation of the proteins. Silver nanoparticles have shown the antibacterial properties against a range of the microorganisms (Jeong *et al.*, 2005, Lok *et al.*, 2006) even at low concentration, which causes over 650 diseases in the body. To address problems associated with the collection and reuse of AgNPs, efforts have been made for the incorporation of the AgNPs into the host matrix which include polymers, oxides of different metals, silica, carbon, fibres and several other commercial materials with different nanostructures.

Due to their antimicrobial properties, silver nanoparticles containing composite materials are highly recommended for the inhibition of bacteria. The antimicrobial potential of the silver-containing composite materials depends on the release of the

silver ions, which relies on various factors, including the concentration of the silver powder, soaking time, the surface area of the silver nanoparticles, their size and the nature of dispersion (Kumar and Münstedt, 2005). In another study, silver was incorporated in polypropylene and developed polypropylene/silver composites, which showed the excellent antimicrobial properties (Radheshkumar and Münstedt, 2006) . There are several fillers containing silver polymers composites using polyethylene, polypropylene and polyamides (Brody *et al.*, 2001, Otake *et al.*, 2001).

There are several methods by which antimicrobial composite materials are developed into either organic or inorganic fillers with the incorporation of volatile or non-volatile antimicrobial agent by coating, or adsorbing onto the matrix or host materials depending on the applications (Brody *et al.*, 2001, Gray *et al.*, 2003, Ishitani, 1995). Silver ions from the matrix releases in aqueous medium and acts as biocidal while the polymers and solid matrix are used to make things such as filter kits, catheters garments, ophthalmic vials, fishnets and cannulae etc (Kumar and Münstedt, 2005, Kawashita *et al.*, 2000). The properties of the polymer or matrix, such as matrix polarity and crystallinity, play an important role in the production of silver ions which carry the diffusion at its proceeding step, the more the crystalline and polar, the more will be the diffusion and production of the silver ions in aqueous solution (Markarian, 2004). The silver-based polypropylene composite material has potential to be used for the production of packaging materials, multifilament yarns and antimicrobial ophthalmic vials (Markarian, 2004).

The use of silver as an antibacterial agent is well known for centuries; however, application at the nanoscale is beginning to explore owing to the size and surface area; hence their efficiency in resisting the growth of microorganisms (Sharma *et al.*, 2009, Kiruba *et al.*, 2013, Jung *et al.*, 2008). Silver nanoparticles are bunches of silver atoms

ranging from 1 to 100 nanometre (nm), and are a class of highly efficient new products for the biocidal applications. They have taken attention for the medical and health applications along with antimicrobial agents for the production of water filter kits and water purification. Furthermore, these are not only used for medical and hygiene purposes, but other metal nanoparticles such as titanium, zinc, copper and gold have also attracted the attention of researchers as antimicrobial agents. (Rai *et al.*, 2009).

The study has shown that silver nanoparticles are more efficient antimicrobial agents compared to their bulk counterpart (Chen *et al.*, 2015, Chen and Schluesener, 2008). Silver nanoparticles have been used for the treatment of hospital water i.e. often contaminated with antimicrobial-immune bacteria (Kong and Jang, 2008). Classical methods of treatment of such water generally involve the use of highly concentrated chlorine compounds that can produce halomethane as a by-product, which is a cancer-causing agent. Smaller silver nanoparticles have a greater bactericidal effect than larger silver nanoparticles (Kvitek *et al.*, 2008). Several studies (Dastjerdi and Montazer, 2010, Priester *et al.*, 2009, Sathishkumar *et al.*, 2009, Kumar *et al.*, 2004) have shown that silver nanoparticles are deposited on the cell wall of the bacteria and produce the toxic effect by forming the complexes which can inactivate the vital enzymes.

AgNPs ultra-small size and high surface area per unit mass help their performance in interacting with the bacteria and viruses. The aggregation of the smaller size (around 20 nm) of silver nanoparticles reduces the antimicrobial activity. Hence these ultra-small particles can be incorporated into the host material, including fibres, activated charcoal, zeolites (Chen *et al.*, 2005) to support the AgNPs in dispersing homogeneously into the solid matrix without aggregation.

Antimicrobial properties were assessed against the *S. aureus* and *C. albicans* to develop these draperies as a wound bandage (Deitch *et al.*, 1987). Antimicrobial activity of silver nanoparticles against *E. coli* was also observed and results of which showed that *E. coli* was damaged (Thomas *et al.*, 2007, Sondi and Salopek-Sondi, 2004) so it was used as an antibacterial water filter. In another study, (Montazer and Maali Amiri, 2013), cotton fabrics were smoked with a suspension of silver oxide in chitosan and its antibacterial action against *S. aureus* was found. Low concentration of colloidal Ag-TiO₂ composite and nanotubes has been reported to damage the *E. coli* and *B. subtilis* (Soroushian *et al.*, 2005). Silver-based nanoparticles have been shown to prevent HIV binding to host cells (Chou *et al.*, 2005, Alt *et al.*, 2004, Yeo and Jeong, 2003, Russell *et al.*, 1994).

1.6 Challenge for the project

The challenge for this project was to develop cost-effective nanocomposites with antimicrobial properties. Numerous disinfectants and biocides have been used for inhibiting the growth of pathogenic microbes that produce dangerous carcinogenic by-products in water. According to the World Health Organisation (WHO) report (Lee, 2004), 80% of diseases are due to the contaminated water caused by waterborne bacteria, for example *E. coli*. Therefore, separation of these life-threatening bacteria from water is the big issue for the developing countries of the world. Nanomaterials and nanotechnology can play an important role for the elimination of the microorganism from water. However, most of the materials used for antimicrobial efficiency involved a complex synthesis protocol and expensive to prepare. Hence, search for a range of simple and cheap nanocomposites are in demand in scientific domain.

In this context, nanoparticles with superparamagnetic properties are vital in the nanobiotechnological perspective for sensitive and reproducible separation of biomolecules, e.g. DNA, RNA, proteins and antibodies. Commercial materials such as silica is generally used as an inorganic matrix as it acts as a good dispersing medium with an efficient and easy surface modification. Silica surface is hydrophilic in nature with bio-compatibility hence can be a suitable agent for water treatment processes. The thesis work involved the development of a range of nanocomposites using cheap commercially available materials by simple post-modification in order to introduce multifunctionality for the inhibition of microbial growth in water and detection of specific DNA of water-borne microorganism.

1.7 Aim and objectives of the project

Aim of the project was to develop novel nanocomposites for the inhibition of water-borne microorganisms and detection in water.

The specific objectives are:

1. Development of multifunctional nanocomposites using commercially available materials and their conversion to antimicrobial materials by simple modification through nano chemistry using iron and silver salts.
2. Characterisation of the nanocomposites and understanding the formation of nanocomposites under the different reaction conditions.
3. Applications of nanocomposites for the inhibition of both Gram-positive (*S. aureus*) and Gram-negative (*E. coli*) bacteria.
4. Surface modification of modified nanocomposites with single stranded DNA primers related to water borne microorganisms for the detection of a specific DNA of *E-coli* using polymerase chain reaction (PCR).

1.7.1 Novelty of the project work

The novelty of this project was to convert a range of raw commercial materials (host matrix) into valuable nanocomposites for antimicrobial applications for water purification. Introduction of nanoparticles (silver and iron oxides) as functional nanomaterials (guests) into the host matrix is novel and their surface functionalisation with DNA primers for the detection of microbes' DNA in water has never been studied or published in the literature.

CHAPTER TWO

2 Materials, methods and characterisation techniques

2.1 Materials and methods

All the materials used in this study were commercially purchased. Multi-walled carbon nanotube (QM1) with catalogue number 773840 (MWCNTs), Activated charcoal (QM2) with catalogue number C9157 (AC), Diatomaceous earth (QM3) with catalogue number D3877 (DAE), Celatom-14 (QM4) with catalogue number 243310 Celatom-80 (QM5) with catalogue number 243345 (CPW-80), Iron (II) chloride tetra hydrate with catalogue number 220299, poly vinyl pyrrolidone (PVP) with catalogue number PVP 40, 3 aminopropyl triethoxy silane (APTS) with catalogue number 440140, and 3 aminopropyl methyl diethoxy silane (APDS) with catalogue number 371890 were purchased from Sigma Aldrich. Furthermore, silver nitrate AgNO_3 with catalogue number 10060340 was purchased from Fisher scientific, iron (III) chloride hexahydrate with catalogue number A16231 was purchased from Alfa Aesar, 28% ammonium hydroxide (NH_4OH) with catalogue number 21190326 was purchased from V.W.R and sodium borohydride (NaBH_4) with catalogue number 12537 was purchased from Avocado research chemicals.

2.1.1 Bio-molecules

All the biomolecules used in this study were commercially purchased, and some buffers were prepared in the laboratory as per the description of the manufacturers. Oligonucleotide sequences specific to *Escherichia coli* (*E. coli*), were purchased from TIB-MOLBIOL, Germany. Bovine Serum Albumen (BSA), glutaraldehyde solution (Grade I, 25% in H_2O), sodium cyanoborohydride was purchased from Sigma-Aldrich, UK. Ethanol (Absolute, 200 proof, Molecular Biology grade) was purchased from Fisher Scientific.

2.1.2 Solutions and buffers

Thermo Scientific Barnstead Nano pure Water Deionisation System was used for the deionised water for the preparation of solutions for this project. Complete list of the solutions and buffers used is shown in the following Table 2-1.

Table 2-1. Complete table of buffers and chemical solutions

Name	Preparation	Use	Storage Temp. (°C)
Coupling solution	1 litre of solution was prepared containing 0.8% w/v acetic acid (glacial) in methanol	UV-Visible colorimetric assays and storage of NH ₂ modified nanoparticles	1 litre capped clear glass bottle at 25°C
Hydrolysis solution	1:1 mixture of methanol and water containing 0.15% acetic acid (glacial)	UV-Visible colorimetric assays	1 litre capped clear glass bottle at 25°C
Glutaraldehyde solution (5% w/v)	10 mL stock solution was typically prepared containing 1.886 mL glutaraldehyde and 8.114 mL 20×SSC buffer	Conversion of surface amine groups to aldehydes	Centrifuge tubes at -18°C
20×SSC stock buffer	Stock solution was made by dissolving 175.3 g NaCl and 88.2 g sodium citrate in 1 L water. The pH was adjusted to 7.4	Conversion of surface amine groups to aldehydes. Grafting and hybrid capture of oligonucleotides	Capped clear glass bottle at 25°C
1×SSC and 13×SSC buffer solutions	20×SSC stock buffer solution was diluted respectively to produce 1× and 13×SSC buffers	Conversion of surface amine groups to aldehydes. Grafting and hybrid	Capped clear glass bottle at 25°C
1×PBS Buffer	PBS tablet (136 mM NaCl, 3 mM KCl, 10 mM Na ₂ HPO ₄ , 2 mM KH ₂ PO ₄) dissolved in 200 mL water	Washing and storage of lipase-materials.	Capped bottle at 25°C

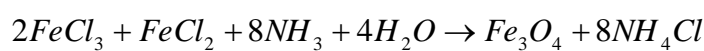
Table 2-2. Amino modified oligonucleotides of *E. coli*, along with the corresponding complementary sequences

Product name	Amino modified oligonucleotide sequence	Concentration (OD)
EC_541_FOR-41	5'-NH ₂ -dC ₆ -GGTCATATCTCTAACGCCATCC	50
EC_637_REV-42	5'-NH ₂ -dC ₆ -TGGCGTCGTGCATTAGTT	50
EC_541_FOR-43	5'-NH ₂ -dC ₁₂ -GGTCATATCTCTAACGCCATCC	50
EC_637_REV-44	5'-NH ₂ -dC ₁₂ -TGGCGTCGTGCATTAGTT	50
Comp FOR -45	GGATGGCGTTAGAGATATGACC	50
Comp REV-46	AACTAATGCACGACGCCA	50

2.2 Method I (Optimised from various trial and error which has been presented in appendix A-1)

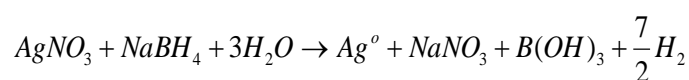
2.2.1 Magnetite nanocomposite

Fifty mL of solution containing ferrous chloride (FeCl₂) and ferric chloride (FeCl₃) with a molar ratio of 1:2 was prepared in a conical flask. 20 mL of the prepared solution was withdrawn into a conical flask and 1g of various commercial materials (see section 2.1) was introduced. The mixture was stirred for about an hour and was filtered. The filtered solid material was transferred into a conical flask and stirred with 50 mL of 1.6M NH₄OH for 1 hour. After stirring, the resultant solid material with black colour was filtered, washed with 5 mL of double deionised water (×3) to bring the pH to neutral (7) and was dried at room temperature for overnight.



2.2.2 Silver nanocomposite

Twenty mL of 0.1M solution of silver nitrate was taken and 1g of various commercial materials which includes, QM1, QM2, QM3, QM4 and QM5 (see section 2.1) were introduced into it and stirred for half an hour before filtration. The filtered solid materials were mixed with 50 mL of 0.2M sodium borohydride (NaBH₄) and stirred for an hour, while stirring 10 drops of PVP, were added to the suspension. After further stirring for 5 minutes, the nanocomposites were filtered, and dried at room temperature and was followed with characterisation with TEM, SEM, EDAX etc.



2.2.3 Silver magnetite nanocomposite

The solid magnetised nanocomposite from section 2.2.1 was introduced into 20 mL of 0.1M solution of AgNO₃ and was stirred for an hour before filtration. Filtered solid material was mixed with 50 mL of 0.2M sodium borohydride (NaBH₄) and was stirred for an hour, while stirring, 10 drops of PVP were added to the suspension. After stirring for further 5 minutes, the nanocomposite was filtered, and dried.

2.2.4 Bacterial culture and growth conditions

Cultures of *E. coli* (K12) and *S. aureus* were grown aerobically in a liquid medium (nutrient broth; Lab M; LAB014) at 37°C for approximately 12 hours by using a shaker incubator set at 180 rpm. After incubation, 1 in 100 dilutions of bacterial culture was prepared with fresh nutrient broth in universal tubes, which were incubated at 37°C in the shaker incubator for four and five hours for *E. coli* (K12) and *S. aureus* respectively, to get the exponential phase of the culture. Bacterial culture was then centrifuged and washed three times by re-suspending the bacterial culture (pellet) in ¼ strength sterile Ringer's solution between each centrifugation step, using a Sigma 3-16PK bench top centrifuge at 2504 sec (×g) for 20 minutes at 5°C. Finally, a bacterial cell pellet was re-suspended in 3 mL of sterile Ringer's solution and placed on ice before testing for antibacterial properties of developed nanocomposite materials along with unmodified commercial host matrices.

2.2.5 Assaying the minimum bactericidal concentration (MBC)

To determine the MBC, the nanocomposite material (900 µL) at the various concentrations were mixed with 100 µL of bacteria. After 0, 1, 2, 3, 4, 5, 6, 7,8,9 and 10 hours contact time with the nanocomposite at room temperature, each suspension was serially diluted and inoculated on nutrient agar (Lab M; LAB008) plates using the

Miles and Misra method (Miles *et al.*, 1938). The plates were incubated at 37°C for up to 7 days and were examined for bacterial growth after 24 hours. The lowest concentration at which no colonies were observed was taken as the MBC of nanocomposite material. Where appropriate, data are presented as the mean \pm SD (N = 3).

2.2.6 Source of bacterial culture

L. pneumophila non-Sgp1 strain ST707 (was collected from Dr Mandy Dillon), who got it from Dr Tim G. Harrison (Respiratory & Systemic Infection Laboratory, Health Protection Agency, Colindale, UK) for his research group. *K. pneumoniae*, a non-commercial strain, was collected from Professor Glyn Morton, which was isolated at UCLan (designated code: LP1 499); *P. aeruginosa* (NCTC 10662), *E. coli* strain DH5- α , *E. coli* (W3110) and *S. aureus* (NCIMB 1671) Gram-positive were maintained in a microbiology teaching laboratory C/O University of Central Lancashire (UCLan).

2.2.7 Growth curve determination

Prior to the determination of the antimicrobial applications of the developed nanocomposite materials on specific Gram-positive and Gram-negative bacteria, the growth curves were determined to see the bacterial growth (log phase). For the biocidal applications of the developed materials, Gram-negative, *E. coli* (W3110) and Gram-positive, *S. aureus* (NCIMB 1671) bacteria were selected.

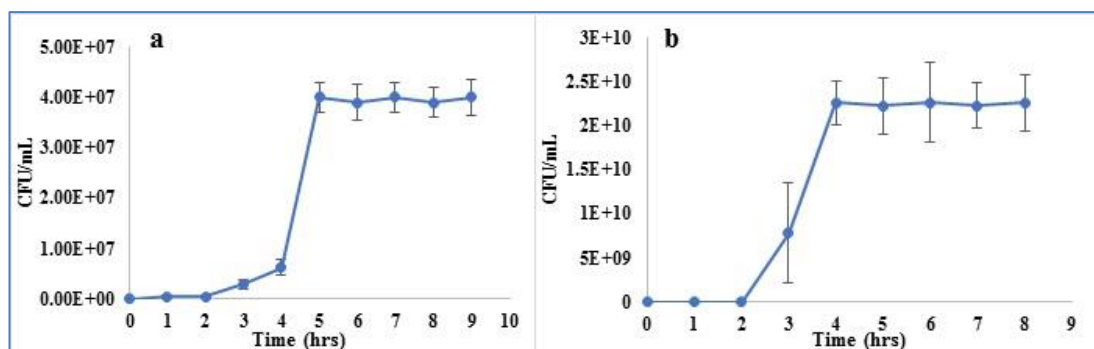


Figure 2-1 Growth curves of (a) *S. aureus* and (b) *E. coli*

Figure 2-1 (a and b) shows the growth curve of *S. aureus* (a) and *E. coli* (b). For the *S. aureus*, hour 5 was considered as the log phase (see figure 2.1 a); where the bacterial population increased to 10^7 CFU/mL. Furthermore, the log phase for the *E. coli* (see figure 2.1 b) was witnessed as hour 4.

2.2.8 Extraction of DNA from *E. coli* pellets

DNA was extracted by the protocol provided with the QIAGEN. There are several steps which were used for the extraction of DNA.

A fresh culture of bacteria was incubated in nutrient broth at 37 °C overnight followed by the preparation of the pellets by centrifugation at 8000 rpm for 3 minutes at normal temperature (15 – 25 °C), followed by addition of 250 µL resuspension buffer into the pellets and the resultant solid was transferred into a microcentrifuge tube. Furthermore, 250 µL of lysis buffer was added into the microcentrifuge tube and was shaken thoroughly by inverting the tube 4 - 6 times until the solution became clear. After the addition of resuspension and lysis buffers, 350 µL of neutralisation buffer was also added and mixed thoroughly by inverting the tube 4 – 6 times.

After mixing, the suspension was centrifuged at 13000 rpm for 10 minutes in a table top centrifuge. Upon completion of centrifugation of the suspension, 800 µL supernatant was taken from the microcentrifuge tube and was introduced into the

QIAprep 2.0 spin column by pipetting. The QIAprep 2.0 spin column containing 800 μ L supernatant was centrifuged for 30 to 60 seconds and the flow through was discarded. Furthermore, the QIAprep 2.0 spin column with extracted material was washed with 0.5 mL binding buffer and was centrifuged for 30 to 60 seconds and flow through was discarded. Furthermore, the QIAprep 2.0 spin column was washed with 0.75 mL elute buffer, followed by centrifugation for 30 to 60s and the flow through was discarded.

Moreover, the QIAprep 2.0 spin column was transferred to the collection tube. The QIAprep 2.0 spin column was centrifuged for further 1 minute in collection tube for the removal of residual wash buffer. Finally, the QIAprep 2.0 spin column was placed into the clean and sterile 1.5 mL microcentrifuge tube in which 50 μ L elution buffer (10mM TrisHCl, pH 8.5) was added to elute the DNA. The buffer was left standing in the QIAprep 2.0 spin column for 1 minute before the final centrifugation. The QIAprep 2.0 spin column was discarded, and the extracted DNA suspension was collected into microtube.

2.3 Characterisation techniques used.

Post-modified nanocomposites were characterised using various physico-chemical techniques and a summary has been presented in Table 2-3.

Table 2-3. Host–guest matrices with characterisation

Sample	Host	Guest	Characterisation						
			XRF	SEM	EDAX	TEM	XRD	FT-IR	BET
QM1	CNT	None	✓	✓	✓	✓	✓	✓	✓
QM1-1	CNT	Fe ₃ O ₄	✓	✓	✓	✓	✓	✓	✓
QM1-2	CNT	Ag	✓	✓	✓	✓	✓	✓	✓
QM1-3	CNT	Fe ₃ O ₄ +Ag	✓	✓	✓	✓	✓	✓	✓
QM2	AC	None	✓	✓	✓	✓	✓	✓	✓
QM2-1	AC	Fe ₃ O ₄	✓	✓	✓		✓	✓	✓
QM2-2	AC	Ag	✓	✓	✓		✓	✓	✓
QM2-3	AC	Fe ₃ O ₄ +Ag	✓	✓	✓	✓	✓	✓	✓
QM3	DAE	None	✓	✓	✓	✓	✓	✓	✓
QM3-1	DAE	Fe ₃ O ₄	✓	✓	✓		✓	✓	✓
QM3-2	DAE	Ag	✓	✓	✓		✓	✓	✓
QM3-3	DAE	Fe ₃ O ₄ +Ag	✓	✓	✓	✓	✓	✓	✓
QM4	CPW-14	None	✓	✓	✓	✓	✓	✓	✓
QM4-1	CPW-14	Fe ₃ O ₄	✓	✓	✓		✓	✓	✓
QM4-2	CPW-14	Ag	✓	✓	✓		✓	✓	✓
QM4-3	CPW-14	Fe ₃ O ₄ +Ag	✓	✓	✓	✓	✓	✓	✓
QM5	CPW-80	None	✓	✓	✓	✓	✓	✓	✓
QM5-1	CPW-80	Fe ₃ O ₄	✓	✓	✓		✓	✓	✓
QM5-2	CPW-80	Ag	✓	✓	✓		✓	✓	✓
QM5-3	CPW-80	Fe ₃ O ₄ +Ag	✓	✓	✓	✓	✓	✓	✓

SEM and EDAX were employed for morphology and elemental detection, TEM was used to study the size, and internal structure, while FT-IR was engaged for the analysis of incorporated iron oxide. XRD was used to study the crystalline nature of the developed nanocomposite; BET was used to measure the surface area and pore volume of the nanocomposite materials. Table 2-3 present various characterisation methods used on various materials.

2.3.1 X-ray fluorescence

X-ray fluorescence (XRF) is a technique which is a non-destructive chemical analyses method and mostly used for the analysis of rocks, minerals and sediments. Elemental analyses were performed by using XRF machine with model (Bruker Tracer 1V- SD). Generally, all the samples were prepared in the XRF sample cells (SC-4331-N) 32 mm double open-ended small plastic holders. Fixed parameters such as time at 15 seconds and energy at 40 KeV were used. Materials produced the spectrum according to their X-ray energy; X-ray produces part of the electromagnetic spectrum in terms of their energy as (KeV) or wavelength (nm). The formation of the X-ray fluorescence is caused by the change taking place in an atom due to the emission of the electron (Wegscheider, 2012).

2.3.2 Scanning electron microscopy

Scanning electron microscopy (SEM) is employed for the determination of the surface morphology of the material whereas EDAX is used for the elemental analysis. Surface morphology of specimens is determined with the scanning electron microscope (SEM) due to its high-resolution system, where electrons are employed to achieve high resolution and magnifications instead of light. For better images, the sputtering system was used for the coating of non-conducting samples with gold or platinum. The incident electrons with a various energy range from 100 eV to 30 KeV passes through the column where condenser lenses focus them into the beams to form the spot size on the sample, afterwards, focused beams are directed on the surface of the specimen. Furthermore, detector collects the emitted secondary electrons and intensity is displayed as an image by using the vacuum, and produced images describe the surface morphology of the sample. Composition, morphology and elemental analysis of the developed nano composites were determined by using 10 μ L of dried samples on

carbon coated grid at room temperature. Afterwards, samples were coated with the gold by employing using low vacuum fine coater for two cycles at 25 mA for 30 seconds (JFC-1200, JEOL, Japan).

2.3.3 Transmission electron microscopy

Transmission electron microscopy (TEM) has been extensively used to determine the size, morphology and internal structure of the particles incorporated into the solid matrix (Sen *et al.*, 2006, Del Campo *et al.*, 2005, Yi *et al.*, 2005, Santra *et al.*, 2001). Images of synthesised nanocomposites were collected using a JEOL JEM-2000 EX electron microscope at 200 kV. Gatan Digital Micrograph Software was used to manage the images. The sample was prepared by diluting the developed nanocomposites 50 times in deionized water. Approximately 2 μ L diluted suspension was added to the copper grid (400 mesh, Agar Scientific, UK), followed by drying in air for one day before inserting to the TEM sample holder.

2.3.4 Fourier transforms infrared spectroscopy

Fourier transforms infrared spectroscopy (FT-IR) is employed to investigate the bonding among the atoms by providing the absorption spectrum. FT-IR spectra were measured on IR 200 (Thermo Scientific, USA) spectrometer by using Omnic (8.0) software. The presence of functional groups is identified by using this technique. A pinch of sample is introduced in the grid of the FT-IR instrument which produces the spectra, and from the spectra, bonding is analysed.

2.3.5 X-ray diffraction

X-ray diffraction (XRD) is widely used to confirm the crystalline structure of materials (Sen *et al.*, 2006, Yi *et al.*, 2005, Petcharoen and Sirivat, 2012, Mürbe *et al.*, 2008). XRD (Bruker D2 Phaser benchtop X-Ray diffractometer) has been used for the

characterisation of all unmodified commercial and post-modified materials. Dry samples were ground into powders and applied for sample preparation using sample holder. The sample holders are made up of silicon crystals (size: 24.5 mm diameter, 1 mm depth). The scanning parameters were adjusted to 2 θ values of 5-80° and measured using step scan mode (each step size was 0.02°).

2.3.6 Brunauer–Emmett Teller surface area measurement

Brunauer–Emmett Teller (BET) is widely employed for the determination of surface area of the materials by adsorption of nitrogen gas due to small sizes and inertness (Zhao *et al.*, 2005, Mürbe *et al.*, 2008, Setyawan *et al.*, 2012).

In this technique, a known amount of nitrogen gas is adsorbed at high pressure in the pores of the materials and desorbed by releasing the pressure. Prior to analysis, solid nanocomposite materials were degassed at 100°C for about 4-8 hours under vacuum. All analyses were performed by using a Micrometrics ASAP 2010 (USA) instrument.

2.4 Surface functionalisation of nanocomposites containing silver and magnetite nanoparticles

2.4.1 Silanisation of composite materials

Surface functionalisation (silanisation) nanocomposites was carried out by utilising (APTS and APDS) as a source of aminosilane, following the modified method developed by Sen *et al* (Bruce and Sen, 2005). The nanocomposites materials (150 mg) were introduced into 35 mL of 99.9% anhydrous methanol with 2% w/v of two different silanes (APTS and APDS) in a 50 mL screw-capped centrifuge tube (Falcon 352070, UNSPSC 41121703, Code 66 Polypropylene). The reaction mixtures were incubated for 24 hours at 50°C with end-over-end rotation at 40 rpm using Memmert

hybridiser (DIN EN 60529-IP 20). A schematic diagram (using molecular modelling) of silanisation process is shown in Figure 2-2. Surface amine densities were determined using a reported colorimetric assay (Moon *et al.*, 1997, Moon *et al.*, 1996) using 4-Nitro benzaldehyde (4-NBA) solution. Surface amine densities of the silanised samples decreases on storage for an extended time, hence, new and fresh batches were prepared for each experiment.

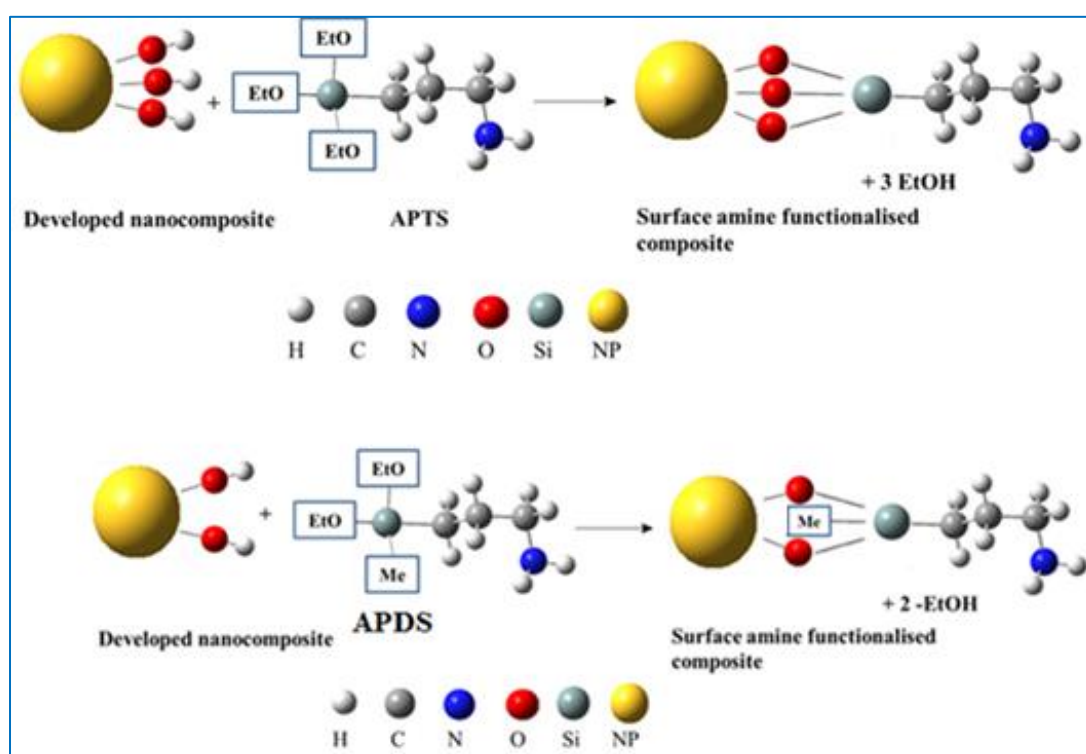


Figure 2-2 Silanisation (molecular modelling) of the nanocomposites with (a) APTS and (b) APDS

2.4.2 Measurement of surface amine density

Five mg of surface amine functionalised nanocomposites suspension (suspension density 15 mg /mL) was taken in a 1.5 mL centrifuge tube and washed 3 times with 1 mL of coupling solution, followed by the addition of 1 mL of 4-NBA. The resultant suspension was left at room temperature with gentle end-over-end rotation for 3 hours. After three hours, the supernatant was separated magnetically from the suspension, and was washed 4 times using 1 mL of coupling solution. 1 mL of hydrolysis solution

was added into the nanocomposites and stirred (end over end rotation) for further 30 mins at room temperature for hydrolysis of immine groups. The solid was magnetically removed and the concentration of 4-NBA in the supernatant was measured (absorbance at 282 nm) by using a Jenway 7315 Spectrophotometer (Bibby Scientific Limited, Stone, Staffordshire, UK). The calibration curves were used for the calculation of the 4-NBA in coupling and the hydrolysis solutions.

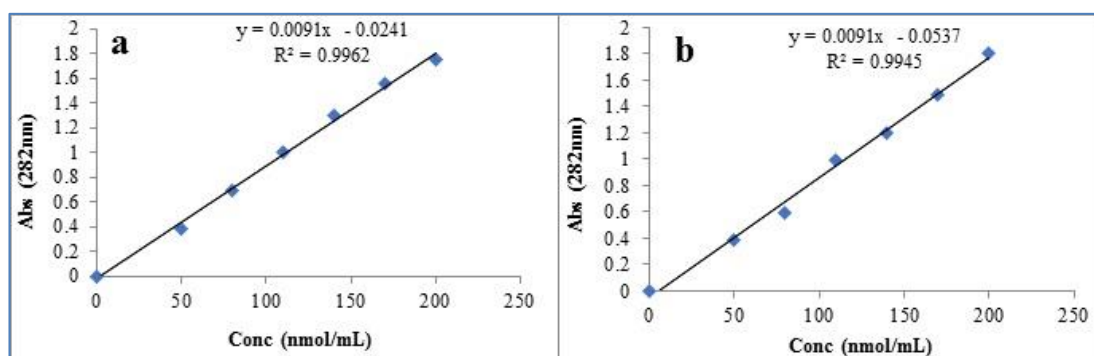


Figure 2-3 Calibration curve for 4-NBA (a) coupling and (b) hydrolysis solution

Figure 2-3 (a and b) presents the standard curve constructed using a series of dilutions of 4-NBA in coupling and hydrolysis solutions respectively. For the preparation of the calibration curves, series of freshly prepared 4-nitrobenzaldehyde solutions were prepared by appropriate dilution in coupling and hydrolysis solutions ranging from 0 to 250 nmol/mL. Complete illustration of measurement is shown in figure 2-4 by using molecular modelling.

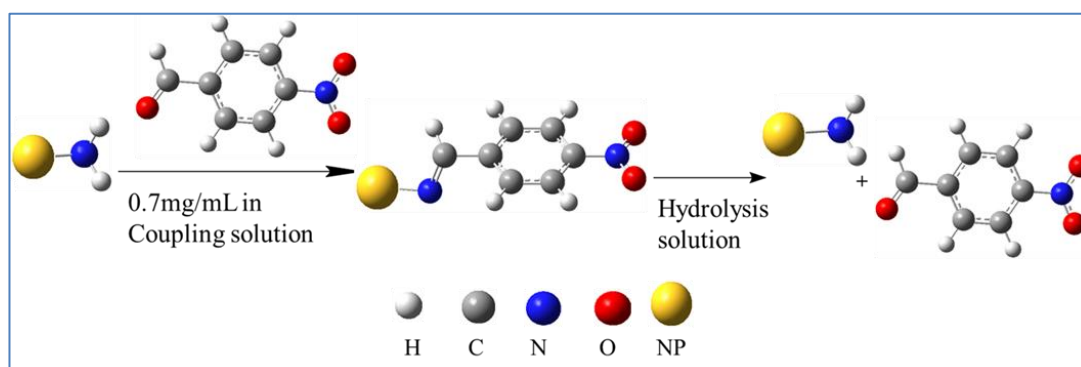


Figure 2-4 Molecular modelling of 4-NBA colorimetric surface assay

2.4.3 Surface amine conversion to aldehyde by reacting with glutaraldehyde solution

Before the conversion of surface amine groups into the aldehyde for the next step, sodium citrate (88.2 g) was dissolved along with (175.3 g) of sodium chloride in 1 litre of distilled, deionised water for the preparation of (20×) SSC buffer solution. Dilute HCl was used to adjust the pH 7.3. Furthermore, 50 mL of stock (20×) SSC buffer solution was added into 950 mL of distilled and deionised water to prepare (1×) SSC buffer solution (diluted buffer). Each time, a freshly prepared solution of glutaraldehyde in (1×) SSC was used for the reaction. 50mg of the amino functionalised nanocomposites were washed 3 times with 10 mL of (1×) diluted SSC. Afterwards, 4 mL of freshly prepared glutaraldehyde (5% w/v) solution was added and the reaction mixture was kept in the incubator for reaction at 18°C for about 3 hours with end-over-end rotation at 40 rpm. -CHO modified nanocomposites were magnetically separated from the suspension and washed 3 times with 5 mL (1×) SSC buffer solution. Glutaraldehyde (-CHO) modified materials were further washed 3 times with 5 mL PBS buffer solution before grafting specific primer sequences of oligonucleotides. Conversion of surface amine of the developed nanocomposites in the aldehyde is shown in the figure 2-5.

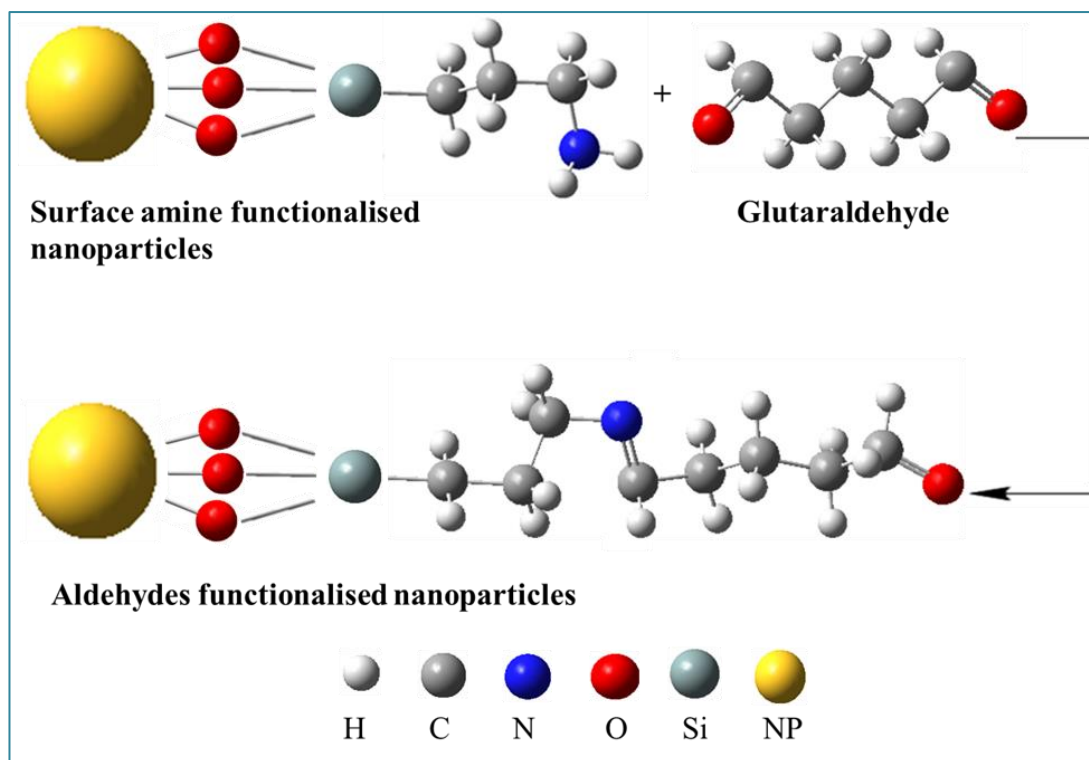


Figure 2-5 Schematic presentation using molecular modelling for the conversion of surface amine to aldehyde

2.4.4 Measurement for oligonucleotide concentration (UV-visible assay)

Nucleic acids consist of aromatic and heterocyclic bases, which absorb light in the UV region. The wavelength of these aromatic, heterocyclic rings lies in between 250-280 nm. Moreover, a set of calibration curves were produced by determining the absorbance at 260 nm of a series of standard solutions prepared with various concentrations ranging from 0 to 6 nmol/mL of the specific sequences of the (*E. coli*) primers listed in table 2.2 in (i) 1×SSC buffer and (ii) deionised water. Figure 2-6 and Figure 2-6 show the calibration curves for the complementary and specific sequence for the *E. coli* respectively.

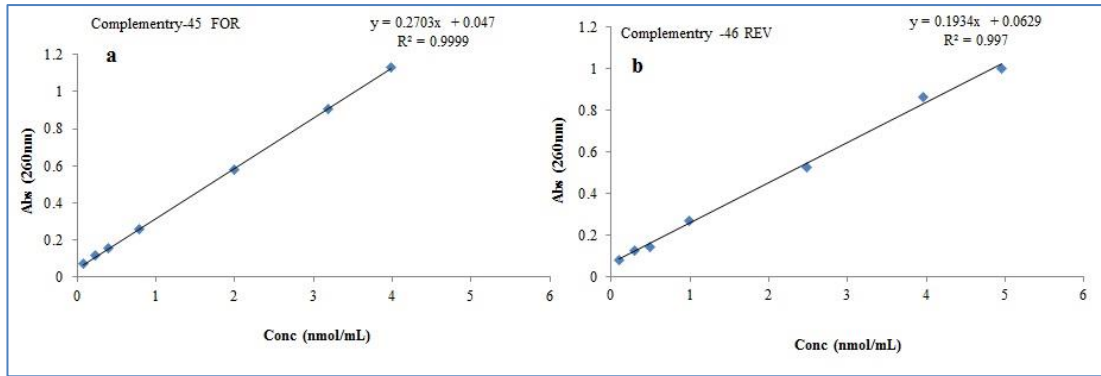


Figure 2-6 Standardisation curves for complementary oligonucleotides specific to *E. coli* (a) forward sequence and (b) reverse. Values are mean (\pm SD, No=3).

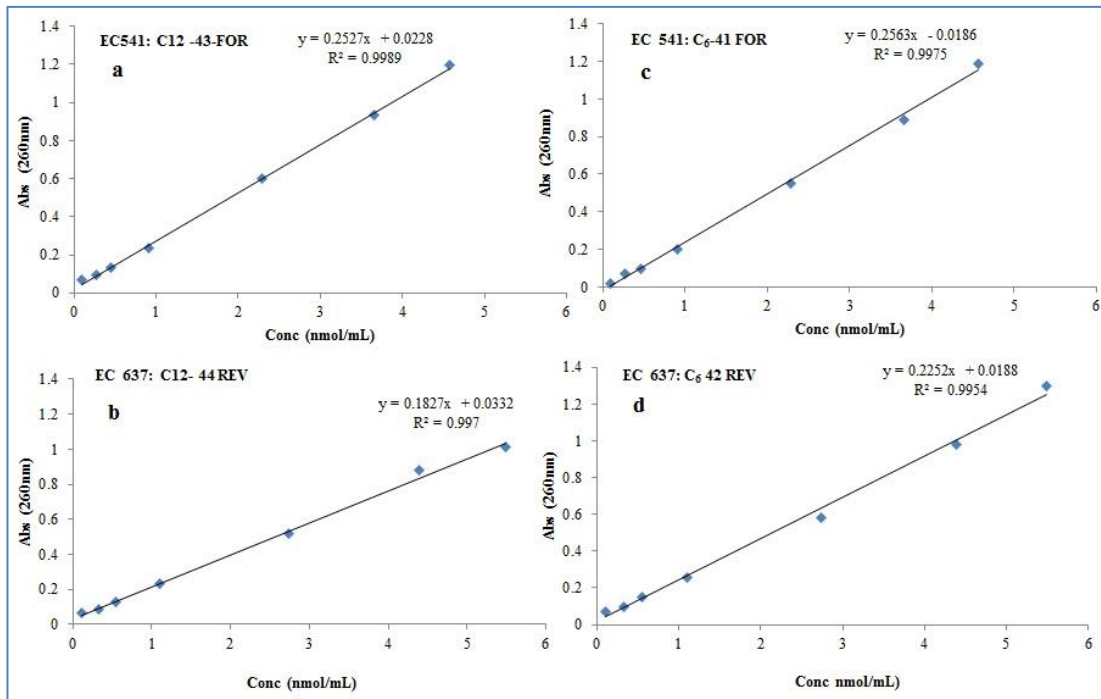


Figure 2-7 Standard curves for oligonucleotides-specific to *E. coli* (a) with spacer C12 forward (b) with spacer C12 reverse, while specific sequence with (c) spacer C6 forward and (d) with spacer C6 reverse. Results are mean (\pm SD, No=3).

Figure 2-7 shows that for the specific sequence of bacteria (see table 2.2) used in the assay of *E. coli*, in the whole series of the concentrations from 0 to 6 nmol/mL linearity was perceived.

2.4.5 Grafting of the primers

Five-hundred microliter of 3.3 μ M solution of oligonucleotides in 1 \times SSC coupling buffer solution (1.65 nmol total in 0.5 mL solution) were added into 4 mg of the glutaraldehyde modified composites and the suspension was left in the incubator at 18 $^{\circ}$ C overnight with end-over-end rotation at 40 rpm. Two different primer sequences (5' NH₂ modified forward primers with C₆ and C₁₂ spacer) of the *E. coli* have been grafted on the surface of five novel synthesised nanocomposites (QM1, QM2, QM3, QM4 and QM5) containing silver and magnetite nanoparticles.

2.4.6 Hybrid capture assay of complementary oligonucleotides (Model Assay)

One milligram of the oligonucleotide grafted nanocomposites listed in Table 2.3, were added into the 1.5 mL Ependrop tube (equivalent to 100 μ L of suspension of grafted composite in 1 \times SSC) and washed twice with 0.5 mL of deionised and sterilised water and finally dispersed in 0.5 mL of water. The aqueous suspension was heated for 4 minutes at 80 $^{\circ}$ C. After heating at 80 $^{\circ}$ C, water was removed, and 200 μ L of complementary sequences (1.65nmol) prepared in 13 \times SSC buffer in 0.05% BSA (Bovine Serum Albumin) was added and was followed by incubation with end-over-end rotation (40 rpm) for 30 minutes at 18 $^{\circ}$ C. The concentration of the free oligonucleotide in the supernatant measured by UV –visible spectrophotometry by measuring the absorbance at 260 nm. The resultant nanocomposites washed three times with 1 mL of 13 \times SSC buffer followed by the addition of 300 μ L of sterilised and deionised water and left at 85 $^{\circ}$ C for 10 minutes for the dissociation of the annealed complementary / captured sequences of the primers. The concentration of the complementary oligonucleotide measured using UV-Visible spectrophotometry at 260 nm in order to obtain the hybrid capture efficiency. A schematic diagram of hybrid

capture is presented in Figure 2-8.

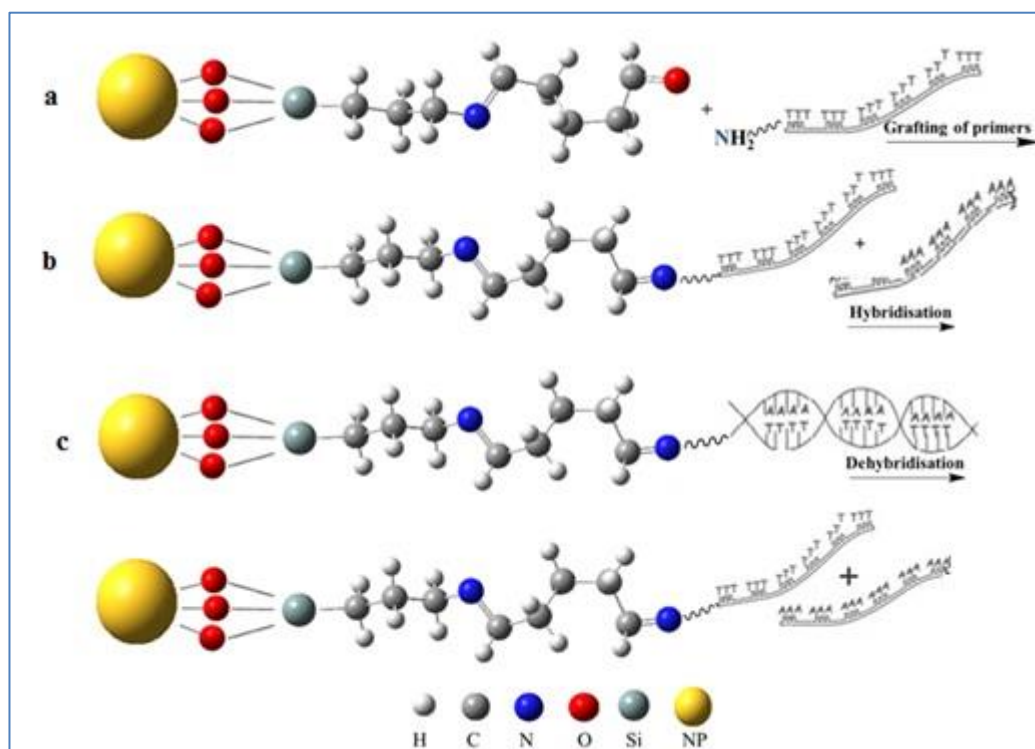


Figure 2-8 Complete illustration using molecular modelling (a) grafting of oligonucleotides (b) Hybrid capture (c) Dehybridisation of the complementary sequence.

2.4.7 PCR sample preparation and optimisation parameters

Materials were taken in following order to make 25 μL sample for the PCR.

1. Water (sterilised and deionised) 2. Master mix 3. Primers 4. Extracted *E. coli* DNA.

For the volume of 25 μL sample, the used volume of each component is given below.

i) Forward primer: 1.25 μL ii) Reverse primer: 1.25 μL iii) Master mix: 1.25 μL
iv) Water: 5 μL v) Extracted *E. coli* DNA.

The components were then mixed and vortexed for 60 seconds. This was then centrifuged for 15 seconds at 8000 rpm and made ready for PCR. The following PCR sampling parameters were used: initial denaturation at 95 $^{\circ}\text{C}$ for 3 minutes followed by denaturation for 30 seconds. Annealing stage of 35 cycles was carried out at 58 $^{\circ}\text{C}$

for 30 seconds, with extension at 72 °C for 30 seconds and final extension at 72 °C for 5 minutes.

CHAPTER THREE

3 Analysis of structure, chemical composition and properties of MWCNTs and its modified composites

3.1 Introduction

In this chapter, physio-chemical characterisations of a series of novel multifunctional nanocomposites have been discussed in detail. These techniques include; X-ray fluorescence (XRF), energy dispersive X-ray analysis (EDAX), scanning electron microscope (SEM), transmission electron microscope (TEM), fourier transforms infrared spectroscopy (FT-IR), powder X-ray diffraction (XRD) and nitrogen gas adsorption (BET surface area analysis). XRF measurements were carried out for the elemental analysis of silver and iron oxide in the nanocomposite materials. Similarly, EDAX/SEM analysis has been used for the elemental analysis along with morphology of the developed nanocomposites. Furthermore, TEM/EDAX analysis was used for the determination of size, internal structure, morphology and elemental composition. FT-IR spectroscopy has been used for the characterisation of bond vibrations in the nanocomposites. Powder X-ray Diffraction (XRD) was used for the determination of crystallinity and phase structure of the iron oxide nanoparticles in the nanocomposites. BET experiments were used to determine the surface area, micropore and mesopore diameters along with pore volume of the nanocomposites.

3.2 Multiwall carbon nanotube-based composite (QM1 to QM1-3)

3.2.1 X-ray fluorescence

Generally, XRF technique is used for the non-destructive chemical analysis of rocks, minerals and sediments. Here it has been employed for the analysis of incorporated silver and iron oxide nanoparticles; the technique is described in section 2.3.1. It produced spectra according to X-ray energy of the elements as (KeV) which is shown in figure 3.1.

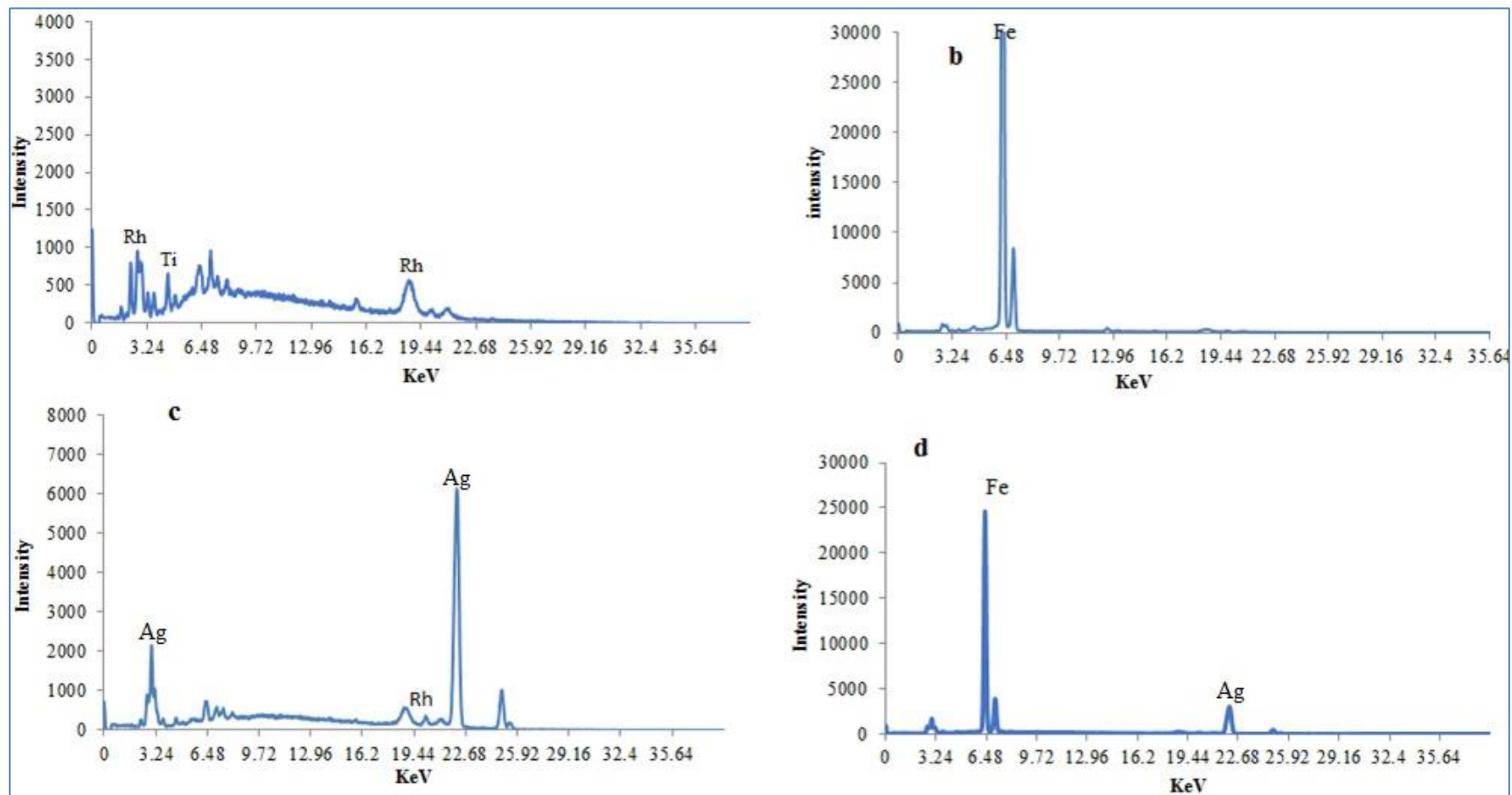


Figure 3-1 XRF of QM1-based composite (a) QM1 (unmodified MWCNTs) (b) QM1-1 (MWCNTs modified with only iron oxide nanoparticles) (c) QM1-2 (MWCNTs modified with only silver nanoparticles) and (d) QM1-3 (MWCNTs modified with silver coating iron oxide nanoparticles)

Figure 3-1 (a, b, c, and d) shows X-ray fluorescence spectra of QM1 (MWCNTs) unmodified, QM1-1 modified with only iron oxide, QM1-2 modified with only silver and QM1-3 modified with silver coating iron oxide nanoparticles respectively. Figure 3-1 (a) shows the spectrum of QM1 (unmodified MWCNTs) nanomaterials as a control sample. Small impurity peaks (intensity less than 1000 counts) of rhodium and titanium due to the x-ray source generated in the system were observed in the spectrum. Figure 3-1(b) shows the X-ray fluorescence of iron oxide modified nanocomposites (QM1-1) where a strong band observed at 6.38 KeV was due to the presence of Fe (K_{α}) radiation. The impurity peaks were suppressed by the presence of a strong Fe band. Figure 3-1 (c) shows the X-ray fluorescence of QM1-2 nanocomposite, where a strong band for silver could be seen at 3.24 (K_{α} or K_{β}) and 22.68 KeV (K_{α} or K_{β}) as reported (Howard, 2011). Figure 3-1 (d) shows the X-ray fluorescence of QM1-3 nanocomposites, where strong bands due to iron and silver were observed at 6.48 and 22.68 KeV respectively, indicating the presence of two different elements in the same nanocomposite.

3.2.2 Energy dispersive X-ray analysis

Generally, EDAX is used for the elemental analysis of the materials; this technique is an additional application of SEM and TEM attached with EDAX. EDAX is considered as one of the analytical techniques, comprehensively providing information such as composite mapping and elemental composition.

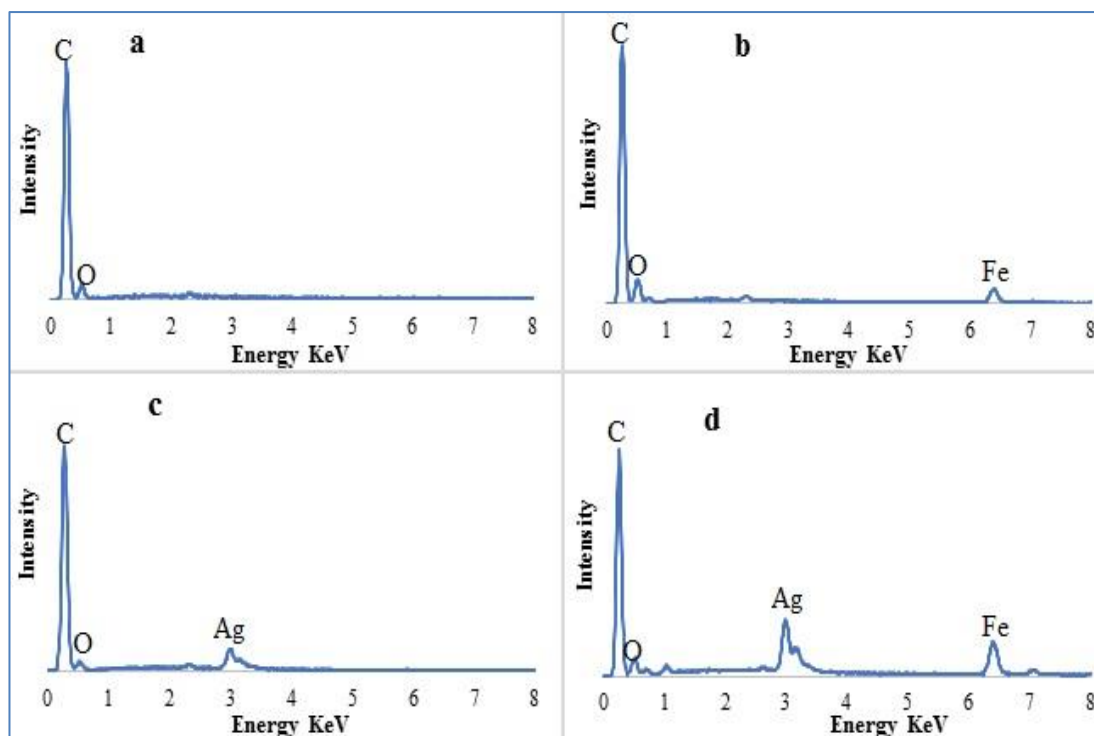


Figure 3-2 EDAX spectrum of QM1-based composite (a) QM1 (unmodified MWCNTs) (b) QM1-1 (MWCNTs modified with only iron oxide nanoparticles) (c) QM1-2 (MWCNTs modified with only silver nanoparticles) and (d) QM1-3 (MWCNTs modified with silver coating iron oxide nanoparticles)

Figure 3-2 (a) shows the EDAX analysis of the unmodified QM1 where peaks due to carbon and oxygen are clearly seen in between 0 to 0.2 KeV as the main components of the material. A weak impurity peak of sodium and sulphur can also be seen at 0.5 and 2.2 KeV respectively. Figure 3-2 (b) shows the QM1-1 nanocomposites, the presence of the iron is explicit from the spectrum located at 6.3 KeV, while carbon and oxygen are the main components of the material and sulphur was also observed due to a component of the unmodified QM1. Figure 3-2 (c) clearly indicates the presence of silver at 3.0 KeV, as previously reported (Ranjbar and Morsali, 2011, Luong *et al.*, 2008). Figure 3-2 (d) is the spectrum of QM1-3 nanocomposite containing both silver and iron oxide nanoparticles. It shows the presence of incorporated elements in the host matrix. Silver can be seen at 3.0 KeV, while iron is located at 6.3 KeV. From the above results, it can be concluded that the modified QM1

materials contain incorporated silver and iron as two different elements.

3.2.3 Scanning electron microscopy

SEM was employed to determine the surface morphology of the developed nanocomposites (QM1 series) and unmodified material (QM1). The microscopic images of the surface of the material were taken at various magnifications. Generally, magnification ranges from $\times 20,000$ to $\times 100,000$ with the best useful magnification subject to the type of sample and the assembly of the instrument (Yao, 2005).

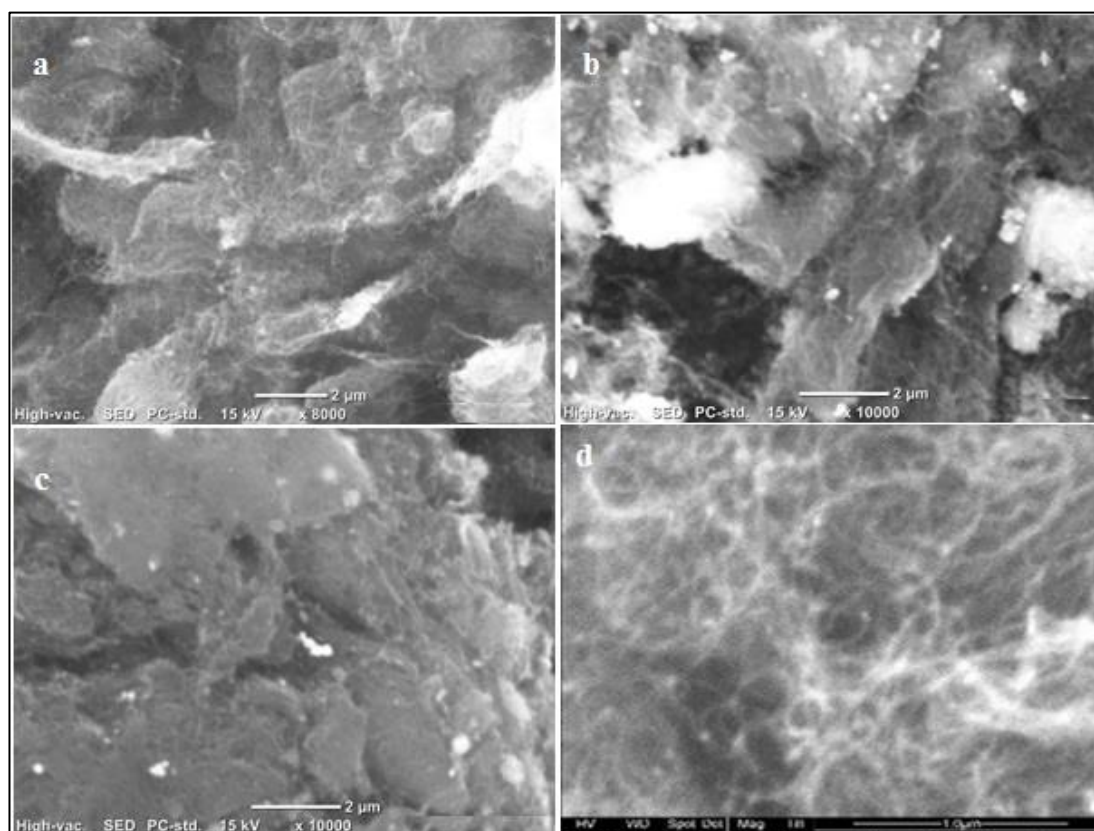


Figure 3-3 SEM shows images of QM1-based composite (a) QM1 (unmodified MWCNTs) (b) QM1-1 (MWCNTs modified with only iron oxide nanoparticles) (c) QM1-2 (MWCNTs modified with only silver nanoparticles) and (d) QM1-3 (MWCNTs modified with silver coating iron oxide nanoparticles)

Figure 3-3 (a, b, c and d) shows the surface morphology of the QM-1, QM1-1, QM1-2 and QM1-3 based composite respectively. The morphology of the material was examined at 15 KeV with 8000, 10000, and at 50000 magnifications (scale 2 μ m) and

50000 with 1 μm magnifications. Figure 3-3 (a) shows the unmodified MWCNTs material without the presence of nanoparticles while nanoparticles are clearly seen with white dots, and this may be due to the presence of magnetite and silver nanoparticles in figure 3-3 (b, c and d).

3.2.4 Transmission electron microscopy

This technique is vital to determine the internal structure, the size of the particles incorporated into the matrix and the shape of the nanoparticles as reported (Sen *et al.*, 2006, Del Campo *et al.*, 2005, Yi *et al.*, 2005, Santra *et al.*, 2001). Images of QM based composite are presented below.

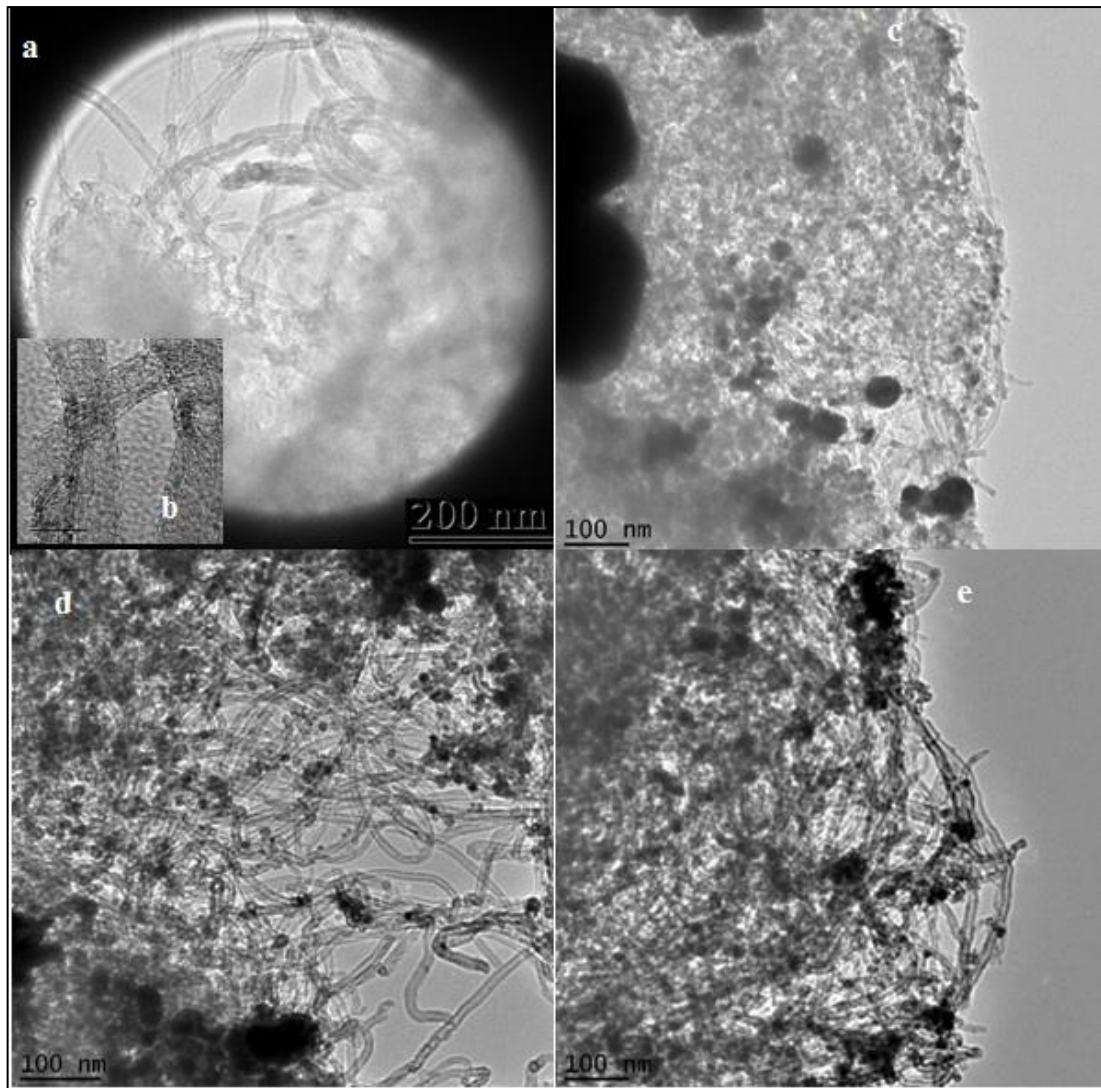


Figure 3-4 TEM images of QM1-based composite (a and b) QM1 (unmodified MWCNTs) (c) QM1-1 (MWCNTs modified with only iron oxide nanoparticles) (d) QM1-2 (MWCNTs modified with only silver nanoparticles) and (e) QM1-3 (MWCNTs modified with silver coating iron oxide nanoparticles)

Figure 3-4 (a) shows the internal structure of the unmodified commercial QM1 sample. The image is clearly showing tubes of (MWCNTs) and the absence of any nanoparticle inside it, while Figure 3-4 (b) demonstrates the diameter of the tube which is equal to 19.53nm.

Figure 3-4 (c, d and e) shows internal structure of QM1-1 (MWCNTs modified with only iron oxide nanoparticles), QM1-2 (MWCNTs modified with only silver

nanoparticles) and QM1-3 (MWCNTs modified with silver coating iron oxide nanoparticles respectively). Figure 3-4 (c) shows the QM1-1 nanocomposite where iron oxide embedded nanoparticles can be seen clearly inside the MWCNTs material with the size distribution of iron oxide core nanoparticles around 19-60 nm in diameter with the average size of 40 nm in diameter. Figure 3-4 (d) shows the QM1-2 nanocomposite where silver embedded nanoparticles can be seen clearly inside the MWCNTs material with size distribution of around 7-13 nm in diameter with the average size of 11 nm diameter. Figure 3-4 (e) shows the QM1-3 nanocomposite where silver coating iron oxide embedded nanoparticles can be seen clearly inside the MWCNTs material. The purpose of the incorporation of the silver nanoparticles was to stabilise its antimicrobial properties as reported (Mukha *et al.*, 2013) while iron oxide nanoparticles have been used for the purpose of one-step magnetic separation, and hence easy recycling ability (Sen *et al.*, 2010).

3.2.5 Fourier transforms infrared spectroscopy

FT-IR is an acceptable technique to determine the bonding between the atoms by vibrational spectrum. This technique has been utilised for functional group detection, especially for the detection of Fe-O vibration in the silver and iron oxide incorporated nanocomposite. The (FT-IR) spectra were recorded in the range 400–4000 cm^{-1} , to confirm the presence of functional groups or bonding between the atoms.

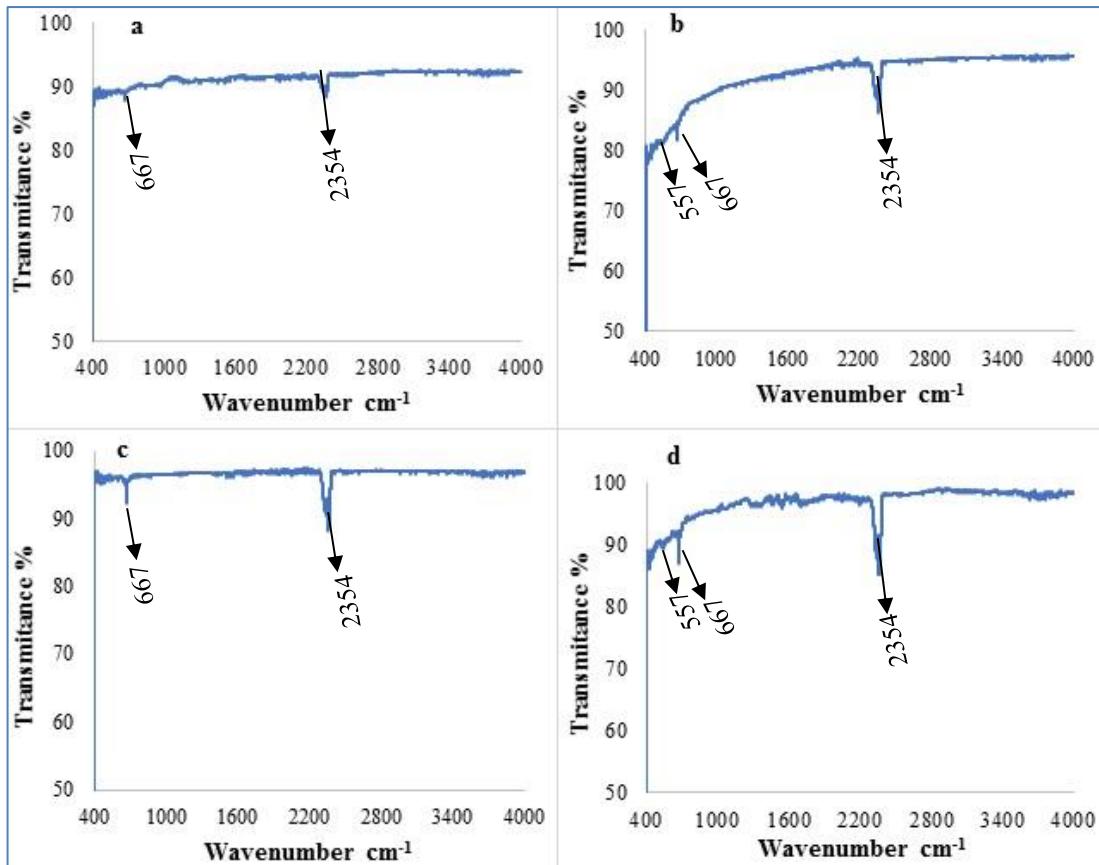


Figure 3-5 FT-IR spectrum of QM1-based composite (a) QM1 (unmodified MWCNTs) (b) QM1-1 (MWCNTs modified with only iron oxide nanoparticles) (c) QM1-2 (MWCNTs modified with only silver nanoparticles) and (d) QM1-3 (MWCNTs modified with silver and iron oxide nanoparticles)

Figure 3-5 (a, b, c and d) shows the FT-IR analysis of all samples of QM1-based unmodified and modified nanocomposites. All the samples have shown the peaks at 667 and 2354 cm^{-1} , which were associated with the CO_2 groups due to the CO_2 coating of the IR optics in the spectrometer (see arrows). Figure 3-5 (a) shows the QM1, commercial raw material while Figure 3-5 (b) shows QM1-1-based composite incorporated with magnetite nanoparticles. The spectrum of the magnetite nanoparticles due to the stretching vibration of iron oxide is reported in the range of 460 -557 cm^{-1} (Sen *et al.*, 2010). Moreover, the presence of incorporated iron oxide into the developed composite was found at 557 cm^{-1} due to the stretching vibration of the Fe -O bond as reported in the literature. Figure 3-5 (c) QM1-2-based composite

containing silver nanoparticles showed similar spectrum like the unmodified QM1-based sample (MWCNTs) carbon nanotube raw material, as AgNPs do not show absorption in the infrared spectral region. While, Figure 3-5 (d) showed the peak of the magnetite at 557 cm^{-1} due to the stretching vibration of the iron oxide bond but slightly different than from the magnetite result. From all the four samples, it was concluded that sample QM1-1 and QM1-3-based material contained the iron oxide and confirmed the XRF and EDAX results for the elemental detections.

3.2.6 X-ray diffraction

The crystallinity of both unmodified and modified materials was determined by the X-ray diffraction (XRD) technique; this is described in section 2.3.5. Diffraction peaks at three different 2θ values (25, 42 and 53), corresponding to some periodicity of carbon nanotubes in unmodified QM1. The incorporation of magnetite and silver nanoparticles has converted the host matrix into crystalline.

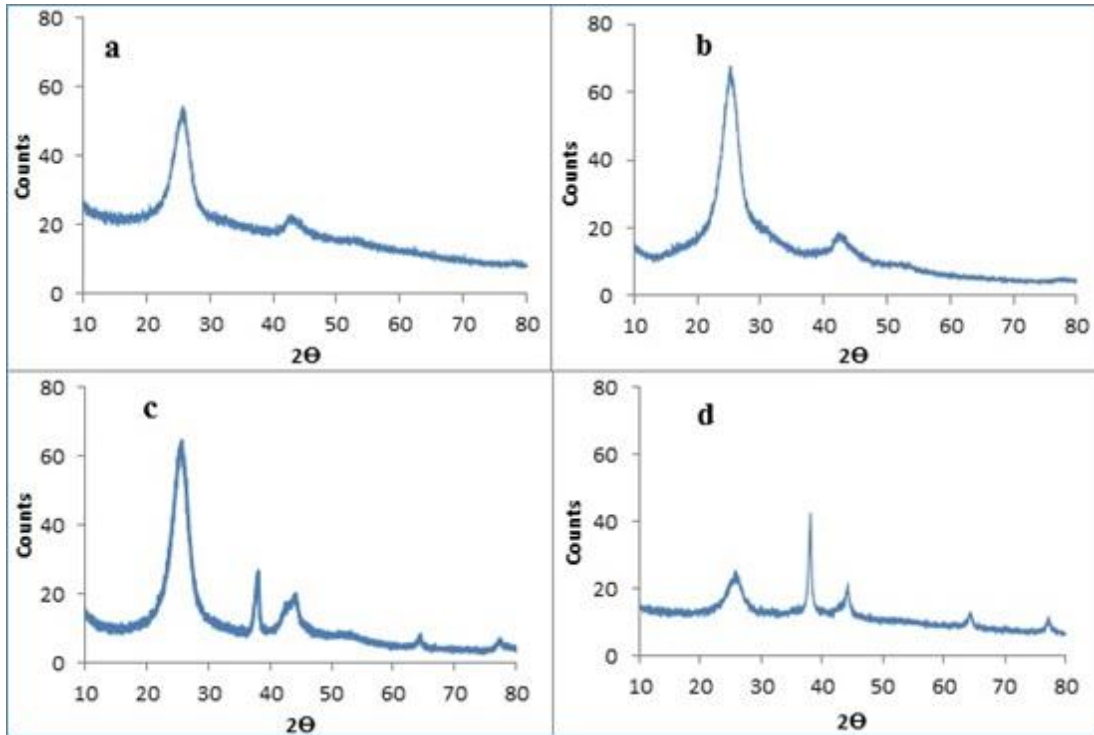


Figure 3-6 XRD pattern of QM1-based composite (a) QM1 (unmodified MWCNTs) (b) QM1-1 (MWCNTs modified with only iron oxide nanoparticles) (c) QM1-2 (MWCNTs modified with only silver nanoparticles) and (d) QM1-3 (MWCNTs modified with silver and iron oxide nanoparticles)

Figure 3-6 (a, b, c, and d) shows the XRD pattern of QM1 unmodified commercial material, modified with iron oxide, silver and silver-iron oxide respectively. Figure 3-6 (a) (shows the amorphous pattern of typical XRD pattern of the unmodified commercial carbon nanotube. Its intensity was recorded as 62 counts. Figure 3-6 (b) shows the XRD pattern of the QM1-1, carbon nanotube incorporated with magnetite nanoparticles; the incorporation of the iron oxide nanoparticles could not show any peak. The reduction in the peak size is caused by the incorporation of the nanoparticles in the host unmodified material, and these embedded nanoparticles have shown the crystalline peaks in the modified materials.

Figure 3-6 (c) QM1-2 shows the number of peaks due to embedded silver nanoparticles in the commercial materials, and the intensity is almost same to that of magnetite composite materials. The XRD spectrum has revealed four peaks of

intensity at 38.9, 44.4, 64.6, and 78.3 in the 2 theta region, corresponding to (1 1 1), (2 0 0), (2 2 0), and (3 1 1) planes of silver due to the face-centered cubic (fcc) structure of the incorporated silver nanoparticles (Kanmani and Lim, 2013, Pandey *et al.*, 2012). Figure 3-6 (d) QM1-3-based composite shows the crystalline structure of the nanocomposites due to the incorporation of the silver and magnetite nanoparticles. The XRD spectrum of the composite has revealed the confirmation of the particles at 38.9, 44.4, 64.6, and 78.3 in the 2-theta region, corresponding to (1 1 1), (2 0 0), (2 2 0), and (3 1 1) planes of silver and iron nanoparticles (Wang *et al.*, 2013). Furthermore, the characteristic peaks of iron oxide were present in the iron-oxide-incorporated composite at 37°, 43°, 53° and 63° which was confirmed with the published data (Bruce and Sen, 2005, Wang *et al.*, 2013). The results obtained are similar to those predicted of pure magnetite samples when they were compared to standard XRD data for magnetite and were found to be similar to what has been reported in the literature.

3.2.7 Brunauer–Emmett–Teller surface area

Samples were prepared, and results were produced according to the method explained in section 2.3.6. It is reported that the BET results would be considered as valid and acceptable when the correlation coefficient is greater than 0.9975 (Tarleton, 2015). The developed nanocomposite of QM1 to QM1-3-based composite has shown a high surface area ranging from 160 to 257 m²/g.

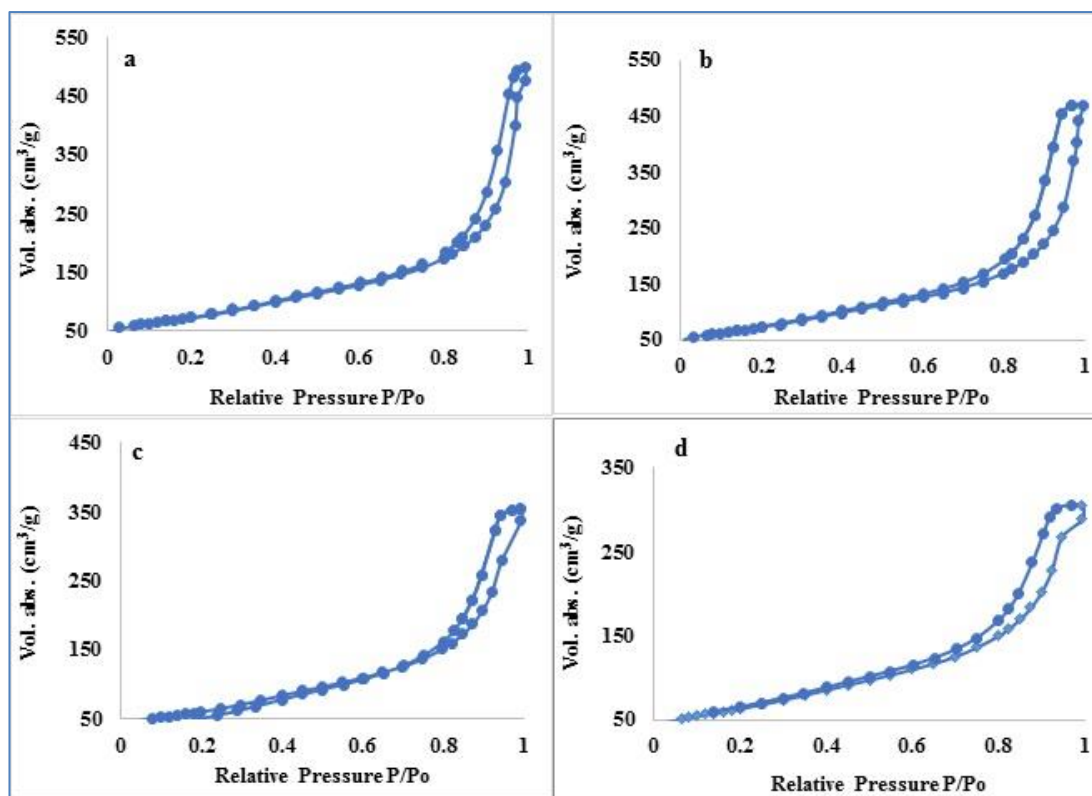


Figure 3-7 Adsorption-desorption isotherm of QM1-based composite (a) QM1 (unmodified MWCNTs) (b) QM1-1 (MWCNTs modified with only iron oxide nanoparticles) (c) QM1-2 (MWCNTs modified with only silver nanoparticles) and (d) QM1-3 (MWCNTs modified with silver coating iron oxide nanoparticles).

Figure 3-7 (a) shows that the material (QM1) is mesoporous in nature as the plot is classified as type 1V isotherm due to the formation of the hysteresis loop, a characteristic of mesoporous structure. A hysteresis loop is produced due to the different pathway of adsorption from desorption of N_2 gas into the pores of the materials (Knežević and Lin, 2013). The BET surface area of the material was measured to be around $257 \text{ m}^2/\text{g}$ by nitrogen adsorption data.

The BET surface area of the composite material (QM1-1) measured to be $209 \text{ m}^2/\text{g}$ from Figure 3-7 (b). The plot is classified as type 1V isotherm due to the formation of the hysteresis loop, indicating no loss of mesoporosity due to the incorporation of iron oxide nanoparticles into the matrix. Figure 3-7 (c) QM1-2 represents the BET surface area of the modified carbon nanotube silver composite material; the BET surface area

of the composite material was measured to be around 180 m²/g. The graph is classified once again as type 1V isotherm. Figure 3-7 (d) QM1-3 shows the BET surface area of the composite modified with silver and iron oxide nanoparticles; the BET surface area of the composite material was measured to be around 160 m²/g. There was no loss of hysteresis loop after the incorporation of iron oxide and silver nanoparticles, indicating that the structure of the host matrix remained unchanged as mesoporous. There was a reduction of surface area (from 257 to 160 m²/g) after the modification, indicating that parts of the mesopores are blocked due to the presence of iron oxide and silver nanoparticles. The BET surface area, micropore volume and pore diameter of unmodified QM1 and modified materials are given in Table 3-1.

Table 3-1. BET analysis of unmodified QM1 and modified QM1-based magnetite silver nanocomposite

Sample	BET surface area (m²/g)	Micropore volume (cm³/g)	BJH Adsorption Average Pore Diameter (Å)
QM1	257	0.011	96
QM1-1	209	0.010	90
QM1-2	180	0.010	83
QM1-3	160	0.010	79

CHAPTER FOUR

4 Analysis of structure, chemical composition and properties of AC based modified composites

4.1 Activated charcoal- based composites (QM2 to QM2-3)

4.1.1 X-ray fluorescence

Elemental analysis QM2-based nanocomposites were determined with X-ray fluorescence. Samples were prepared according to the method described in section 2.3.1. XRF analysis of QM2-based materials are shown on next page.

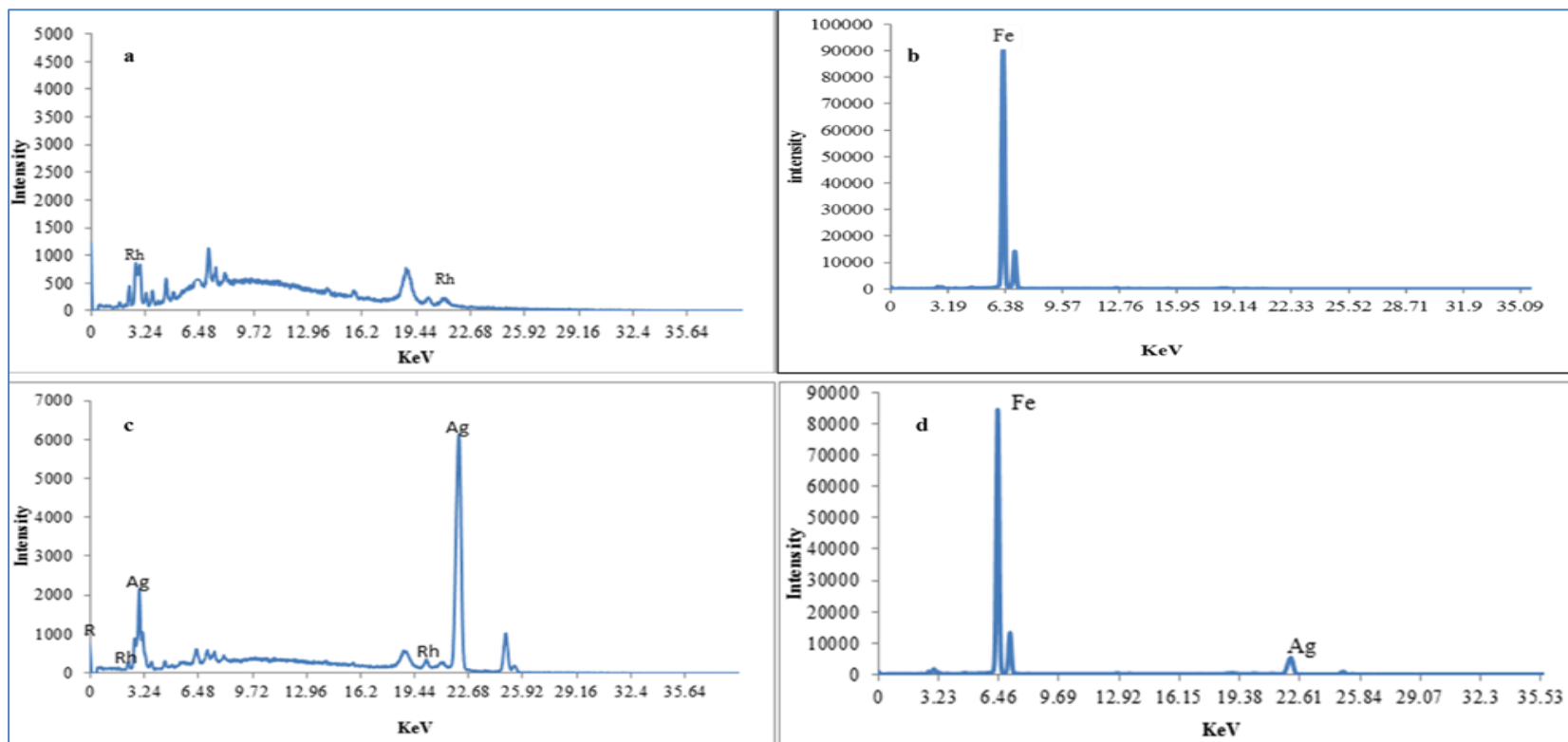


Figure 4-1 XRF of QM2-based composite (a) QM2 (AC-unmodified) (b) QM2-1 (AC- modified with only iron oxide nanoparticles) (c) QM2-2 (AC- modified with only silver nanoparticles) and (d) QM2-3 (AC- modified with silver coating iron oxide nanoparticles)

Figure 4-1 (a) shows the spectrum of QM2 as a control sample. Small impurity peaks (intensity less than 1000 counts) of Rhodium and Titanium were observed in the spectrum due to the X-ray source generated in the system. The x-ray fluorescence spectrum Figure 4-1 (b) of QM2-1(iron oxide modified activated charcoal) indicates the presence of Fe (K_{α}) from embedded iron oxide at 6.38 KeV. Small peaks of Rhodium and Titanium were suppressed due to the presence of a strong peak of Fe. Figure 4-1 (c) shows the X-ray fluorescence of QM2-2 (activated charcoal containing silver) nanocomposite material by looking at the spectrum, the presence of the silver particles can be seen, at 3.24 (K_{α} or K_{β}) and 22.68 KeV (K_{α} or K_{β}) as reported (Howard, 2011).

Figure 4-1 (d) shows the X-ray fluorescence of QM2-3-based composite containing iron oxide and silver nanoparticles. Furthermore, by looking at the spectrum, the presence of the magnetite and silver particles can be clearly seen, at 6.46 and at 22.61 KeV, respectively, as reported (Howard, 2011, Preoteasa *et al.*, 2002).

4.1.2 Energy dispersive X-ray analysis

EDAX was engaged for the elemental analysis of the compounds and this technique is an additional application of SEM and TEM; both instruments have attached an application for element determination. EDAX is considered as one of the analytical methods which provide information comprehensively for developed material such as composite mapping and detection of the elements. In order to confirm the presence of the incorporated elements in the composite EDAX was carried out and the spectrum clearly showed the signals. The EDAX analysis of all batches was performed in SEM; it included commercial material: its own and modified material with magnetite and silver nanoparticles.

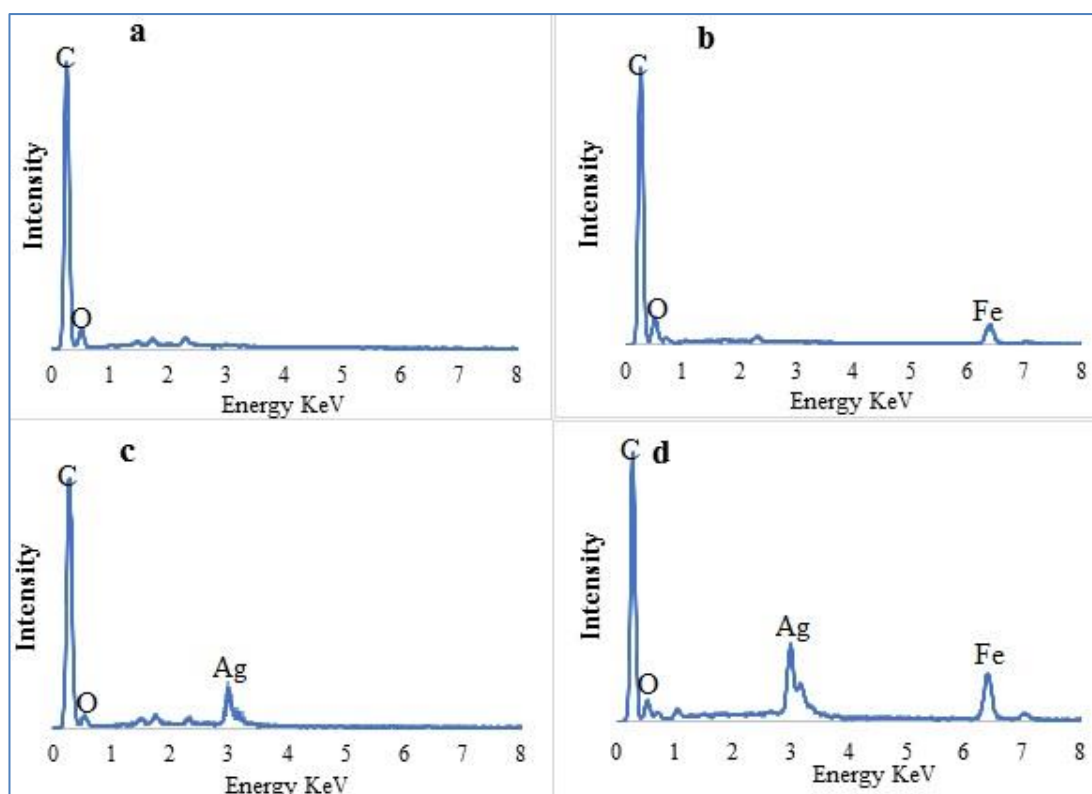


Figure 4-2 EDAX Spectrum of QM2-based composite (a) QM2 (AC-unmodified) (b) QM2-1 (AC- modified with only iron oxide nanoparticles) (c) QM2-2 (AC- modified with only silver nanoparticles) and (d) QM2-3 (AC- modified with silver coating iron oxide nanoparticles)

Figure 4-2 (a, b, c, and d) show the EDAX spectrum of QM2 unmodified commercial material, modified with iron oxide, silver and silver coating iron oxide respectively.

Figure 4-2 (a) shows the EDAX analysis of the unmodified QM2 (activated charcoal), the peak of carbon is prominent while oxygen, aluminium, silicon and sulphur are also the components of the commercial material in trace amounts which are clearly seen in this figure at their respective energy levels (KeV). For analysis, produced energy values of the spectrum were compared with the wavelength of emitted X-rays.

Figure 4-2 (b) shows the QM2 embedded with iron oxide, the presence of the iron in the developed composite is pretty explicit from the spectrum located at 6.3 KeV (K_{α}) radiation while carbon, oxygen and sulphur are also present as these are the components of the commercial QM2- based material. Figure 4-2 (c) shows the spectrum of the QM2-2-based silver nanocomposite. This figure clearly indicates the

presence of the silver at 3.0 KeV (K_{α} or K_{β}) as was reported (Ranjbar and Morsali, 2011, Luong *et al.*, 2008), this experiment confirmed the XRF results of this project by showing the incorporated nanoparticles. Figure 4-2 (d) shows the presence of the incorporated silver and iron in the QM2-3 based composite. Silver can be seen at 3.00 KeV while iron is located at 6.3 KeV. In addition to this, traces of the other elements are seen, which are the components of the activated charcoal such as oxygen, aluminium and silicon, while sodium is present due to the use of sodium borohydride, which was used as a reducing agent for the synthesis of the silver nanoparticles.

4.1.3 Scanning electron microscopy

Scanning electron microscopy, as described in section 2.3.2, was engaged to examine the morphology of the synthesised activated-charcoal based nanocomposites and unmodified activated charcoal. For the surface study, images were taken which are discussed below.

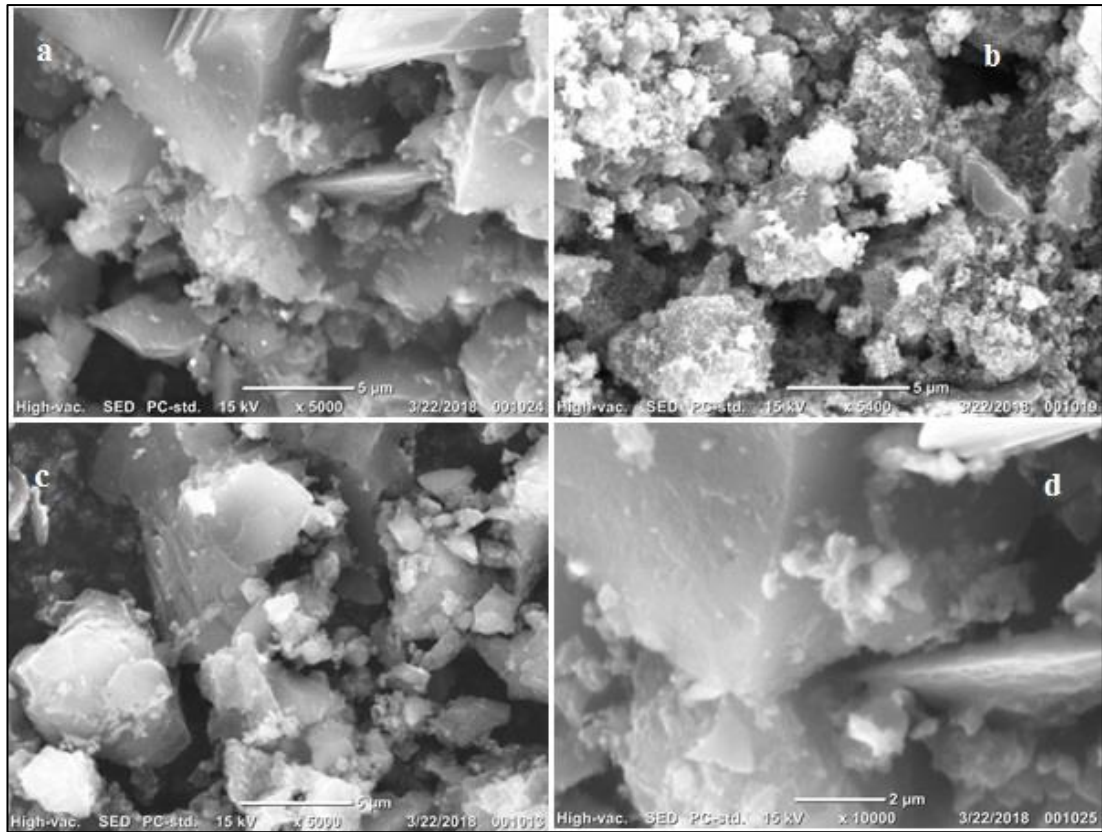


Figure 4-3 SEM of QM2 based composite (a) QM2 (AC-unmodified) (b) QM2-1 (AC-modified with only iron oxide nanoparticles) (c) QM2-2 (AC-modified with only silver nanoparticles) and (d) QM2-3 (AC-modified with silver and iron oxide nanoparticles)

Figure 4-3 (a, b, c and d) shows the surface morphology of the activated charcoal based composites. Figure 4-3 (a) is unmodified activated charcoal and morphology is unsmooth. Figure 4-3 (b, c and d) are modified with iron oxide, silver and silver coating iron oxide nanoparticles respectively. Moreover, there was no difference on the morphology of the raw material and coated with magnetite, silver and with both silver coating iron oxide nanoparticles and was found rough.

4.1.4 Transmission electronic microscopy

For the determination of the size and shape of the incorporated nanoparticles into the QM2 matrix (activated charcoal), TEM was employed, samples were prepared and images were produced according to the method described in section 2.3.3. TEM images of QM2 and QM2-3 based composites are discussed below.

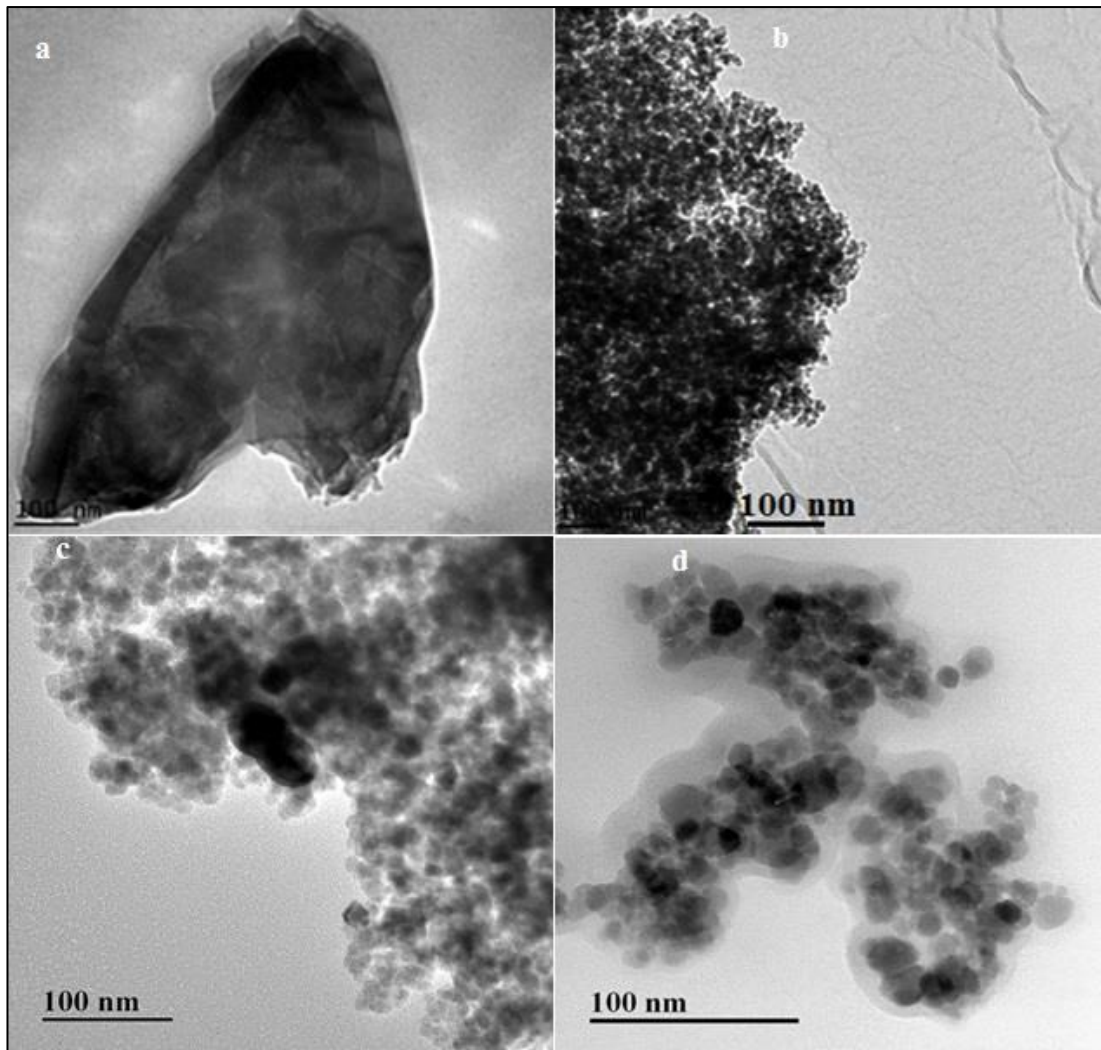


Figure 4-4 TEM images of QM2-based composite (a) QM2 (AC-unmodified) (b) QM2-1 (AC-modified with only iron oxide nanoparticles) (c) QM2-2 (AC-modified with only silver nanoparticles) and (d) QM2-3 (AC-modified with silver coating iron oxide nanoparticles)

Figure 4-4 (a, b, c, and d) show the internal structure of QM2 unmodified commercial material, modified with iron oxide, silver and silver coating iron oxide respectively. Figure 4-4 (a) shows the unmodified commercial activated charcoal (QM2) prior to modification. No specific morphology or presence of nanoparticles was observed. Figure 4-4 (b) shows the QM2 embedded with iron oxide nanoparticles, the presence of the iron oxide nanoparticles can be visualised in the developed composite with the size distribution of iron oxide core nanoparticles around 15-25 nm in diameter with the average size of 20 nm in diameter. Figure 4-4 (c) shows the QM2-2

nanocomposite, where the presence of silver embedded nanoparticles was found inside the modified activated charcoal material with size distribution of around 15-17 nm in diameter with the average size of 16 nm diameter. Figure 4-4 (d) shows the QM2-3 nanocomposite where silver coating iron oxide embedded nanoparticles can be seen clearly inside the modified material.

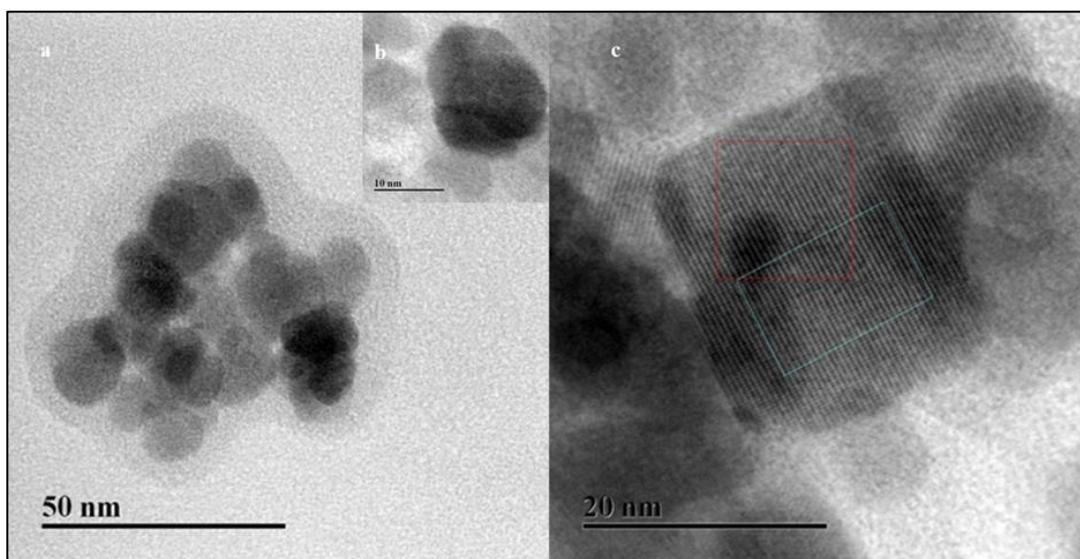


Figure 4-5 High resolution STEM images of QM2-3-based composite (a,b and c) QM2-3 (AC -modified with silver coating iron oxide) (b) QM2-3 (AC- modified with silver and iron oxide) shows the nano-size of silver nanoparticle and (c) presence of well crystalline iron oxide nanoparticles in QM2-3.

Figure 4-5 (a and b) shows silver coating iron oxide nanoparticles, where iron oxide nanoparticles were around 20 nm with rhombic morphology. The lattice spacings of the crystalline iron oxide nanoparticles were measured to be around 0.36 nm. The size, distribution and shape of the nanoparticles in the nanocomposite was in agreement with reported literature (Sen *et al.*, 2006, Sen *et al.*, 2012, Sharifabad *et al.*, 2013). Both iron and silver nanoparticles were observed in QM2-3. Silver nanoparticles were observed to be around 15-17 nm in diameter with spherical symmetry (see figure 4-6).

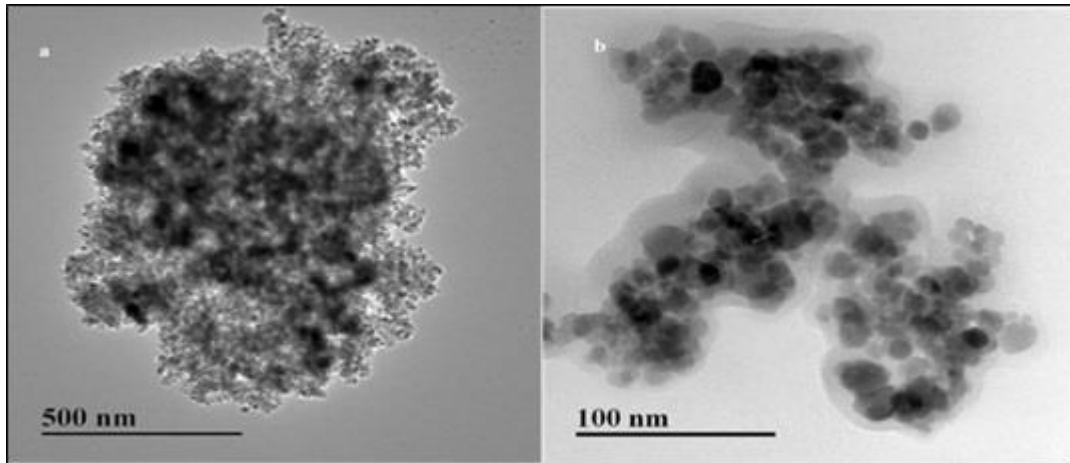


Figure 4-6 (a and b) QM2-3-based composite, modified with iron and silver nanoparticles.

4.1.5 Fourier transform infrared spectroscopy

FT-IR spectra were recorded in the range of 400 – 4000 cm^{-1} to confirm the presence of functional groups or bonding between the atoms.

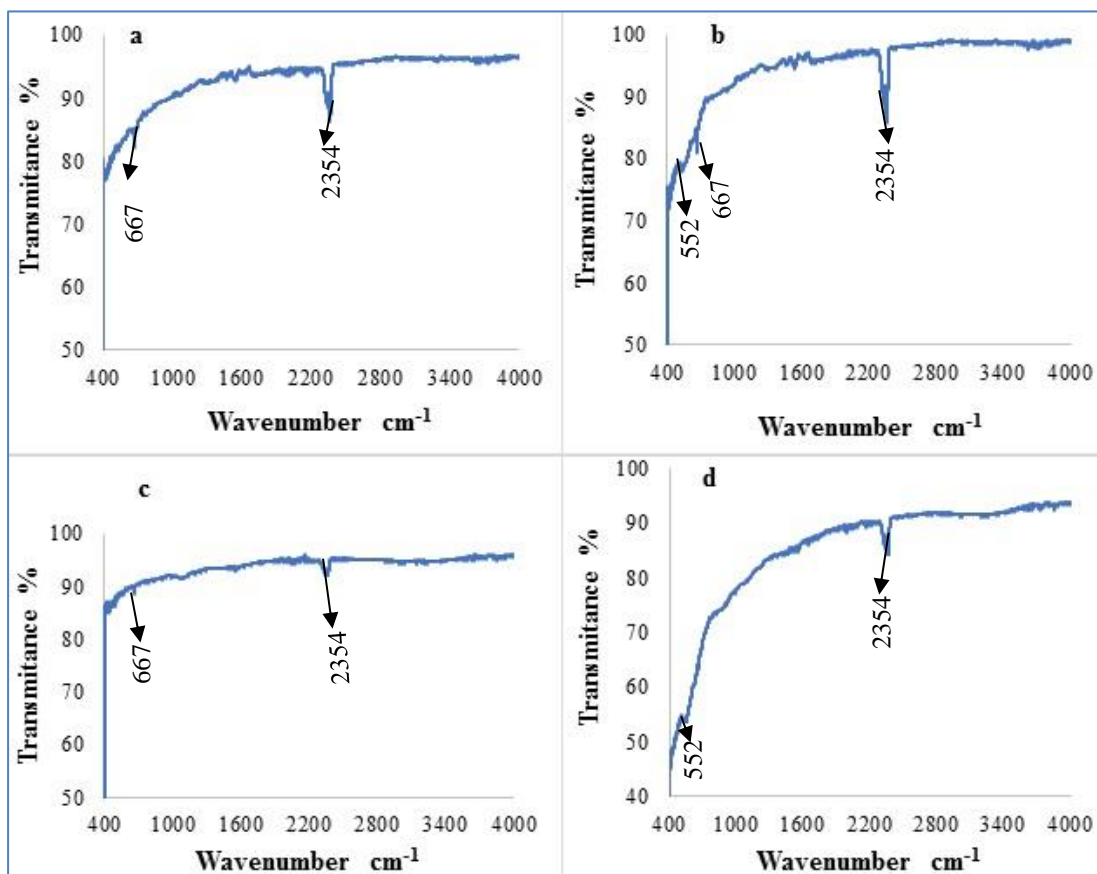


Figure 4-7 FT-IR spectra of QM2-based composite (a) QM2 (AC-unmodified) (b) QM2-1 (AC- modified with only iron oxide nanoparticles) (c) QM2-2 (AC- modified with only silver nanoparticles) and (d) QM2-3 (AC- modified with silver coating iron oxide nanoparticles)

Figure 4-7 (**a**, **b**, **c** and **d**) shows the FT-IR analysis of all samples of the QM2-based unmodified and modified material, all the samples have shown the peaks at 667 and 2354 cm^{-1} , which were associated with the CO_2 groups due to the CO_2 coating of the IR optics in the spectrometer. Figure 4-7 (**b** and **d**), have shown the peaks at 552 cm^{-1} which were associated with the Fe-O due to stretching vibration of the Fe-O bond of the core (Zou *et al.*, 2014). Figure 4-7 (**c**) contains the silver; AgNPs do not show absorption in the infrared spectral region (Wang *et al.*, 2013). This result agrees with the EDAX interpretation of the developed composite.

4.1.6 X-ray diffraction

The crystallinity of the modified and unmodified activated charcoal was determined by the X-ray diffraction (XRD) technique; which is described in section 2.3.5; due to the embedded silver and magnetite nanoparticles in the host matrix, the developed composite has acquired crystallinity. No diffraction peaks corresponding to activated charcoal were observed because of their amorphous nature, while the incorporation of magnetite and silver nanoparticles has changed into crystalline.

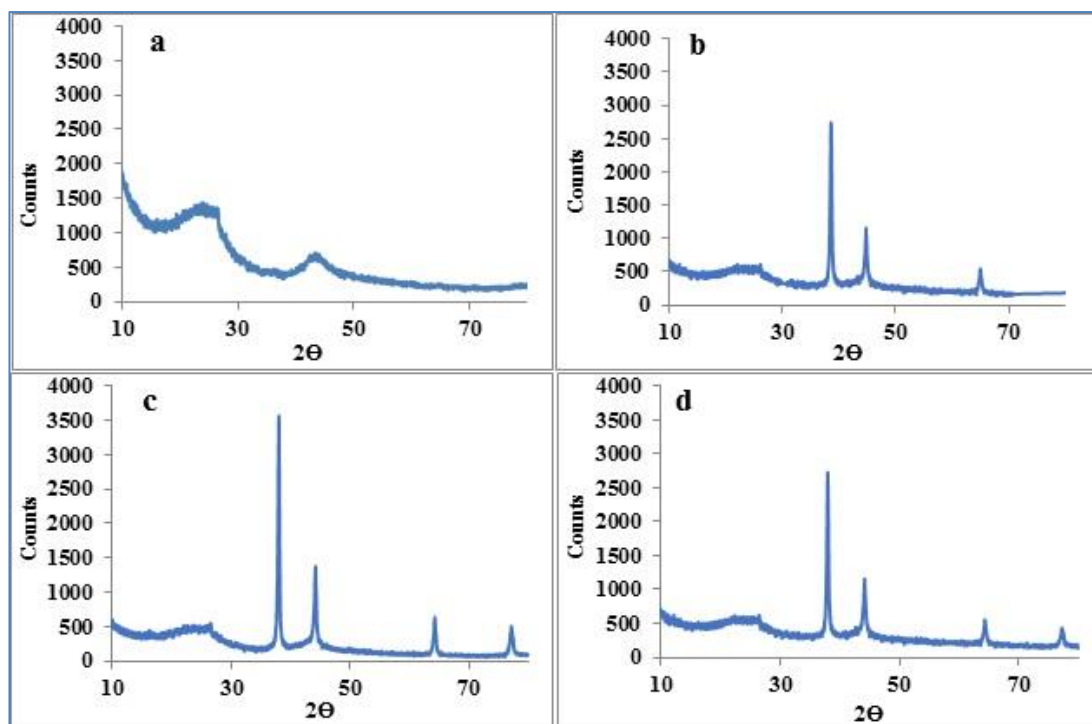


Figure 4-8 XRD of QM2-based composite (a) QM2 (AC-unmodified) (b) QM2-1 (AC-modified with only iron oxide nanoparticles) (c) QM2-2 (AC- modified with only silver nanoparticles) and (d) QM2-3 (AC- modified with silver and iron oxide nanoparticles).

Figure 4-8 (a, b, c, and d) show the XRD pattern of QM2 unmodified commercial material, QM2-1-modified with iron oxide, QM2-2 modified with silver and QM2-3 modified with silver coating iron oxide respectively. Figure 4-8 (a) shows the XRD pattern of unmodified activated charcoal; it reveals the amorphous structure of the activated charcoal, having no diffraction peaks. On the other hand, the modified materials with embedded silver and iron oxide nanoparticles are showing the peaks due to embedded metallic particles.

Figure 4-8 (b) shows the magnetite peaks due to the incorporation of the iron oxide in the activated charcoal in the range of 37°, 43°, 53° and 63° in the 2-theta region, which was confirmed by the published data (Wang *et al.*, 2013), Bruce & Sen 2005) and causes the reduction in the intensity of the commercial material used from 100 counts to 50 counts. Figure 4-8 (d) XRD pattern of activated charcoal containing silver and iron nanoparticles has revealed the confirmation of the incorporated particles at 38.9,

44.4, 64.6, and 78.3 in the 2-theta region, corresponding to (1 1 1), (2 0 0), (2 2 0) and (3 1 1) planes of silver and iron oxide nanoparticles (Wang *et al.*, 2013). It has been observed that the incorporation of the silver and iron oxide in the activated charcoal changes the amorphous material into the crystalline and has shown the respective peaks in the embedded area of the material.

4.1.7 Brunauer–Emmett–Teller surface area measurement

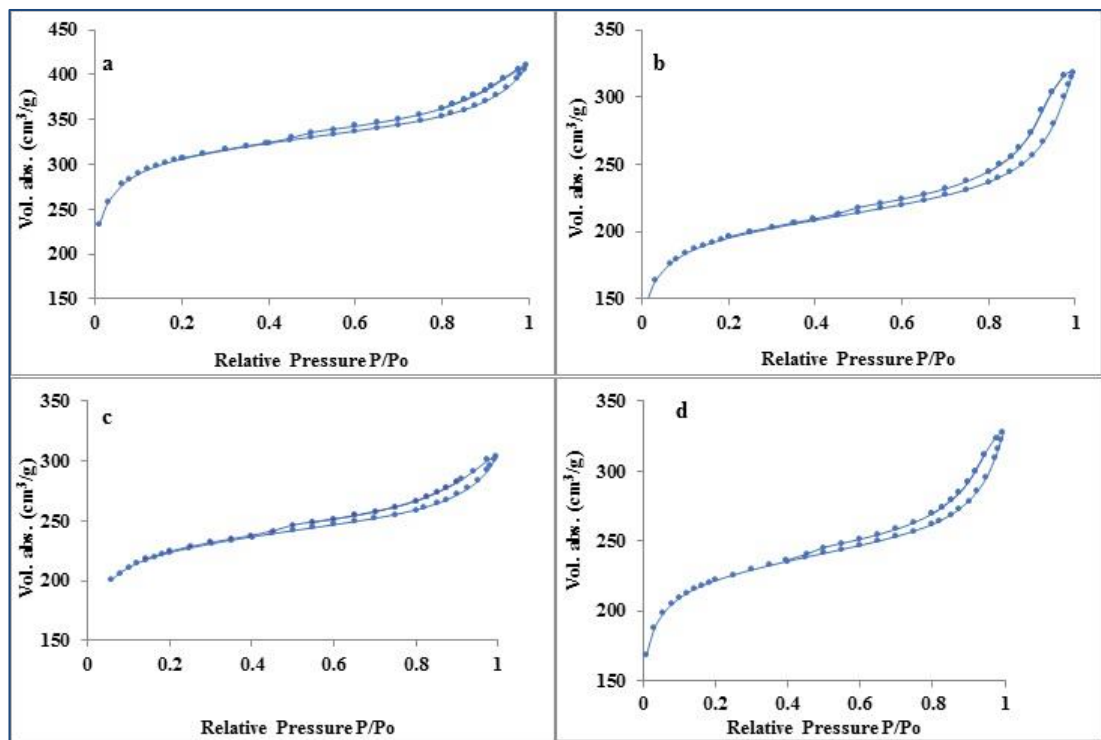


Figure 4-9 N₂ gas adsorption isotherm of QM2-based composite (a) QM2 (AC-unmodified) (b) QM2-1 (AC- modified with only iron oxide nanoparticles) (c) QM2-2 (AC- modified with only silver nanoparticles) and (d) QM2-3 (AC- modified with silver coating iron oxide nanoparticles).

Figure 4-9 (a, b, c, and d) show the N₂ gas adsorption-desorption isotherm of QM2 unmodified commercial material, modified with iron oxide, silver and silver coating iron oxide respectively. The graphs of all samples are classified as type IV isotherm due to the hysteresis loop from 0.6 to 1.0 relative pressure (P/P_o) which is the indication for mesoporous composite. Figure 4-9 (a) represents the BET surface area

of the unmodified activated charcoal; the surface area of the composite material was measured to be 1050 m²/g by nitrogen adsorption data. The graph shows the hysteresis, which means the material is mesoporous in nature. Figure 4-9 (b) shows the BET surface area of the activated charcoal containing iron oxide, the surface area of the composite material was measured to be 701 m²/g by nitrogen adsorption data. The graph is also showing the hysteresis which means the material is mesoporous (Howard, 2011). Figure 4-9 (c) shows the BET surface area of the activated charcoal containing silver nanoparticles, the surface area of the composite material, was measured to be 600 m²/g by nitrogen adsorption data. The graph also shows the hysteresis which means the material is mesoporous in nature. Figure 4-9 (d) shows the BET surface area of the activated charcoal composite material. The surface area of the composite material was measured to be 560 m²/g by nitrogen adsorption data. The graph also shows hysteresis which means the material is mesoporous in nature.

Table 4-1. BET analysis of unmodified QM2 and modified QM2-based magnetite silver nanocomposite

Sample	BET surface area (m ² /g)	Micropore volume (cm ³ /g)	BJH Adsorption Average Pore Diameter (Å)
QM2	1050	0.33	70.
QM2-1	701	0.21	60.
QM2-2	600	0.16	55.
QM2-3	560	0.16	50.

CHAPTER FIVE

5 Analysis of structure, chemical composition and properties of DAE based modified composites

5.1 Diatomaceous earth-based composite (QM3 to QM3-3)

5.1.1 X-ray fluorescence

XRF is a non-destructive chemical analysis, which is used for the analysis of rocks, minerals and sediments. Here, it has been used for elemental analysis; the technique is described in section 2.3.1. It produced the spectrum according to their X-ray energy; X-ray develops part of the electromagnetic spectrum and is represented in terms of their energy as (KeV). The formation of the X-ray fluorescence is caused by the change that takes place in an atom due to the emission of the electron (Wegscheider, 2012).

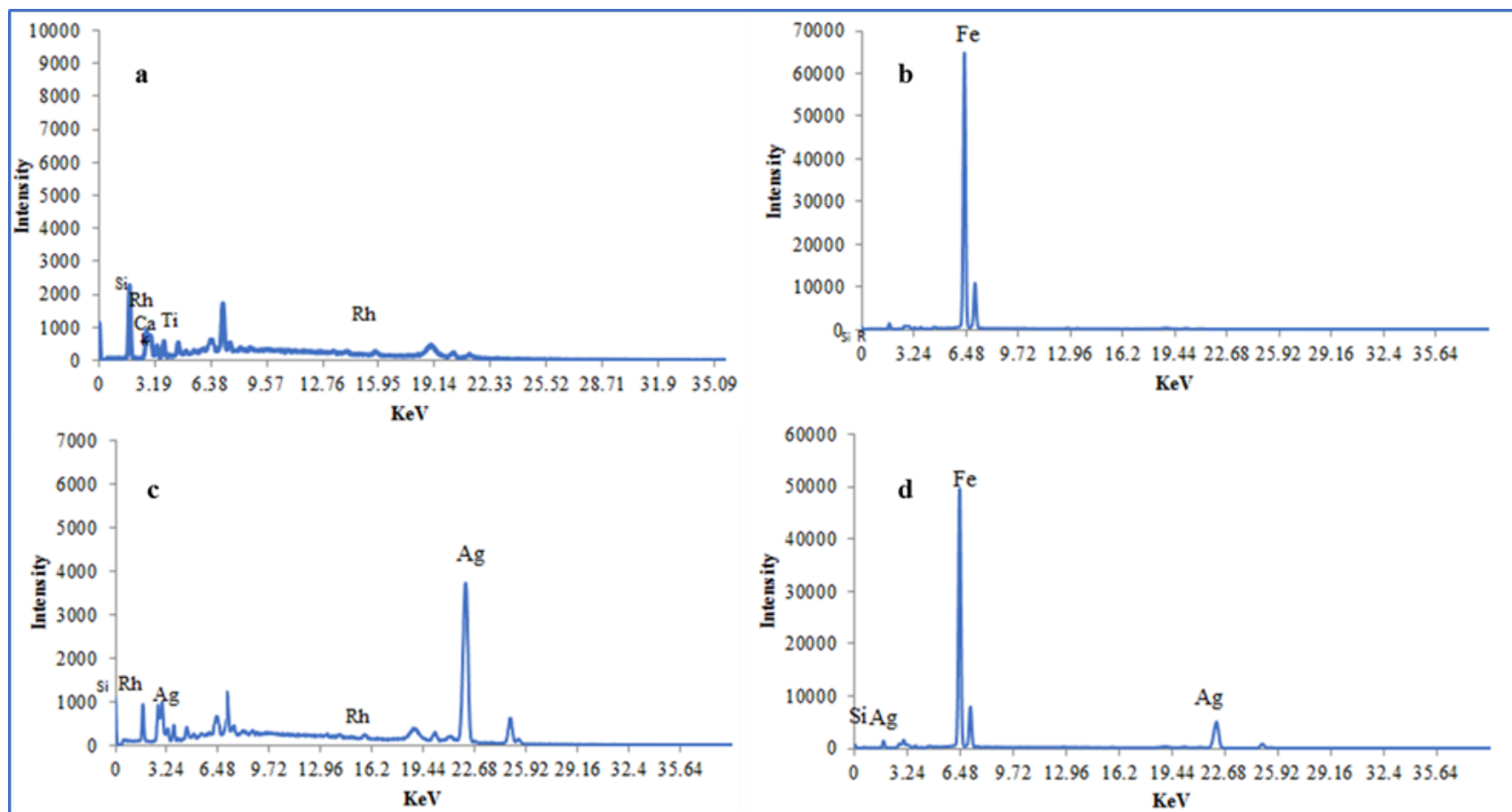


Figure 5-1 X-ray fluorescence of QM3-based composite (a) QM3 (DAE-unmodified) (b) QM3-1 (DAE- modified with only iron oxide nanoparticles) (c) QM3-2 (DAE- modified with only silver nanoparticles) and (d) QM3-3 (DAE- modified with silver and iron oxide)

Figure 5-1 (**a**, **b**, **c**, and **d**) show X-ray fluorescence of QM3 unmodified material, modified with iron oxide, silver and silver iron oxide respectively. Figure 5-1 (**a**) is amorphous and unmodified solid material so no incorporated metal appears in the material. Furthermore, the small peaks of rhodium and titanium, could be witnessed in the spectrum which are the source of the X-ray in the machine.

Figure 5-1 (**b**) shows the x-ray fluorescence QM3-1-based magnetite composite. By looking at the spectrum, it can be clearly seen that there is only one strong peak for the iron at 6.38 KeV due to the presence of Fe (K_{α}) radiation, while other peaks are suppressed due to strong band of the iron. Figure 5-1 (**c**) shows the X-ray fluorescence of QM3-2-based silver-containing composite, where a strong band for silver could be seen at 3.24 (K_{α} or K_{β}) and 22.68 KeV (K_{α} or K_{β}).

Figure 5-1 (**d**) shows the X-ray fluorescence of QM3-3-based composite containing iron oxide and silver nanoparticles. Furthermore, the presence of magnetite and silver particles can be clearly seen, at 6.46 and at 22.61 KeV due to the presence of radiations (K_{α} or K_{β}) of incorporated particles.

5.1.2 Energy dispersive X-ray analysis

This analytical instrument was engaged to determine the presence of the incorporated elements; EDAX is considered as one of the analytical techniques, comprehensively providing information for the composition of material such as composite mapping and detection of the elements. The EDAX analysis of all batches were performed in SEM. It included unmodified DAE and modified DAE containing magnetite and silver nanoparticles.

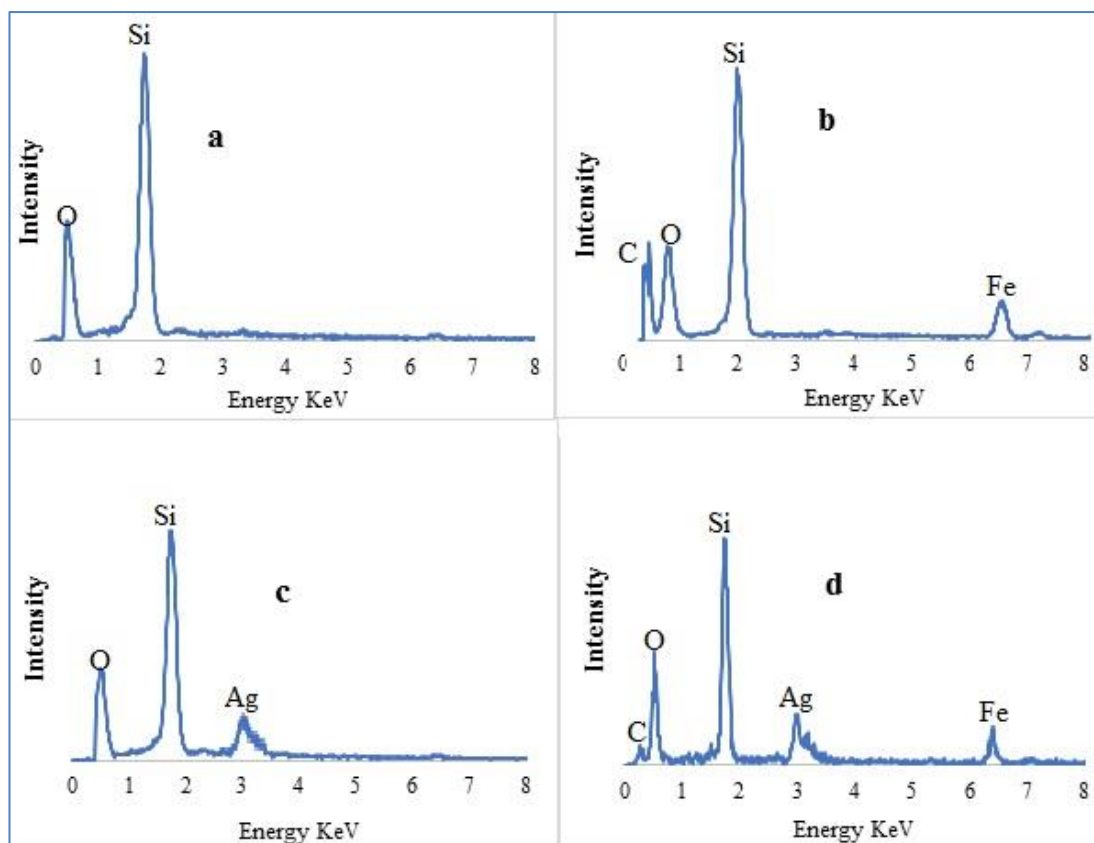


Figure 5-2 EDAX spectrum of QM3-based composite (a) QM3 (DAE-unmodified) (b) QM3-1 (DAE- modified with only iron oxide nanoparticles) (c) QM3-2 (DAE- modified with only silver nanoparticles) and (d) QM3-3 (DAE- modified with silver coating iron oxide nanoparticles)

Figure 5-2 (a, b, c, and d) EDAX spectrum of QM3 unmodified commercial material, modified with iron oxide, silver and silver coating iron oxide respectively. Figure 5-2 (a) shows the EDAX analysis of pure diatomaceous earth; the silicon, oxygen and carbon are clearly seen in this figure. The EDAX analysis of the QM3 shows the presence of carbon due to the grid, which was made of carbon. At the same time, oxygen and silicon were the main components of the material, which can be seen in figure 5-2. Furthermore, along with essential elements of the material some metals can be seen as well, which are the part of the material such as, magnesium and aluminum while sodium is present at 1.00 KeV due the sodium borohydride, which was used as a reducing agent for the preparation of the silver nanoparticles. Figure 5-2 (b) shows

the spectrum of QM3-containing magnetite, iron was located at 6.3 KeV, and major peaks of silicon, oxygen and carbon are clearly seen in the graph. Figure 5-2 (c) is the spectrum of diatomeous earth-based silver nanocomposite material. This figure clearly shows the presence of silver at 3.0 KeV as it was analysed before (Ranjbar and Morsali, 2011, Luong *et al.*, 2008) and confirmed the results of X-ray fluorescence. Figure 5-2 (d) shows the presence of incorporated elements in the diatomeous earth. Silver can be seen at 3.00 while iron is located at 6.3 KeV. Moreover, the components of the commercial diatomeous earth like silicon which has been estimated at about 90% is present at 2.00 KeV, oxygen is shown at 1.00 KeV and carbon could be seen in the spectrum due to the SEM grid which was coated with carbon.

5.1.3 Scanning electron microscopy

SEM was employed to determine the surface morphology of the developed nanocomposite and unmodified material. The microscopic images of the surface of the material were taken at various magnifications. The technique is explained in detail in section 2.3.2.

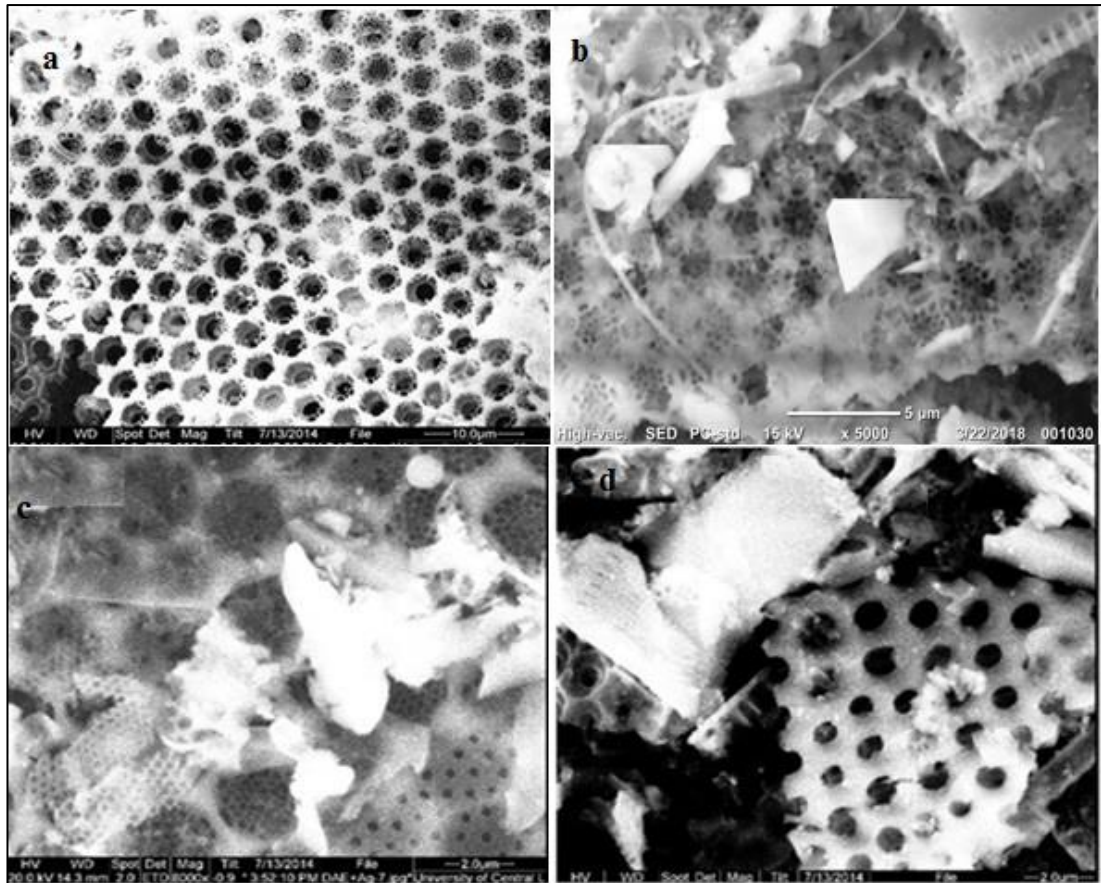


Figure 5-3 Surface morphology of QM3-based composite (a) QM3 (DAE-unmodified) (b) QM3-1 (DAE- modified with only iron oxide nanoparticles) (c) QM3-2 (DAE- modified with only silver nanoparticles) and (d) QM3-3 (DAE- modified with silver coating iron oxide nanoparticles)

Figure 5-3 shows the surface morphology of the QM3 based unmodified and modified materials. Figure 5-3 (a) QM3 (Diatomeous earth unmodified commercial material) shows the porous structure. The experiment was performed at 15 KeV with 5000 magnifications at 5.0 μm . From the above picture, the porous surface of the material can be seen clearly. The morphology of the commercial material shows that the purchased material was porous in nature and can be used as a matrix for the incorporation of the nanoparticles in the holes of the material. Figure 5-3 (b, c and d) shows the surface morphology of the QM3-1, QM3-2 and QM3-3 based composite contains iron oxide, silver and silver coating iron oxide nanoparticles. Experiment was performed at 15 KeV with 5000 magnifications at 5.0 μm . Figure 5-3(b, c and d) shows

the porous surface of the material along with the incorporation of the magnetite, silver and silver coating magnetite nanoparticles. The morphology of the QM3-based modified with silver and magnetite nanoparticles show that there is not much change on the surface of the commercial material. The developed material was porous in nature and can be used as matrix for different applications along with antimicrobial applications (Reisfeld *et al.*, 2008).

5.1.4 Transmission electron microscopy

This technique is vital to determine the internal structure. The size of the incorporated particles into the matrix and shape of the nanoparticles as reported (Sen *et al.*, 2006, Del Campo *et al.*, 2005, Yi *et al.*, 2005, Santra *et al.*, 2001) was examined with TEM. The technique is described in section 2.3.3.

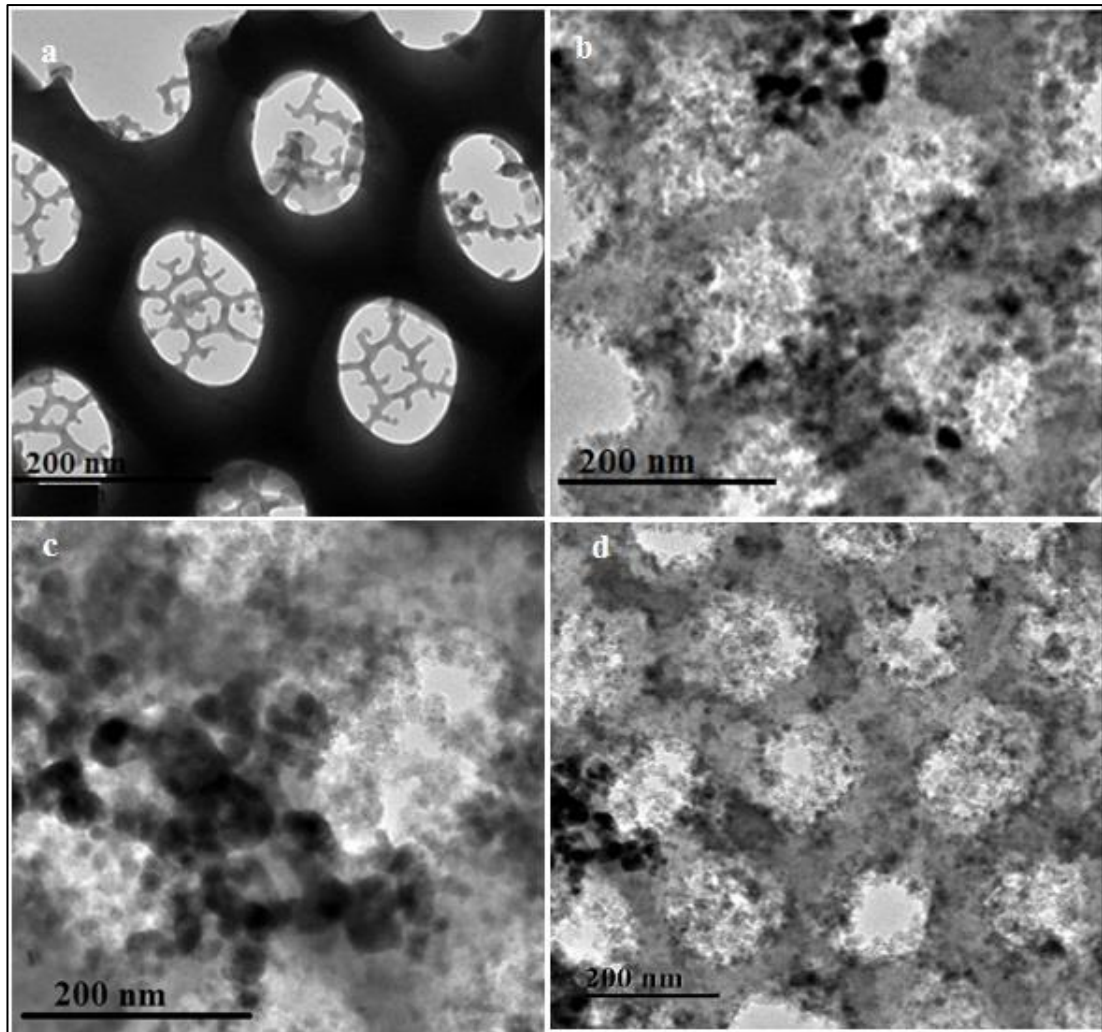


Figure 5-4 TEM images of QM3-based composite (a) QM3 (DAE-unmodified) (b) QM3-1 (DAE- modified with only iron oxide nanoparticles) (c) QM3-2 (DAE- modified with only silver nanoparticles) and (d) QM3-3 (DAE- modified with silver coating iron oxide nanoparticles)

Figure 5-4 (a, b, c, and d) show the internal structure of QM3 unmodified commercial material, modified with iron oxide, silver and silver coating iron oxide respectively.

Figure 5-4 (a) show the unmodified commercially purchased diatomaceous earth, TEM revealed the macro porous structure of the unmodified QM3. The image of unmodified material revealed the high porosity of the material, which was measured at around 200nm. Figure 5-4 (b) shows the QM3-1 nanocomposite where iron oxide embedded nanoparticles can be seen clearly inside the matrix with the size distribution around

20-37 nm in diameter with the average size of 22 nm in diameter. Figure 5-4 (c) shows the QM3-2 nanocomposite modified with the silver embedded nanoparticles which are present in the material with size distribution of around 15-17 nm in diameter with the average size of 16 nm in diameter. Figure 5-4 (d) shows the QM3-3 nanocomposite where silver coating iron oxide embedded nanoparticles can be seen inside the matrix. The incorporated nanoparticles showed size distribution of silver coated iron oxide nanoparticle 15-17 nm and 20- 35 nm diameter with an average size of 16 nm and 30 nm respectively.

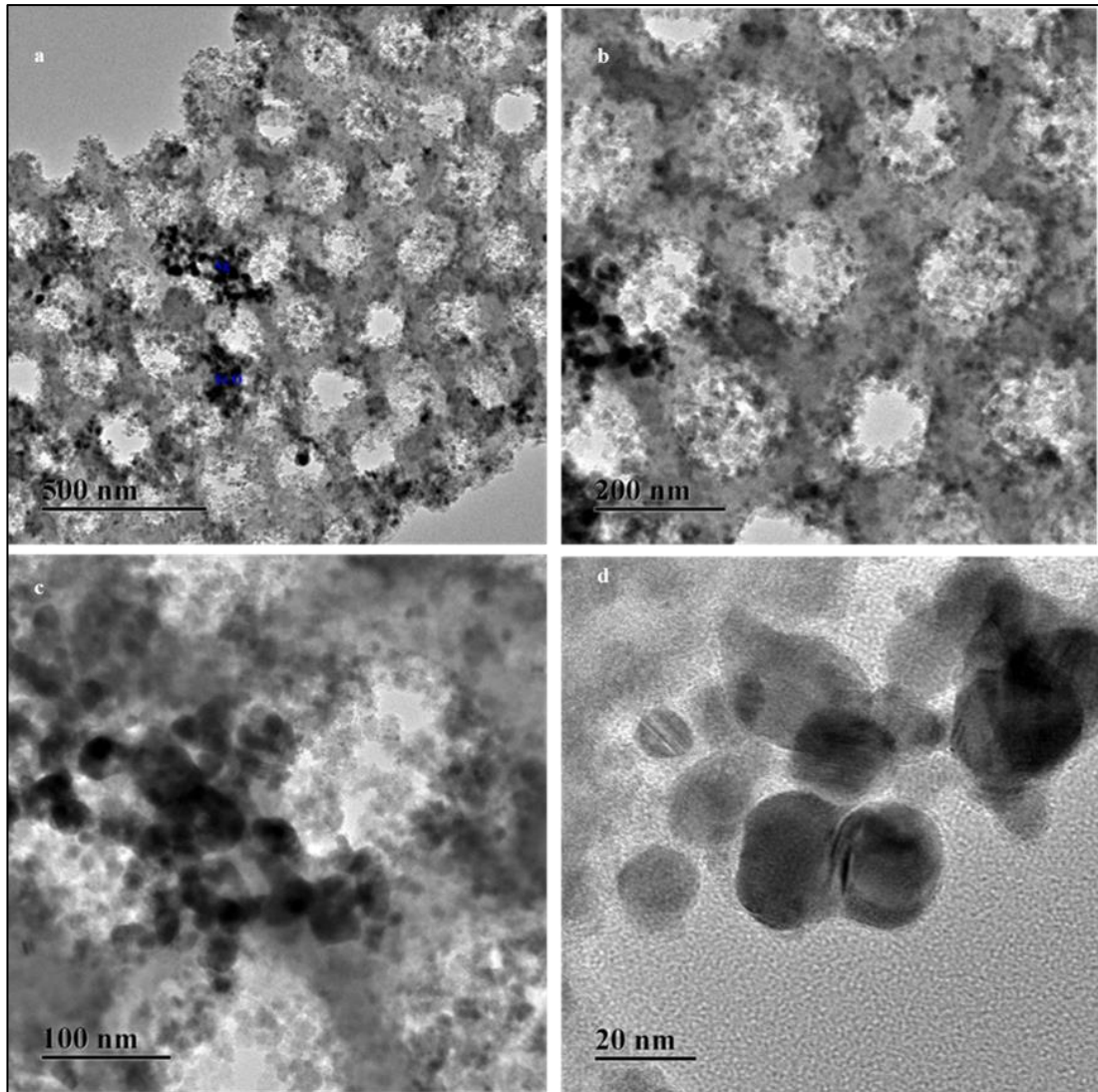


Figure 5-5 High resolution HTEM images of QM3-3 materials (a, b, c and d) (DAE-modified with silver coating iron oxide nanoparticles).

Figure 5-5 (a, b, c and d) show QM3-3-based composite containing silver coating iron oxide nanoparticles. Figure 5-5 (a, b, c and d) show the internal structure of the modified material, all the images of modified composite showed size distribution of silver and iron oxide nanoparticle 15-17 nm and 20- 35 nm diameter with an average size of 16 nm and 30 nm respectively. The images of two different nanoparticles are more polydispersed with a size of $15-35 \pm 2$ nm. The core shell nanoparticles with spherical shape can be visualised from (a to d). The size, distribution and shape of silver and iron oxide are agreed with the literature data (Sen *et al.*, 2006, Sen *et al.*,

2012, Sharifabad *et al.*, 2013, Iglesias-Silva *et al.*, 2007). Images were taken at different magnifications to view the shape and size of the particles. Furthermore, due to silver nanoparticles being spherical in shape and iron oxide being a mixture of spherical and orthorhombic. The main purpose of the incorporation of the silver nanoparticles into the host matrix was to stabilise its antimicrobial properties as reported (Mukha *et al.*, 2013), while magnetite nanoparticles have been used for recycling purposes (Sen *et al.*, 2010).

5.1.5 Fourier transform infrared analysis

The developed modified nanocomposite material and unmodified (DAE) commercial material were characterized by FT-IR spectroscopy (Nicolet IR200 FT-IR), for iron oxide bond analysis, pinches of modified and unmodified materials were examined and spectra were taken after 32 scans, as described in section 2.3.4. The Fourier transform infrared (FT-IR) spectra were recorded in the range 400–2900 cm^{-1} , to confirm the presence of iron oxide.

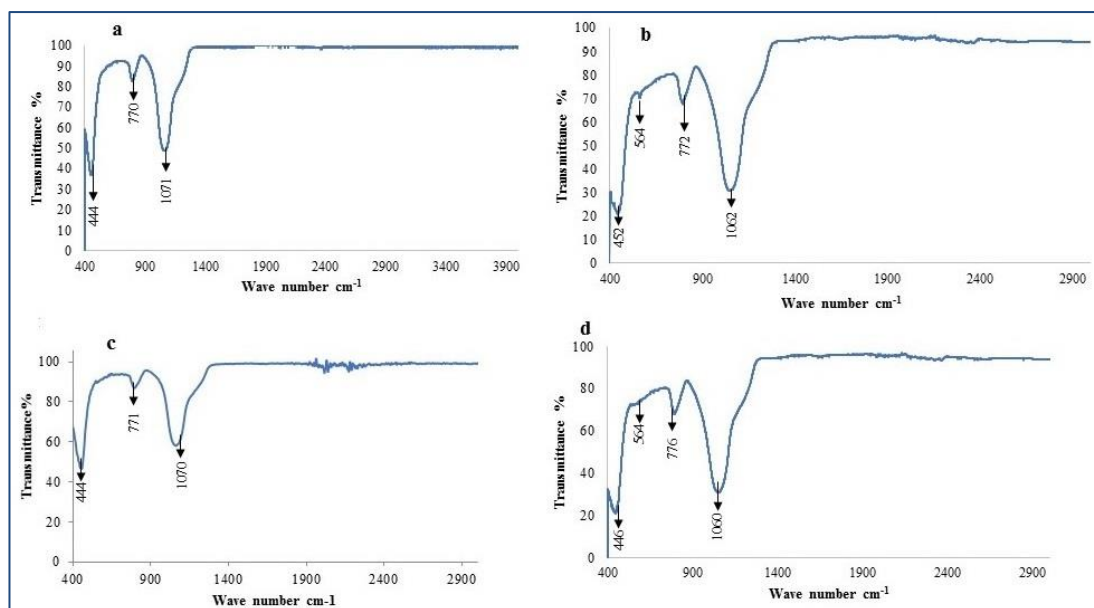


Figure 5-6 FT-IR analysis of all samples of QM3-based composite (a) QM3 (DAE-unmodified) (b) QM3-1 (DAE- modified with only iron oxide nanoparticles) (c) QM3-2 (DAE- modified with only silver nanoparticles) and (d) QM3-3 (DAE- modified with silver and iron oxide nanoparticles).

Figure 5-6 (a, b, c and d) shows the FT-IR spectra of the diatomaceous earth, magnetite, silver composite and silver coating magnetite nanocomposite respectively. Figure 5-6 (a and c) shows the unmodified and modified with silver nanoparticles respectively, where few peaks were observed at 767 cm^{-1} and 1020 cm^{-1} , to which are attributed Si–O–Si bending and Si–O–Si stretching respectively (Zou *et al.*, 2014). Same peaks are found in all the four samples while Figure 5-6 (b and d) have shown the peaks for the magnetite nanoparticles at 460 to 580 cm^{-1} due vibration of F–O bond along with other peaks which are found in samples of (a and c). This result agrees with the EDAX interpretation of the composite in this project. AgNPs do not show adsorption in the infrared spectral region (Wang *et al.*, 2013) so no peak can be

observed for the silver.

5.1.6 X-ray diffraction

The crystallinity of the modified and unmodified activated charcoal was determined by the X-ray diffraction (XRD) technique; which is described in section 2.3.5. Due to the embedded silver and magnetite nanoparticles in the host matrix, the developed composite has acquired crystallinity. A characteristic XRD pattern of diffracted peaks, corresponding to QM3 was observed.

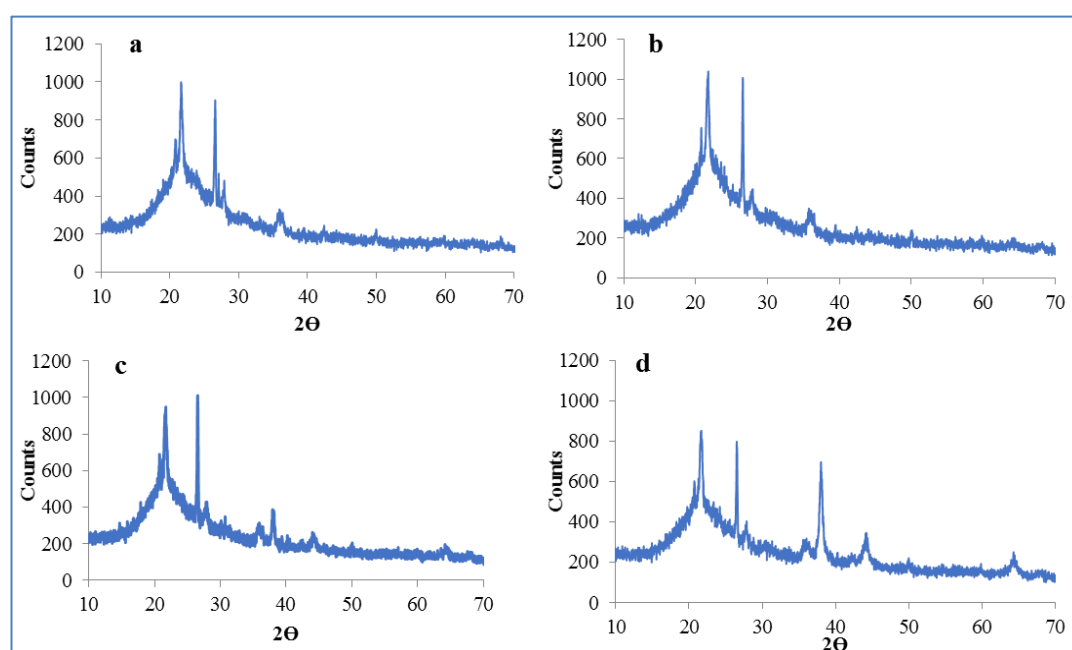


Figure 5-7 XRD of QM3-based composite (a) QM3 (DAE-unmodified) (b) QM3-1 (DAE-modified with only iron oxide nanoparticles) (c) QM3-2 (DAE- modified with only silver nanoparticles) and (d) QM3-3 (DAE- modified with silver coating iron oxide nanoparticles)

Figure 5-7 (a, b, c, and d) show the XRD pattern of QM3 unmodified commercial material, QM3-1-modified with iron oxide, QM3-2 modified with silver and QM3-3 modified with silver coating iron oxide, respectively in the wide-angle region. The crystalline nature of modified nanocomposite and unmodified material was examined by XRD. Figure 5-7 (a and b) show the typical XRD pattern of the QM3 (pure commercial unmodified diatomaceous earth) and QM3-1 modified with iron particles.

Figure 5-7 (c) QM3-2 shows the peaks due to embedded silver nanoparticles in the commercial material and the intensity is almost same as that of magnetite composite materials. Figure 5-7 (d) QM3-3 shows the crystalline structure of the nanocomposite materials due to the incorporation of the silver and magnetite nanoparticles and results are in agreement with the published data (Iglesias-Silva *et al.*, 2007). The XRD spectra of silver and magnetite containing composite show the presence of incorporated atoms at (1 1 1), (2 0 0), (2 2 0), and (3 1 1) in 2Θ planes; Ag was located at 37.5, 43.5, 63.7 and 76.7 respectively, (Wang *et al.*, 2013, Ali *et al.*, 2017). The results obtained are similar to those expected of pure magnetite when compared to standard XRD data for magnetite, and are also in accordance with those reported in the literature (Wang *et al.*, 2013, Ali *et al.*, 2017).

3.3.7 Brunauer–Emmett–Teller surface area

BET was employed for the determination of the surface area, and the nature of the material such as micropore volume (cm^3/g) and pore diameter (\AA) of the composite material containing silver and magnetite nanoparticles. This technique is processed with the adsorption of a known amount of nitrogen gas at relative pressure in the pores of the materials and desorbed by releasing the pressure at low temperature as described in section 2.3.6.

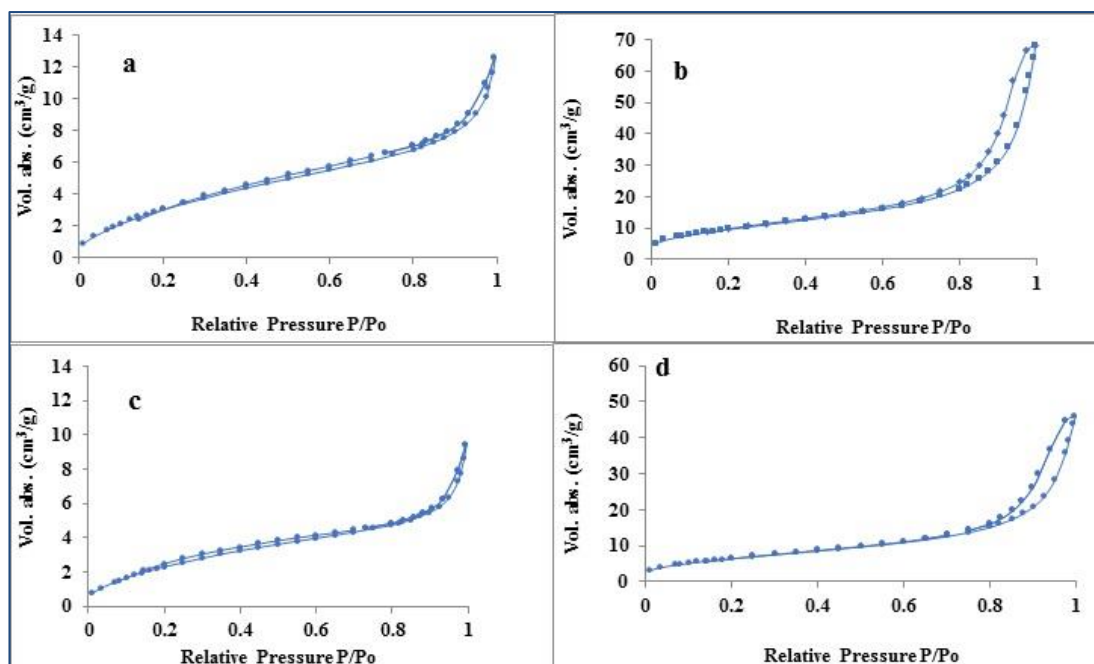


Figure 5-8 N₂ gas adsorption-desorption isotherm of QM3-based composite (a) QM3 (DAE-unmodified) (b) QM3-1 (DAE- modified with only iron oxide nanoparticles) (c) QM3-2 (DAE- modified with only silver nanoparticles) and (d) QM3-3 (DAE- modified with silver coating iron oxide nanoparticles).

Figure 5-8 (a, b, c, and d) show the N₂ gas adsorption-desorption isotherm of QM3 unmodified commercial material, modified with iron oxide, silver and silver-iron oxide respectively. The nitrogen gas adsorption-desorption isotherm of the QM3-3-based composite revealed a type IV isotherm signifying the mesopores structure. The hysteresis loop detected showed non-uniform shapes and sizes of mesopores (Haul 1982). Figure 5-8 (a) represents the BET surface area of the unmodified QM3; the surface area of the material was measured to be 36 m²/g by nitrogen adsorption data. The graph shows the hysteresis due to its mesoporous nature. Figure 5-8 (b) represents the BET surface area of the modified diatomaceous earth magnetite composite material; the surface area of the composite material was measured to be 13 m²/g by nitrogen adsorption, data indicating the material is mostly macroporous in nature. The graph shows the hysteresis, which means the material is mesoporous in nature. Figure 5-8 (c) shows the BET surface area of the (QM3-2) (Diatomaceous earth containing

silver nanoparticles), the surface area of the composite material, was measured to be 11 m²/g by nitrogen adsorption data. The graph shows the hysteresis which means the material is macroporous in nature. Figure 5-8 (d) shows the BET surface area of the QM3 -3 (Diatomaceous earth composite material modified with silver and iron), the surface area of the composite material was measured to be 10 m²/g by nitrogen adsorption data. The surface area has reduced from 36 m²/g to 10 m²/g due to the modification with nanoparticles, this has also been reflected in the BJH pore size reduction, while, no microporosity. The BET analysis of unmodified and modified material is given in Table 5-1.

Table 5-1. BET analysis of unmodified QM3 and modified QM3-based magnetite silver nanocomposite

Sample	BET surface area (m²/g)	Micropore *volume(cm³/g)	BJH Adsorption Average Pore Diameter (Å)
QM3	36	-0.002	91
QM3-1	13	-0.002	56
QM3-2	11	-0.002	50
QM3-3	10	-0.003	46

* Negative values are experimental artefact, hence, materials do not have microporosity

CHAPTER SIX

6 Analysis of structure, chemical composition and properties of Celatom-14 and Celatom- 80 based modified composites

6.1 Celatom-14-based composite (QM4 to QM4-3)

6.1.1 X-ray fluorescence

Analysis for the presence of incorporated elements in the QM4-based modified composite material and unmodified (Celatom CPW-14 commercially purchased material) was performed by using XRF with a model (Bruker Tracer 1V- SD). Generally, all the samples were prepared in the XRF sample cells (SC-4331-N) in 32 mm double open ended small plastic holders. The analysis was performed according to the method given in section 2.3.1, the results of materials are presented in Figure 6.1.

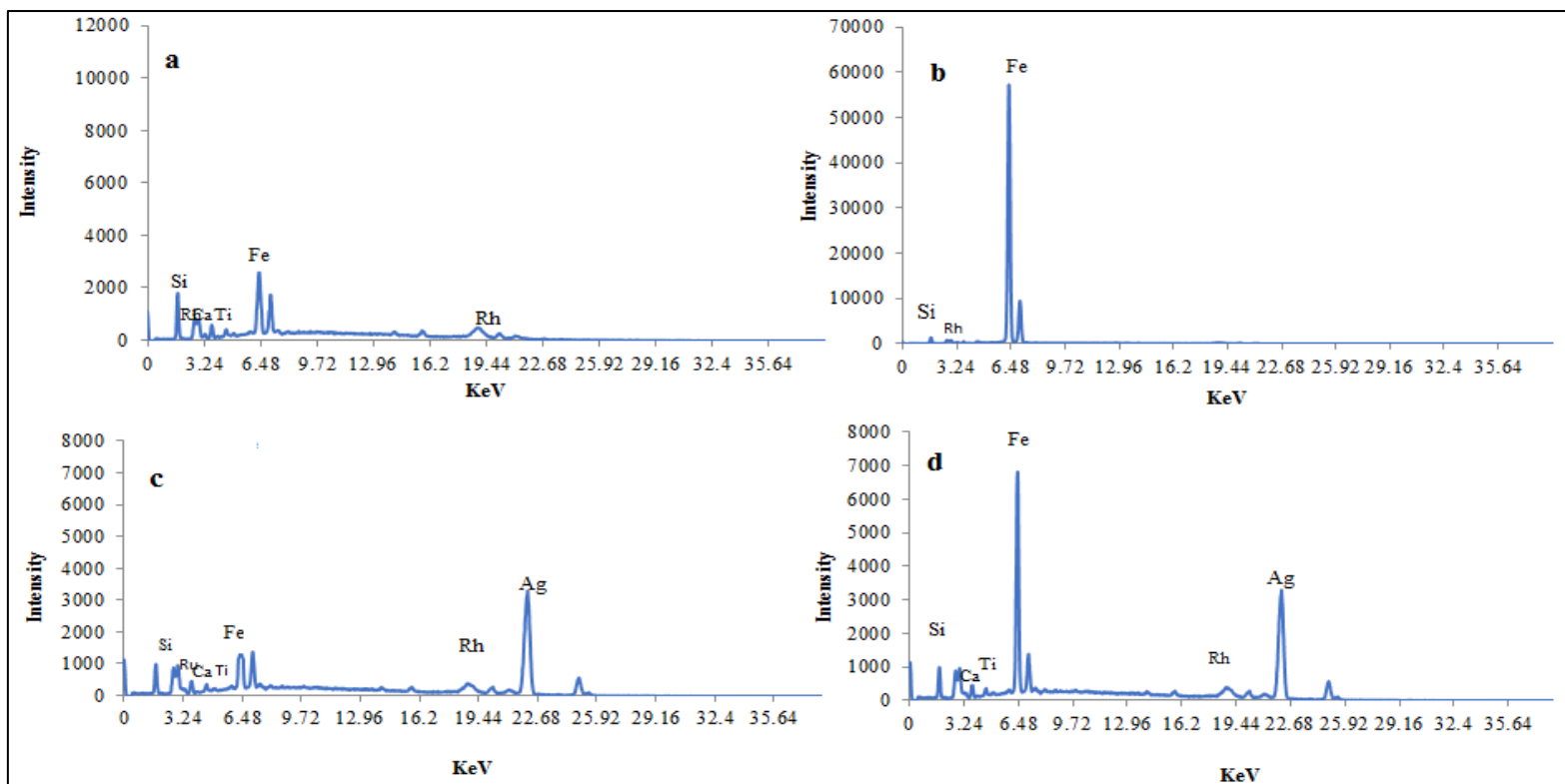


Figure 6-1 X-ray fluorescence of QM4-based composite (a) QM4 (CPW-14-unmodified) (b) QM4-1 (CPW-14- modified with only iron oxide nanoparticles) (c) QM4-2 (CPW-14- modified with only silver nanoparticles) and (d) QM4-3 (CPW-14- modified with silver coating magnetite nanoparticles)

Figure 6-1 (a, b, c, and d) show X-ray fluorescence of QM4 unmodified commercial material, modified with iron oxide, silver and silver coating iron oxide nanoparticles respectively. Figure 6-1 (a) is powder and unmodified solid material, iron and silicon are the natural components of the material, so their peaks appeared at 1.64 and 6.48 KeV respectively. Furthermore, the small peaks of Rhodium, Calcium and Titanium can be witnessed in the spectrum which is the source of the X-ray in the machine. Figure 6-1 (b) shows the X-ray fluorescence of QM4-1-based magnetite composite, by looking at the spectrum, it can be clearly seen that there is only one peak for the iron oxide, at 6.38 KeV due to (K_{α}) radiation, while other peaks are suppressed due to the strong peak of Fe. Figure 6-1 (c) shows the X-ray fluorescence of QM4-2-based silver containing composite where silver is located at 3.24 and 22.68 KeV. Figure 6-1 (d) shows the incorporated iron and silver in the spectrum at 6.48 KeV and 22.68 KeV respectively.

6.1.2 Energy dispersive X-ray analysis

EDAX was applied for the detection of the incorporated elements. It provides, comprehensive information of the developed materials such as composite mapping, detection of the elements and to confirm the presence of the incorporated elements in the composite. The measurement was conducted parallel to the SEM system. EDAX was carried out, the spectrum clearly showed the signals. It included commercial material as well as its own and modified material with magnetite and silver nanoparticles.

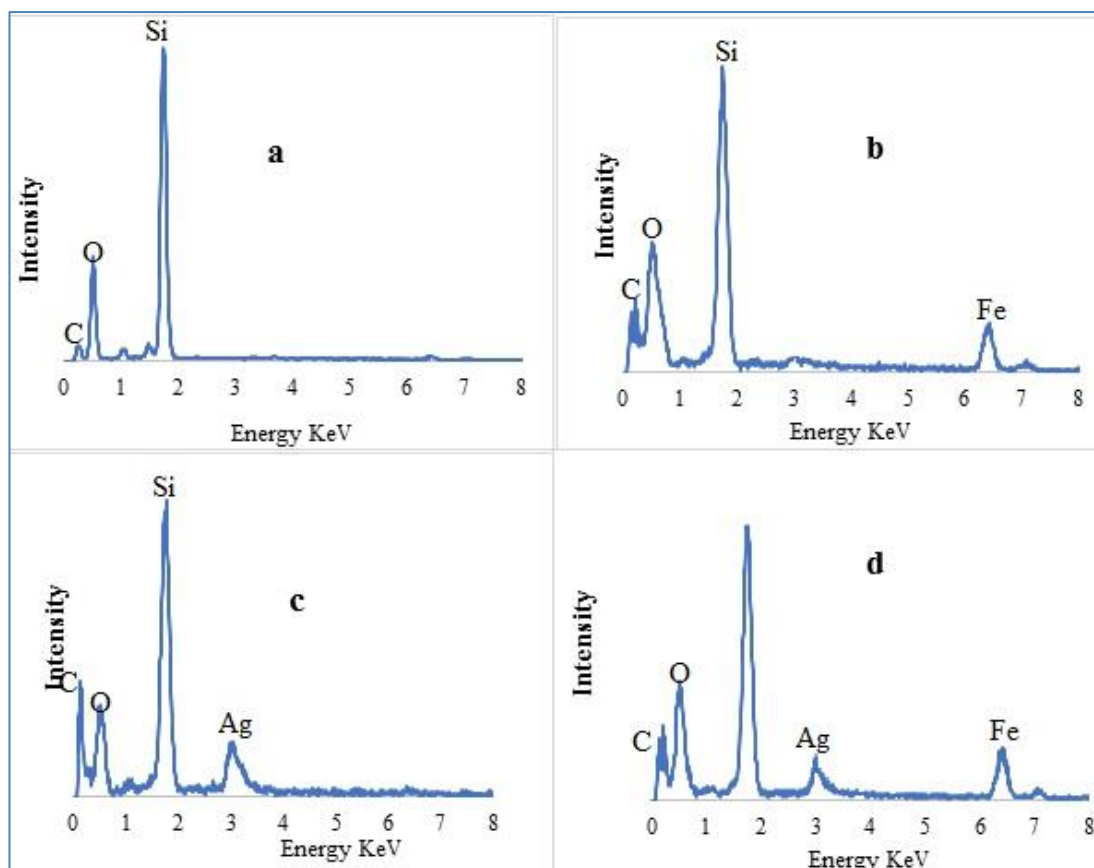


Figure 6-2 EDAX spectrum of QM4-based composite (a) QM4 (CPW-14-unmodified) (b) QM4-1 (CPW-14-modified with only iron oxide nanoparticles) (c) QM4-2 (CPW-14-modified with only silver nanoparticles) and (d) QM4-3 (CPW-14-modified with silver coating iron oxide nanoparticles)

Figure 6-2 (a) shows the EDAX analysis of the QM4 (unmodified CPW-14), silicon, oxygen and carbon are clearly seen. The EDAX spectrum shows the peaks of carbon due to the grid which was made of carbon while, oxygen and silicon were the main components of the material which can be seen in the above image. Furthermore, along with essential elements of the material some metals can be seen as well, which are the part of the material such as, magnesium, aluminium and iron oxide while sodium is present at 1.00 KeV due to the sodium borohydride, which was used as a reducing agent for the preparation of the silver nanoparticles.

Figure 6-2 (b) shows the spectrum of incorporated magnetite, though the unmodified material contains iron oxide as a natural component but by the incorporation of the

iron oxide nanoparticles has increased the intensity of the iron peaks. Figure 6-2 (c) is the spectrum of QM4-2 based composite, which shows the presence of incorporated silver nanoparticles at 3.0 KeV due to (K_{α} or K_{β}) radiation, as it was analysed before and confirmed the results of X-ray fluorescence (Ranjbar and Morsali, 2011, Luong *et al.*, 2008). Figure 6-2 (d) QM4-3 based composite shows the incorporated elements in the host matrix. Silver can be seen at 3.00 while iron is located at 6.3 KeV.

6.1.3 Scanning electron microscopy

Scanning electron microscopy was performed to determine the morphology of the synthesised nanocomposite materials and pure commercial materials. For the morphology analysis, samples were prepared, and images were taken according to the method described in section 2.3.2.

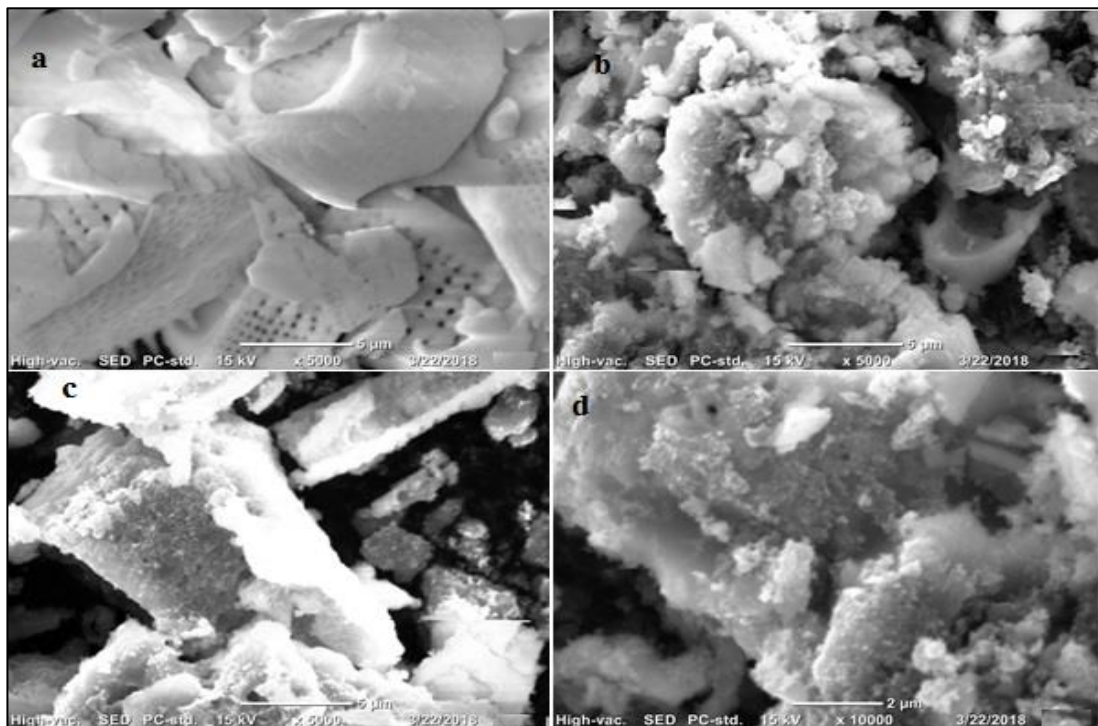


Figure 6-3 Surface morphology of QM4-based composite (a) QM4 (CPW-14-unmodified) (b) QM4-1 (CPW-14-modified with only iron oxide nanoparticles) (c) QM4-2 (CPW-14-modified with only silver nanoparticles) and (d) QM4-3 (CPW-14-modified with silver coating iron oxide nanoparticles)

Figure 6-3 (a, b, c and d) show the surface morphology of the QM4-3-based composite

containing silver and iron oxide nanoparticles. The experiment was performed at 15 KeV with 5000 to 10000 magnifications at 2.0 to 5.0 μm . The surface of the unmodified- material was unsmooth and porous which could be witnessed in Figure 6-3 (a). Figure 6-3 (b, c and d) shows the modified composites with magnetite, silver and silver coating magnetite respectively which has decreased the porosity compared to the raw materials due to the incorporation of nanoparticles in its porous but there was no remarkable change in the host matrix with the incorporation of nanoparticles.

6.1.4 Transmission electron microscopy

TEM was used to determine the internal structure, the size of the particles incorporated into the matrix and shape of the nanoparticles as reported (Sen *et al.*, 2006, Del Campo *et al.*, 2005, Yi *et al.*, 2005, Santra *et al.*, 2001). Therefore, in this project, it has been engaged to analyse the nano-sized of silver and magnetite nanoparticles incorporated into the host matrix along the shape of the incorporated nanoparticles. That has been utilised as a matrix or filler. Samples were prepared and images were taken according to the method described in section 2.3.3. TEM images at different magnifications are discussed below.

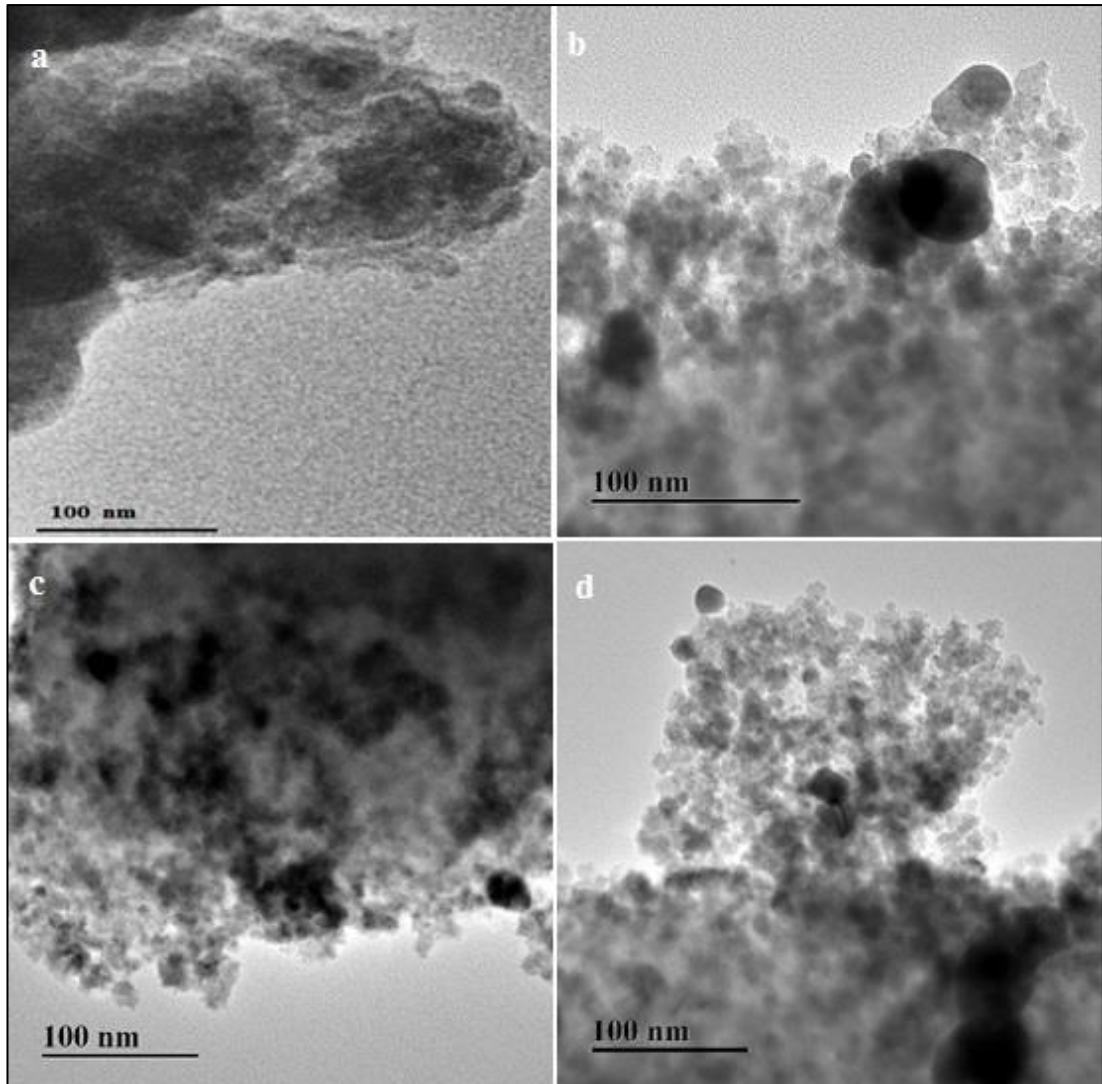


Figure 6-4 TEM images of QM4-based composite (a) QM5 (CPW-14-unmodified) (b) QM4-1 (CPW-80-modified with only iron oxide nanoparticles) (c) QM4-2 (CPW-80-modified with only silver nanoparticles) and (d) QM4-3 (CPW-14-modified with silver coating iron oxide nanoparticles only silver nanoparticles) and (d) QM5-3 (CPW-80-modified with silver coating iron oxide nanoparticles)

Figure 6-4 (a, b, c, and d) shows the internal structure of QM4 unmodified commercial material, modified with iron oxide, silver and silver coating iron oxide nanoparticles respectively. Figure 6-4 (a) shows the unmodified commercial CPW-14 (QM4) prior to the incorporation of the nanoparticles. No presence of nanoparticles was observed. Figure 6-4 (b) shows the QM4-1 embedded with iron oxide nanoparticles, iron oxide nanoparticles were confirmed in the developed composite with the size distribution of

iron oxide core nanoparticles ranging from 27, 30, and 42 nm and with an average diameter of 33 nm in diameter. Figure 6-4 (c) shows the QM4-2 nanocomposite, where the presence of silver embedded nanoparticles was found inside the modified commercial material with size distribution ranging from 10, 12, 14 and 20 nm with an average diameter of 18 nm in diameter. Figure 6-4 (d) shows the QM4-3 nanocomposite where silver coating iron oxide embedded nanoparticles can be seen clearly inside the modified material. TEM images of all modified with silver and iron oxide samples have shown the presence of silver and iron nanoparticle. The modified composite has shown the spherical shape and is in full agreement with the published data (Iglesias-Silva *et al.*, 2007, Prucek *et al.*, 2011). The main purpose of the incorporation of the silver nanoparticles was to stabilise its antimicrobial properties as reported (Mukha *et al.*, 2013) while magnetite nanoparticles have been used for the purpose of recycling (Sen *et al.*, 2010).

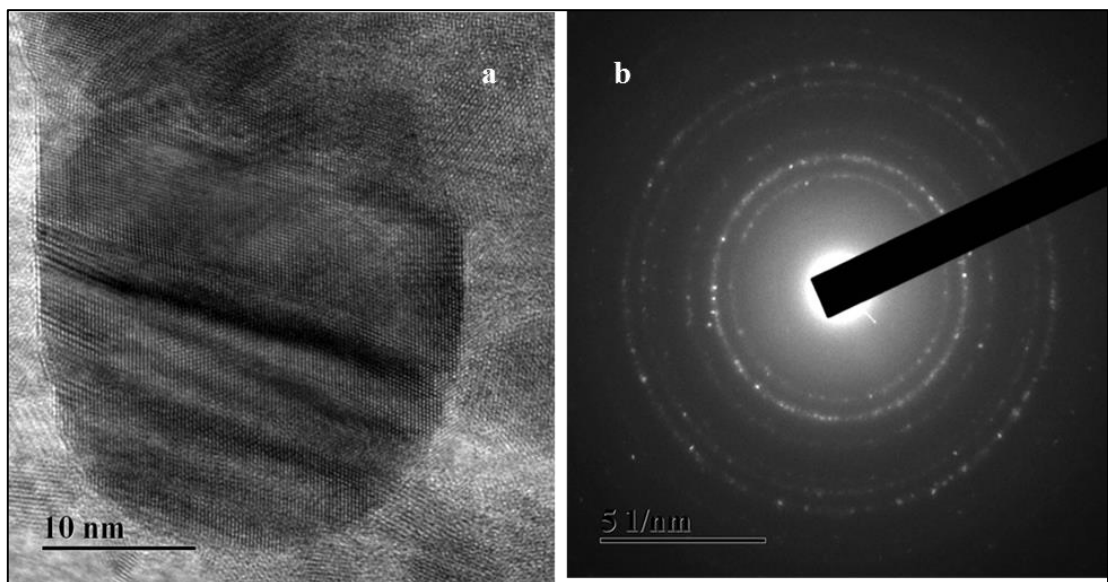


Figure 6-5 HTEM image (a), and electron diffraction pattern (b) of QM4-3 (CPW-14-modified with iron and silver nanoparticles)

6.1.5 Fourier transform infrared spectroscopy

The Fourier transform infrared (FT-IR) spectra were recorded in the range 400–2900 cm^{-1} , to confirm the presence of incorporated iron oxide bond into the host matrix or bonding between the oxygen and iron atoms.

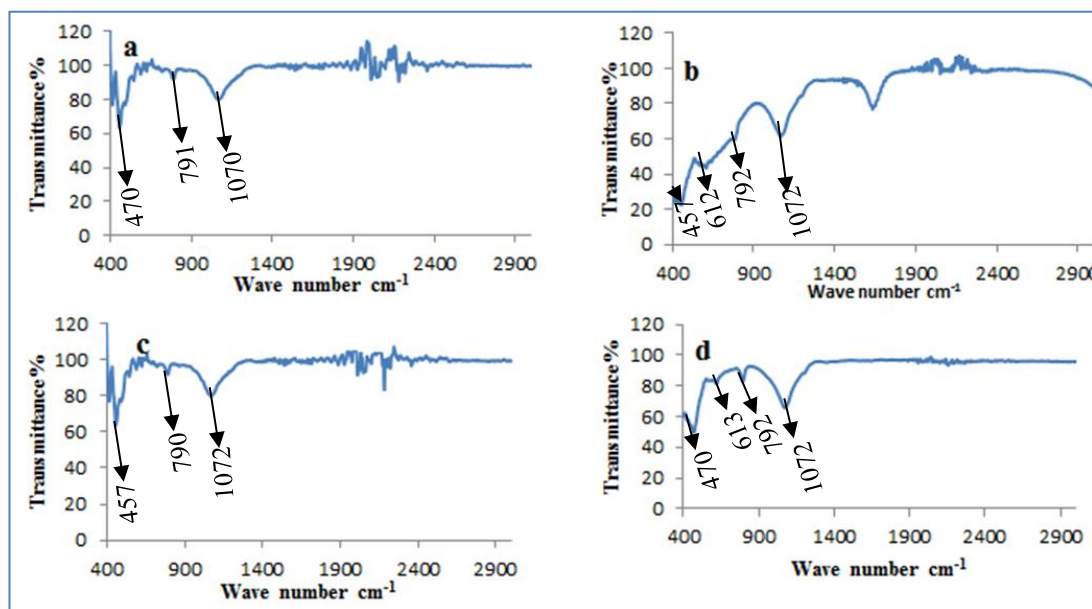


Figure 6-6 FT-IR spectrum of QM4-based composite (a) QM4 (CPW-14-unmodified) (b) QM4-1 (CPW-14-modified with only iron oxide nanoparticles) (c) QM4-2 (CPW-14-modified with only silver nanoparticles) and (d) QM4-3 (CPW-14-modified with silver coating iron oxide nanoparticles)

Figure 6-6 (a, b, c and d) shows the FT-IR analysis of all samples of QM4-based unmodified and modified material, where few peaks were observed at 792 cm^{-1} and 1072 cm^{-1} in all the samples, to which are attributed Si–O–Si bending and Si–O–Si stretching respectively (Zou *et al.*, 2014). Figure 6-6 (a) shows the QM4, commercial raw material, the peak of the iron oxide is located at 470 cm^{-1} . This material contains iron oxide naturally, while Figure 6-6 (b) QM4-1-based composite was incorporated with iron nanoparticles which is clearly shown in the spectrum at 457 and 612 cm^{-1} (see arrows in figure 6.6) In Figure 6-6 (c) QM4-2-based composite is incorporated with silver nanoparticles, which is not shown in the spectrum, as AgNPs do not show absorption in the infrared spectral region, while the peak of iron oxide is prominent in

it. Figure 6-6 (d) shows the peak of the magnetite at 470 and 613 cm^{-1} due to the vibration of the iron oxide bond as reported by Sen *et al.*, 2010. Furthermore, the peaks observed at 771 cm^{-1} and 1072 cm^{-1} were assigned to Si–O–Si bending and Si–O–Si stretching respectively (Zou *et al.*, 2014) as these elements are the constituents of the material. From all the four samples, it was concluded that sample QM4 to QM4-3-based material contained iron oxide and have confirmed the XRF and EDAX results for the elemental detections.

6.1.6 X-ray diffraction

The crystalline structure of the modified and unmodified QM4-based material (CPW-14) was observed with XRD. Diffraction peaks corresponding to QM4 (celatom CPW-14) were observed because of their crystalline nature as it contains aluminium and iron as its constituents, while incorporated magnetite and silver nanoparticles have shown the peaks and caused the material crystalline in their embedded area.

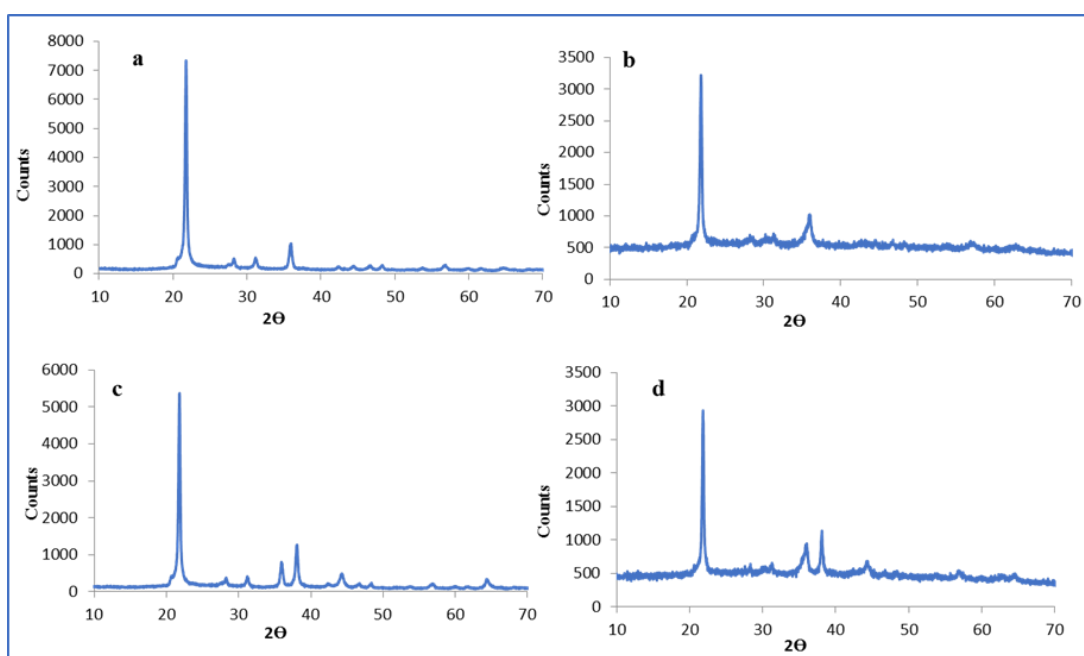


Figure 6-7 XRD pattern of of QM4-based composite (a) QM4 (CPW-14-unmodified) (b) QM4-1 (CPW-14-modified with only iron oxide nanoparticles) (c) QM4-2 (CPW-14-

modified with only silver nanoparticles) and (d) QM4-3 (CPW-14-modified with silver and iron oxide nanoparticles)

Figure 6-7 (a) shows the typical XRD pattern of the unmodified QM4 unmodified celatom-14 its intensity has been recorded at about 7500 counts. Figure 6-7 (c) and (d) are the samples containing magnetite and silver nanoparticles both have shown the characteristic XRD peak for silver and silver iron oxide. Moreover, the samples (b,c and d) have confirmed the presence of the incorporated particles in the host matrix QM4 at (1 1 1), (2 0 0), (2 2 0) and (3 1 1) in 2-theta region located at 37.5, 43.5, 63.7 and 76.7, respectively. Furthermore, Figure 6-7 (c and d) have two peaks at 40 positions, and magnetite has one, while there is no remarkable difference in the intensity and the number of peaks between the magnetite and silver-containing material are almost equal to each other. Figure 6-7 (d) XRD pattern of the QM4 with silver magnetite composite shows the characteristic peaks, due to embedded nanoparticles of magnetite silver inside the matrix, which caused the material crystalline.

6.1.7 Brunauer–Emmett–Teller surface area

BET was employed for the determination of the surface area, nature of the material like micropore volume (cm^3/g) and pore diameter (\AA) of the composite material containing silver and magnetite nanoparticles. This technique is processed with the adsorption of a known amount of Nitrogen gas at relative pressure. Samples were prepared and results were produced according to the method explained in section 2.3.6.

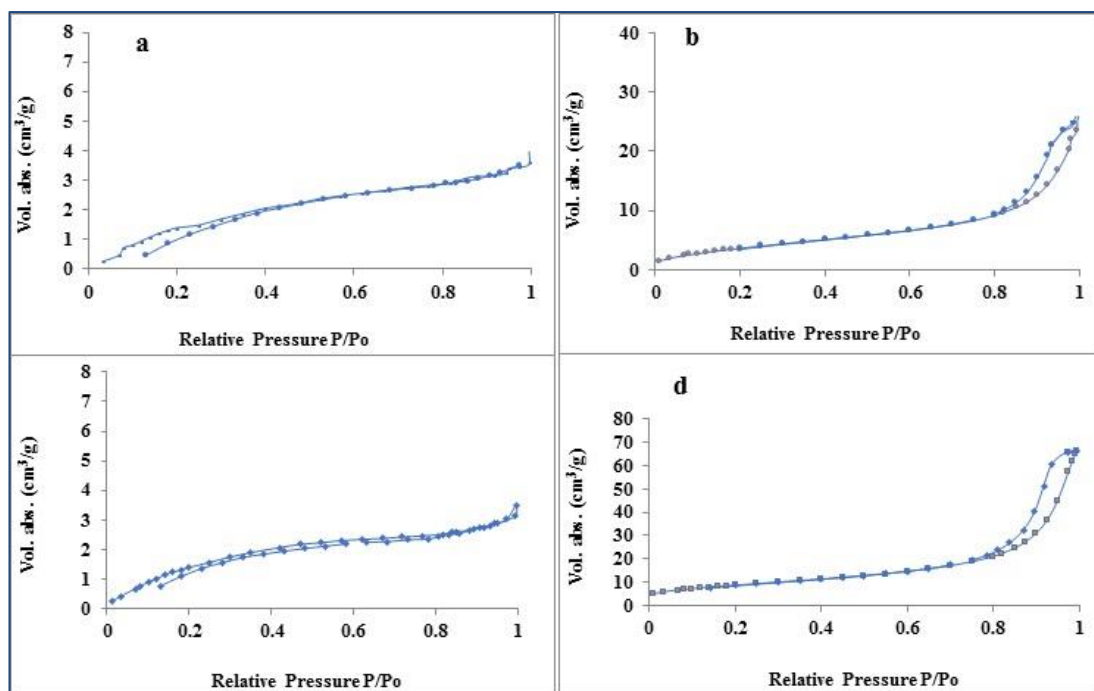


Figure 6-8 N₂ gas adsorption-desorption isotherm of QM4-based composite (a) QM4 (CPW-14-unmodified) (b) QM4-1 (CPW-14-modified with only iron oxide nanoparticles) (c) QM4-2 (CPW-14-modified with only silver nanoparticles) and (d) QM4-3 (CPW-14-modified with silver coating iron oxide nanoparticles).

Figure 6-8 (a, b, c, and d) shows the N₂ gas adsorption-desorption isotherm of QM4 unmodified commercial material, modified with iron oxide, silver and silver iron material was measured 44 m²/g by nitrogen adsorption-desorption data. The graph is also showing the hysteresis which means the material is mesoporous. The nitrogen adsorption-desorption isotherm has shown a linear increase in the volume of adsorbed gas at lower relative pressure less than (< 0.2) which is considered as mono-layer adsorption of N₂ gas on the surface of the material. This severe variation in adsorbed gas at low pressure may be due to the nitrogen capillary condensation inside the mesopores which is the indication for the narrow slit-shaped pores (Haul, 1982). Figure 6-8 (b) represents the BET surface area of the QM4-1 modified with magnetite nanoparticles. The surface area of the composite material was measured at 14 m²/g by nitrogen adsorption data. The graph shows the hysteresis which indicates that the material is mesoporous. Figure 6-8 (c) represents the BET surface area of QM4-2,

modified with silver nanoparticles, the surface area of the composite material was measured to be 8 m²/g by nitrogen adsorption data. Figure 6-8 (d) represents the BET surface area of the QM4-3-based composite material containing silver and magnetite nanoparticles, the surface area of the composite material was measured to be 5 m²/g by nitrogen adsorption-desorption data. The *negative values of the micropore volumes are artefacts, hence, materials do not have microporosity.

Table 6-1. BET analysis of unmodified QM4 and modified QM4-based magnetite silver

Sample	BET surface area (m²/g)	Micropore* volume(cm³/g)	BJH Adsorption Average Pore Diameter (Å)
QM4	44	-0.002	173
QM4-1	14	-0.003	116
QM4-2	8	-0.002	74
QM4-3	5	-0.002	30

*experimental artefact

6.2 Celatom-80-based composite (QM5 to QM5-3)

6.2.1 X-ray fluorescence

Elemental analysis for the composition of commercially purchased QM5 and its composite was performed by using an XRF machine with the model (Bruker Tracer 1V-SD). Generally, all the samples were prepared in the XRF sample cells (SC-4331-N) in 32 mm double open-ended small plastic holders. The analysis was performed to the method described in section 2.3.1, the results of materials are presented in figure 6.9.

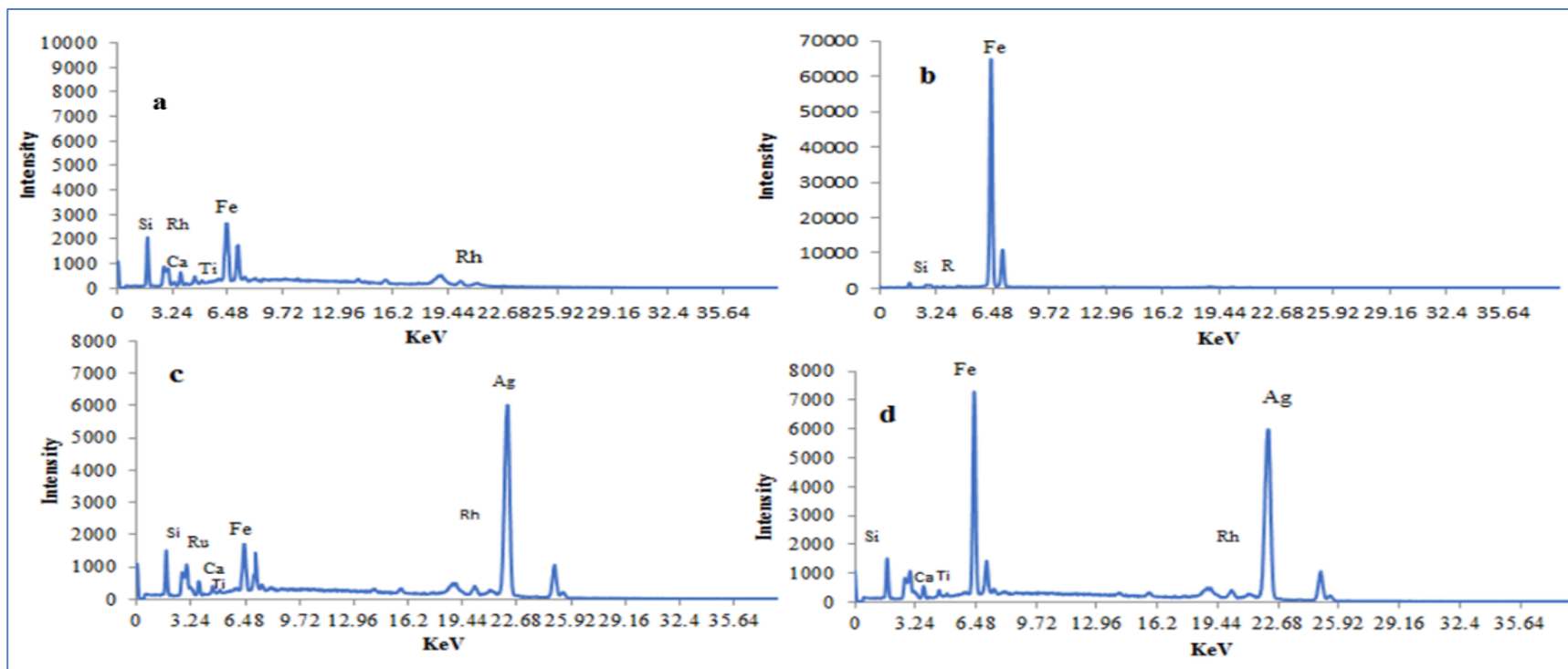


Figure 6-9 XRF of QM5-based composite (a) QM5 (CPW-80-unmodified) (b) QM5-1 (CPW-80-modified with only iron oxide nanoparticles) (c) QM5-2 (CPW-80- modified with only silver nanoparticles) and (d) QM5-3 (CPW-80-modified with silver coating iron oxide nanoparticles)

Figure 6-9 (a, b, c, and d) show X-ray fluorescence of QM5 unmodified commercial material, modified with iron oxide, silver and silver coating iron oxide, respectively. Figure 6-9 (a) shows the spectrum of unmodified QM5 (Celatom-CPW-80) as a control sample. It is unmodified solid material and contains silicon as a main component along with trace amount of iron as a natural constituent in its composition; peaks for the components appeared at 1.8 and at 6.48 KeV respectively. Figure 6-9 (b) shows the X-ray fluorescence QM5-1-based iron oxide composite, the intensity of the iron peak was increased with the incorporation of the iron oxide nanoparticles located at 6.38 KeV due to Fe (K_{α}) radiation, while other peaks are suppressed due to the stability of the iron. Figure 6-9 (c) XRF of QM5-2-based silver containing composite where silver is located at 3.24 (K_{α} or K_{β}) and 22.68 KeV (K_{α} or K_{β}) as reported (Howard, 2011). Figure 6-9 (d) confirms the incorporation of iron and silver nanoparticles in the spectrum at 6.48 KeV and 22.68 KeV respectively.

6.2.2 Energy dispersive X-ray analysis

EDAX is considered as one of the analytical techniques; comprehensively provide information of the developed material such as composite mapping, detection of the elements, to confirm the presence of the incorporated elements in the composite. The EDAX spectrum clearly showed the signals characteristic for elements. The EDAX analyses of all batches were performed parallel to the SEM to achieve EDAX graphs. EDAX spectrum of QM5 based composite is given below.

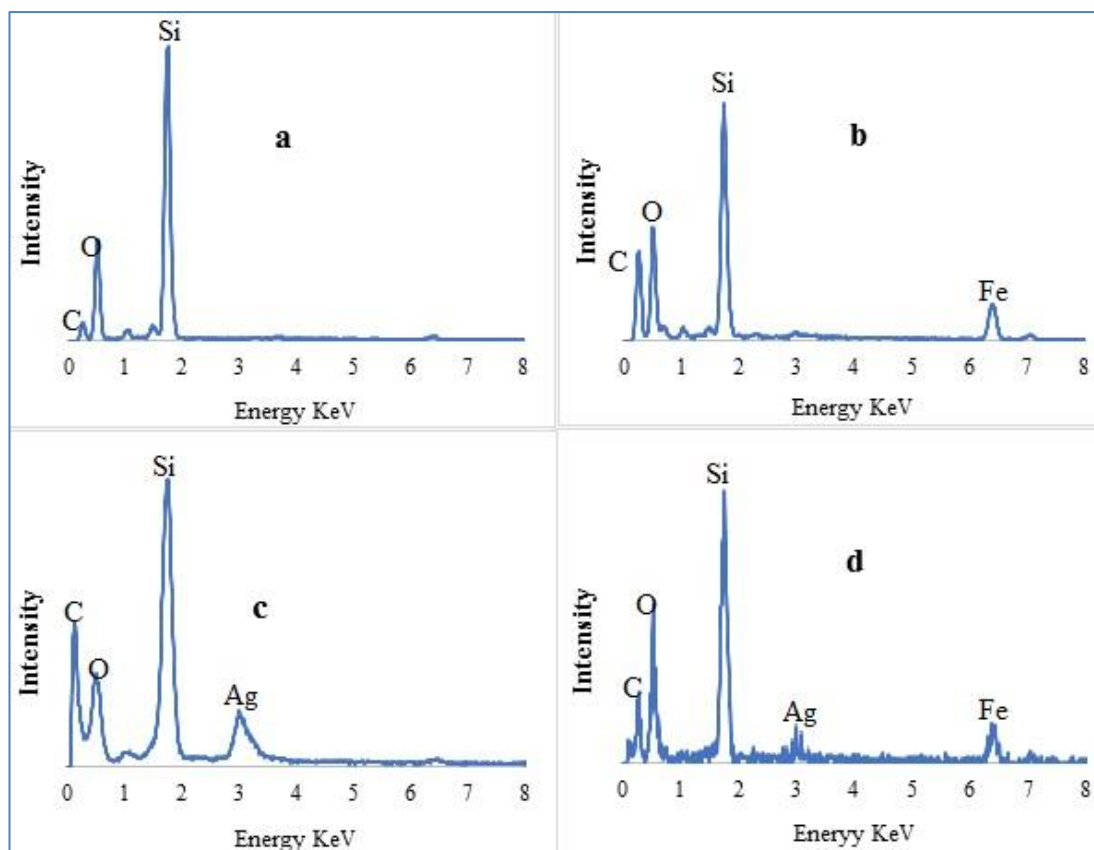


Figure 6-10 EDAX spectrum of QM5-based composite (a) QM5 (CPW-80-unmodified) (b) QM5-1 (CPW-80-modified with only iron oxide nanoparticles) (c) QM5-2 (CPW-80-modified with only silver nanoparticles) and (d) QM5-3 (CPW-80-modified with silver coating iron oxide)

Figure 6-10 (a, b, c, and d) shows the EDAX spectrum of QM5 unmodified commercial material, modified with iron oxide, silver and silver coating iron oxide, respectively. Figure 6-10 (a) shows the EDAX analysis of the QM5 (unmodified CPW-80), silicon, oxygen are shown along with carbon in the spectrum. The EDAX spectrum shows the peaks of carbon due to the grid which was made of carbon, oxygen and silicon as the main components of the material which could be seen at 0.00, 0.5 and 1.90 KeV respectively, in the spectrum. Furthermore, along with essential elements of the material some metals could be seen, which were part of the material including; magnesium aluminum and iron oxide. Figure 6-10 (b) shows the spectrum of incorporated magnetite, though this unmodified material contains the iron peaks is

increased, located at 6.3 KeV. Figure 6-10 (c) is the spectrum of QM5-2 based composite, which shows the presence of incorporated silver nanoparticles at 3.0 KeV as it was analysed before and confirmed the results of X-ray fluorescence (Ranjbar and Morsali, 2011, Luong *et al.*, 2008). Figure 6-10 (d) QM5-3 based composite shows the incorporated elements in the host matrix. Silver can be seen at 3.00 KeV while the iron is located at 6.3 KeV. The EDAX of unmodified and modified with core-shell nanoparticles were determined, showing no impurities in the developed composite.

6.2.3 Scanning electron microscopy

The surface morphology of the QM5-based unmodified material and that of modified composites were determined by employing scanning electron microscopy. For the surface morphology analysis, samples were prepared and images were taken by using the method described in section 2.3.2.

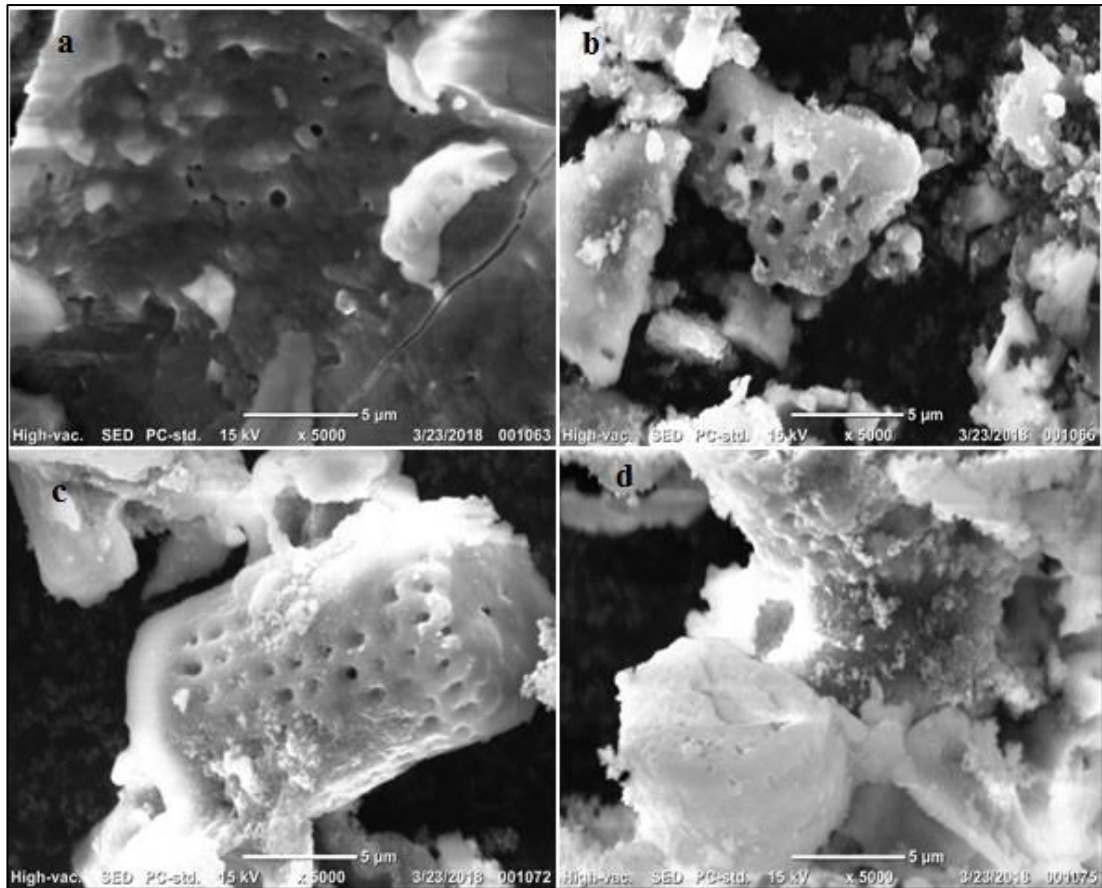


Figure 6-11 Surface morphology of QM5-based composite (a) QM5 (CPW-80-unmodified) (b) QM5-1 (CPW-80-modified with only iron oxide nanoparticles) (c) QM5-2 (CPW-80-modified with only silver nanoparticles) and (d) QM5-3 (CPW-80-modified with silver coating iron oxide nanoparticles)

Figure 6-11 (a, b, c and d) shows the surface morphology of the QM5-3-based unmodified and modified composite with silver and iron oxide nanoparticles. The experiment was performed at 5000 magnifications with (5 μ m scale). Figure 6-11 (a) shows the unmodified raw CPW 14 material, the surface of the material was found to be porous and unsmooth. Figure 6-11 (b, c and d) shows the modified composites with magnetite, silver and with both silver coating magnetite respectively. The modified with the nanoparticles have reduced the porosity of the materials due to incorporation of nanoparticles but there was no remarkable change in the host matrix with the incorporation of nanoparticles and it might be due to smaller size of the nanoparticles.

6.2.4 Transmission electron microscopy

TEM was engaged to analyse the internal structure and size of the incorporated particles, and the shape of the incorporated particles into the QM5 matrix. Samples were prepared, and images were taken by using the method described in detail in section 2.3.3.

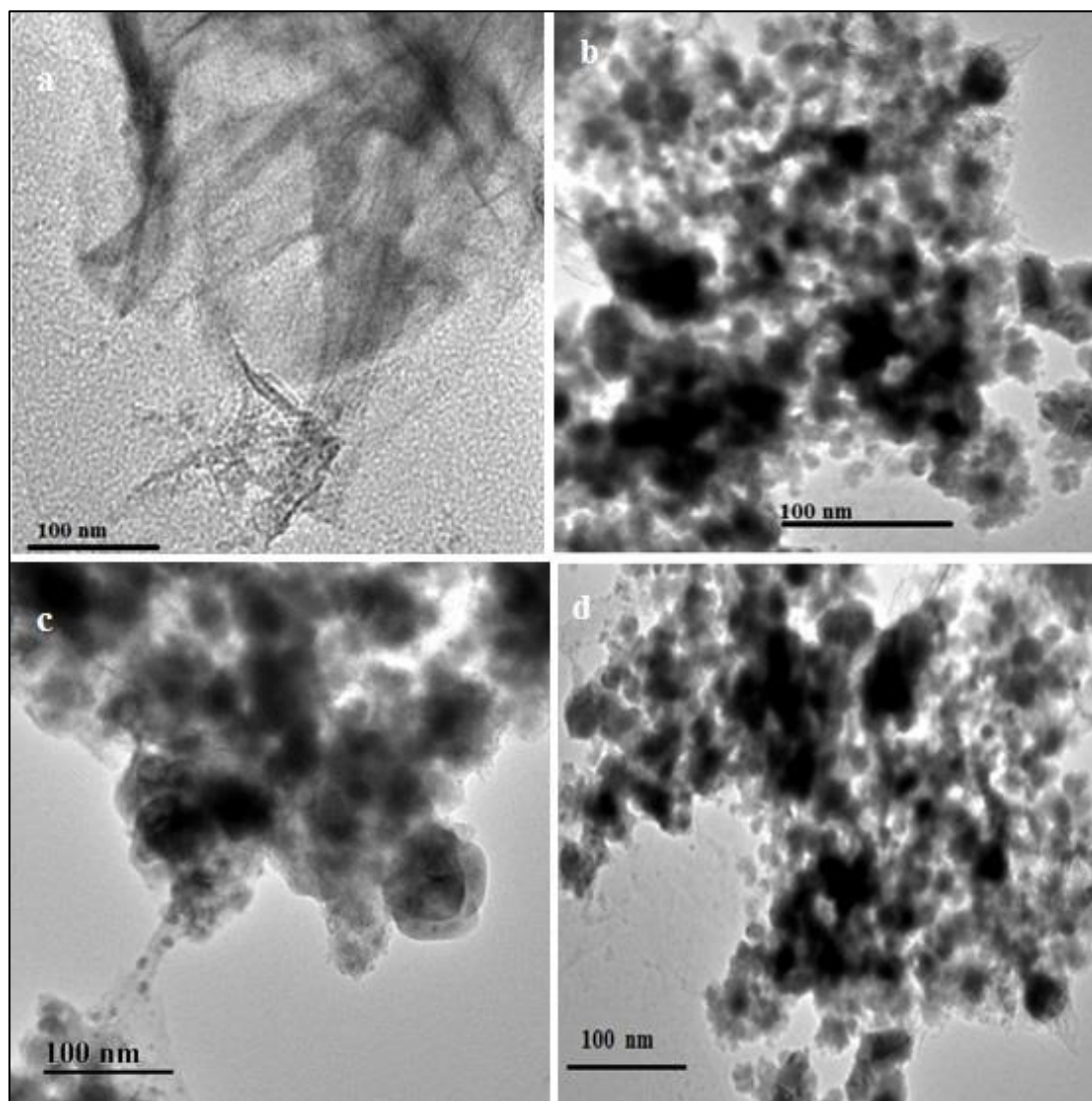


Figure 6-12 TEM images of QM5-based composite (a) QM5 (CPW-80-unmodified) (b) QM5-1 (CPW-80-modified with only iron oxide nanoparticles) (c) QM5-2 (CPW-80-modified with only silver nanoparticles) and (d) QM5-3 (CPW-80-modified with silver coating iron oxide nanoparticles)

Figure 6-12 (a, b, c, and d) shows the internal structure of QM5 unmodified

commercial material, modified with iron oxide, silver and silver coating iron oxide nanoparticles respectively. Figure 6-12 (a) shows the unmodified commercial CPW-80 (QM5) prior to the incorporation of the nanoparticles. The presence of nanoparticles was absent. Figure 6-12 (b) shows the QM5-1 embedded with iron oxide nanoparticles, iron oxide nanoparticles were confirmed in the developed composite with the size distribution of iron oxide core nanoparticles ranging from 25, 30, and 40 nm and with an average diameter of 31 nm in diameter. Figure 6-12 (c) shows the QM5-2 nanocomposite, where the presence of silver embedded nanoparticles was found inside the modified commercial material with size distribution ranging from 7, 10, 12 and 26 nm with an average diameter of 13 nm in diameter. Figure 6-12 (d) shows the QM5-3 nanocomposite where silver coating iron oxide embedded nanoparticles can be seen clearly inside the modified material.

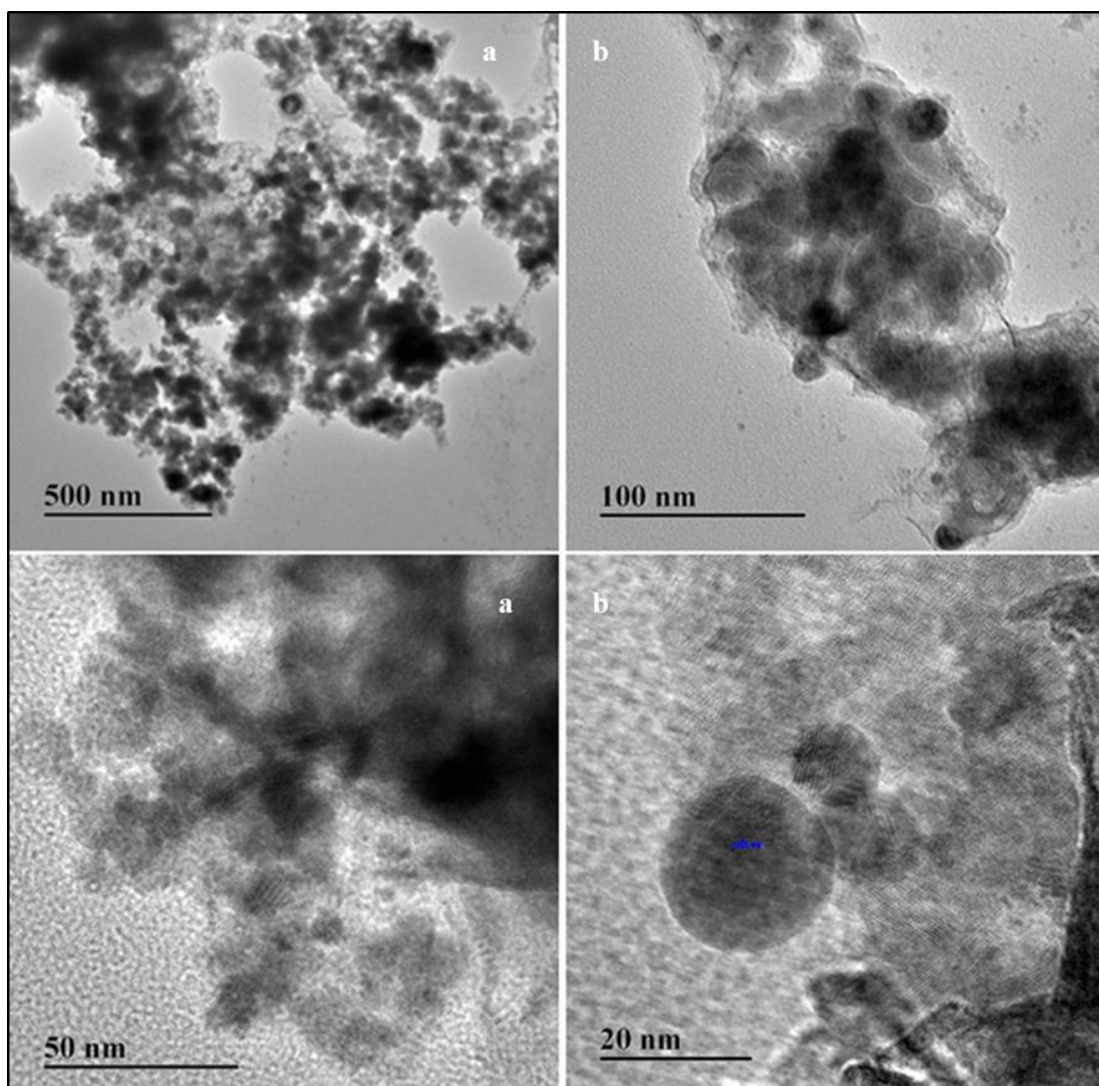


Figure 6-13 High resolution HTEM images of (a, b, c and d) QM5-3-based composite (CPW-80-modified with iron oxide and silver nanoparticles)

Figure 6-13 (a, b, c and d) shows the TEM images of the QM5-3-based composite containing iron oxide and silver nanoparticles. TEM images were taken with different magnifications that show the internal structure of the modified material, the size of the particles and shape of the particles into the host matrix, as well as the presence of silver nanoparticles and iron oxide. TEM images of the developed composites have clearly shown the core-shell structure of nanoparticles with the mesoporous shell of celatom-80. Synthesised composites have shown the spherical shape of incorporated silver and iron oxide in the size ranging from 7, 10, 12 and 26 nm and with an average diameter

of 13 nm, which is highly effective for the antimicrobial applications and are in agreement with the published data (Iglesias-Silva *et al.*, 2007, Pucek *et al.*, 2011). To view the shape and size of the particles, images were taken at different magnifications. The main purpose of the incorporation of the silver nanoparticles was to stabilise its antimicrobial properties as reported (Mukha *et al.*, 2013), while magnetite nanoparticles have been used for the purposes of recycling (Sen *et al.*, 2010). Due to the uniform and spherical shape of added nanoparticles, the composite was characterised with BET, XRD and FT-IR to explore their other properties.

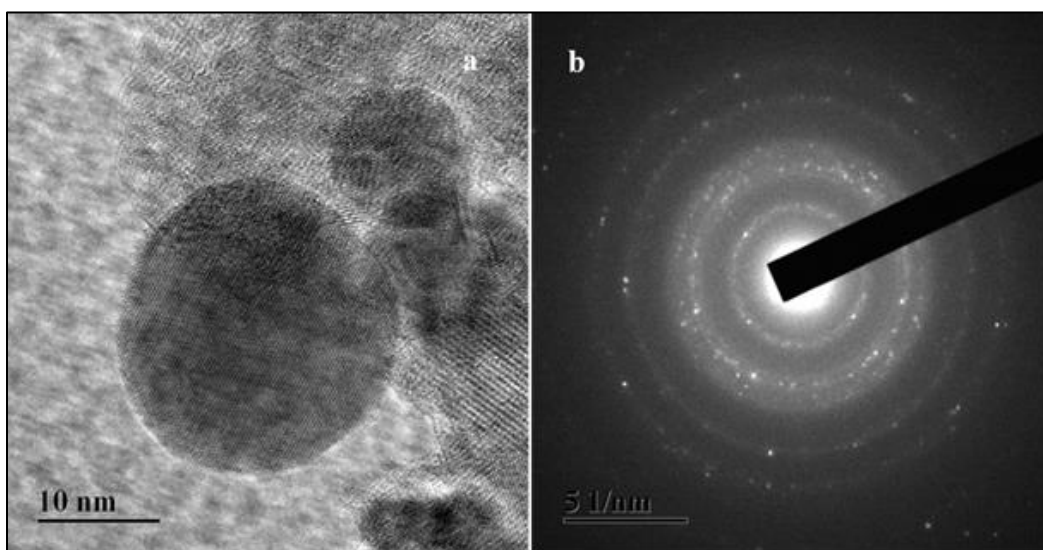


Figure 6-14 HTEM image (a), QM5-3(CPW-80-modified with iron and silver nanoparticles) and electron diffraction pattern (b) of QM5-3 nanocomposite

Figure 6-14 (a and b) shows the size, shape of the incorporated silver nanoparticles and diffraction pattern of the developed material, respectively.

6.2.5 Fourier transform infrared spectroscopy

The Fourier transform infrared (FT-IR) spectra were recorded in the range 400–2900 cm^{-1} , to confirm the presence of iron oxide or bonding between iron and oxygen atoms in the modified material.

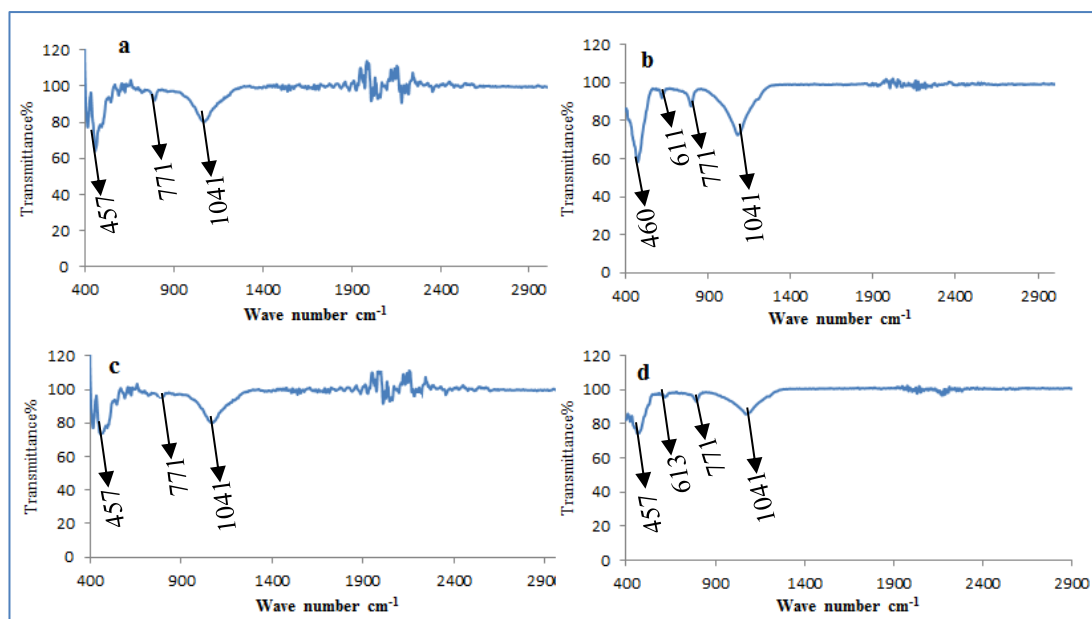


Figure 6-15 FT-IR spectrum of QM5-based composite (a) QM5 (CPW-80-unmodified) (b) QM5-1 (CPW-80-modified with only iron oxide nanoparticles) (c) QM5-2 (CPW-80-modified with only silver nanoparticles) and (d) QM5-3 (CPW-80-modified with silver coating iron oxide nanoparticles)

Figure 6-15 (a, b, c and d) show the FT-IR analysis of all samples of QM5 based unmodified and modified material. Figure 6-15 (a) shows the QM5 unmodified material, it contains iron oxide naturally, which is located at 457 and is assigned to vibration of Fe-O bond (Zou *et al.*, 2014). The peaks observed at 771 cm^{-1} , 1041 cm^{-1} were assigned to Si-O-Si bending and Si-O-Si stretching, respectively (Zou *et al.*, 2014). Figure 6-15 (b) QM5-1 composite was incorporated with iron nanoparticles which are clearly shown in the spectrum at 460 cm^{-1} and 611 cm^{-1} due to stretching vibration of the Fe-O bond of core particles (Zou *et al.*, 2014). Figure 6-15 (c) QM5-2 composite is incorporated with silver nanoparticles, which are not shown in the spectrum as AgNPs do not show absorption in the infrared spectral region, while the peak of iron oxide is prominent in it. Figure 6-15 (d) QM5-3 composite containing silver and iron oxide, the peak of the iron oxide in the spectrum is shown at 457 cm^{-1} and 613 cm^{-1} due to the stretching vibration of the iron oxide bond as reported (Sen *et*

al., 2010, Zou *et al.*, 2014). Silver nanoparticles do not show absorption in the infrared spectral region hence the peak for the silver cannot be seen in the spectrum. From all the four samples, it was concluded that iron oxide was detected in sample QM5-1 and QM5-3.

6.2.6 X-ray diffraction

The crystalline phase of the composite and pure commercial material was performed with the XRD, the method is described in detail in section 2.3.5. Results have shown that the incorporation of the silver and magnetite particles into the QM5-matrix caused the material to crystalline. Diffraction peaks corresponding to QM5 were observed because of their crystalline nature as it contains the aluminium and iron naturally, while incorporated magnetite and silver nanoparticles have shown the peaks and caused the material crystalline. Results are shown below.

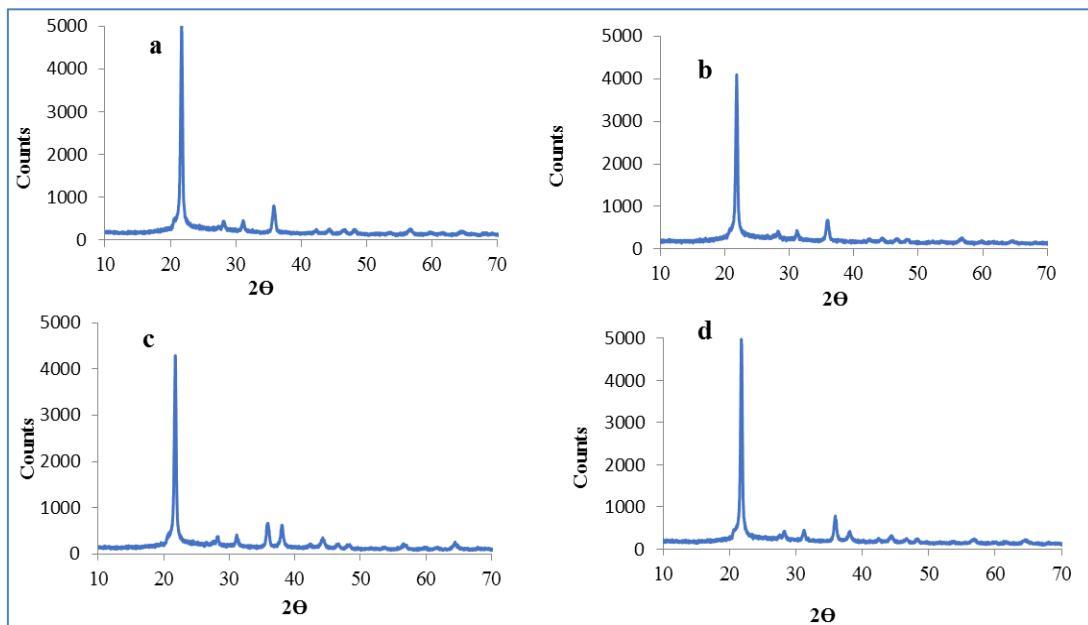


Figure 6-16 XRD pattern of QM5-based composite (a) QM5 (CPW-80-unmodified) (b) QM5-1 (CPW-80-modified with only iron oxide nanoparticles) (c) QM5-2 (CPW-80-modified with only silver nanoparticles) and (d) QM5-3 (CPW-80-modified with silver and iron oxide nanoparticles).

Figure 6-16 (a, b, c, and d) show the XRD pattern of QM5 unmodified commercial

material, modified with iron oxide, silver and silver iron oxide, respectively. All the samples showed multiple peaks Figure 6-16 (a) QM5-1 shows the typical XRD pattern of the unmodified QM5 commercial celatom-80, its intensity being recorded at about 5000 counts; the material shows the peaks due to the crystalline nature of the unmodified material. Figure 6-16 (b) and (c) QM5-1 and QM5-2 are the samples containing magnetite and silver nanoparticles, respectively, both are different on peak produced at 4300 and 4100 counts, respectively. Furthermore, Figure 6-16 (c and d) have two peaks at 40, 2-theta positions, and magnetite has one, while there is no remarkable difference in the intensity and the number of peaks between the magnetite and silver-containing material, which are similar to each other. Figure 6-16 (d) XRD QM5-3 composite containing silver magnetite, the intensity of composite is recorded at 5000 counts due to embedded nanoparticles of magnetite and silver inside the matrix, which caused the material crystalline. Furthermore, the XRD pattern of the material has shown the existence of incorporated particles at (1 1 1), (2 0 0), (2 2 0) and (3 1 1) in the 2-theta region, located at 37.5, 43.5, 63.7 and 76.7, respectively (Wang *et al.*, 2013, Iglesias-Silva *et al.*, 2007).

6.2.7 Brunauer–Emmett–Teller surface area

Samples were prepared, and results were produced according to the method explained in the characterisation section 2.3.6.

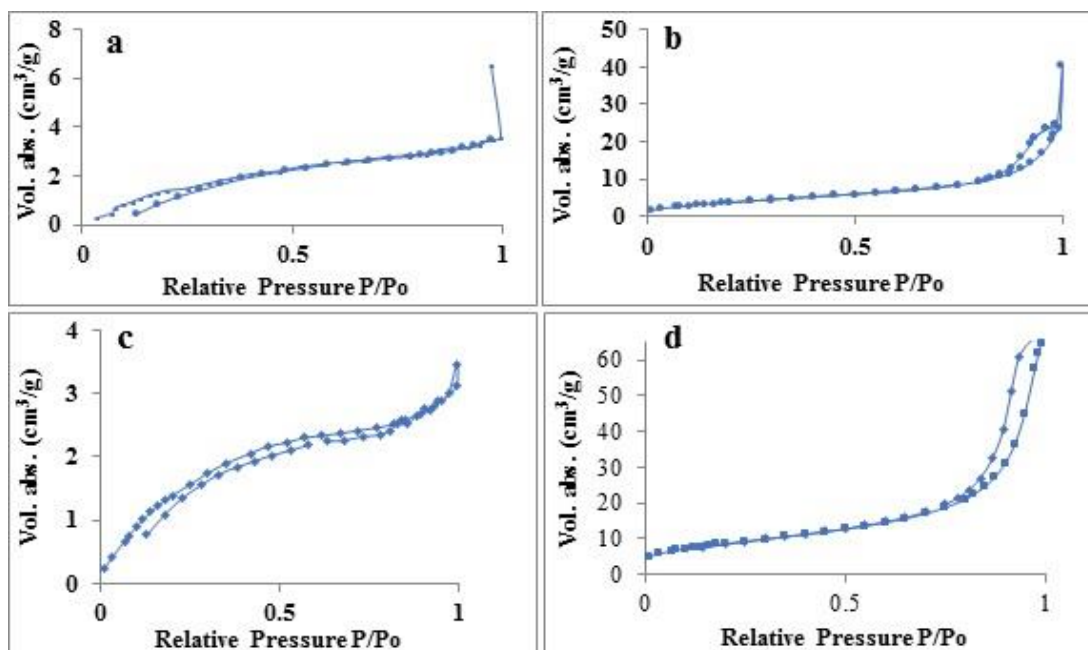


Figure 6-17 N₂ gas adsorption -desorption isotherm of QM5-based composite (a) QM5 (CPW-80-unmodified) (b) QM5-1 (CPW-80-modified with only iron oxide nanoparticles) (c) QM5-2 (CPW-80- modified with only silver nanoparticles) and (d) QM5-3 (CPW-80-modified with silver coating iron oxide nanoparticles)

Figure 6-17 (a, b, c, and d) showed the N₂ gas adsorption-desorption isotherm of QM5 unmodified commercial material, modified with iron oxide, silver and silver-iron oxide, respectively. Figure 6-17 (a) QM5 represents the BET surface area of the unmodified material; the surface area of the material was measured at 31 m²/g by nitrogen adsorption data. The graph is showing the hysteresis which means the material is mesoporous. Figure 6-17 (b) QM5-1 represents the BET surface area of the modified with magnetite nanoparticles, the surface area of the composite material was measured at 15 m²/g by nitrogen adsorption data. Figure 6-17 (c) QM5-2 represents the BET surface area of the modified celatom CPW-80 with silver nanoparticles, the surface area of the composite material was measured 8 m²/g by nitrogen adsorption data. Graph is showing the hysteresis, which means the material is mesoporous. Figure 6.17 (d) QM5-3 shows the surface area of the composite material, was measured at 7 m²/g by nitrogen adsorption data. The surface area has reduced from 36 m²/g to 10 m²/g due to the modification with nanoparticles, this has also been reflected in the BJH pore size reduction, no microporosity

Table 6-2. BET analysis of unmodified QM5 series nanocomposites

Sample	BET surface area (m ² /g)	Micropore volume(cm ³ /g)	BJH Adsorption Average Pore Diameter (Å)
QM5	31	-0.001	124
QM5-1	15	-0.002	88
QM5-2	8	-0.002	32
QM5-3	7	-0.002	28

* Negative values are experimental artefact, hence, materials do not have microporosity

6.3 Comparison of different nanocomposites with respects to their physicochemical properties

The elemental determination, structure, size and properties of the synthesised QM1-3, QM2-3, QM3-3, QM4-3 and QM5-3 nanocomposites were determined. X-ray fluorescence (XRF) showed the strong bands of iron and silver particles at 6.48 and 22.68 KeV respectively in all the nanocomposites, (EDAX), measurements confirmed the incorporation of the iron oxide and silver nanoparticles in the series of modified composites at 3.0 KeV, and 6.3 KeV respectively. FT-IR spectroscopy has confirmed the iron oxide bond vibrations in the series of developed nanocomposites at 460 to 570 cm⁻¹ of all the developed materials.

TEM images showed the internal structure, nano-size of the incorporated silver nanoparticles with average diameter ranges from 10 - 13 nm in all modified with silver composite while iron oxide nanoparticles embedded into the matrix with an average diameter of 50 nm were determined. SEM determined the surface morphology of the modified and unmodified material. XRD spectrum of the synthesised nanocomposites have revealed the confirmation of the incorporated particles at 38.9, 44.4, 64.6, and 78.3 in the 2 θ region, corresponding to (1 1 1), (2 0 0), (2 2 0), and (3 1 1) planes of silver and iron nanoparticles. The embedded nanoparticles have shown the sharp peaks at embedded part of the material for the five developed nanocomposites. BET data

depicted the surface area ranges from 5 to 560 m²/g. It was observed that the lowest BET surface area 5 m²/g was found in QM4-3 and highest 560 m²/g was seen in QM2-3 after modification. The comparison of the surface area of the developed materials after incorporation of silver coating iron oxide nanoparticles is shown in Figure 6-18.

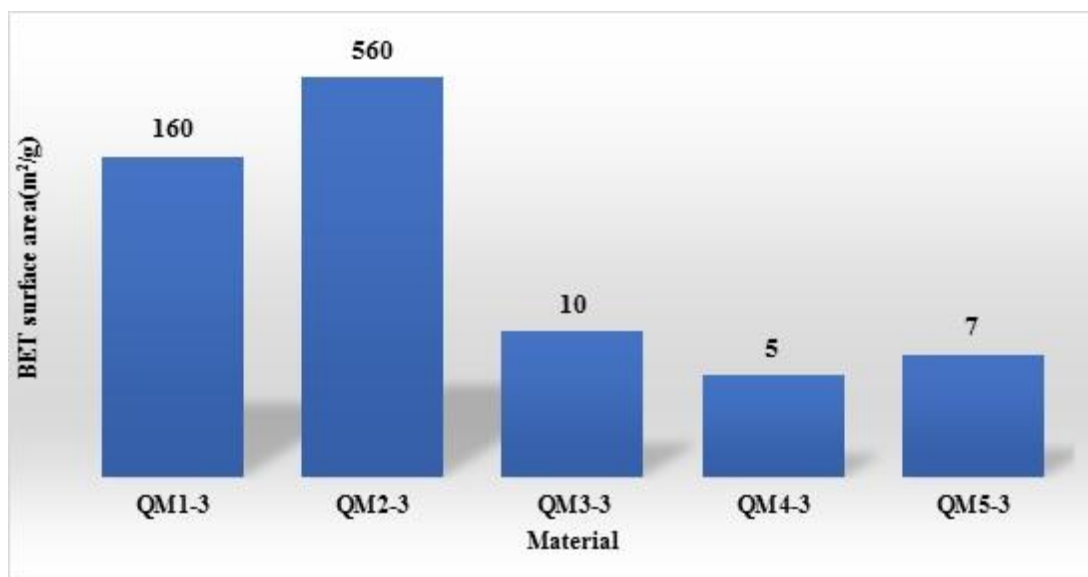


Figure 6-18 A comparison of BET surface area of all developed materials.

6.4 Conclusions

Chemical and physical properties of synthesised nanocomposites were analysed by several techniques. The composition, structure, size and properties of the nanoparticles were determined prior to their applications. X-ray fluorescence (XRF) showed the strong bands of iron and silver at 6.48 and 22.68 KeV respectively, EDAX, measurements confirmed the incorporation of the iron and silver particles in the series of modified composites at 3.0 KeV and 6.3 KeV respectively.

FT-IR spectroscopy has confirmed the of iron oxide bond vibrations in the series of developed nanocomposites at 460 to 570cm⁻¹, SEM revealed the QM1-3 and QM2-3 as unsmooth materials with tubes and cubic structure respectively, while QM3-3, QM4-3 and QM5-3 were found as porous surface materials. Furthermore, TEM

analysis has determined the size of the incorporated particles in the series of host matrix ranging from 16- 30 nm and core shell structure of the added nanoparticles in series of the developed composites. Moreover, porosity internal structure and morphology of the materials were also determined. The XRD spectrum of the composite has revealed the confirmation of the incorporated particles at 38.9, 44.4, 64.6, and 78.3 in the 2Θ region, corresponding to (1 1 1), (2 0 0), (2 2 0), and (3 1 1) planes of silver and iron nanoparticles. Nitrogen gas adsorption-desorption experiments suggest the presence of average pore diameter 28 to 79 Å.

CHAPTER SEVEN

7 Antimicrobial applications

Part A: Antimicrobial efficiency of developed nanocomposites

7.1 Introduction

In this part, antimicrobial application of synthesised novel multifunctional nanocomposites has been discussed on both Gram-positive and Gram-negative bacteria, which are frequently found in water. Silver nanoparticles were incorporated into the matrix for antimicrobial properties and iron oxide nanoparticles were incorporated for the magnetically recycling applications.

To maintain the antimicrobial properties of the AgNPs, these were incorporated into the magnetite nanocomposite with various cheap commercial host matrices, which stabilised the silver nanoparticles and changed the host matrices into strong magnetic materials. The antimicrobial efficient developed materials (part A) are presented in two sections: in section-1 antimicrobial applications of all developed materials are discussed on two bacterial strains, they are being Gram-negative *E. coli* (W3110) and Gram-positive *S. aureus* (NCIMB 1671).

Section-2 is based on the antimicrobial applications of all Gram-negative bacteria listed in Table 7-1, commonly found in water. Biocidal properties were examined on the basis of the colony forming units per millilitre (CFU/mL) by counting the number of colonies grown by the media on the Petri dishes. Several concentrations of the nanocomposite materials were prepared from 2 µg/mL to 300 µg/mL.

7.2 Antibacterial activity of the nanocomposite materials

The antimicrobial effects of developed nanomaterials were tested against Gram-negative *E. coli* and Gram-positive *S. aureus*. Developed nanocomposite contains the host matrix, which retains the properties of the incorporated nanoparticles. In this project, five different host commercial materials have been used, which are shown in section 2.1. The schematic illustration of the nanocomposites is given in Figure 7-1.

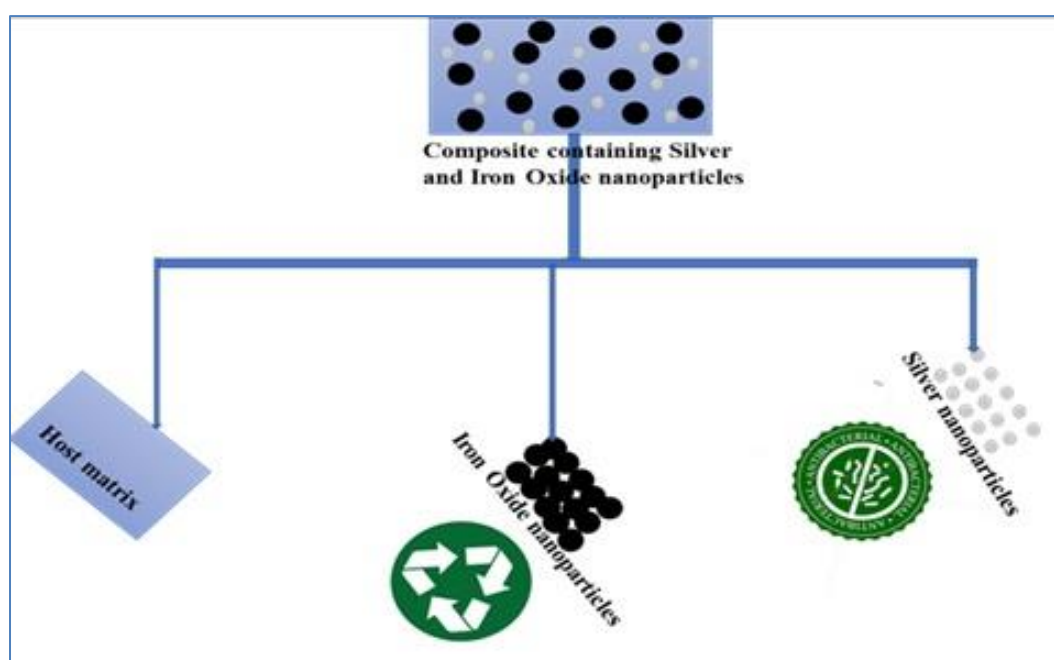


Figure 7-1 schematic illustration for the composition of the composite and their functions

Schematic diagram 7-1 shows that the commercial materials described in section 2.1, have been used as a host matrix for the incorporation of guest iron oxide and silver nanoparticles. Iron oxide nanoparticles were incorporated for the re-use of developed nanocomposites for magnetic separation, while silver nanoparticles were introduced for the antimicrobial applications. The sample name for the antimicrobial application of all developed nanocomposites and the names of bacterial strains are given in the Table 7-1.

Table 7-1. Applied nanocomposites (QM1-3, QM2-3, QM3-3, QM4-3 and QM5-3 (MWCNTs, AC, DAE, CPW-14 and CPW-80-based nanocomposites respectively, modified with iron and silver nanoparticles) and bacterial strains

Sample ID	Bacterial strains
QM1-3	<i>E. coli</i> (DH5- α , and K12), <i>S. aureus</i> , <i>L. pneumophila</i> , <i>K. pneumoniae</i>
QM2-3	<i>E. coli</i> (DH5- α , and K12), <i>S. aureus</i> , <i>L. pneumophila</i> , <i>P. aeruginosa</i>
QM3-3	<i>E. coli</i> (DH5- α , and K12), <i>S. aureus</i> , <i>L. pneumophila</i>
QM4-3	<i>E. coli</i> (DH5- α , and K12), <i>S. aureus</i> ,
QM5-3	<i>E. coli</i> (DH5- α , and K12), <i>S. aureus</i>

Section-1

7.3 Antimicrobial applications of synthesised nanocomposites containing silver and iron oxide nanoparticles on Gram-positive and Gram-negative bacteria

The antimicrobial efficiencies of all modified materials were tested on the Gram-negative *E. coli* and Gram-positive *S. aureus* strains of bacteria, which are listed in Table 7-1, by employing the method described in section 2.2.5. In this section, the antimicrobial applications of five different nanocomposites (QM1-3, QM2-3, QM3-3, QM4-3 and QM5-3) were tested against Gram-negative strain *E. coli* (W3110) and Gram-positive Strain *S. aureus* (NCIMB 1671). The sample name, the bacteria and methods used for testing antimicrobial efficiency are given in the Table 7-2.

Table 7-2. Tested bacterial strains

Specific strains used	Methods used for Antimicrobial efficiency
<i>Staphylococcus aureus</i> (<i>S. aureus</i>) NCIMB 1671	Drop-plate (DP) method was used and colonies (CFU/mL) were counted by using colony counter
<i>Escherichia coli</i> (W3110)	

7.3.1 Control plates of *E. coli*

Prior to the antimicrobial applications of all developed nanocomposites, control plates of both Gram-negative and Gram-positive strains (*E. coli* and *S. aureus*) were prepared for the comparison with the plates of employed nanocomposites against above strains. Same method was followed, which is described in section 2.2.5.

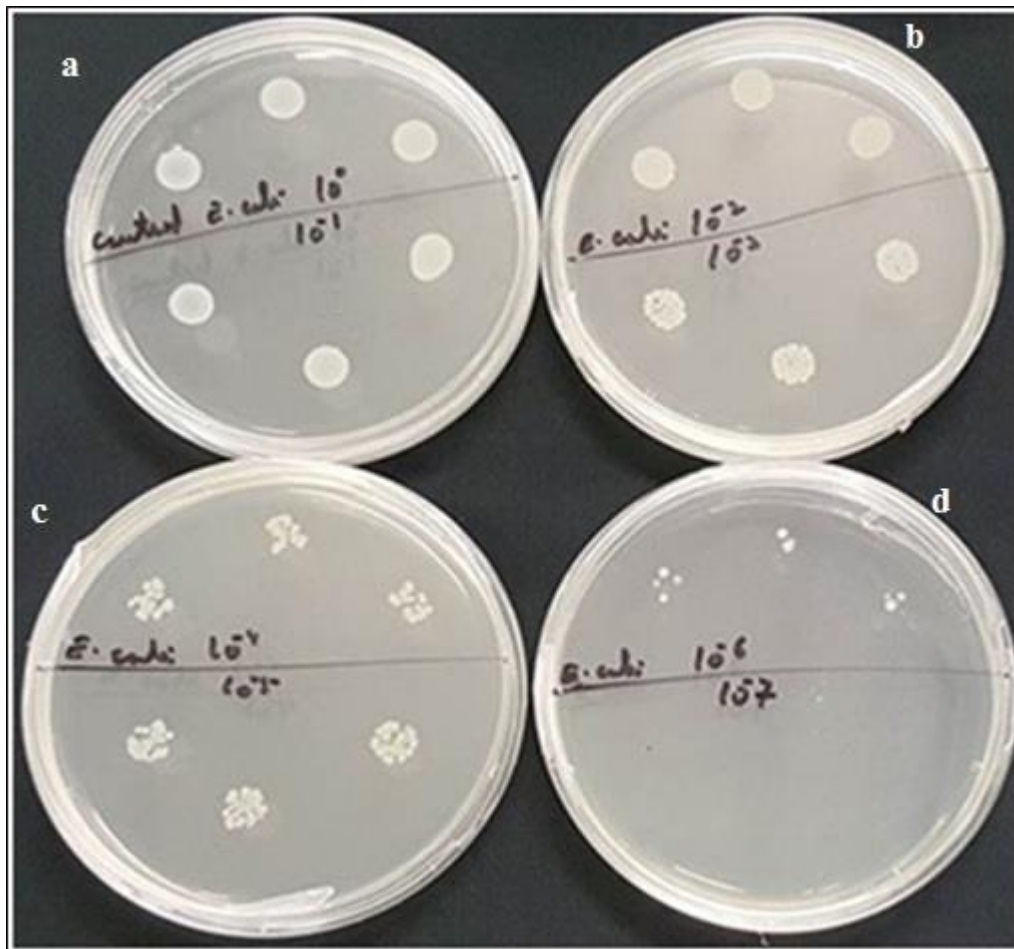


Figure 7-2 Control plates of *E. coli* K12 (a) upper half 10^0 dilution and lower half 10^{-1} bacterial dilution, (b) upper half 10^{-2} dilution and lower half 10^{-3} bacterial dilution, (c) upper half 10^{-4} dilution and lower half 10^{-5} bacterial dilution and (d) upper half 10^{-6} lower half 10^{-7} bacterial dilution

Figure 7-2 shows the growth of the *E. coli* on nutrient agar plates, which were used as control plates; results are shown in triplicate by using a reported method (Miles *et al.*, 1938). Furthermore, the growth of the *E. coli* can be easily seen on control plates of

nutrient agar medium. Furthermore, Figure 7-2 (d) shows the maximum growth of *E. coli* K12 at 10^{-6} CFU/mL which is the countable control plate as the grown colonies of *E. coli* can be counted easily on each drop (spot) of the plate, that has represented in the Figure 7-4.

7.3.2 Control plates of *S. aureus*

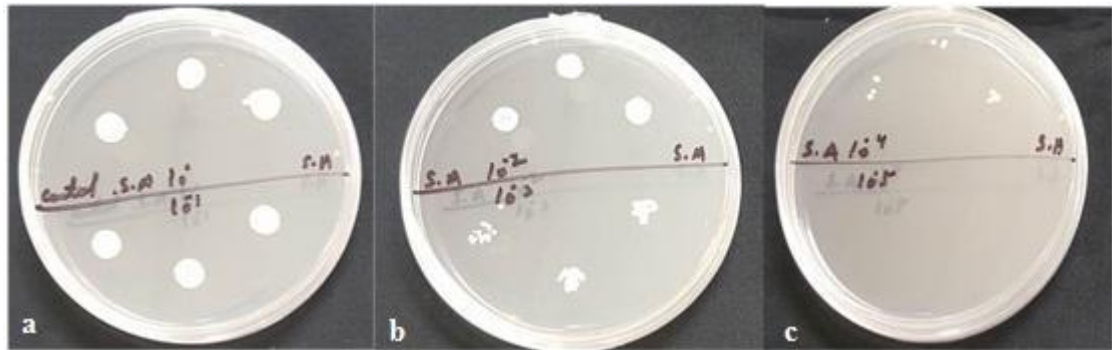


Figure 7-3 Control plates *S. aureus* (a) upper half 10^0 dilution and lower half 10^{-1} bacterial dilution, (b) upper half 10^{-2} dilution and lower half 10^{-3} bacterial dilution and (c) upper half 10^{-4} dilution and lower half 10^{-5} bacterial dilution

Figure 7-3 shows the growth of the *S. aureus* on nutrient agar plates, which are used as control plates; growth was shown in triplicate by using a reported method (Miles *et al.*, 1938). Furthermore, the growth of the *S. aureus* Gram-positive coccal bacterium can be easily seen on control plates of nutrient agar medium (see figure 7-3 a, b and c). Moreover, Figure 7-3 shows the maximum growth of *S. aureus* at 10^{-4} CFU/mL due to high concentration, in its dilution at 10^{-4} , the grown colonies of *S. aureus* can be counted easily on each spot of the plates, which are countable control plates and are shown in quantitative growth assay (see figure 7-4).

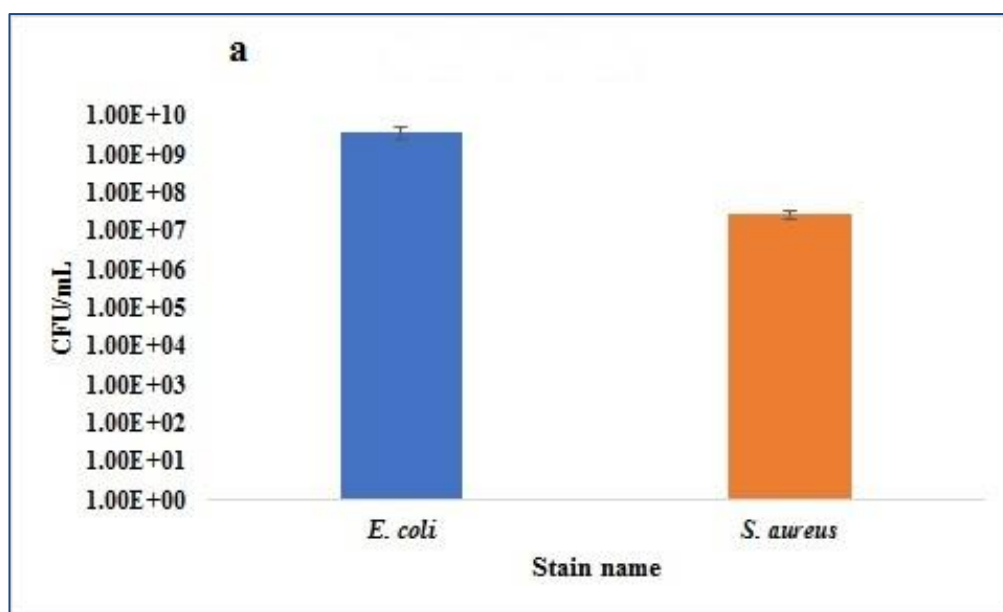


Figure 7-4 Quantitative Growth assay of control of *E. coli* and *S. aureus*

Figure 7-4 shows the quantitative growth assay of the control plates of *E. coli* (blue) and *S. aureus* (orange). This graph shows the total growth of the *E. coli* which is 10^9 CFU/mL and *S. aureus* 10^7 CFU/mL (see figure 7-2 and 7-3 (a, b, c and d)) respectively. This control of both strains has been used for the comparison of the antimicrobial applications of all developed (QM1-3, QM2-3, QM3-3, QM4-3 and QM5-3) silver coated iron oxide nanoparticles composites against *E. coli* and *S. aureus* while, for all other samples, separate controls were prepared which are given in Appendix -A3 and their quantitative assay.

7.3.3 QM1-3-based nanocomposite (MWCNTs-modified with iron-silver nanoparticles) against *E. coli* K12 and *S. aureus*

i) QM1-3 nanocomposite against *E. coli* K12

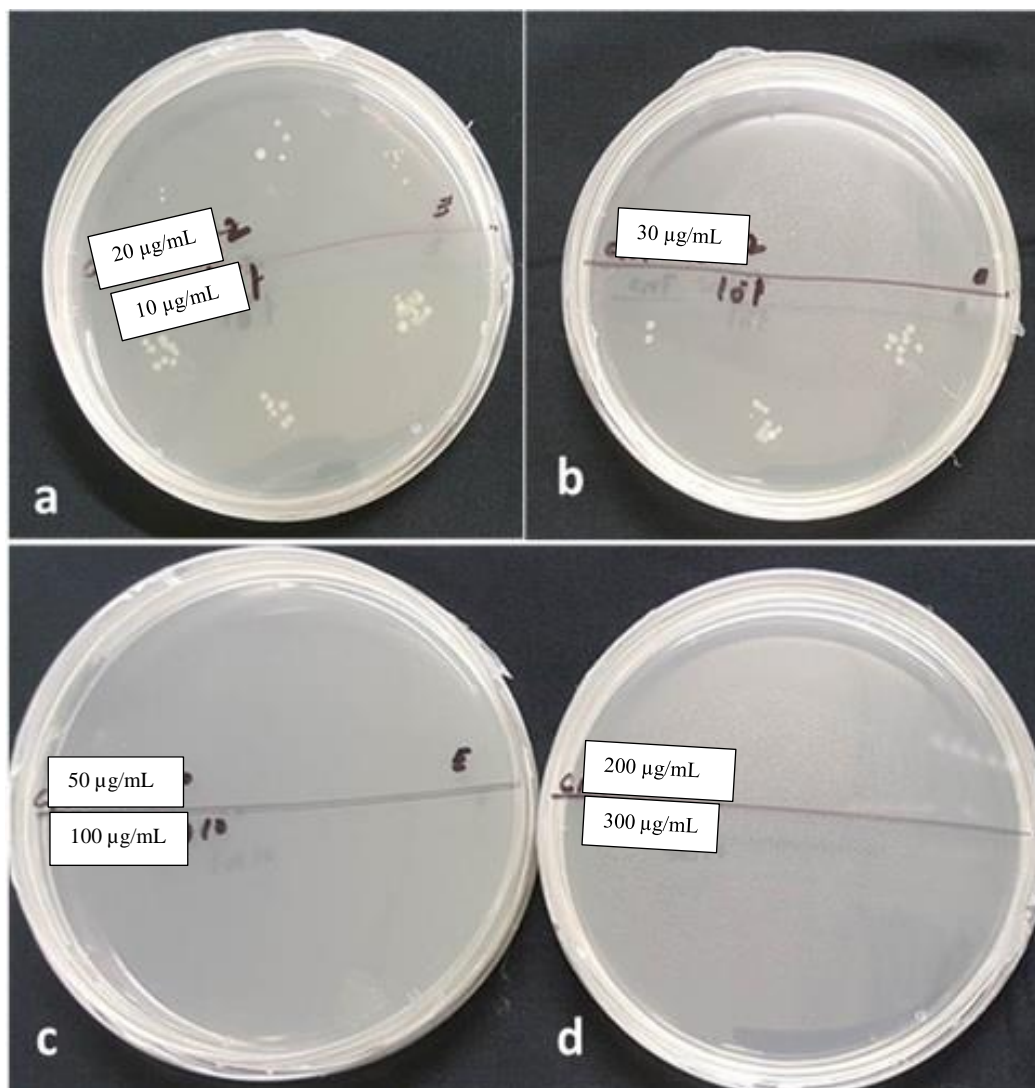


Figure 7-5 Antimicrobial efficiency of QM1-3(MWCNTs-modified with silver coating iron oxide nanoparticles) at various concentrations i.e. (a) 10 and 20 µg/mL (b) 30 µg/mL (c) 50 and 100 µg/mL and (d) 200 and 300 µg/mL against *E. coli* K12.

Figure 7-5 (a to d) shows that as the concentration of the nanocomposite materials increases, the growth of the bacteria decreases. There is a maximum growth of the bacteria at 20 µg/mL, while the 50 µg/mL composite completely inhibited the growth of the bacteria after the contact time of 7 hours (see figure 7-6 a and b) due to its

antimicrobial properties (Yamanaka *et al.*, 2005, Klasen, 2000). The mechanism for the action of the silver nanoparticles is not clear; however, it is thought that sulphur / thiol has been found in the respiratory system of the bacterial cell; therefore, silver nanoparticles can interact, enter the cell wall and cell membrane and stop the respiration system (biochemical path way) (Klasen, 2000) and inhibit their growth (Yamanaka *et al.*, 2005).

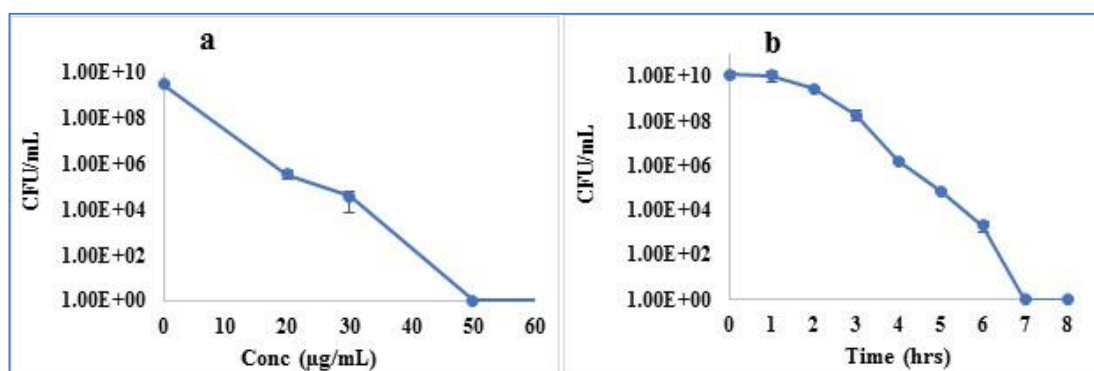


Figure 7-6 (a) Minimum bactericidal concentration assay against *E. coli*, (b) Time-kill assay using 50 µg/mL nanocomposite

ii) **QM1-3 nanocomposites against *S. aureus***

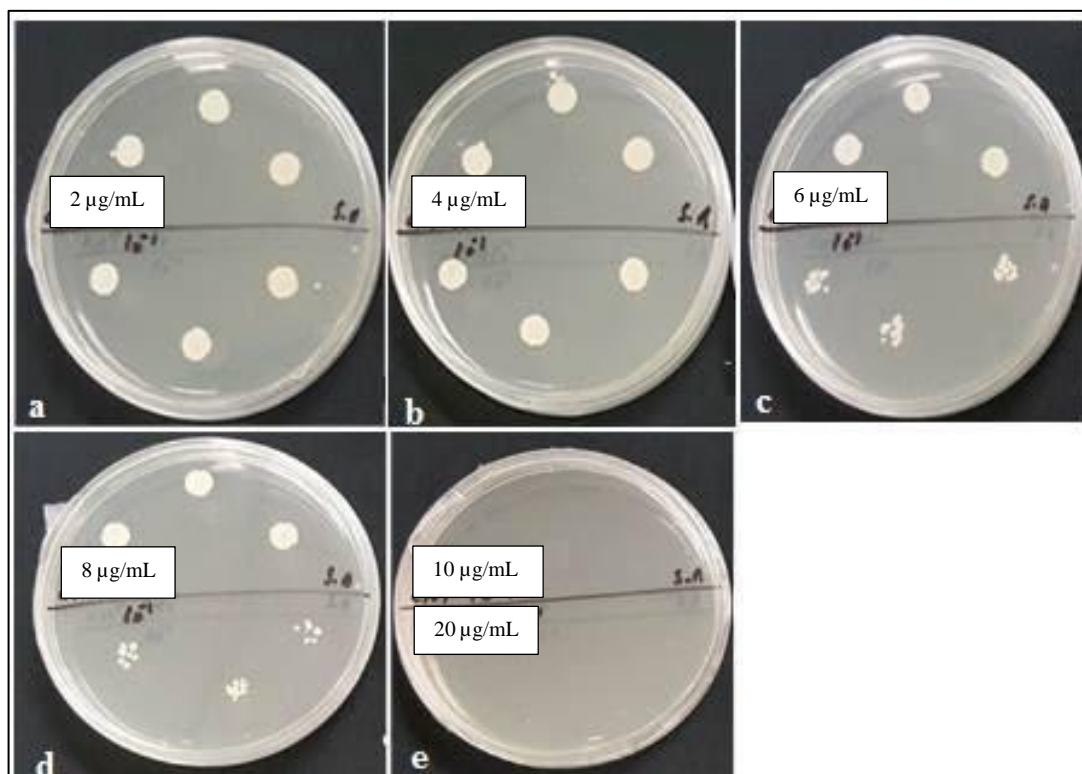


Figure 7-7 QM1-3 nanocomposite (MWCNTs-modified with silver coating iron oxide nanoparticles) against *S.aureus* with (a) 2 µg/mL, (b) 4 µg/mL, (c) 6 µg/mL, (d) 8 µg/mL, (e) (upper half 10 µg/mL and lower half 20 µg/mL).

Figure 7-7 (a, b, c, d and e) shows the different concentrations of (2, 4, 6, 8 and 10 µg/mL) the QM1-3 (containing silver coating and iron oxide) nanocomposite against the *S. aureus*. Figure 7-7 (a to e) showed that as the concentration of the composite material increases, the growth of the bacteria decreases. It was found as an efficient antimicrobial nanocomposite at 10 µg/mL, as it completely inhibited the growth of gram-positive bacteria after the contact time of 6 hours (see figure 7-8 a and b), which is much less than that of gram-negative bacteria *E. coli*. The cell wall of the Gram-positive is composed of peptidoglycan which is attached to the teichoic acids (Scott and Barnett, 2006), while physically and chemically the cell wall of the Gram-negative is more complicated, consists of an outer membrane along with the peptidoglycan

layer which covers the surface membrane and is resistant to the nanoparticles (Roberts, 1996) and needs higher concentrations to inhibit the growth of the bacteria as compare to Gram-positive. There is a maximum growth of the bacteria at 2 $\mu\text{g/mL}$, while, 10 $\mu\text{g/mL}$ of composite completely inhibited the growth of the bacteria due to its biocidal properties (Klasen, 2000). In addition to this, apart from the surface of the membrane it can enter the bacteria and inhibit their growth (Yamanaka *et al.*, 2005).

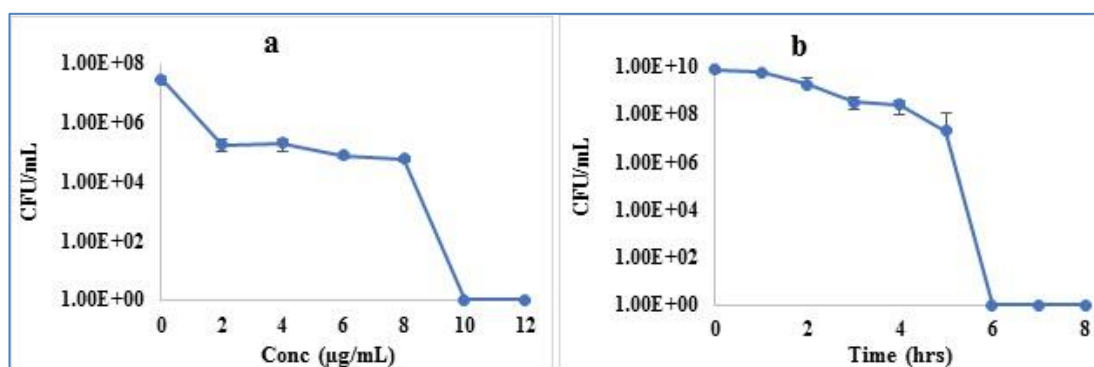


Figure 7-8 (a) Minimum bactericidal concentration assay against *S. aureus* (b) Time-kill assay using 10 $\mu\text{g/mL}$ nanocomposite

For the comparison of the antimicrobial efficiency of the MWCNTs based silver coated iron oxide nanocomposite (QM1-3) along with other samples (controls) QM1, QM1-1 and QM1-2 against *E. coli* and *S. aureus* is presented in Figure 7-9 and their plates are given in Appendix-A-3

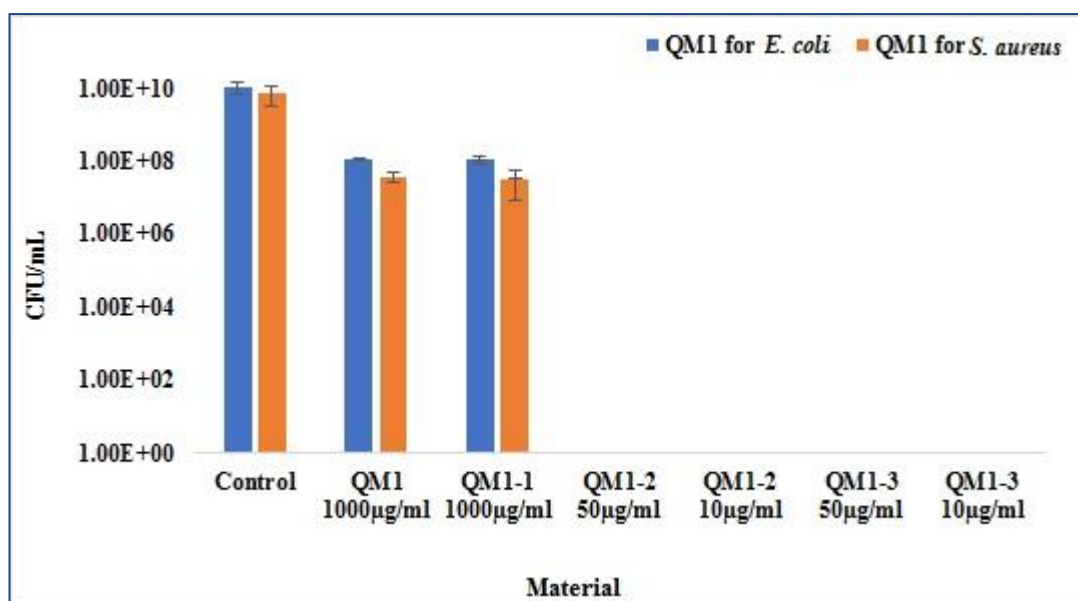


Figure 7-9 Quantitative growth assay of QM1-based composite: QM1 (unmodified MWCNTs), QM1-1 (MWCNTs modified with only iron oxide nanoparticles), QM1-2 (MWCNTs modified with only silver nanoparticles) and QM1-3 (MWCNTs modified with silver coating iron oxide nanoparticles) against *E. coli* (blue bar) and *S. aureus* (orange bar) at various concentrations of nanocomposites.

Figure 7-9 shows the quantitative growth curve assay for the QM1 based modified materials against *E. coli* and *S. aureus*. There is slightly decrease in the growth of both strains *E. coli* and *S. aureus* in QM1 and QM1-1 materials due to less antimicrobial efficiency while, QM1-2 and QM1-3 (containing silver nanoparticles) have completely inhibited the growth of the bacteria at very low concentration from 10 µg/mL to 50 µg/mL for *S. aureus* and *E. coli* respectively. Hence, it is concluded that MWCNTs is antimicrobial material but their antimicrobial properties are increased by the incorporation of the silver nanoparticles.

7.3.4 Summary of QM1-3-based composite

The nanocomposite material based on QM1-3 containing silver and iron oxide nanoparticles showed antibacterial activity against standard *E. coli* and *S. aureus*. The MBC of nanocomposite material obtained for the *E. coli* and *S. aureus* were found to be 50 µg/mL and 10 µg/mL, respectively. On the other hand, time-kill assay for the *E.*

coli and *S. aureus* was found to be 7 and 6 hours for both strains respectively. The result showed that the novel nanocomposite (QM1-3) is effective on Gram-positive as well as Gram-negative bacteria. Furthermore, the bacteria failed to grow back after 7 days of incubation following treatment under laboratory conditions.

7.3.5 QM2-3 nanocomposites (AC-modified with iron and silver nanoparticles) against *E. coli* and *S. aureus*

i) QM2-3 nanocomposite against *E. coli* K12

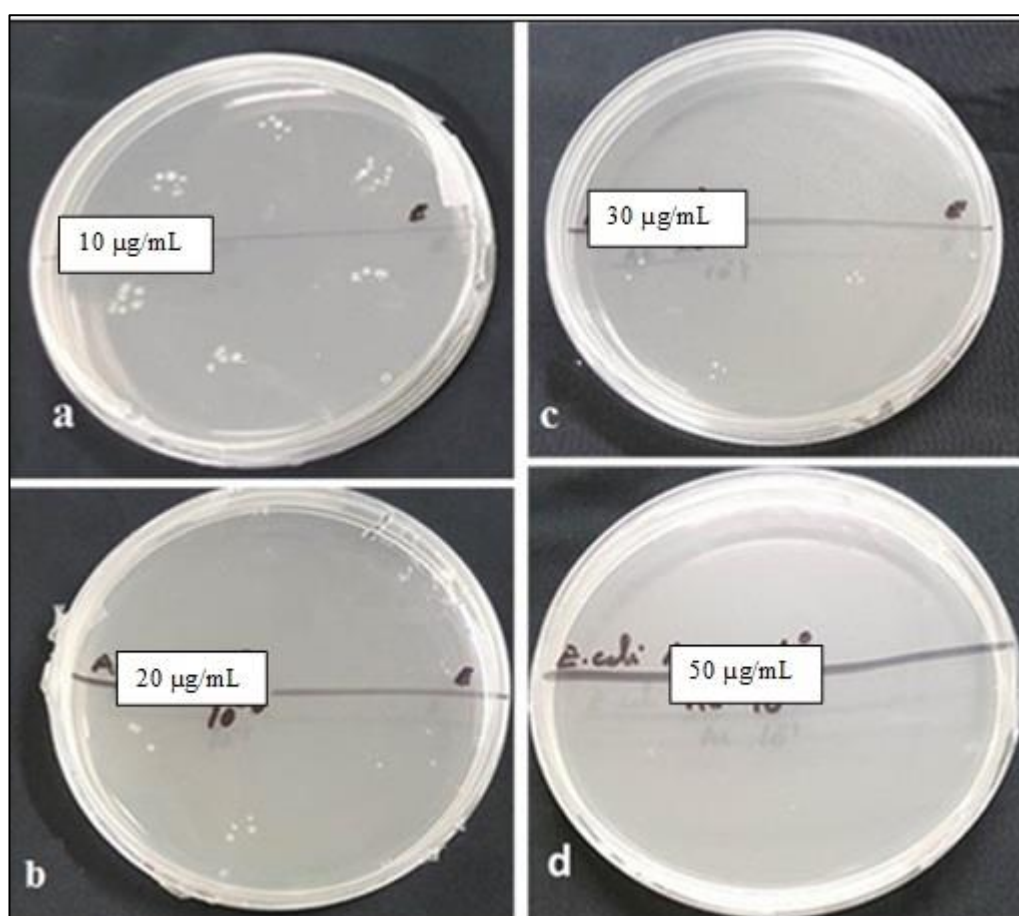


Figure 7-10 QM2-3 nanocomposite (AC-modified with silver coating iron oxide nanoparticles) against *E. coli* K12: (a) 10 µg/mL, (b) 20 µg/mL, (c) , 30 µg/mL and (d) 50 µg/mL

Figure 7-10 (a, b, c and d) shows the different concentrations of the QM2-3-based silver magnetite nanocomposite of various concentrations 10, 20, 30, and 50 µg/mL, used for the antimicrobial test against *E. coli*. Figure 7-10 from (a to d) shows that as

the concentration of the composite material increases, the growth of the bacteria decreases. There is a maximum growth of bacteria at 10 $\mu\text{g/mL}$, while 50 $\mu\text{g/mL}$ composite completely inhibited the growth after the contact time of 7 hours (see figure 7-11 a and b). It was observed that commercially purchased activated charcoal has reduced the growth of *E. coli* and possesses antimicrobial properties. Furthermore, with the incorporation of the silver nanoparticles their biocidal properties were improved. The presence of the silver nanoparticles in the composite causes the composite to act as antimicrobial agent, where silver nanoparticles destroys the respiratory system of the bacteria by going into the cell wall and cell membrane of the microbes (Klasen, 2000). In addition to this, apart from the surface of the membrane, silver nanoparticles enter the bacteria and inhibit their growth (Yamanaka *et al.*, 2005).

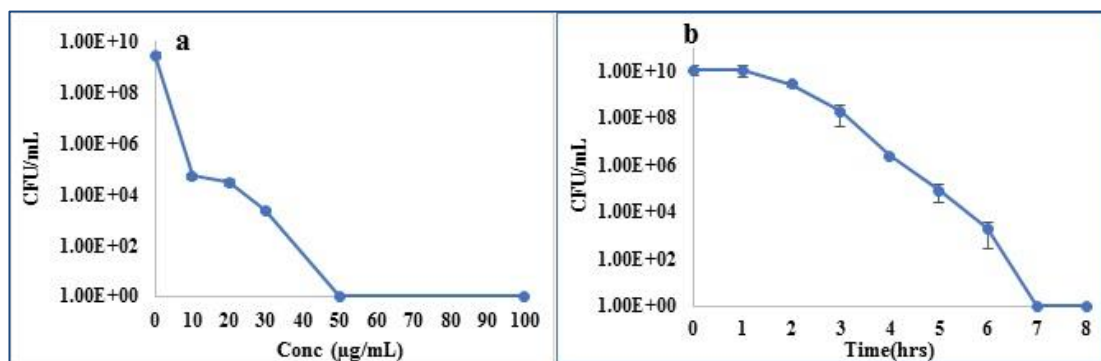


Figure 7-11 (a) Minimum bactericidal concentration assay against *E. coli*, (b) Time-kill assay using 50 $\mu\text{g/mL}$ of nanocomposite

ii) QM2-3-based nanocomposite against *S. aureus*

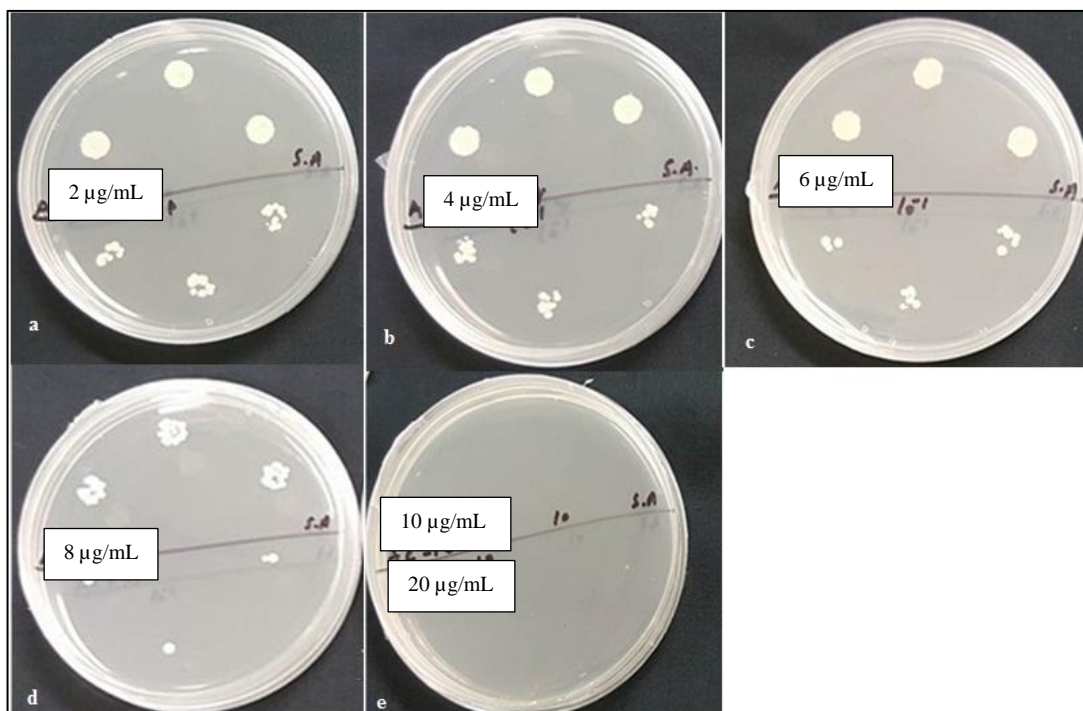


Figure 7-12 QM2-3 nanocomposite (AC-modified silver coating iron oxide nanoparticles) against *S.aureus*: (a) 2 µg/mL, (b) 4 µg/mL, (c) 6 µg/mL, (d) 8 µg/mL, (e) (upper half 10 µg/mL and lower half 20 µg/mL).

Figure 7-12 (a, b, c, d and e) show the different concentrations of the QM2-3-based composite incorporated with silver and iron oxide ranging from 2, 4, 6, 8, 10 and 20 µg/mL, used for the antimicrobial test against the *S. aureus*. Commercial activated charcoal was used as a host or carrier for small-sized silver nanoparticles to avoid the agglomeration and increase the antimicrobial properties (Chen *et al.*, 2015). Figure 7-12 (a to e) shows that as the concentration of the composite increases, the growth of the bacteria decreases and 10 µg/mL inhibited the growth of gram-positive bacteria after contact time of 6 hours (see figure 7-13 a and b) which is much less than that of gram-negative bacteria *E. coli* and much lower than the reported results (Chen *et al.*, 2015). There is a maximum growth of the bacteria at 2 µg/mL, while 10 µg/mL of composite completely inhibited the growth of the bacteria, due to its strong biocidal properties.

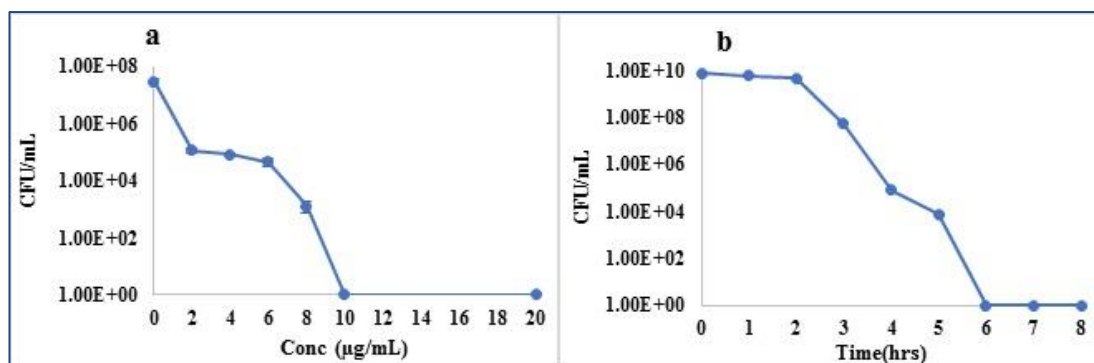


Figure 7-13 (a) Minimum bactericidal concentration assay against *S. aureus*, (b) Time-kill assay using 10 µg/mL.

The growth curve assay of the AC based silver coated iron oxide nanocomposite (QM2-3) along with other samples (controls) QM2, QM2-1 and QM2-2 against *E. coli* and *S. aureus* is shown in Figure 7-14 while their experimental data is given in Appendix.A-3

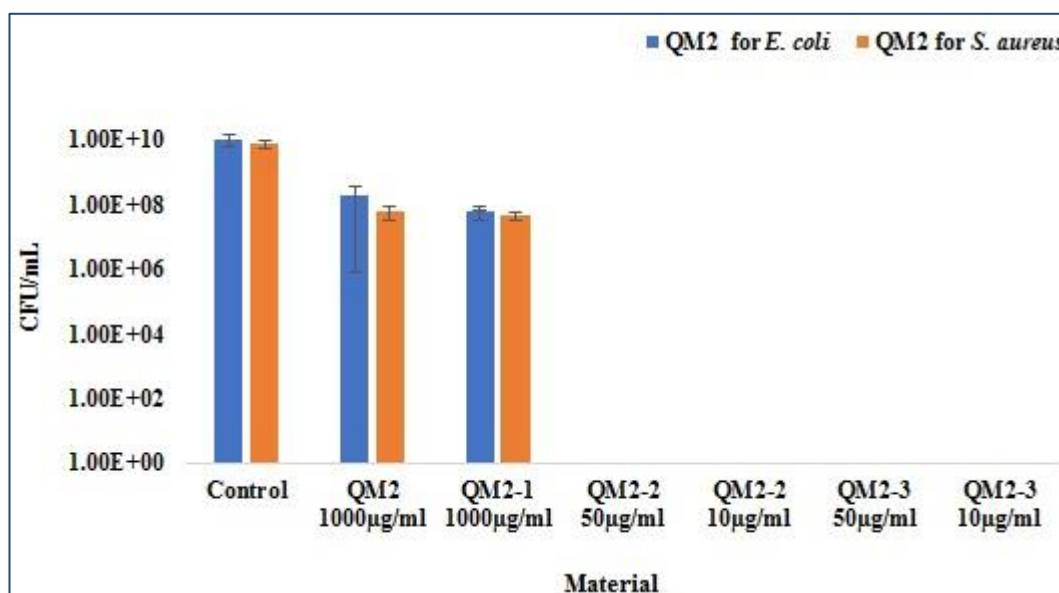


Figure 7-14 Quantitative growth assay of QM2-based composite: QM2 (unmodified AC), QM2-1 (AC modified with only iron oxide nanoparticles), QM2-2 (AC modified with only silver nanoparticles) and QM2-3 (AC modified with silver coating iron oxide nanoparticles) against *E. coli* (blue bar) and *S. aureus* (orange bar).

Figure 7-14 shows the quantitative growth curve assay of QM2 based modified materials against *E. coli* and *S. aureus*. The growth of both strains *E. coli* and *S. aureus*

slightly reduces in QM1 and QM1-1 materials (controls) due to less antimicrobial efficiency while, QM2-2 and QM3-3 have completely inhibited the growth of the bacteria at very low concentration from 50 to 10 $\mu\text{g/mL}$ for *E. coli* and *S. aureus* respectively due to their antimicrobial properties.

7.3.6 Summary of QM2-3-based composite

QM2-3 silver coated magnetite nanoparticles have shown to prevent the accumulation and dissolution of the AgNPs into the Ag^+ . They can be separated readily from the aqueous solution using an external magnetic field for recycling. Silver nanoparticles were incorporated into the magnetite composite shell to enhance the antimicrobial properties as there is no antimicrobial effect of magnetite incorporated material (QM2-1) (see figure 7-14). QM2 (unmodified activated charcoal) was used to stabilise the AgNPs, improving the strength. MBC for the *E. coli* was found to be 50 $\mu\text{g/mL}$ after 7-hours, while 10 $\mu\text{g/mL}$ concentration of the silver coating iron oxide nanoparticles activated charcoal based composite was found the MBC of Gram-positive *S. aureus* bacteria in the period of 6-hours. This developed material has shown high potential for the antimicrobial applications against both Gram-positive and Gram-negative bacteria in water treatment, and has the advantage of being recyclable.

7.3.7 QM3-3 nanocomposite (DAE-modified with iron and silver nanoparticles) against *E. coli* and *S. aureus*

i) QM3-3-based nanocomposite against *E. coli*

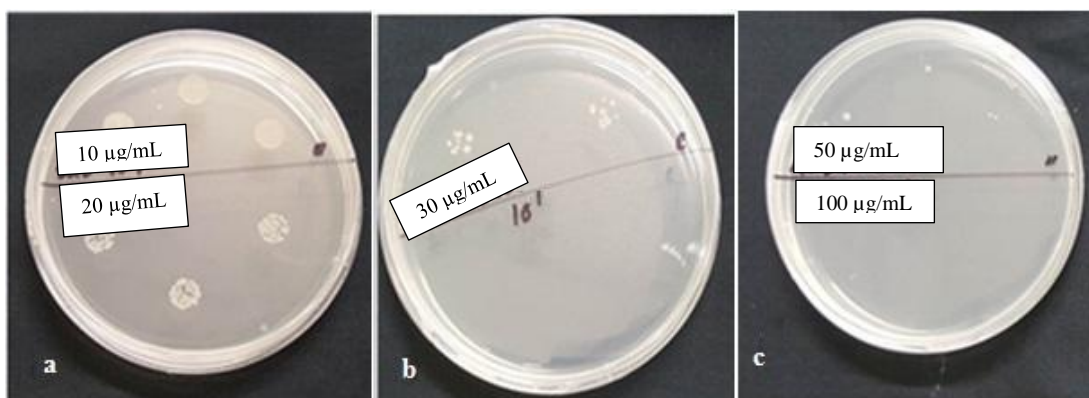


Figure 7-15 QM3-3 nanocomposite (DAE-silver coating iron oxide nanoparticles) against *E. coli*: (a) (upper half 10 µg/mL and lower half 20 µg/mL), (b) 30 µg/mL and (c) (upper half 50 µg/mL and lower half 100 µg/mL)

Figure 7-15 (a, b and c) shows the different concentrations (10, 20, 30, and 50 and 100 µg /mL) of QM3-3- based silver coating magnetite nanocomposite, used for the antimicrobial test against the *E. coli* K12. Figure 7-15 (a to c) shows that the concentration of the composite is inversely proportional to the growth of the bacteria; the growth of the bacteria decreases due to the increase in the concentration of the composite. There is maximum growth of the bacteria at 10 µg/mL, while the 100 µg/mL concentration completely inhibited the growth of the bacteria after contact time of 8 hours (see figure 7-16 a and b) due to its antimicrobial properties. Diatomaceous earth has been used as host matrix which helps the small-sized silver nanoparticles to retain their antimicrobial properties by releasing slowly (Chen *et al.*, 2015, Yamanaka *et al.*, 2005, Klasen, 2000). The antimicrobial mechanism of the developed composite proceeds due to the presence of silver nanoparticles, where silver nanoparticles rupture the cell membrane and stop the respiratory system of the bacteria, which cause the microbes to die. Furthermore, small size silver nanoparticles enter the bacterial cell

and inhibited the growth (Yamanaka *et al.*, 2005, Klasen, 2000)

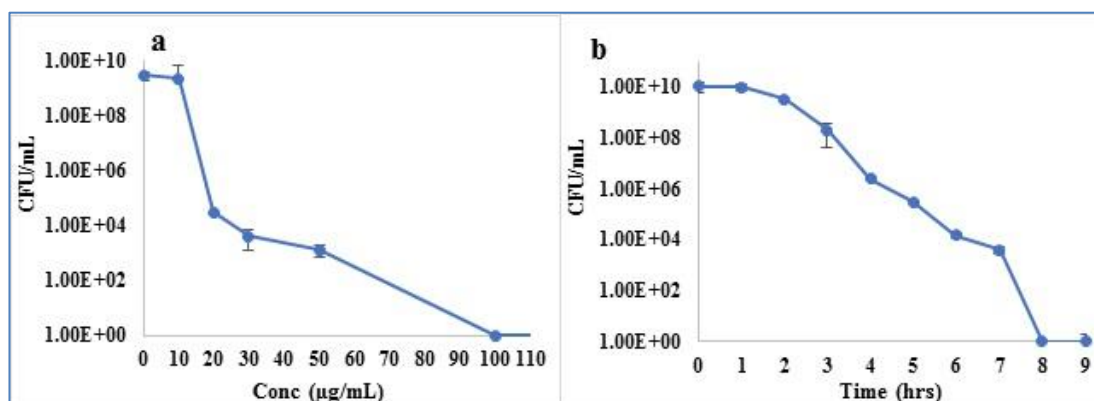


Figure 7-16 Antimicrobial activity of QM3-3 against *E. coli* (a) Minimum bactericidal concentration assay, (b) Time-kill assay at 100 µg/mL

ii) **QM3-3-based nanocomposite against *S. aureus***

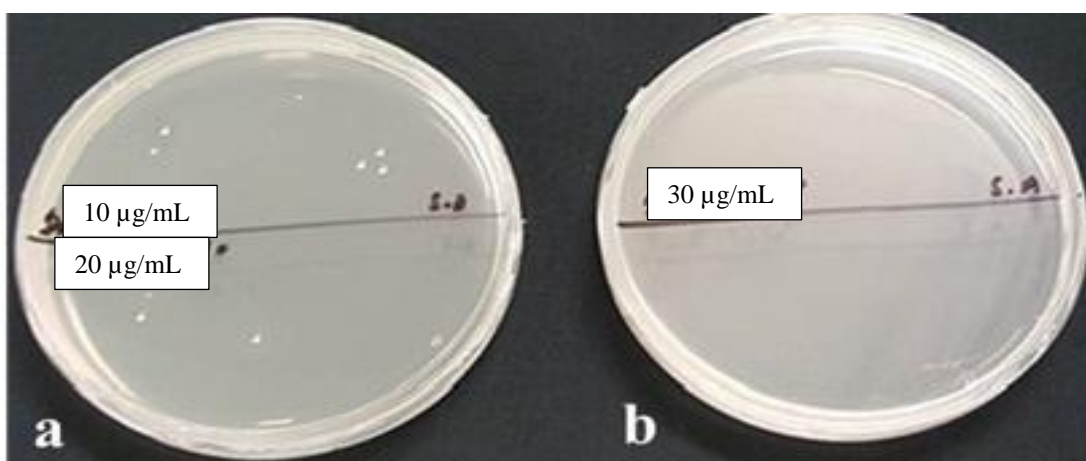


Figure 7-17 QM3-3 nanocomposite (DAE-modified with iron and silver nanoparticles) against *S. aureus*: (a) (upper half 10 µg/mL and lower half 20 µg/mL) and (b) 30 µg/mL

Figure 7-17 (a and b) shows the different concentrations of (10, 20 and 30 µg/mL) QM3-3-based nanocomposite for the antimicrobial test against the *S. aureus*. Figure 7-17 shows that lower concentration of the developed material is sufficient to inhibit the growth of the bacteria. The cell wall of the Gram-positive is composed of peptidoglycan which is attached to the teichoic acids (Scott and Barnett, 2006), while physically and chemically the cell wall of the Gram-negative is more complicated, consists of an outer membrane along with the peptidoglycan layer which covers the

surface membrane and is resistant to the nanoparticles (Roberts, 1996) and needs higher concentrations to inhibit the growth of the bacteria as compare to Gram-positive. It has been suggested that nanoparticles produce more reactive oxygen species in Gram-positive as compared to Gram-negative bacteria along with DNA damage, in result growth of bacteria is inhibited (Pramanik *et al.*, 2012). The composite material disrupts the membrane of the bacteria where silver ions reacts with the sulphur, nitrogen and oxygen to inhibit the growth of the bacteria (Juan *et al.*, 2010). In fact, QM1 based material damages the cell wall of the Gram-positive bacteria more as compared to Gram-negative bacteria and binds to the DNA which causes the cell death (Devi and Joshi, 2012).

The result showed that 30 $\mu\text{g/mL}$ has completely inhibited the growth of the bacteria after contact time of 8 hours (see figure 7-18 a and b) of Gram-positive bacteria, which is much less than that of Gram-negative bacteria *E. coli* but three times more than that of QM1-3 and QM2-based composite material. There is a maximum growth of the bacteria at 10 $\mu\text{g/mL}$, while 30 $\mu\text{g/mL}$ of composite completely inhibited the growth of the bacteria due to its biocidal properties (Klasen, 2000). Antimicrobial properties of the composite depend upon the size of silver nanoparticles: as size decreases biocidal properties increase. The use of the host material for the development of nanocomposite is helpful to release the silver ions slowly and enters the cell of the bacteria and destroys the respiratory system (Yamanaka *et al.*, 2005, Klasen, 2000).

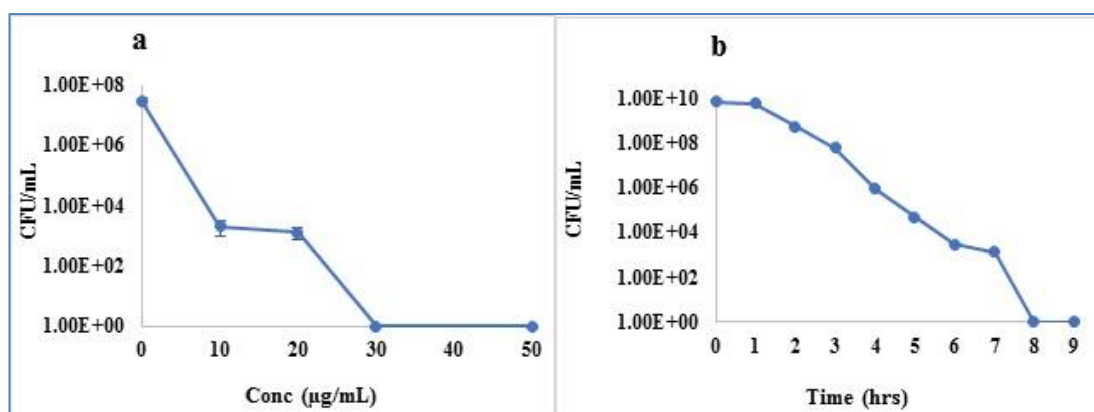


Figure 7-18 Antimicrobial activity of QM3-3 against *S. aureus* (a) Minimum bactericidal concentration assay, (b) Time-kill assay at 30 µg/mL

Antimicrobial efficiency of DAE based silver coating iron oxide nanocomposite (QM3-3) along with (controls) QM3, QM3-1 and QM3-2 against *E. coli* and *S. aureus* was also determined which are presented in figure 7-19, while, their experimental data along with plates are given in Appendix. A-3

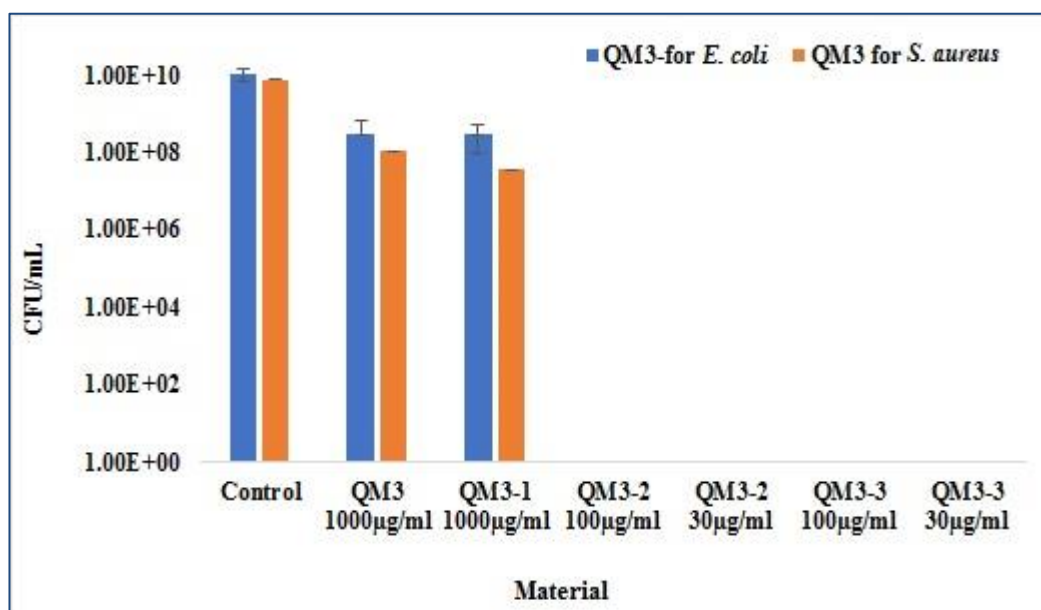


Figure 7-19 Quantitative growth assay of QM3-based composite QM3 (unmodified DAE), QM3-1 (DAE modified with only iron oxide nanoparticles), QM3-2 (DAE modified with only silver nanoparticles) and QM3-3 (DAE modified with silver coating iron oxide) against *E. coli* (blue bar) and *S. aureus* (orange bar).

Figure 7-19 shows the quantitative growth curve assay of QM3 based modified nanocomposite against *E. coli* and *S. aureus*. The growth of *E. coli* and *S. aureus*

slightly reduces in QM3 and QM3-1 materials due to less antimicrobial efficiency as compared to two other samples while, QM3-2 and QM3-3 have completely inhibited the growth of the bacteria at 100 and 30 $\mu\text{g/mL}$ for *E. coli* and *S. aureus* respectively due to incorporated silver nanoparticles.

7.3.8 Summary of QM3-3-based composite

The nanocomposite prepared in this study showed antibacterial activity against standard *E. coli* and *S. aureus*. The MBC of nanocomposite material obtained for *E. coli* and *S. aureus* were found to be 100 $\mu\text{g/mL}$ and 30 $\mu\text{g/mL}$, respectively. On the other hand, time-kill assay was found to be 8-hours for both of strains. Results showed that the novel developed material is effective against Gram-negative as well as Gram-positive bacteria but first one strain needs higher concentration compared to the second strain. Furthermore, the microbes failed to grow back after one week of incubation following treatment under laboratory conditions.

7.3.9 QM4-3-based composite (CPW-14-modified with iron and silver nanoparticles) against *E. coli* K12 and *S. aureus*

i) QM4-3-based composite against *E. coli*

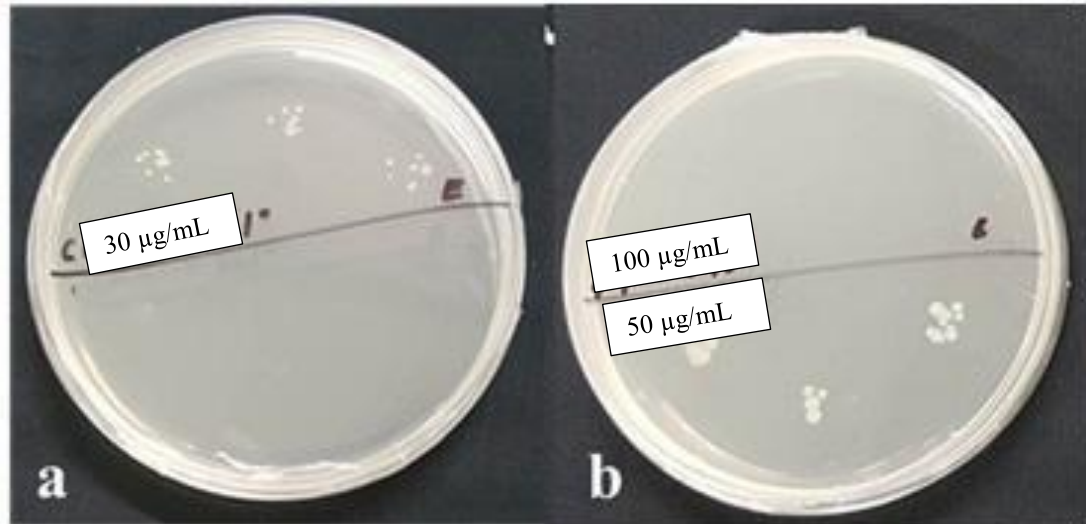


Figure 7-20 QM4-3 nanocomposite (CPW-14-modified with iron and silver nanoparticles) against *E. coli* with (a) 30 µg/mL, (b) 50 and 100 µg/mL (upper half 100 µg/mL and lower half 50 µg/mL).

Figure 7-20 (a, and b) shows the different concentrations of the QM4-3 based nanocomposite ranges from 30, 50 and 100 µg/mL used for the antimicrobial test against the *E. coli* K12. Moreover, the above plates showed that as the concentration of the composite material increases, the growth of the bacteria decreases. There is a maximum growth of the bacteria at 30 µg/mL, while at 100 µg/mL concentration completely inhibited the growth of the bacteria after contact time of 8 hours (see figure 7-21 a and b) of bacteria, due to the antimicrobial properties of silver nanoparticle (Yamanaka *et al.*, 2005, Klasen, 2000).

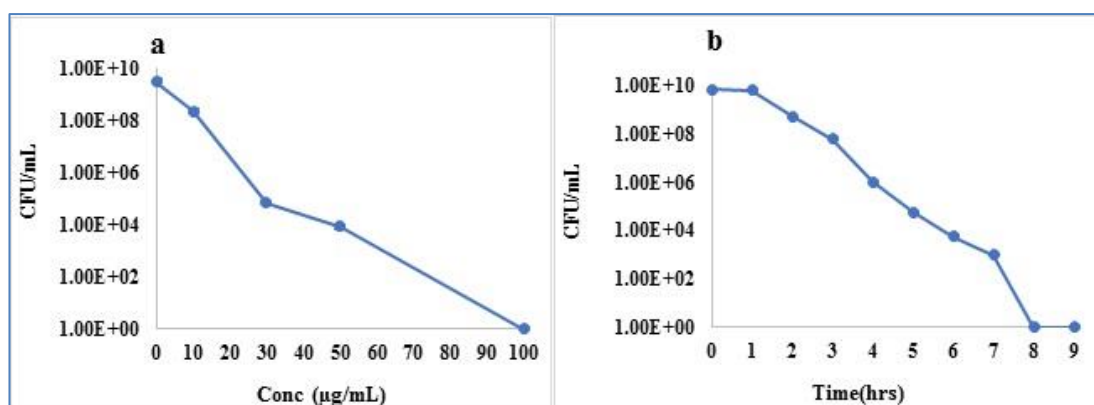


Figure 7-21 Antimicrobial activity of QM4-3 against *E. coli* (a) Minimum bactericidal concentration assay, (b) Time-kill assay at 100 $\mu\text{g/mL}$ concentration.

ii) **QM4-3-based composite against *S. aureus***

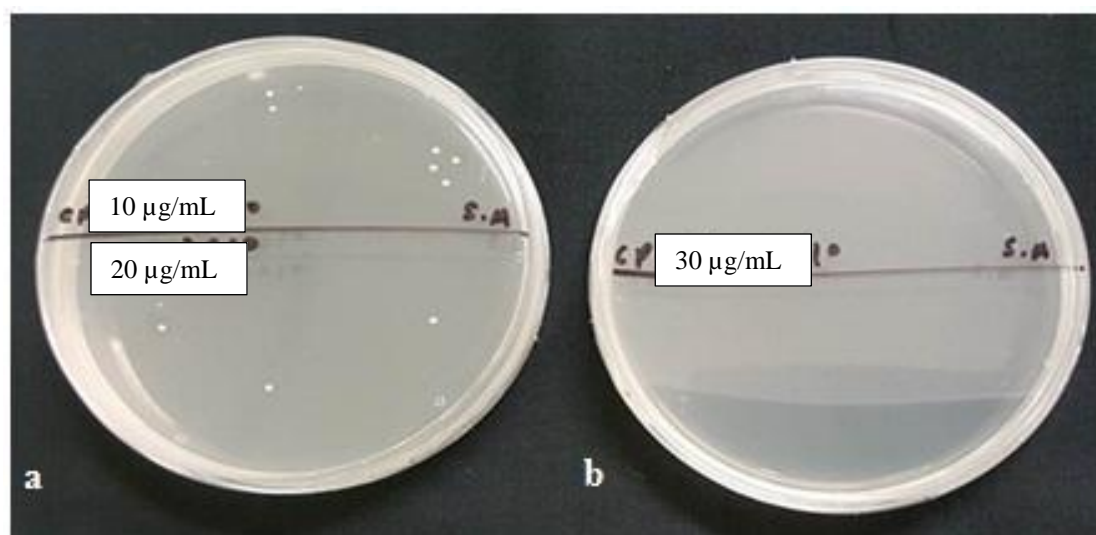


Figure 7-22 QM4-3 nanocomposite (CPW-14-modified with silver coating iron oxide nanoparticles) against *S. aureus* at various concentrations (a) (upper half 10 $\mu\text{g/mL}$ and lower half 20 $\mu\text{g/mL}$) and (b) 30 $\mu\text{g/mL}$

Figure 7-22 shows the different concentrations (10, 20 and 30 $\mu\text{g/mL}$) of QM4-3-based nanocomposite ranges from for the antimicrobial test against the *S. aureus*.

Figure 7-22 showed that as concentration of the composite decreases the growth of the bacteria increases. The growth of the bacteria was completely inhibited at 30 $\mu\text{g/mL}$ after contact time of 8 hours (see figure 7-23 a and b) of Gram-positive bacteria which is much lower than that of gram-negative *E. coli*. There is maximum growth of the bacteria at 10 $\mu\text{g/mL}$, while 30 $\mu\text{g/mL}$ concentration completely inhibited the growth

of the bacteria due to its biocidal properties (Klasen, 2000).

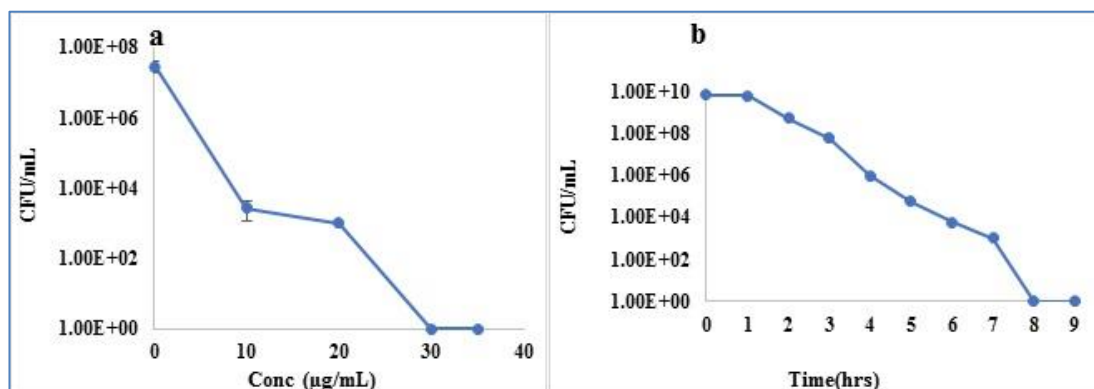


Figure 7-23 Antimicrobial activity of QM4-3 against *S. aureus* (a) Minimum bactericidal concentration assay, (b) Time-kill assay at 30 µg/mL

Antimicrobial analysis of QM4 (CPW-14) based silver coating iron oxide nanocomposite (QM4-3) along with (controls) QM4, QM4-1 and QM4-2 against *E. coli* and *S. aureus* was also determined and presented as quantitative growth assay (see figure 7-24), their experimental data along with plates are given in Appendix-A3.

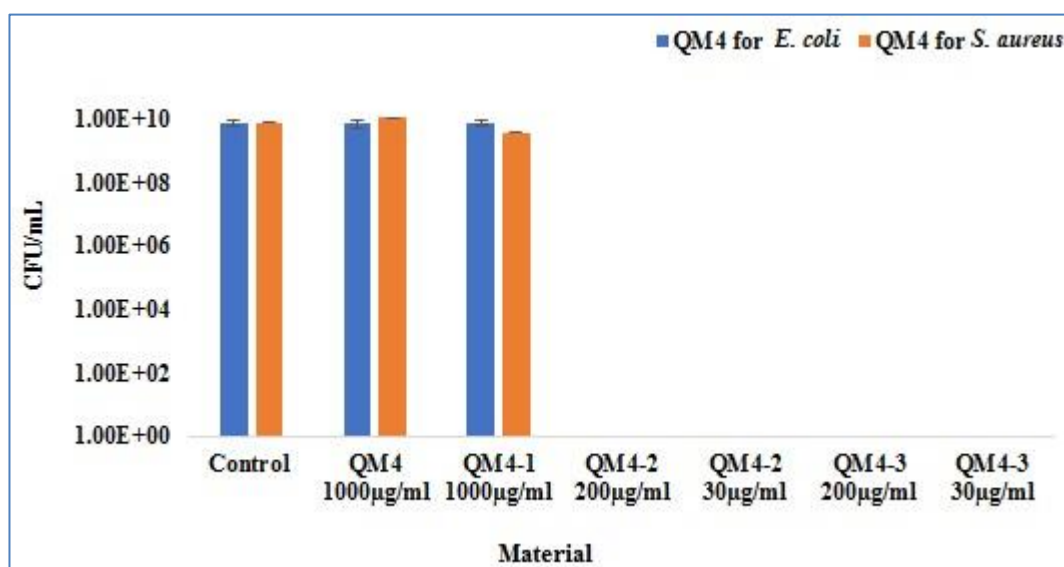


Figure 7-24 Quantitative growth assay of QM4-based composite: QM4 (unmodified CPW-14), QM4-1 (CPW-14 modified with only iron oxide nanoparticles), QM4-2 (CPW-14 modified with only silver nanoparticles) and QM4-3 (CPW-14 modified with silver coating iron oxide) against *E. coli* (blue bar) and *S. aureus* (orange bar)

Figure 7-24 shows the quantitative growth curve assay of QM4 based unmodified and modified nanocomposites against *E. coli* and *S. aureus*. The growth of *E. coli* and *S.*

aureus in QM4 and QM4-1 (see figure 7-24) is similar to that of control, there is no antimicrobial efficiency of the unmodified and modified with iron oxide materials respectively. Moreover, QM4-2 and QM4-3 (modified with silver and silver coated iron oxide nanoparticles respectively have completely inhibited the growth of the bacteria at 100 and 30 $\mu\text{g/mL}$ for *E. coli* and *S. aureus* respectively due to the incorporated silver nanoparticles.

7.3.10 Summary of QM4-3-based composite

QM4-3-based composite has shown efficient antimicrobial properties against two above mentioned strains of bacterial cells. Several concentrations (30, 50, 100, 200 to 300 $\mu\text{g/mL}$) were used and MBC for both strains were found to be different. MBC of gram-positive *S. aureus* was found to be 30 $\mu\text{g/mL}$, while the MBC for the *E. coli* K12 was found 100 $\mu\text{g/mL}$. Furthermore, there is no inhibition of the microbes in sample QM4, QM4-1 as they do not exhibit antimicrobial properties. The developed material could be separated from the aqueous solution by using an external magnetic field for recycling due to the presence of iron oxide nanoparticles.

7.3.11 QM5-3-based nanocomposite (CPW-80-modified with iron and silver nanoparticles) against *E. coli* and *S. aureus*

i) QM5-3 composite against *E. coli* K12

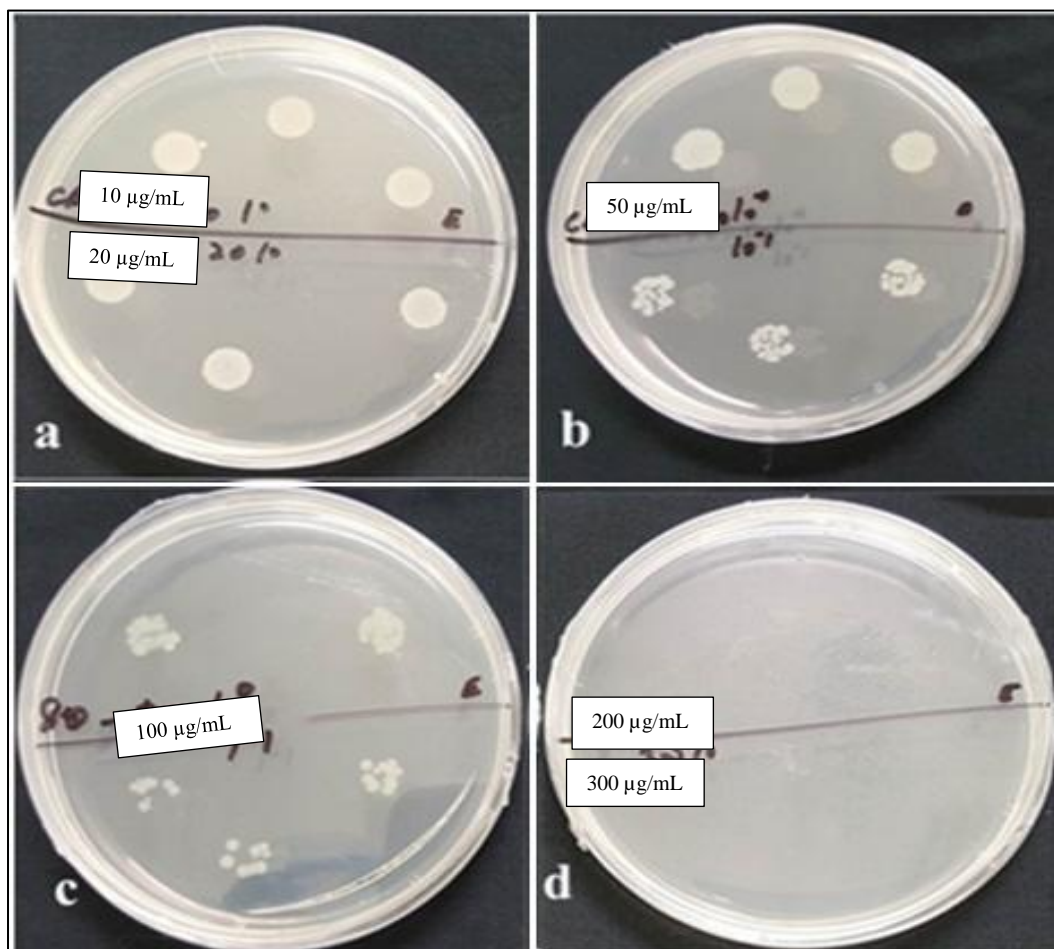


Figure 7-25 QM5-3 nanocomposite (CPW-80-modified with silver coating iron oxide nanoparticles) against *E. coli*. (a) (upper half 10 $\mu\text{g/mL}$ concentration and lower half 20 $\mu\text{g/mL}$ concentration), (b) 50 $\mu\text{g/mL}$, (c) 100 $\mu\text{g/mL}$ and (d) (upper half 200 $\mu\text{g/mL}$ and lower half 300 $\mu\text{g/mL}$).

Figure 7-25 (a, b, c and d) shows the different concentrations (10, 20, 50, 100, 200, and 300 $\mu\text{g/mL}$) of QM5-3- based nanocomposite for the antimicrobial test against the *E. coli* K12. Moreover, the above plates show that as the concentration of the composite material increases, the growth of the bacteria decreases. There is a maximum growth of the bacteria at 10 $\mu\text{g/mL}$, while 200 $\mu\text{g/mL}$ composite completely inhibited the growth of the bacteria after contact time of 8 hrs (see figure 7-26 a and

b) of Gram-negative bacteria due to the antimicrobial properties of silver nanoparticle (Yamanaka *et al.*, 2005, Klasen, 2000). Among all developed composite material, QM5-3 has poor results compared to other samples due to its lack of antimicrobial properties.

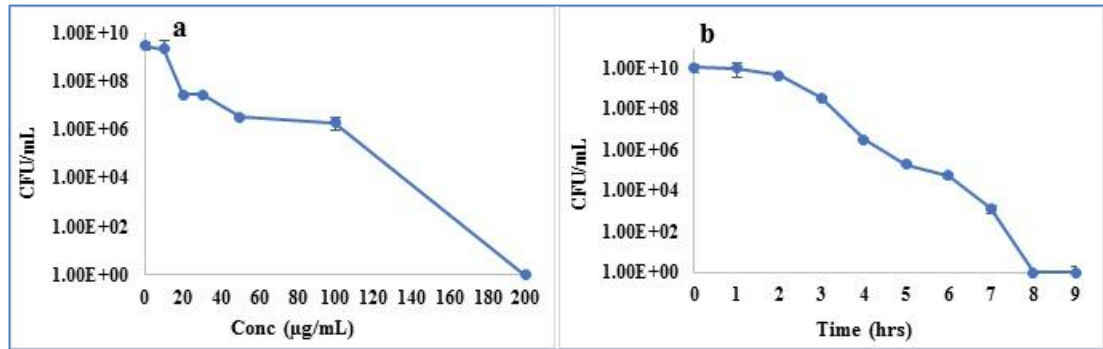


Figure 7-26 Antimicrobial activity of QM5-3 against *E. coli* (a) Minimum bactericidal concentration assay, (b) Time-kill assay at 200 µg/mL

ii) QM5-3-based nanocomposite against *S. aureus*

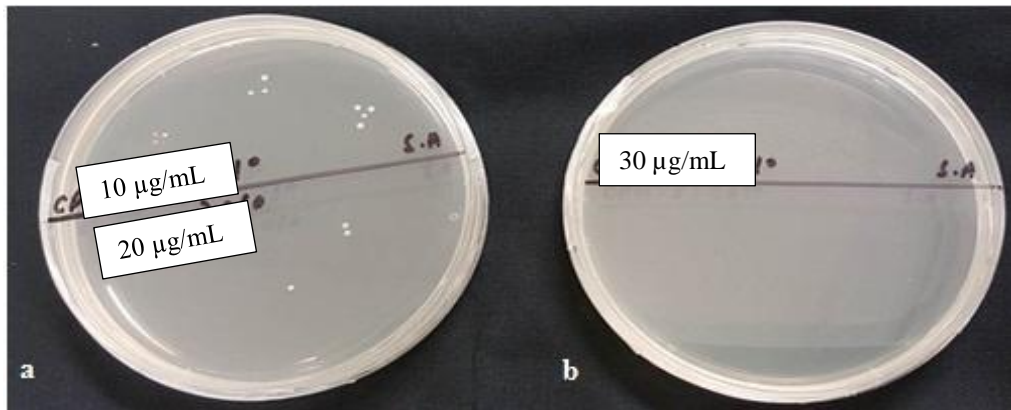


Figure 7-27 QM5-3 nanocomposite (CPW-80-modified with silver coating iron oxide nanoparticles) against *S. aureus* with various concentrations, (a) (upper half 10 µg/mL concentration and lower half 20 µg/mL concentration) and (b) 30 µg/mL.

Figure 7-27 shows the different concentrations (10, 20 and 30 µg/mL) of QM5-3-based silver coating iron oxide nanocomposite for the antimicrobial test against the *S. aureus*. This experiment showed that 30 µg/mL has inhibited the growth of Gram - positive bacteria after contact time of 8 hours (see figure 7-28 a and b), which is much lower than that of Gram-negative bacteria *E. coli*. There is a maximum growth of the bacteria at 10 µg/mL, while 30 µg/mL of composite has completely inhibited the growth of the bacteria due to its biocidal properties (Klasen, 2000).

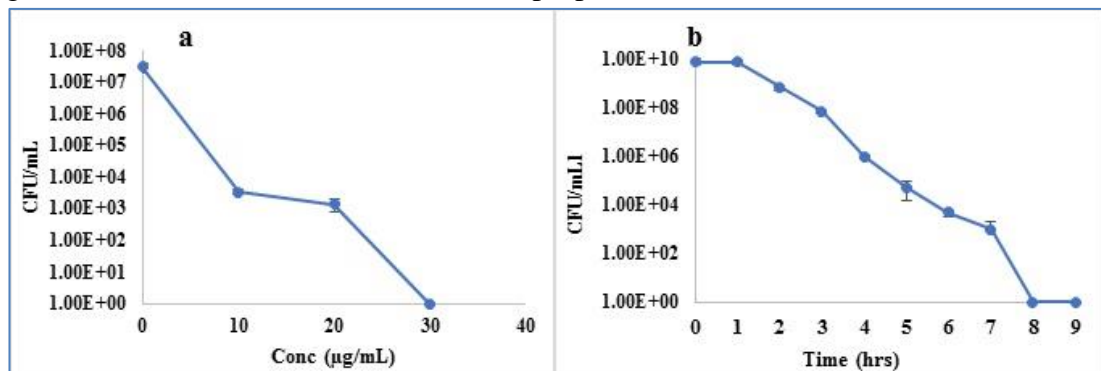


Figure 7-28 (a) Antimicrobial activity of QM5-3 against *S. aureus* Minimum bactericidal concentration assay, (b) Time-kill assay at 30 µg/mL concentration

Antimicrobial analysis of QM5 (CPW-80)-based silver coated iron oxide nanocomposite (QM5-3) along with (controls) QM5, QM5-1 and QM5-2 against *E.*

coli and *S. aureus* was determined with quantitative growth assay (see figure 7-29), while their experimental data along with plates are given in Appendix-A3.

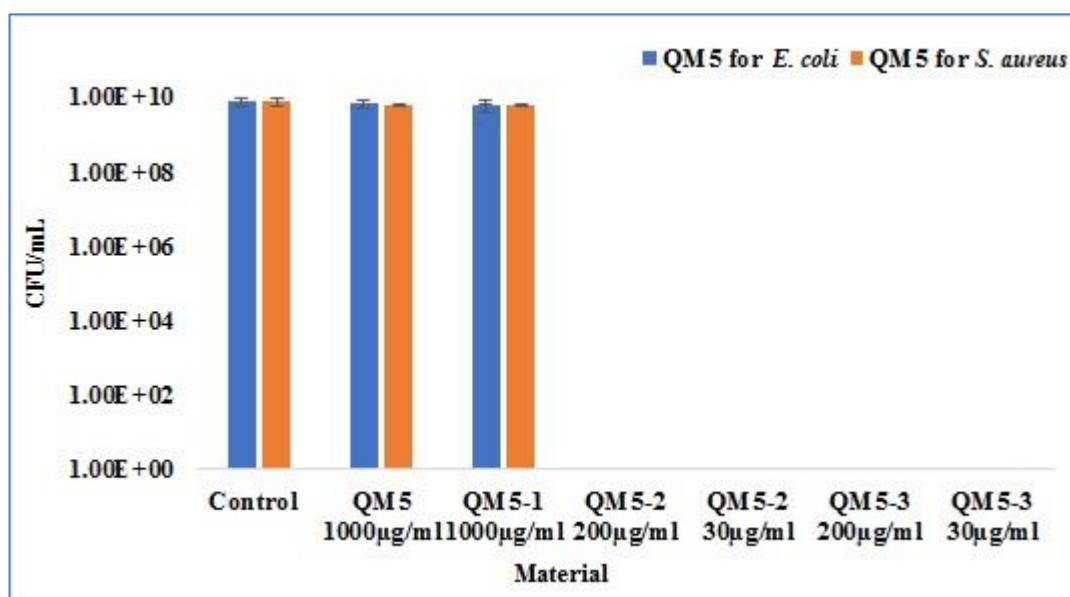


Figure 7-29 Quantitative growth assay of QM5-based composite QM5 (unmodified CPW-80), QM5-1 (CPW-80 modified with only iron oxide nanoparticles), QM5-2 (CPW-80 modified with only silver nanoparticles) and QM5-3 (CPW-80 modified with silver coating iron oxide) against *E. coli* (blue bar) and *S. aureus* (orange bar)

Figure 7-29 shows the growth curve assay of QM5 based un modified and modified nanocomposites against *E. coli* and *S. aureus*. The growth of *E. coli* and *S. aureus* in QM5 and QM5-1 (see figure 7-29) is similar to that of control, there is no antimicrobial efficiency to the unmodified and modified with iron oxide nanomaterial respectively. Moreover, QM5-2 and QM5-3 (modified with silver and silver coating iron oxide nanoparticles respectively) have completely inhibited the growth of the bacteria at 200 and 30 µg/mL for *E. coli* and *S. aureus* respectively due to the incorporated silver nanoparticles.

7.3.12 Summary of QM5-3-based nanocomposite

QM5-3-based nanocomposite has potential for the antimicrobial applications against Gram-positive *S. aureus* and growth was inhibited at 30 µg/mL, while the MBC for

Gram-negative *E. coli* was found to be 200 µg/mL. Furthermore, it was observed that there was no antimicrobial effect of QM5 and QM5-1 against *E. coli* and *S. aureus*.

Section -2

7.4 Antimicrobial efficiency of synthesised materials against Gram-negative bacteria by SP method

The modified and unmodified materials were also tested against several other waterborne bacterial strains by using the SP method, The MBC for the bacterial cells was different for different strains, which are given below. Furthermore, the bacterial plates and graphs are given in the appendix A-2.

The MBC of QM1-3, against *L. pneumophila*, *E. coli* and *K. pneumoniae* was 20, 12 and 20 µg/mL, respectively, while MBC of QM2-3 against *L. pneumophila*, *E. coli* and *P. aeruginosa* was 20, 12 and 20 µg/mL, respectively. Furthermore, the MBC of QM3-3 against *L. pneumophila*, and *E. coli* was found to be 50 and 12 µg/mL, respectively in the present study, the MBC of QM4-3 against *E. coli* was to be 20 µg/mL in the present study. The MIC and MBC were determined by using agar dilution tests. Both Gram-positive and Gram-negative bacteria were inoculated on the nutrient agar plates with several concentrations. The growth of the bacteria was analysed by a number of colony forming units (CFU) on the nutrient agar plates. The concentration of the nanocomposites where no bacterial growth was observed after 24-hours was taken for the MBC determinations. The minimum concentration from which the bacteria do not grow when transferred to fresh medium is MBC, while MIC is the lowest concentration in which the colonies appeared on top of the fresh medium.

7.5 Recycling of the modified nanocomposites

Antimicrobial composites containing silver and iron oxide were developed for the antimicrobial applications and reusable purposes. These recycling nanocomposites are cheap, save on raw materials, reduce the total cost of the projects and are eco-friendly, which keeps the environment clean and decreases the production of the contaminants. The developed materials have both properties as an antimicrobial agent due to the incorporation of the silver nanoparticles and is reusable, due to the presence of iron oxide. Therefore, an external magnetic field was applied to separate the aqueous dispersion of the composite with the bacterial cells after incubation of 8 hours. The recycling process is shown in Figure 7-30. *E. coli* was used as the model bacteria for the recycling experiment for two most efficient developed composites. In the Log phase growth bacteria were incubated with these developed composites at 50 µg/mL for 8 hours. With the help of a magnet, composites containing silver coating iron oxide nanoparticles were separated from the bacteria suspension, which was taken for turbidity assay to determine the relative bacterial viability and the famous spread-plate method was used for the growth of bacteria. The remaining iron oxide, silver-based nanocomposites were washed to remove the adsorbed protein during the incubation and remaining bacterial cells with nutrient broth, and was followed with the introduction of dispersion into the sterilised and deionized water for repeated use.

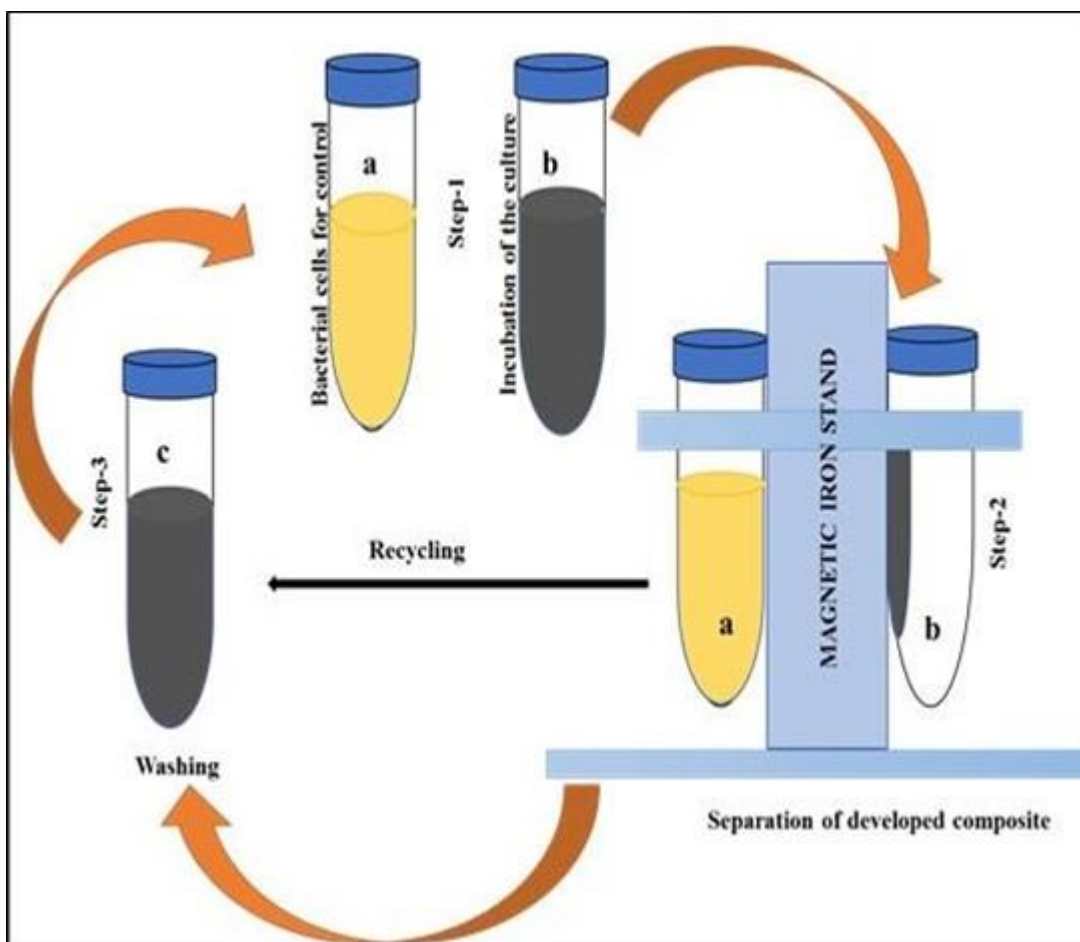


Figure 7-30 Schematic representation of recycling of the developed nanocomposite
 Figure 7-30 (a) represents the control tube of the bacterial cell *E. coli* K12. Figure 7-30 (b) shows the bacterial suspension dispersed in the developed composite containing silver coating iron oxide nanoparticles which was incubated at 37 °C in a shaking incubator. Figure 7-30 (c) tube containing washed, repeatedly used and separated suspension of developed composite. Figure 7-30 shows the recycling application of developed composite containing silver and iron oxide nanoparticles which completes in three steps. Firstly, in step 1, first tube from left was filled with log phase bacterial cells as a control tube and second tube contains brown suspension (from right) was filled with log phase bacterial cells along with developed nanocomposite and was incubated for 8 hours at 37 °C. Furthermore, the Log phase growth bacteria were incubated with two developed nanocomposites QM1-3 and QM2-3 with 50 µg/mL,

for 8 hours. After 8 hours, both tubes were placed on the magnetic iron stand. Composites containing silver coating iron oxide nanoparticles with bacterial cells were separated from the bacterial suspension with the magnetic stand and were found to be transparent, which shows that the growth of the bacteria was effectively inhibited, while the control sample appeared as a turbid suspension due to the maximum growth of bacterial cells. The supernatant was taken for turbidity assay to determine the relative bacterial viability and the famous spread-plate method was used for the growth of bacteria, which revealed the inhibition of the bacterial cells. Furthermore, in step 3, separated iron oxide, silver-based nanocomposites were washed with sterilised and deionised water three times to remove the adsorbed protein during the incubation and remaining bacterial cells with nutrient broth, and was followed with introduction of dispersion into the sterilised and deionized water for the next cycle of antibacterial application. The results of recyclable material were found highly effective after being reused for three-times (see figure 7-32 and 7-35). Recycling experiments were performed with the method already reported (Dong *et al.*, 2013, Dong *et al.*, 2011). This experiment showed that silver coating iron-oxide nanoparticles can be used as recyclable nanocomposites and can be used repeatedly to save the cost, environment and health. The qualitative and quantitative analysis for the recycling of the two most efficient composites QM1 -3 and QM2-3 are given in the following pages.

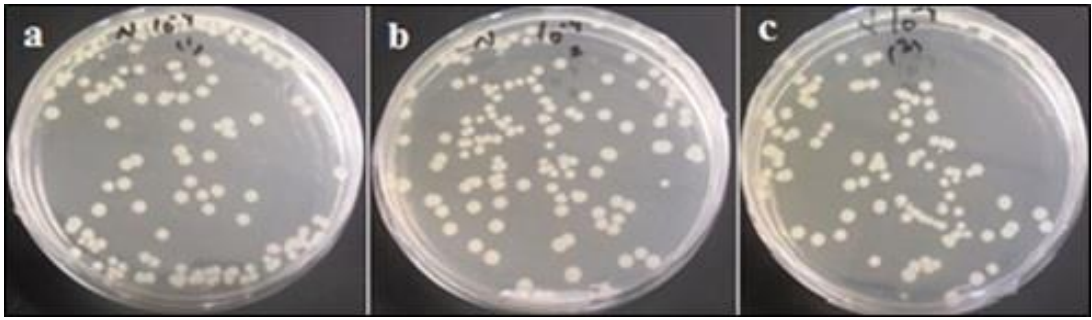


Figure 7-31 (a,b and c) control plates of *E. coli* in triplicate

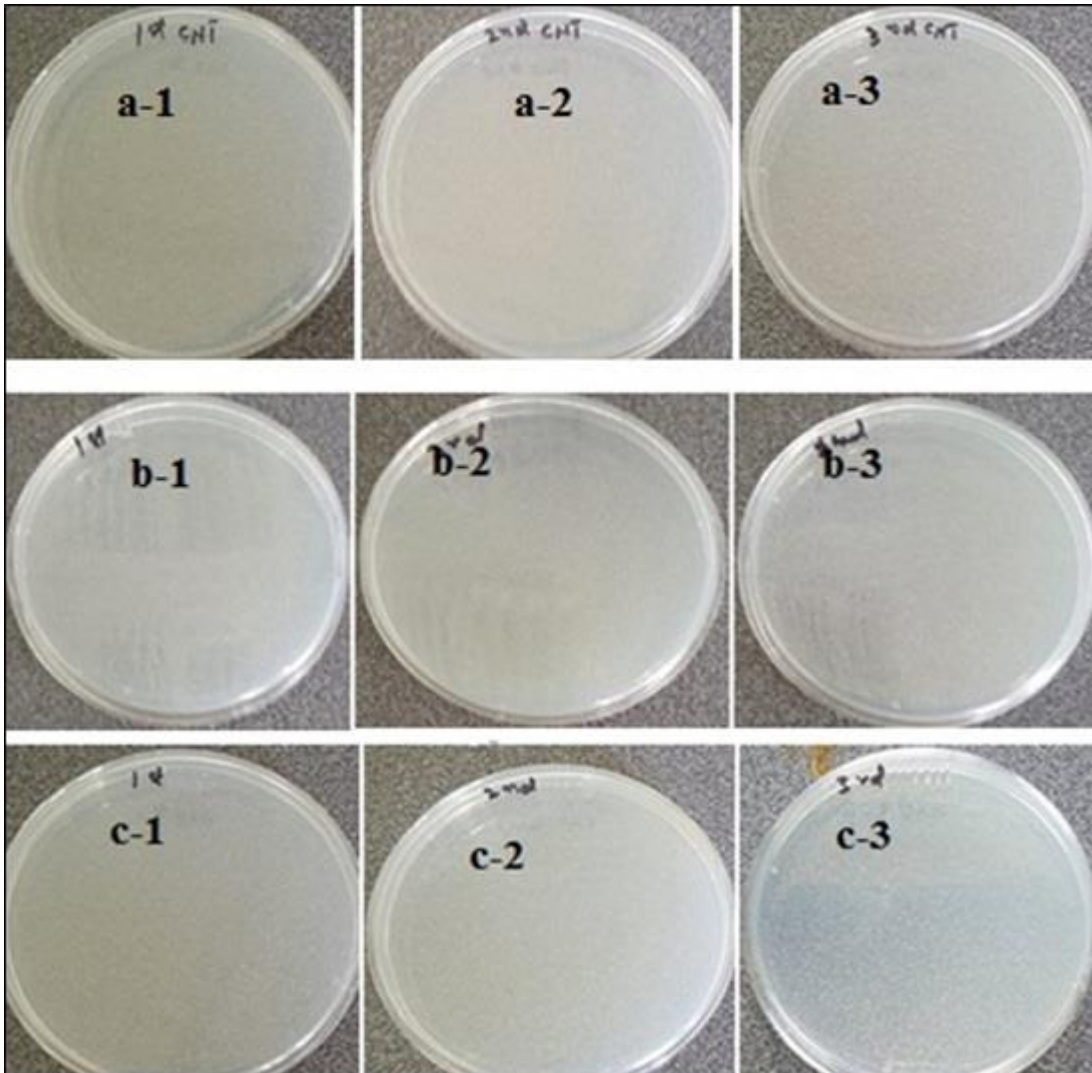


Figure 7-32 Recycling of QM1-3 composite against *E. coli* in triplicate three times: (a-1,a-2 and a-3) are the first use of the QM1-3 composite against *E. coli*, (b-1,b-2 and b-3) are the re-use of composite for the second time, (c-1,c-2 and c-3) are the re-use of the composite for the third time against *E. coli*

Figure 7-32 shows the inhibition of *E. coli* growth for three times re-use, while the growth of the bacteria was observed on recycling the material for fourth and fifth

times.

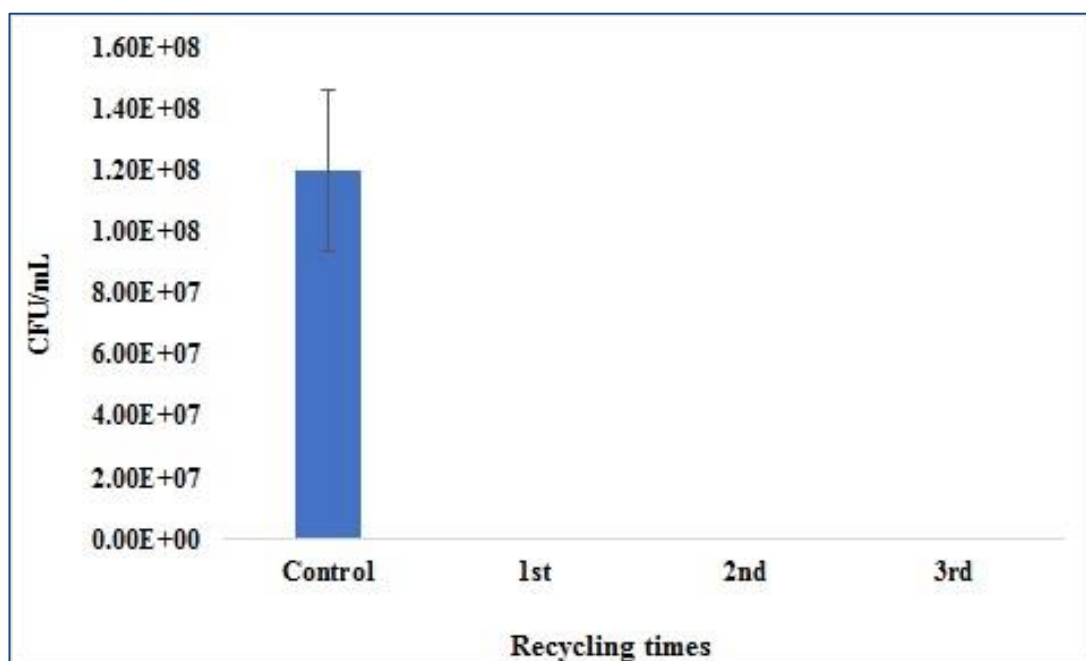


Figure 7-33 Harvesting of QM1-3 against *E. coli*

Figure 7-33 shows harvesting of QM1-3 composite against *E. coli*. Graph indicates that there was no growth of the bacteria when it was used 1st, 2nd and 3rd times (see figure 7-32).

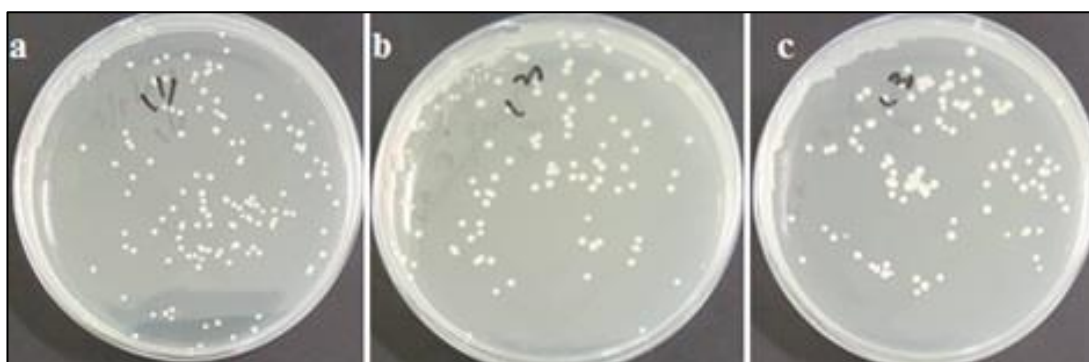


Figure 7-34 (a,b and c) control plates of *E. coli* in triplicate for QM2-3 nanocomposite

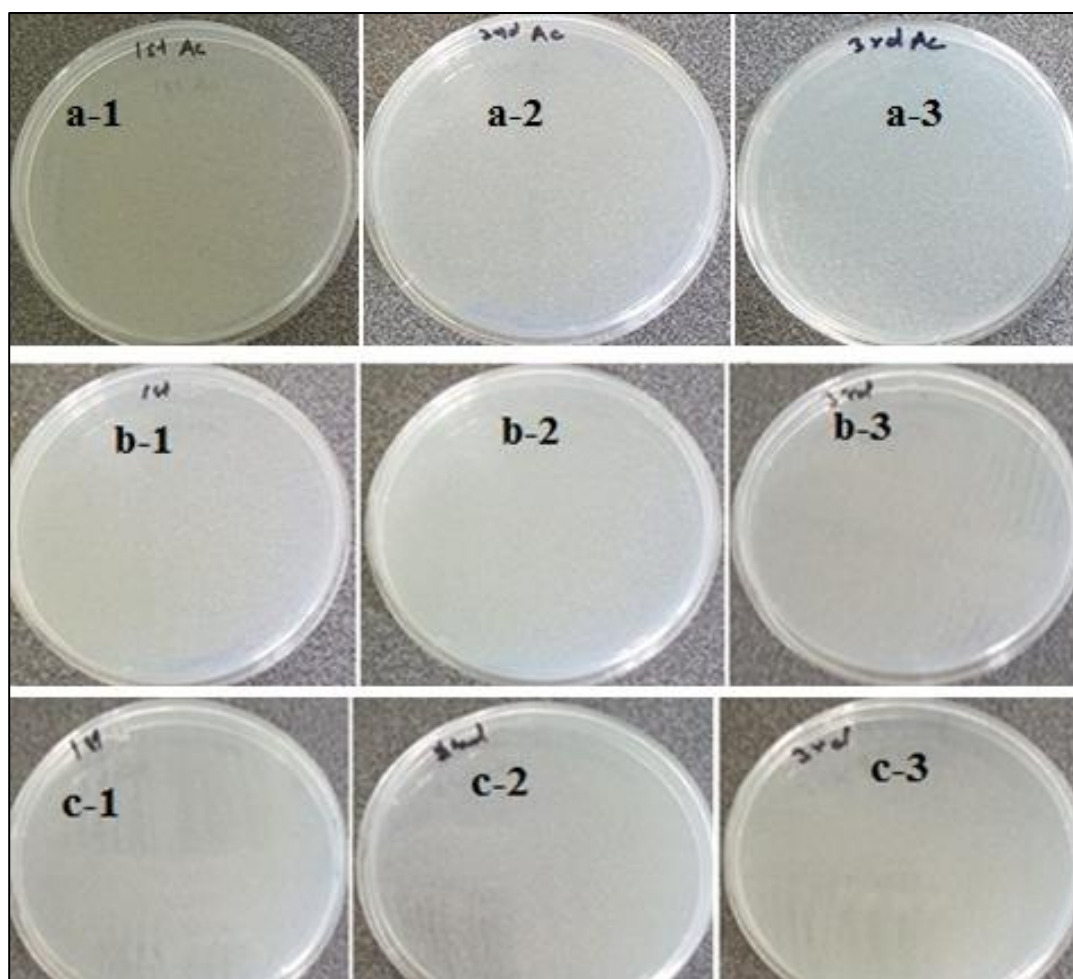


Figure 7-35 Harvesting of QM2-3 composite against *E. coli* in triplicate three times: (a-1,a-2 and a-3) are the first use of the QM2-3 composite against *E. coli*, (b-1,b-2 and b-3) are re-use of composite second time and (c-1,c-2 and c-3) are the re-use of the composite third time

Figure 7-35 shows the inhibition efficiency of (QM2-3) nanocomposite for the growth of the *E. coli* for three times re-use (see figure 7-36)

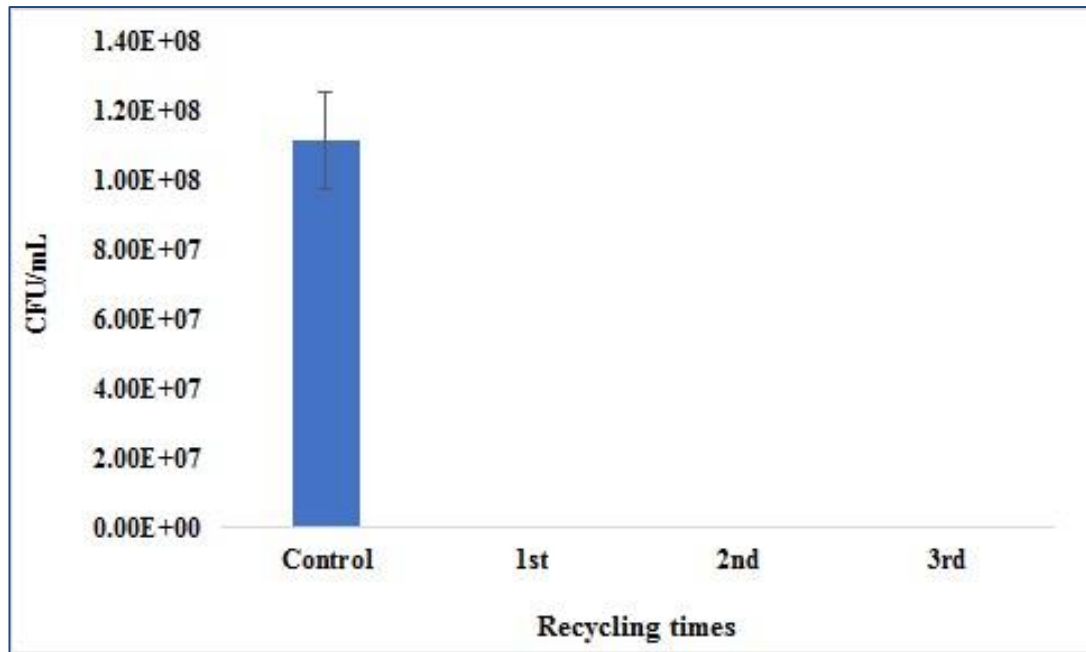


Figure 7-36 Harvesting of of QM2 -3 against *E. coli*

Figure 7-36 shows harvesting of QM2-3 composite against *E. coli*. Figure 7-36 shows that there was no growth of the bacteria when it was used 1st, 2nd and 3rd times and no any growth was seen on the plates (see figure 7-35).

Comparison of both developed nanocomposites

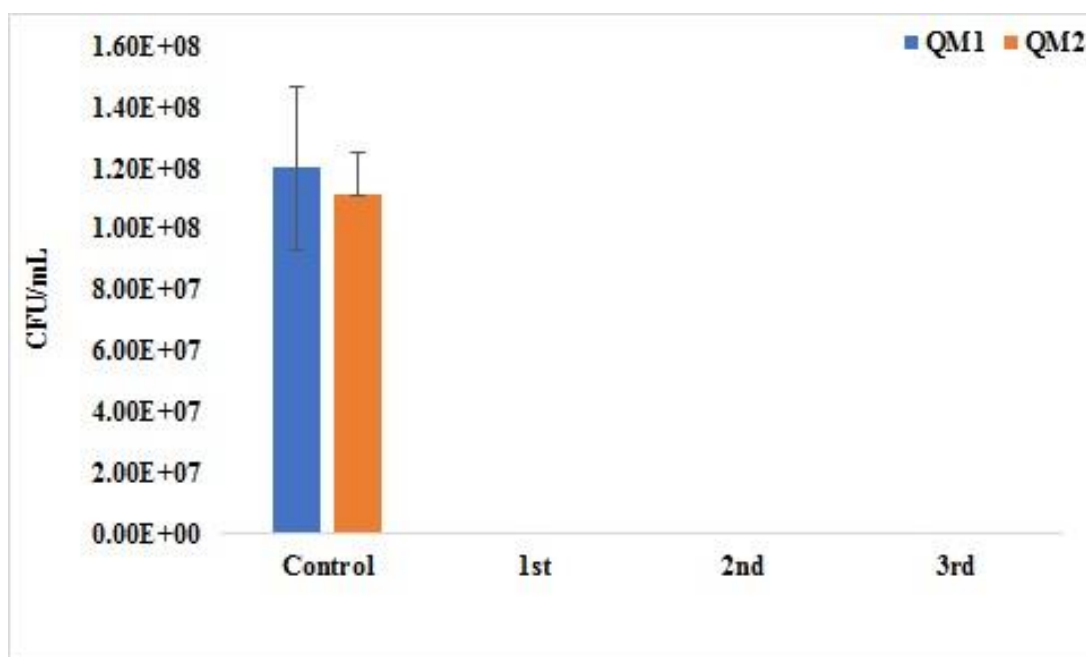


Figure 7-37 (a) shows the recycling of QM1-3 (blue) and QM 2-3 (orange) against *E. coli* respectively

Figure 7-37 show the antimicrobial efficiency of QM1-3 (blue bar) and QM2-3 (orange bar) against *E. coli* respectively. It was observed that both composites QM1-3 and QM2-3 harvested three times very effectively with completely inhibition of the *E. coli* (see figure 7-32 and 7-35).

7.6 Comparison of antimicrobial applications of all modified (QM1-3, QM2-3, QM3-3, QM4-3 and QM5-3) nanocomposites

The most efficient antimicrobial (QM1-3.QM2-3) nanocomposites were used as an antimicrobial composite against Gram-positive *S. aureus* and Gram-negative *E. coli* and have shown excellent antimicrobial efficiency. The MBC of different composites were different for both strains. The MBC of QM1-3 and QM2-3 was found 10 $\mu\text{g/mL}$ for the *S. aureus* and 50 $\mu\text{g/mL}$ for *E. coli*, while the MBC of QM3-3, QM4-3 and QM5-3 were higher ranging from 30 $\mu\text{g/mL}$ against *S. aureus* and 100 to 200 $\mu\text{g/mL}$ against *E. coli* respectively (see figure 7-38). From obtained results, it was concluded

that QM1-3 and QM2-3 nanocomposite materials were efficient antimicrobial composites compared to the QM3-3, QM4-3 and QM5-3-based nanocomposites. Overall, these composites were found very efficient antimicrobial materials and reusability owing to their magnetic properties. Furthermore, the time-kill assay for the both strains was calculated as 6 to 8 hours (see figure 7-39).

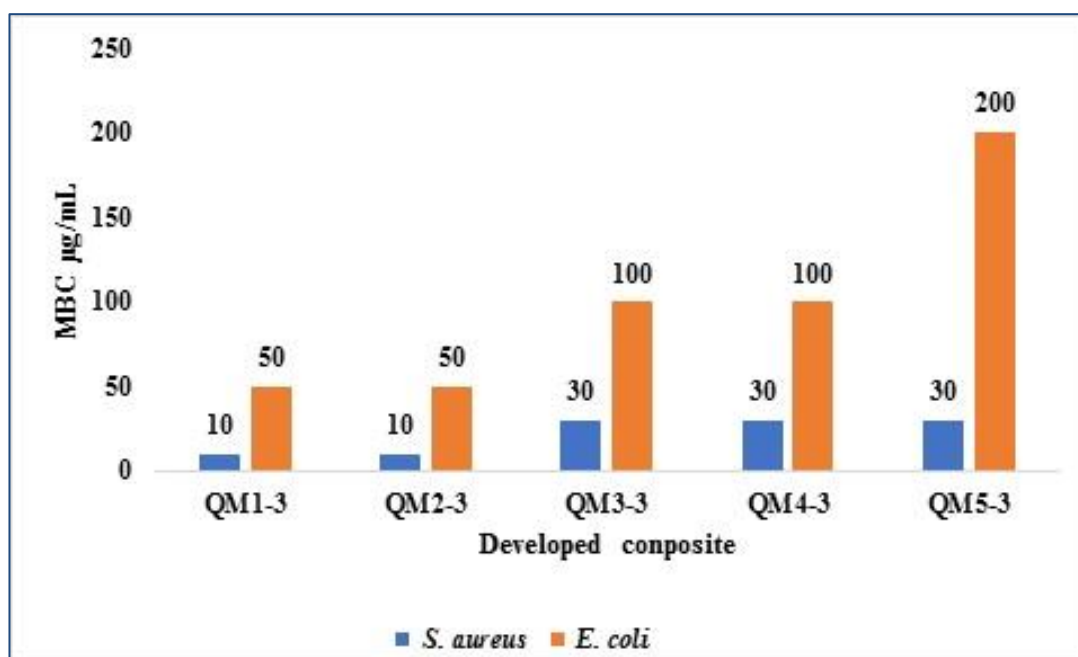


Figure 7-38 MBC of all developed composites. (\pm SD, No=3)

Figure 7-38 shows a concentration of antimicrobial efficiency of all the developed nanocomposites (QM1-1, QM2-3, QM3-3, QM4-3 and QM5-3) against Gram-positive *S. aureus* and Gram -negative *E. coli*. It was found that QM1-3 and QM2-3 modified with silver coating iron oxide nanoparticles are the most efficient against both strains and their MBC was found to be 10 and 50 μ g/mL respectively. Moreover, QM3-3, QM4-3, QM5-3 were less effective as compared to QM1-3 and QM2-3 and their MBC were found to be 30 to 200 μ g/mL against *S. aureus* and *E. coli* respectively. Furthermore, time-kill-assay for the QM1-3 and QM2-3 for the *S. aureus* and *E. coli* was 6 and 7 hours respectively while for all other composites, time-kill assay was found 8 hours (see figure 7-39).

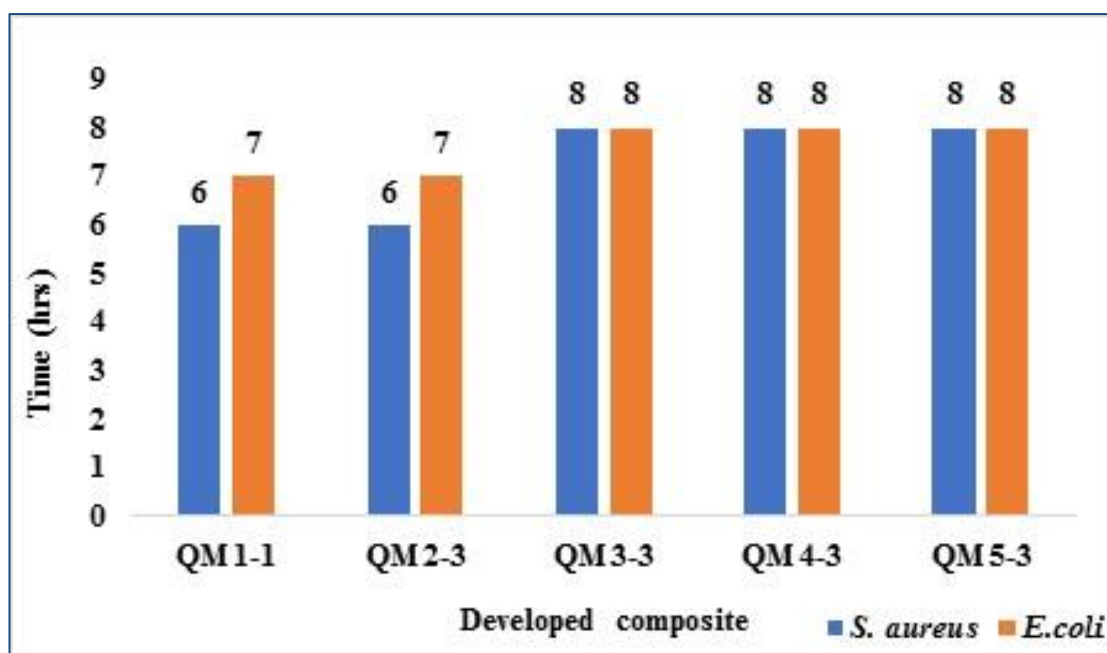


Figure 7-39 Time-kill assay of all developed composites. (\pm SD, No=3)

7.7 Conclusions

The nanocomposite materials prepared in this study showed efficient antibacterial activity against the Gram-negative and Gram-positive bacterial strains by using the DP and SP methods. These bacterial strains were selected as these are frequently found in water and are considered as the common indicators bacterium for a microbiological quality of drinking water. The obtained results for all the developed composites are very productive and promising. The determined MBC of all nanocomposites at various concentrations (10 μ g/mL to 200 μ g/mL), against waterborne bacterial strains are highly encouraging. Moreover, QM1-3 and QM2-3 samples are highly effective against utilised bacteria among all five composites. The developed composites have inhibited the growth of bacteria, including *E. coli*, *S. aureus*, *L. pneumophila*, *K. pneumoniae* and *P. aeruginosa* with low concentrations compared to reported results (Jung *et al.*, 2008, Espinosa-Cristobal *et al.*, 2009, Lee and Ji, 2008). The novel developed composites could be reused several times against these bacterial strains,

which saves natural resources and time as well it can help to maintain a clean environment due to magnetic separation.

Part B: Surface functionalisation of nanocomposites and detection of microorganisms

7.8 Introduction

Surface chemistry deals with the study of the surface of the materials, combination of different components with each other on the surface. In this chapter, the surface, chemistry of the synthesised nanocomposite would be discussed. For applications in detecting water borne bacteria i.e. *E. coli*, developed nanocomposites were surface functionalised with two different amino-silanes (APTS and APDS) in order to generate $-NH_2$ functional groups on the surface. The amine groups can be used for further modification with glutaraldehyde in order to create $-CHO$ functional groups. The $-CHO$ functional groups can be conjugated with bio-molecules with amine functional group (Rother *et al.*, 2011). For example, primers, proteins and enzymes, etc. contains amine and carboxyl functional groups. Hence, amino-modified oligonucleotides were used for grafting on the surface of glutaraldehyde modified nanocomposite. It has been reported (Bruce and Sen, 2005) that aminosilanes are organosilanes which contain amine groups as a functional group for bio-molecular attachment. For surface functionalisation, the following methods were used.

Initially, materials were surface functionalised by using APDS and APTS in 99.9% anhydrous methanol as a solvent by using modified method developed by Bruce (Bruce and Sen, 2005) , which was followed by determination of surface amine densities through colorimetric assay using 4-NBA (Moon *et al.*, 1997) described in section 2.4.2. Secondly, surface amine was converted into the aldehyde as described in section 2.4.3, by engaging glutaraldehyde for the oligonucleotide grafting on the developed nanocomposites. Same protocol was used as reported by (Bruce and Sen,

2005). Finally, chemical conjugation of DNA primers was carried out to the –CHO modified surface of the developed nanocomposites. Surface functionalised oligonucleotide-grafted nanocomposites described in section 2.4.4, were used for the applications for the detection of extracted *E. coli* DNA in water sample, and the method has been described in section 2.2.8.

7.9 Surface amine density

The density of amine was calculated from the solution by measuring the amount of 4-nitrobenzaldehyde and was compared with the initial concentration. Amount of 4-nitro benzaldehyde absorbed and remaining in the solution was measured based on standard curves. The standard curves of 4-nitrobenzaldehyde were prepared in coupling and hydrolysis solutions. The amine density values were calculated in coupling solution by calculating the amount of unbound 4-nitrobenzaldehyde in the solution by comparing with the standard curves and was followed by measuring the amount of 4-nitrobenzaldehyde bonded with the nanocomposite with coupling and hydrolysis solution by hydrolysis the imine bond see figure (7-40 and 7-41). Surface amine density was measured by the amine values calculated from the calorimetric assay. The surface amine density of APTS functionalised nanocomposites (QM1-3, QM2-3, QM3-3, QM4-3 and QM5-3-based) listed in Table 2.3 which are ranging from 316 to 544 nmol/mg of nanocomposites. Figure 7-40 (a and b) shows the surface amine densities of QM1-3, QM2-3, QM3-3, QM4-3 and QM5-3 nanocomposites.

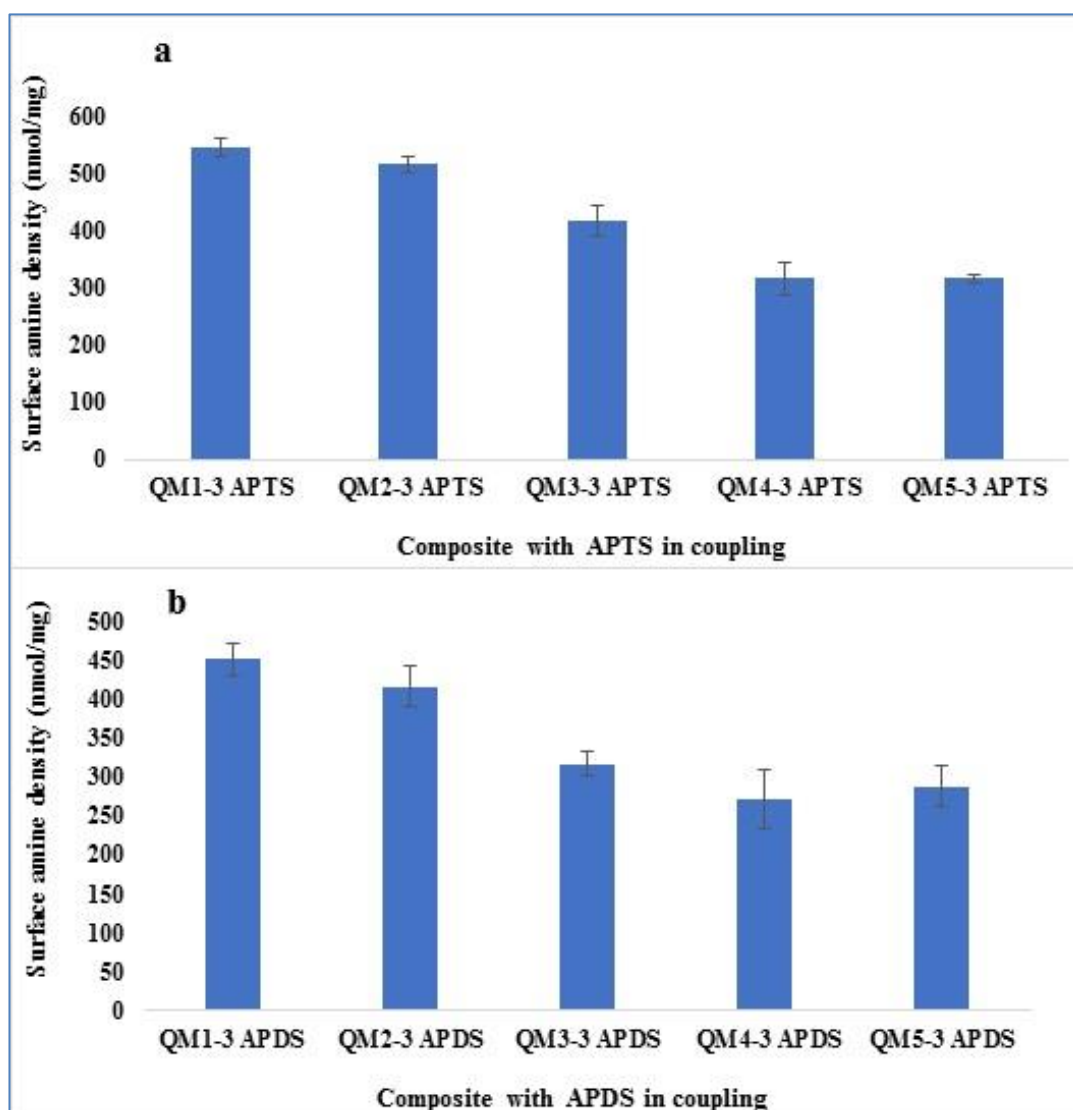


Figure 7-40 Surface amine densities of nanocomposite (a) APTS functionalised measuring in coupling solution (b) APDS functionalised measuring in coupling solution (\pm SD, No=3)

[QM1-3, QM2-3, QM3-3, QM4-3 and QM5-3 are symbolic representation of the (MWCNTs-modified with iron and silver nanoparticle, AC-modified with iron and silver nanoparticle, AE-modified with iron and silver nanoparticle, CPW-14-modified with iron and silver nanoparticle and CPW-80-modified with iron and silver nanoparticle respectively)]

Figure 7-40 (a) shows the amine densities of all five different nanocomposites using APTS are calculated to be 525, 509, 402, 331, 327 nmol/mg, and using APDS (see figure 7-40 b), they are lower in values (456, 441, 315, 242 and 252 nmol/mg) respectively, following the standard curves generated in coupling solution.

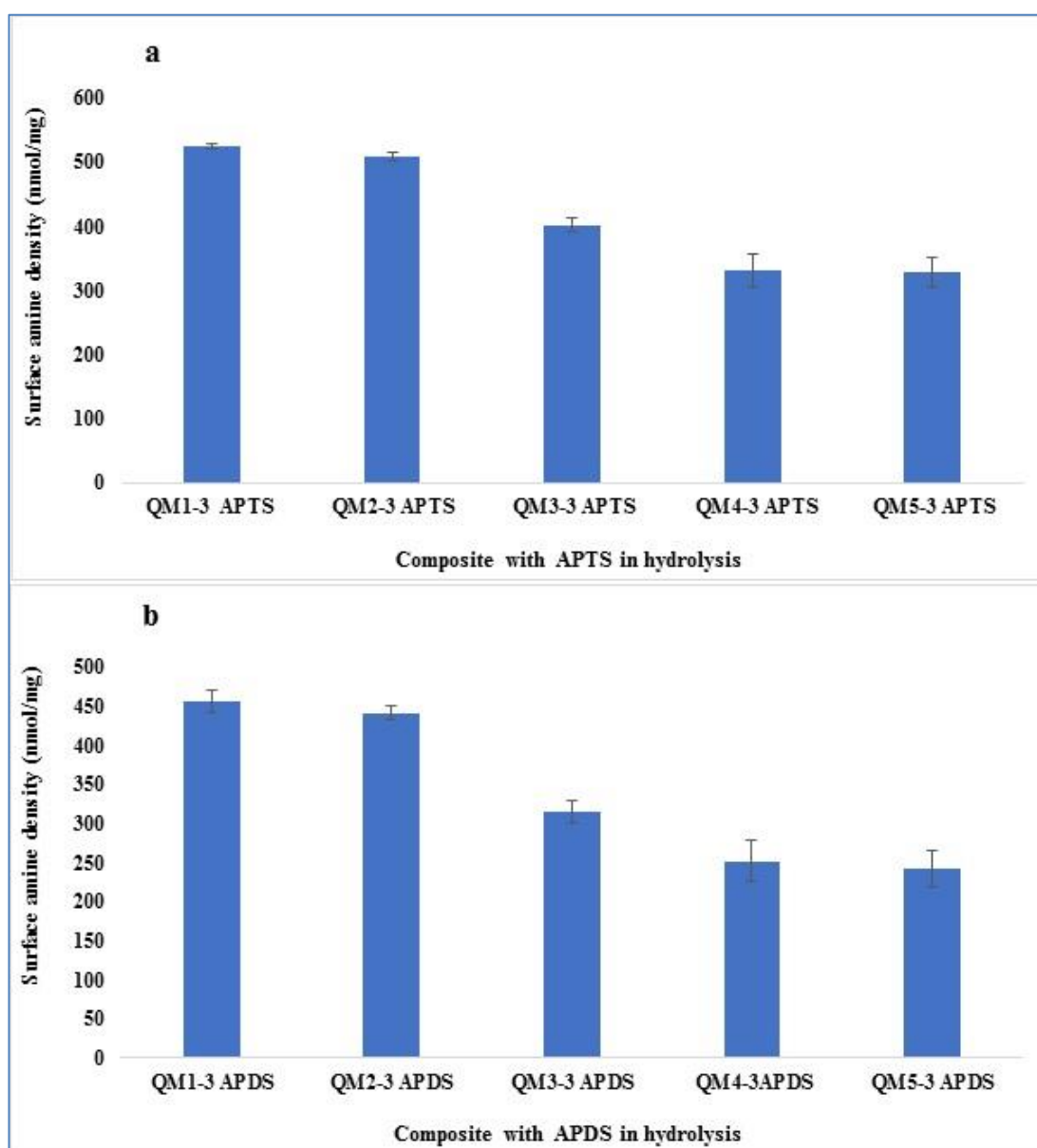


Figure 7-41 Surface amine density of five modified commercial nanomaterials (QM1-3 to QM5-3), (a) APTS functionalised measuring in hydrolysis solution, (b) APDS functionalised in hydrolysis solution. (\pm SD, No=3)

[[QM1-3, QM2-3, QM3-3, QM4-3 and QM5-3 are symbolic representation of the (MWCNTs-modified with iron and silver nanoparticle, AC-modified with iron and silver nanoparticle, DAE-modified with iron and silver nanoparticle, CPW-14-modified with iron and silver nanoparticle and CPW-80-modified with iron and silver nanoparticle respectively]

Figure 7-41 (a and b) both show that the developed nanocomposites listed in Table 2.3, APTS functionalised nanocomposites possesses higher amine densities than APDS surface functionalised materials. This may be due to different condensation

mechanism as the alkoxy groups can also react with each other, allowing extra dense amino silicate layer on the surface of the modified composites as reported earlier (Hodgson B.J., 2013). Similarly various authors have reported (Sen and Bruce, 2012, Del Campo *et al.*, 2005, Waterbeemd and Van, 2009), the higher surface amine density on the surface of the material was due to more controlled condensation of aminosilane onto the surface of nanoparticles. The obtained results for the surface functionalisation of nanocomposites with aminosilanes supports the earlier report (Sen and Bruce, 2012). Generally, the surface amine density is determined as average of several batches of samples prepared with similar method at every time. There was a decrease in surface amine densities from APTS to APDS, due to decrease in ethoxy groups, which supports the similar results as already been reported (Hodgson B.J., 2013, Moon *et al.*, 1996). The silanisation of all the developed nanocomposite with APTS and APDS are given in the Table 7-3.

Table 7-3. Summary for the silanisation of the modified materials in APTS and APDS. (\pm SD, No=3)

Silanisation of the materials with APTS and APDS in coupling solution(nmol/mg)										
	QM1-3		QM2-3		QM3-3		QM4-3		QM5-3	
	APTS	APDS								
Avg	544	450	515	416	416	317	316	272	316	288
Silanisation of the materials with APTS and APDS in hydrolysis solution(nmol/mg)										
	QM1-3		QM2-3		QM3-3		QM4-3		QM5-3	
	APTS	APDS								
Avg	525	456	509	441	402	315	331	242	327	252

7.10 Grafting of the oligonucleotides on the surface of the nanocomposite materials produced

Surface amine groups were converted into the aldehyde by using glutaraldehyde outlined in section 2.4.3, followed by the grafting of oligonucleotides of specific sequences of water borne *E. coli* described in section 2.4.5. The grafting of specific oligonucleotides on the surface of glutaraldehyde modified nanocomposites are shown in figure 7-42.

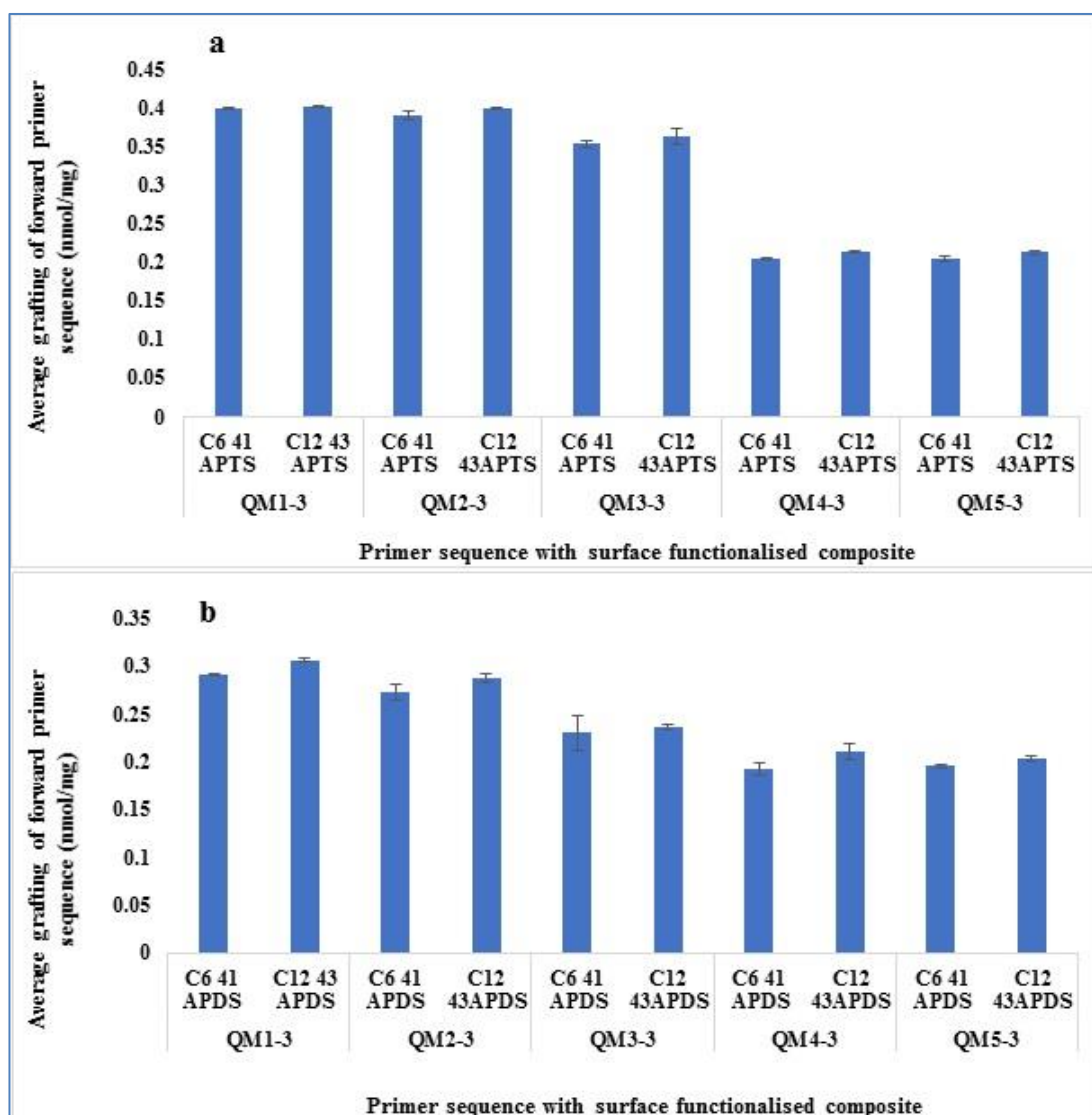


Figure 7-42 (a) Oligonucleotide-grafted composite of QM1-3, QM2-3, QM3-3, QM4-3 and QM5-3 on APTS surface functionalised materials, (b) Oligonucleotide-grafted composites of QM1-3, QM2-3, QM3-3, QM4-3 and QM5-3 on APDS surface functionalised material. (\pm SD, No=3)

[QM1-3, QM2-3, QM3-3, QM4-3 and QM5-3 are symbolic representation of the (MWCNTs-modified with iron and silver nanoparticle, AC-modified with iron and silver nanoparticle, DAE-modified with iron and silver nanoparticle, CPW-14--modified with iron and silver nanoparticle and CPW-80-modified with iron and silver nanoparticle respectively)].

Figure 7-42 (a) shows that the grafting of specific sequence of oligonucleotide (C₆- 41 and C₁₂- 43) on the APTS surface functionalised nanocomposites of QM1-3, QM2-3- and QM3-3 were calculated to be 0.399 to 0.402, 0.391 to 0.399 and 0.358 to 0.360 nmol/mg respectively. On the other hand, coupling for the rest of samples, QM4-3 and QM5-3 material with APTS were low ranging from 0.204 to 0.215 and 0.202 to 0.213 nmol/mg respectively, due to low amine density on the surface of composites.

Figure 7-42 (b) shows that the grafting of specific sequence of amine-modified oligonucleotide (C₆ -41 and C₁₂-43) on the APDS surface functionalised composites of QM1-3, QM2-3, QM3-3, QM4-3 and QM5-3- based nanocomposites were in range from 0.291 to 0.307, 0.273 to 0.287, 0.230 to 0.235, 0.192 to 0.211 and 0.195 to 0.204 nmol/mg respectively. Figure 7-46 (a and b) showed that the glutaraldehyde-modified surface-functionalised nanocomposites of QM1-3, QM2-3-and QM3-3-based materials were efficient and useful for the coupling of the specific primers of *E. coli* strains with relatively higher concentrations compared to QM4-3 and QM5-3-based developed materials. The grafting or immobilisation of the oligonucleotides onto the surface functionalised material depends on the amount of amine density, where glutaraldehyde treats with surface amine of materials and produces the aldehyde group which reacts with the amine-modified oligonucleotides as reported by Del Campo *et al.*, 2005, Moon *et al.*, 1997. In this study, two forward amine-modified sequences specific to *E. coli* with spacers have been used (C₆ -41 and C₁₂-43). Imines are produced when aldehyde reacts with amine group of amine-modified oligonucleotides (Del Campo *et al.*, 2005). Furthermore, NaBH₃CN was used for the reduction of imine

bond to produce more stable secondary amine groups (Del Campo *et al.*, 2005). Moreover, the grafting of the primers on the APTS surface functionalised materials were higher compared to APDS silanes, due to higher surface amine densities. Hence, the glutaraldehyde-modified surface-functionalised nanocomposites of QM1-3, QM2-3 and QM3-3 were used for the hybrid capture assay, as they have an excellent coupling efficiency at optimised conditions. The summary for the conjugation of oligonucleotides with all the developed oligonucleotide-grafted material is given in the table 7-4.

Table 7-4. Conjugation of oligonucleotides on APTS and APDS surface functionalised material. (\pm SD, No=3).

No:	Sample with Oligonucleotides modified with spacers	Conjugation of oligonucleotides on two silanes surface functionalised composites (nmol/mg)	
		APTS	APDS
1	QM1-3 – C ₆ -41	0.399	0.291
2	QM1-3 – C ₁₂ -43	0.402	0.307
3	QM2-3- C ₆ -41	0.391	0.273
4	QM2-3– C ₁₂ - 43	0.399	0.288
5	QM3-3 – C ₆ -41	0.354	0.230
6	QM3-3– C ₁₂ - 43	0.363	0.236
7	QM4-3 – C ₆ -41	0.204	0.192
8	QM4-3– C ₁₂ - 43	0.215	0.211
9	QM5-3 – C ₆ -41	0.206	0.195
10	QM5-3– C ₁₂ - 43	0.213	0.204

7.11 Hybrid capture assay of complementary oligonucleotide

The performance of hybrid capture of complementary sequence of grafted amine-modified oligonucleotides were experimented by developing a model system, the method is described in detail in section 2.4.6.

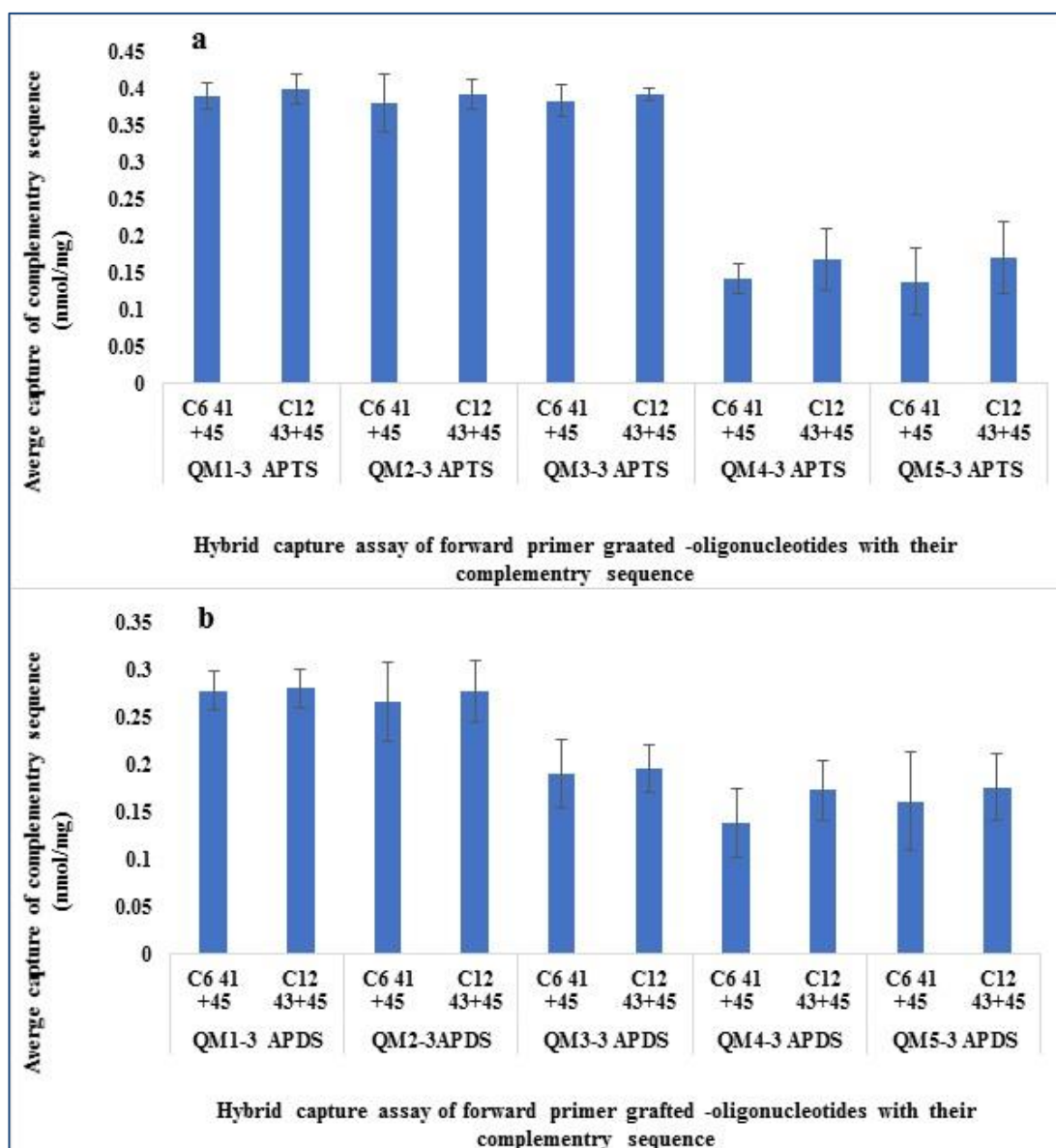


Figure 7-43 (a) Hybrid capture assay of complementary sequence of all APTS functionalised oligonucleotide-grafted nanocomposites (b) Hybrid capture assay with complementary sequence of all APDS functionalised oligonucleotide-grafted nanocomposites. (\pm SD, No=3)

[QM1-3, QM2-3, QM3-3, QM4-3 and QM5-3 are symbolic representation of the (MWCNTs-modified with iron and silver nanoparticle, AC-modified with iron and silver nanoparticle, DAE-modified with iron and silver nanoparticle, CPW-14-modified with iron and silver nanoparticle and CPW-80-modified with iron and silver nanoparticle respectively)].

Figure 7-43 (a and b) shows the capture efficiency of five different developed and surface functionalised nanocomposites with oligonucleotides various commercial materials. The assay was performed on the capturing of complementary oligonucleotides. Five different developed nanocomposites QM1-3, QM2-3, QM3-3, QM4-3 and QM5-3-based surface functionalised oligonucleotide-grafted nanocomposites were used. Figure 7-43 (a) shows the hybrid captured assay of specific sequence of oligonucleotides (C_6 - 41 and C_{12} - 43) with their complementary sequence (Comp-For-45) on QM1-3, QM2-3, QM3-3, QM4-3 and QM5-3 via APTS route. Results showed that the forward sequence with spacers (C_6 - 41 and C_{12} - 43) of oligonucleotide specific to the *E. coli* functionalised with APTS have high hybrid captured efficiency (0.170 to 0.389 nmol/mg) compared to the APDS functionalised composites (0.176 to 0.278) nmol/mg. APTS surface functionalised composite of QM1-3, QM2-3-and QM3-3-based composites gave high hybrid captured efficiency using (C_6 - 41 and C_{12} - 43) ranging from 0.389 to 0.400 (QM1-3), 0.381 to 0.392 (QM2-3) and 0.384 to 0.392 nmol/mg (QM3-3) respectively. On the other hand, hybrid capture assay for rest QM4-3 and QM5-3 were low (0.142 to 0.168) and (0.138 to 0.170 nmol/mg) respectively.

There was no significant difference in results, due to the presence of two different spacers (C_6 and C_{12}), in the amino-modified oligonucleotide sequences. Figure 7-43 (a) showed the hybrid capture assay for QM1-3, QM2-3, QM3-3, QM4-3 and QM5-3-based composites immobilised with forward amine-modified (C_6 - 41 and C_{12} - 43) oligonucleotides on APTS surface functionalised composites. Both QM1-3, QM2-3

and QM3-3-based material have shown high capture efficiency of the complementary sequences (Comp-For-45), while rest two materials QM4-3 and QM5-3-based composites have shown poor hybrid capture efficiency. Moreover, Figure 7-43 (b) shows the hybrid capture efficiency QM1-3, QM2-3, QM3-3, QM4-3 and QM5-3-based oligonucleotides (C₆- 41 and C₁₂- 43) grafted nanocomposites via APDS route were calculated to be 0.278 to 0.281, 0.267 to 0.278, 0.190 to 0.196, 0.139 to 0.173 and 0.161 to 0.176 nmol/mg respectively. They have shown poor capture efficiency for the complementary sequences due to the steric hindrance effect (Del Campo *et al.*, 2005). The summary for the capture of complementary sequences of all the APTS and APDS surface functionalised with forward amine –modified oligonucleotides (C₆ -41 and C₁₂ – 43) along with spacers are given in the Table.7-5.

Table 7-5. Summary for the capture efficiency of complementary sequences of all the surface functionalised materials. (\pm SD, No=3)

No:	Surface functionalised composite	Captured complementary oligonucleotides	Captured amount (nmol/mg)	
			APTS	APDS
1	QM1-3 C ₆ -41	Forward	0.389	0.278
2	QM1-3 C ₁₂ -43	Forward	0.400	0.281
QM2-3 based composite material				
1	QM2-3 C ₆ -41	Forward	0.381	0.267
2	AQM2-3 C ₁₂ -43	Forward	0.392	0.278
QM3-3 based composite material				
1	QM3-3 C ₆ -41	Forward	0.384	0.190
3	QM3-3 C ₁₂ -43	Forward	0.392	0.196
QM4-3 based composite				
1	QM4-3 C ₆ -41	Forward	0.142	0.139
3	QM4-3 C ₁₂ -43	Forward	0.169	0.173
QM5-3 based composite				
1	QM5-3 C ₆ -41	Forward	0.138	0.162
3	QM5-3 C ₁₂ -43	Forward	0.170	0.176

From the summary of the hybridisation results, it is concluded that the APTS surface functionalised materials are efficient for the hybrid capture assay due to more amine density compared to APDS functionalised nanocomposites. Furthermore, QM1-3-

based nanocomposite is highly efficient for the hybridisations of complementary oligonucleotides, this commercial material was originally purchased with hydroxyl (OH) functional group, where silanes reacted with it, produced more surface amine density, which promoted the oligonucleotide grafting. Moreover, the QM2-3 and QM3-3-based composites were also efficient for the complementary oligonucleotides hybridisations, due to same reason given above, while the two-other surface functionalised oligonucleotide-grafted composites of QM4-3 and QM5-3-based were found weak for the hybridisation of complementary oligonucleotides due to less amine density.

7.12 Dehybridisation of complementary oligonucleotide

The captured complementary oligonucleotide of specific strain was separated from the surface of grafted oligonucleotides of the composite material at 95°C. The dehybridisation of the captured oligonucleotides of all developed composites are shown in the following graphs.

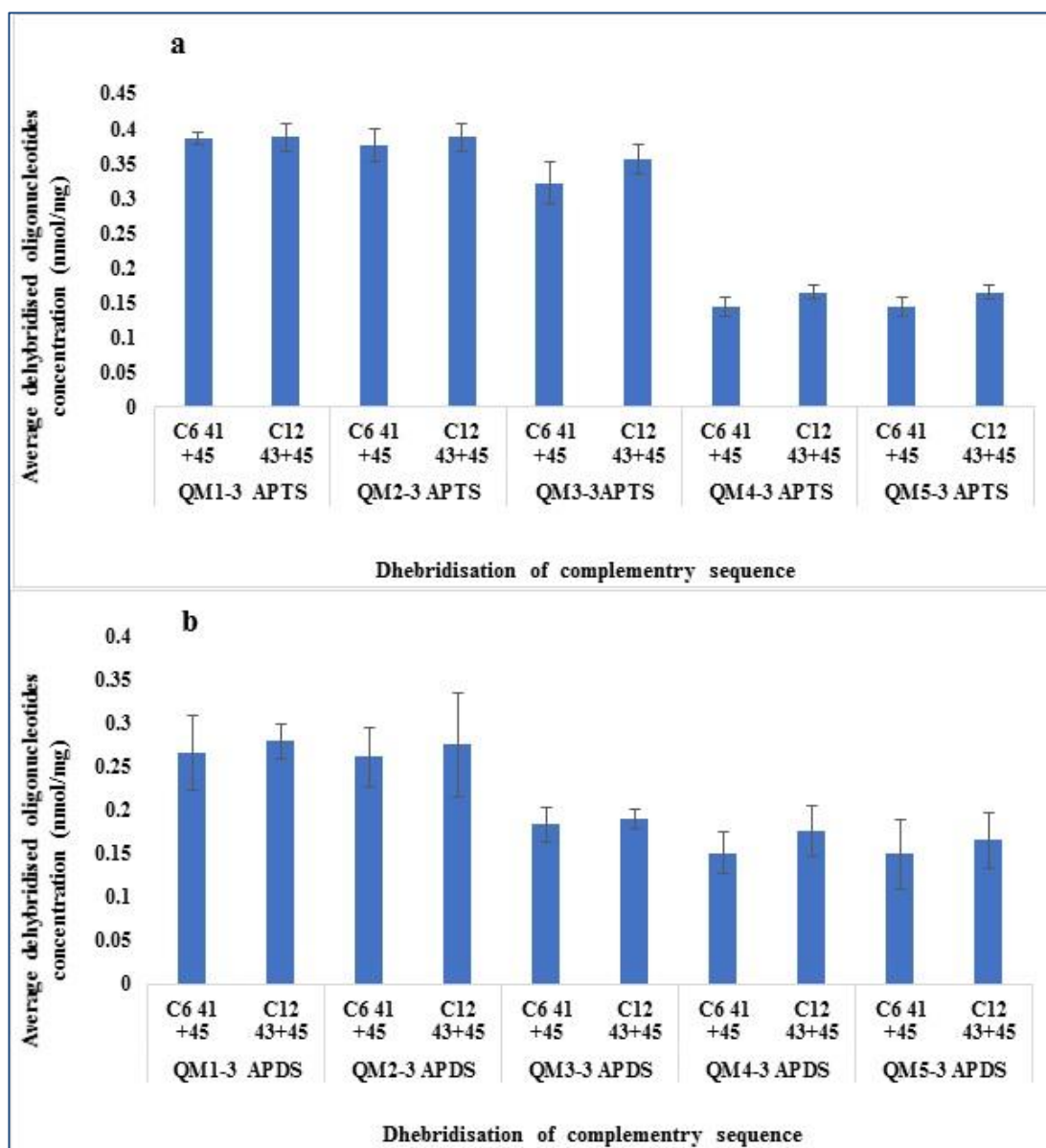


Figure 7-44 Dehybridisations of captured *E. coli* specific oligonucleotides via APTS functionalisation route (b) Dehybridisations of captured *E. coli* specific oligonucleotides via APDS functionalisation route. (\pm SD, No=3)

[QM1-3, QM2-3, QM3-3, QM4-3 and QM5-3 are symbolic representation of the (MWCNTs-modified with iron and silver nanoparticle, AC-modified with iron and silver nanoparticle, DAE-modified with iron and silver nanoparticle, CPW-14-modified with iron and silver nanoparticle and CPW-80-modified with iron and silver nanoparticle respectively)

Figure 7-44 (a and b) shows the dehybridisation efficiency of specific complementary sequence of *E. coli* of five different developed composites of QM1-3, QM2-3, QM3-3, QM4-3 and QM5-3-based hybridised nanocomposites with their complementary sequence (Comp-Forward-45).

Figure 7-44 (a) shows dehybridisation efficiency of complementary sequence (Comp-Forward-45) from the surface of QM1-3, QM2-3, QM3-3, QM4-3 and QM5-3-based nanocomposites prepared *via* APTS route. Figure 7-44 (b) shows dehybridisation efficiency of complementary sequence (Comp-Forward-45) from QM1-3, QM2-3, QM3-3, QM4-3 and QM5-3-based nanocomposites *via* APDS route.

Results showed that the dehybridisation efficiency of nanocomposites prepared *via* APTS route have high dehybridisation as compared to the APDS route which are ranging from 0.170 to 0.389 nmol/mg and 0.176 to 0.278nmol/mg respectively.

Table 7-6. Summary for the dehybridisation of complementary sequences of all the surface functionalised materials. (\pm SD, No=3)

No:	Oligonucleotide-grafted hybridised composite	Dehybridised complementary oligonucleotides	Dehybridised amount (nmol/mg)	
			APTS	APDS
1	QM1-3 C ₆ -41	Forward-45	0.385	0.266
2	QM1-3 C ₁₂ -43	Forward-45	0.388	0.280
QM2-3 based composite				
1	QM2-3 C ₆ -41	Forward-45	0.376	0.262
2	QM2-3 C ₁₂ -43	Forward-45	0.388	0.276
QM3-3 based composite				
1	QM3-3 C ₆ -41	Forward-45	0.322	0.184
3	QM3-3 C ₁₂ -43	Forward-45	0.356	0.191
QM4-3 based composite				
1	QM4-3 C ₆ -41	Forward-45	0.151	0.143
3	QM4-3 C ₁₂ -43	Forward-45	0.176	0.164
QM5-3based composite				
1	QM5-3 C ₆ -41	Forward-45	0.150	0.144
3	QM5-3 C ₁₂ -43	Forward-45	0.166	0.163

7.13 Optimisation of the extracted DNA

The optimisation of the *E. coli* DNA was carried out with the specific sequenced primers, which are given in Table 2-2. The optimisation conditions were used: initial denaturation at 95 °C for 3 minutes followed by denaturation for 30 seconds. Annealing stage of 35 cycles was carried out at 58 °C for 30 seconds, with extension at 72 °C for 30 seconds and final extension at 72 °C for 5 minutes.

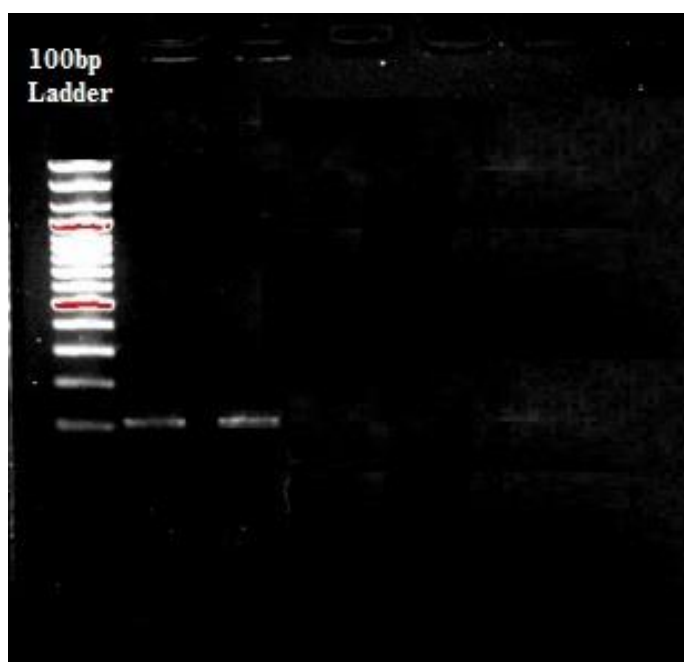


Figure 7-45 Optimisation of extracted *E. coli* DNA

Figure 7-45 shows the bands of the specific *E. coli* DNA which are expected for the *E. coli* strains of 97 bp amplicon size.

7.13.1 Determining the capturing efficiency and sensitivity for the detection of *E. coli* DNA from water sample.

The isolation of the *E. coli* DNA was carried out from water containing *E. coli* DNA using PCR with same parameters described in section 2.4.7. A slight modification was made to the PCR components using 10 μ L dehybridised DNA from the oligonucleotide-grafted sample. 1 mg of oligonucleotide-grafted composite was added to 200 μ L of *E. coli* K12 extracted DNA. This was heated at 95 °C for 3 minutes for initial denaturation of the DNA and then followed denaturation at 95 °C for 30 seconds. For hybridisation and annealing of DNA, with grafted oligonucleotides on the surface of the material, the temperature was reduced at 58 °C for 30 seconds for 35 cycles and was taken out. The sample was washed with deionised and sterilised water three times to remove the unbonded DNA in the suspension. Furthermore, 50 μ L deionised and sterilised water was added and then heated at 95 °C for 3 minutes for the dehybridisation or removal of captured DNA from the grafted oligonucleotides on the surface of developed nanocomposite. This was followed by 95 °C incubation for 30 seconds. The sample was immediately taken out from the PCR machine after heating, and the dehybridised or separated DNA were recovered by a magnetic iron stand. A 10 μ L of isolated DNA from the recovered dehybridised DNA sample was added to the PCR sample for the DNA detection.

7.13.2 PCR results of grafted and modified material with oligonucleotides

Water containing *E. coli* DNA sample was extracted by the inoculation of the fresh culture of *E. coli* K12 followed by the extraction of DNA of *E. coli* compatible to the primer sequences of the cells (see table 2-2). PCR and sample preparation were carried out as described in section 2.4.7.

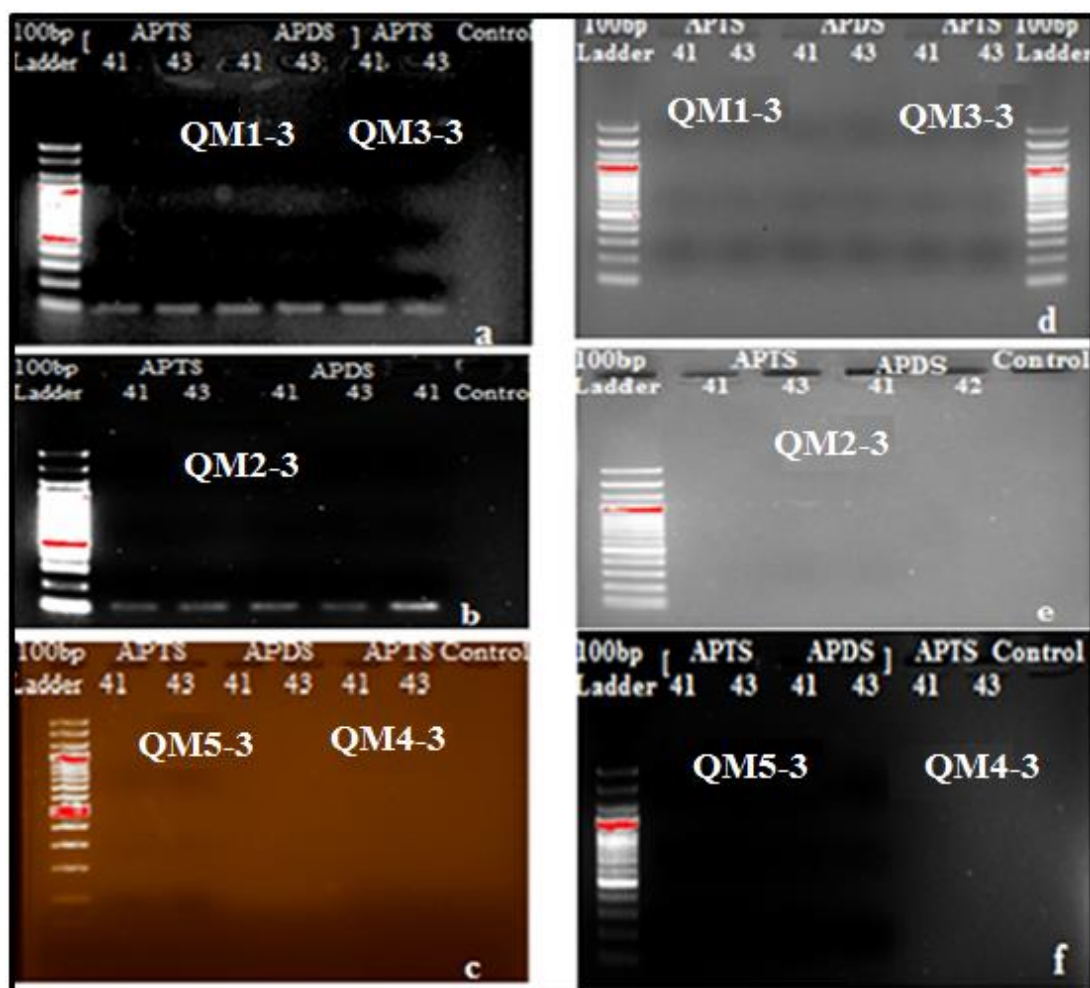


Figure 7-46 PCR results: of samples (a) Oligonucleotide grafted QM1-3 with APTS and APDS along with oligonucleotide QM3-3 with APTS and control, (b) Oligonucleotide grafted QM2-3 with APTS and APDS along with control. (c) Oligonucleotide grafted QM4-3 QM5-3 with APTS and APDS along with control, (d) QM1-3 and QM3-3 with APTS, APDS (without grafted oligonucleotides), ladders 100pb, (e) QM2-3 with APTS, APDS (without grafted oligonucleotides), along with control and (f) QM5-3 and QM4-3 with APTS and APDS (without grafted oligonucleotides), with control

Figure 7-46 (a) shows the oligonucleotide grafted QM1-3 composite with APTS and APDS silanes along with QM3-3 oligonucleotide grafted with above named silanes and control sample without added DNA. The bands of the 97 amplicons of the *E. coli* were determined by the PCR and gel electrophoresis using 100 bp ladder. No band was displayed for the control samples in the experiment. This result showed that the grafted oligonucleotides on the QM1-3 and QM3-3 were capable of capturing the

DNA of specific bacteria of an amplicon size of 97 bp using the optimised parameters. Here, the important factor for the annealing of the sequence was the grafting of the specific sequence of the oligonucleotides on the surface of the composites. Less amine density on the composite causes the negligible grafting of the primers, because amino groups are converted into the aldehyde group by treating with the glutaraldehyde. That group reacts with the amino group of the primers for the grafting of the oligonucleotides by the elimination of the water molecule.

Figure 7-46 (b) shows the oligonucleotide grafted QM2-3 composite with APTS and APDS silanes with both forward (C₆-41 and C₁₂-43 spacers) sequences along with control sample without DNA. The annealing of the *E. coli* strain with the 97 bp amplicon size can be seen clearly in Figure 7-48 (b), while the band for control is absent. This is the evidence for the capturing of DNA by oligonucleotide-grafted surface functionalised composite.

Figure 7-46 (c) shows the oligonucleotide grafted QM4-3 and QM5-3 composite with APTS and APDS silanes with both forward (C₆-41 and C₁₂-43 spacers) sequences along with control sample without added DNA. Here, annealing is not seen due to the poor grafting of the oligonucleotides on the surface of the developed materials. The poor grafting is the result of the less and negligible surface amine density, which did not produce the aldehyde group by treating with the glutaraldehyde.

Similarly, same PCR process and optimised conditions were applied to all five-developed surface functionalised composites without grafting of the oligonucleotides, which are shown in Figure 7-46 (d, e, and f). It was found that due to the absence of the grafted oligonucleotide on the surface of the functionalised materials, the hybridisation of the DNA in water was zero hence bands were not seen. The obtained

results could be summarised that oligonucleotide surface functionalised composites of QM1-3, QM2-3 and QM3-3 captured the DNA of specific strains of the bacteria which were compatible to the primer sequences. The formation of the bands can be seen clearly in Figure 7-46, (a and b). These results are same as were taken during the hybridization and dehybridisation process. The grafted specific primers on the surface of developed nanocomposites have captured the *E. coli* DNA as above-named oligonucleotides have shown high amine density and remarkable hybrid and dehybrid assay. Conversely, the developed material based on QM4-3 and QM5-3 have shown poor results for the amine density.

7.14 Comparison properties of all modified (QM1-3, QM2-3, QM3-3, QM4-3 and QM5-3) nanocomposites for hybrid capture efficiency

7.14.1 Surface amine density

It was measured that QM1-3, QM2-3 and QM3-3 based composites have higher surface amine density as compared to QM4-3 and QM5-3 in both silanes (APDS and APTS) (see figure 7-51). The amine density of the nanocomposite materials treated with APTS was more due to the formation of ordered monolayer around the nanocomposite-coated surface, due to low steric hindrances than APDS, which has two ethoxy and one capped methyl group.

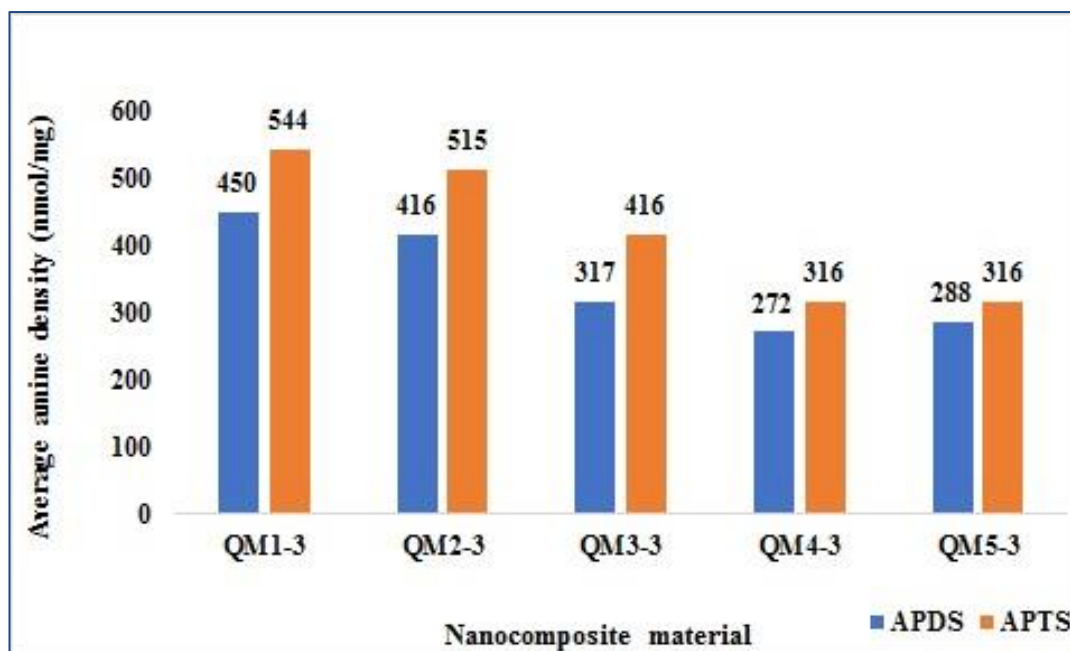


Figure 7-47 Surface amine density of five commercial nanomaterials (QM1-3 to QM5-3), (a) APTS and APDS functionalised measuring in hydrolysis solution. (\pm SD, No=3)

Figure 7-47 shows the surface amine density of modified nanocomposites. A graph shows that APTS surface functionalised materials possess higher amine densities than APDS surface functionalised materials. This may be due to different condensation mechanisms as the alkoxy groups can also react with each other, allowing an extra dense amino silicate layer on the surface of the modified composites.

7.14.2 Grafting of oligonucleotides

It was found that the conjugation was high with APTS surface functionalised materials ranging from 0.213 to 0.399 nmol/mg while the grafting of oligonucleotides was much lower in the case of materials surface functionalised with APDS ranging from 0.204 to 0.291 nmol/mg. Moreover, the QM1-3, QM2-3 and QM3-3 based surface functionalised nanocomposites have shown higher conjugation of specific primers while QM4-3 and QM5-3 based composites have shown lower conjugation due to less

amine groups density with APTS as well as APDS (see figure 7-48).

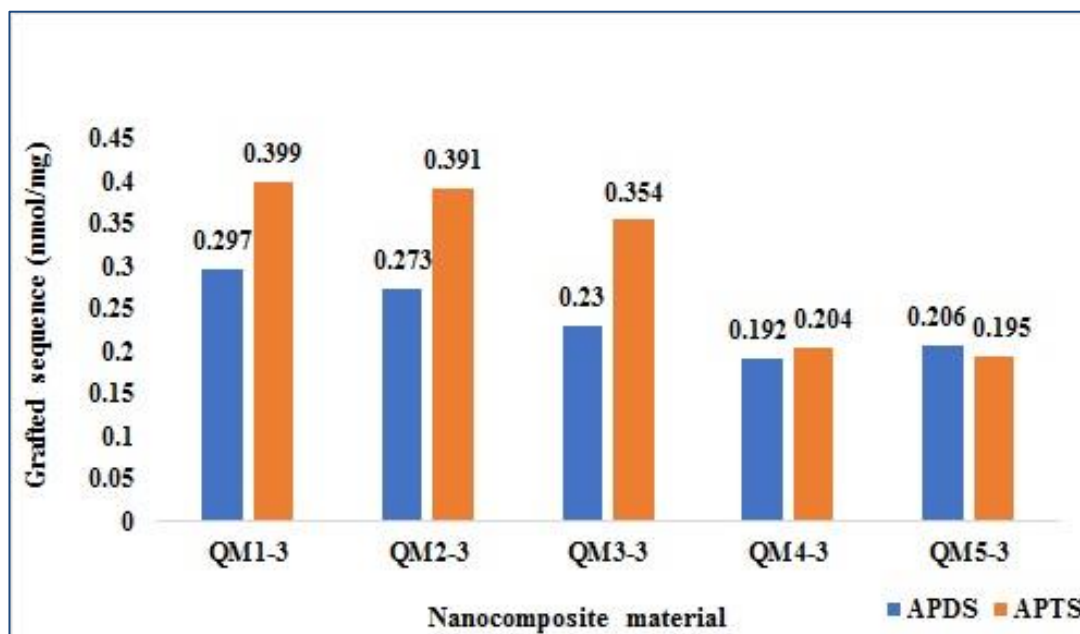


Figure 7-48 Oligonucleotide-grafted composite of QM1-3, QM2-3, QM3-3, QM4-3 and QM5-3 on APTS and APDS. . (\pm SD, No=3)

7.14.3 Hybridisation

The complementary sequences were hybridised with APTS surface functionalised oligonucleotide grafted QM1-3, QM2-3-and QM3-3-based developed nanocomposite materials (coupled *via* glutaraldehyde modification) was high ranging from 0.389 to 0.400, 0.381 to 0.392 nmol/mg respectively, due to the high surface amine density. While, grafting of QM4-3 and QM5-3 APTS were low for forward sequences modified with carbon spacer (C_6 and C_{12}) ranging from 0.142 to 0.167 nmol/mg respectively, due to the low surface amine density. Furthermore, the hybrid captured assay for the APDS surface functionalised oligonucleotides-grafted nanocomposites of QM1-3, QM2-3, QM3-3, QM4-3 and QM5-3-based were less as compared to the APTS surface

functionalised composites (see figure 7-49).

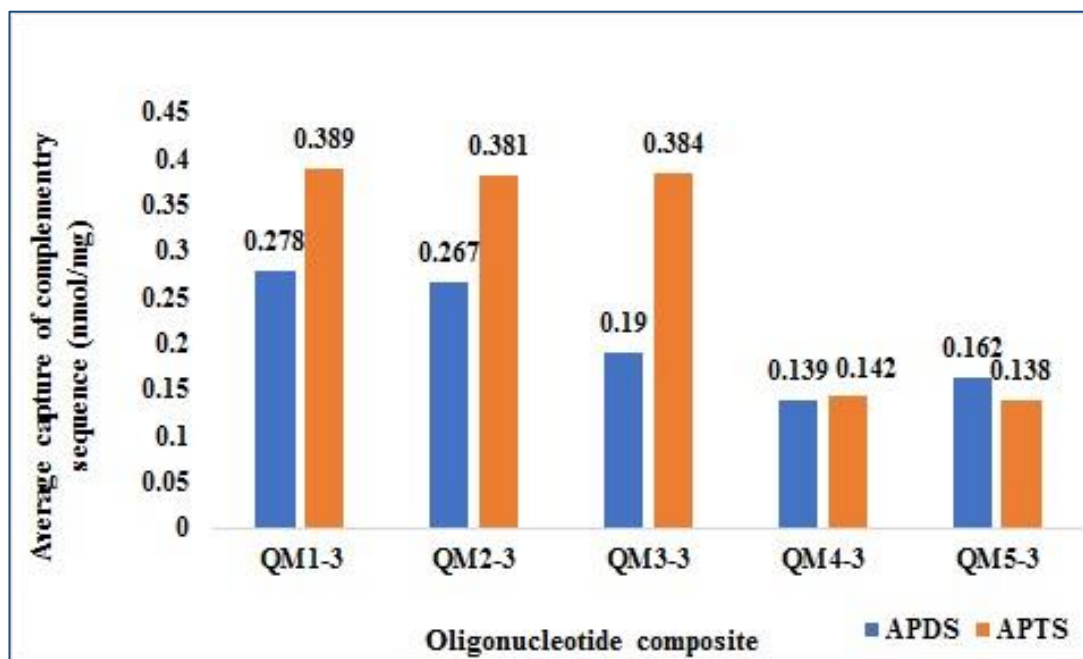


Figure 7-49 Hybrid capture assay of complementary sequence of all APTS and APDS functionalised oligonucleotide-grafted composites. (\pm SD, No=3).

7.14.4 Dehybridisation

For dehybridisations of the captured complementary sequence for QM1-3, QM2-3, QM3-3, were found to be high, while for QM4-3 and QM5-3-based composites were poor due to less amine density. It was found that QM1-3, QM2-3, QM3-3 oligonucleotide grafted nanocomposites were highly effective for the specific hybrid capture assay (testing *via* dehybridisation) from the solution (see figure 7-50).

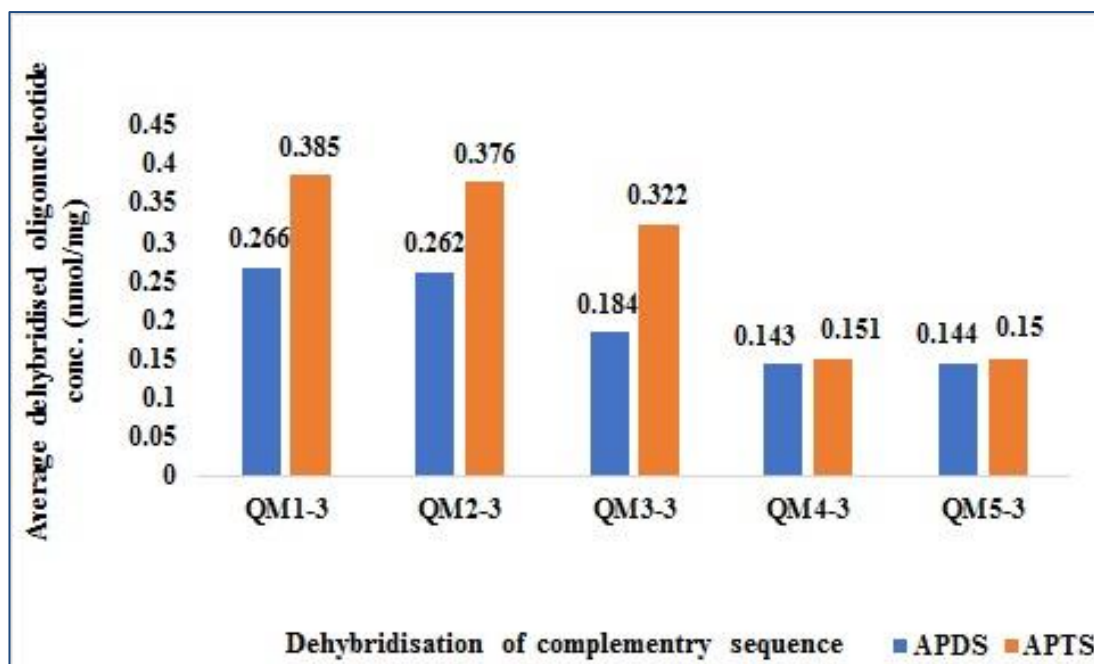


Figure 7-50 Dehybridisations of captured *E. coli* specific oligonucleotides of all APTS and APDS functionalised material. (\pm SD, No=3).

The oligonucleotide-grafted nanocomposites of QM1-3 QM2-3 and QM3-3 were successful at detecting EC in water samples, while QM4-3 and QM5-3 with oligonucleotide-grafted nanocomposites failed to detect *E. coli* DNA in water samples using PCR techniques.

7.15 Conclusions

It was observed that the surface amine density of nanocomposite materials with APTS was higher compared to those materials, which were treated with APDS. Furthermore, due to the formation of ordered monolayer of surface amine around the nanocomposite-coated surface and the presence of more ethoxy groups with low steric hindrances than APDS. Furthermore, the grafting efficiency of oligonucleotide-grafted sequences of primer was high in APTS surface functionalised materials while, the grafting of oligonucleotides was much lower in the case of materials functionalised with APDS. Moreover, the QM1-3, QM2-3-and QM3-3-based surface functionalised

nanocomposites have shown higher conjugation of specific primers while QM4-3 and QM5-3-based nanocomposites have shown lower conjugation due to less surface amine densities. The captured complementary sequence hybridised and dehybridised with APTS surface functionalised was high due to the high surface amine densities, while the hybridisation and dehybridisation of APDS surface functionalised was low due to low surface amine density. 5'-NH₂ EC-specific forward primers amine modified with spacers (C₆-41 and C₁₂-43 spacers) on QM1-3, QM2-3 and QM3-3 were successful to detect *E. coli* in water sample.

CHAPTER EIGHT

8 Conclusions and future work

8.1 Conclusions

Water pollution is a major concern worldwide. Bacteria, viruses and fungi present in drinking water causes various diseases as a result of poor hygienic conditions in developing countries. Similarly, presence of microorganisms in drinking water are a threat to public health. Numerous disinfectants and biocides are used for inhibiting the growth of pathogenic microbial contamination, producing carcinogenic by-products, which are dangerous to human health.

This work involved the synthesis, characterisation and application of novel multifunctional nanocomposites for antimicrobial treatment of contaminated water and DNA detection applications of water-borne bacteria. In this project, nanocomposite materials have been developed by using five-different commercial host matrices (see section 2.1), with the incorporation of the silver and magnetite nanoparticles to modify their properties into the antimicrobial composites. In the first step, magnetite nanocomposites were synthesised by chemical co-precipitation of Iron (II) chloride tetrahydrate and Iron (III) chloride hexahydrate ($\text{FeCl}_2 \cdot 4\text{H}_2\text{O}$ and $\text{FeCl}_3 \cdot 6\text{H}_2\text{O}$) sources in the presence of ammonium hydroxide, while silver nanoparticles were prepared from silver nitrate as a source.

The nanocomposites containing commercial materials embedded with iron oxide and silver nanoparticles were prepared by one-pot synthesis method. Iron oxide nanoparticles were incorporated into the commercial material for the magnetic properties or recycling purposes, and silver nanoparticles were included for the antimicrobial applications. Furthermore, synthesised nanocomposites were characterised by several techniques for their physical and chemical properties. The elemental determination, structure, size and properties of the synthesised

nanocomposite were determined. X-ray fluorescence (XRF) showed the strong bands of iron and silver particles at 6.48 and 22.68 KeV respectively, EDAX, measurements confirmed the incorporation of the iron and silver particles in the series of modified composites at 3.0 KeV, and 6.3 KeV respectively.

FT-IR spectroscopy has confirmed the iron oxide bond vibrations in the series of developed nanocomposites at 460 to 570 cm^{-1} . TEM images showed the internal structure, nano-size of the incorporated silver nanoparticles with average diameter ranging from 10 - 13 nm in all modified with silver nanocomposite and iron oxide nanoparticles embedded into the matrix with an average diameter of 50 nm. SEM determined the surface morphology of the modified and unmodified material. XRD spectrum of the synthesised nanocomposites have revealed the confirmation of the incorporated particles at 38.9, 44.4, 64.6, and 78.3 in the 2θ region, corresponding to (1 1 1), (2 0 0), (2 2 0), and (3 1 1) planes of iron oxide nanoparticles. Surface area measurement (BET) depicted the average pore diameter ranging from 28 to 79 Å, micropore volume ranges from 0.01 to 0.16 cm^3/g , and surface area ranging from 5.0 to 560 m^2/g .

Developed nanocomposites were used as an antimicrobial composite against Gram-positive *S. aureus* and Gram-negative *E. coli* K12 and have shown excellent antimicrobial efficiency. Moreover, the modified materials were also tested against several other Gram-negative water-borne bacteria including *L. pneumophila*, *K. pneumoniae* and *P. aeruginosa* and encouraging results were found. The MBC of different composites were different for both strains. The MBC of QM1-3 and QM2-3 was found 10 $\mu\text{g}/\text{mL}$ for the *S. aureus* and 50 $\mu\text{g}/\text{mL}$ for *E. coli* K12, while the MBC of QM3-3, QM4-3 and QM5-3 were higher ranging from 30 $\mu\text{g}/\text{mL}$ against *S. aureus*

and 100 to 200 $\mu\text{g/mL}$ against *E. coli* respectively. Furthermore, the antimicrobial efficiency against *L. pneumophila*, *K. pneumoniae*, *P. aeruginosa* and *E. coli* (DH5- α) were also encouraging. The MBC of QM1-3, against *L. pneumophila*, *K. pneumoniae* and *E. coli* (DH5- α) was 20, 20 and 12 $\mu\text{g/mL}$ respectively. MBC of QM2-3 against *L. pneumophila*, *P. aeruginosa* and *E. coli* (DH5- α) were 20, 20 and 12 $\mu\text{g/mL}$ respectively, the MBC of QM3-3 against *L. pneumophila*, and *E. coli* (DH5- α) was noticed from 50 and 12 $\mu\text{g/mL}$ respectively. Furthermore, the MBC of QM4-3 against *E. coli* (DH5- α) was found to be 20 $\mu\text{g/mL}$. From obtained results, it was concluded that QM1-3 and QM2-3 nanocomposite materials were efficient antimicrobial composites compared to the QM3-3, QM4-3 and QM5-3-based nanocomposites. Results have shown that the novel developed nanomaterials are more efficient on Gram-positive compared to the Gram-negative bacterial cells. Overall, these composites were found very efficient antimicrobial materials and reusable owing to their magnetic properties. Furthermore, the time kill assay for the bacteria was calculated from 6 to 8 hours and microbes failed to grow back after seven days of incubation following treatment under laboratory conditions.

Following the synthesis of the multifunctional nanocomposites, it was surface-functionalised with two different amino silanes (APTS and APDS) by using 99.9% anhydrous methanol as a non-ionic surfactant. QM1-3, QM2-3 and QM3-3-based nanocomposites gave higher surface densities as compared to QM4-3 and QM5-3-based nanocomposites. It was observed that the surface amine density of nanocomposites functionalised with APTS was higher ranging from 316 to 544 nmol/mg as compared to those nanomaterials which were treated with APDS ranging from 288 to 450 nmol/mg. The higher amine density of the nanocomposite material, treated with APTS was more due to the formation of ordered monolayer around the

nanocomposite-coated surface due to low steric hindrances than APDS, which has two ethoxy and one capped methyl group. Moreover, surface amine groups of surface-functionalised nanocomposites were converted into aldehyde groups by using glutaraldehyde as a cross-linking reagent, which was followed by the grafting of oligonucleotides for the DNA detection of compatible strains of *E. coli* K12 with the used primers.

Amine-modified oligonucleotide sequences specific to *E. coli* were conjugated onto glutaraldehyde-modified nanocomposite material. *E. coli* specific forward (C₆-41 and C₁₂-43) oligonucleotides modified with C₆ and C₁₂ spacers were used; conjugation was high with APTS surface functionalised materials ranging from 0.213 to 0.399 nmol/mg while, the grafting of oligonucleotides was much lower (0.204 to 0.291 nmol/mg) in the case of materials surface functionalised with APDS. Moreover, the QM1-3, QM2-3 and QM3-3 based surface functionalised nanocomposites have shown higher conjugation of specific primers, while QM4-3 and QM5-3 based nanocomposites have shown lower conjugation due to less amine densities with APTS as well as APDS. Furthermore, the conjugation of oligonucleotides of all five developed nanocomposite materials were lower with APDS due to lower surface amine densities. There was no notable difference of grafting of the specific primers between them, regardless of the different spacer group. The capture efficiency of complementary sequence *via* hybridised on oligonucleotides, functionalised QM1-3, QM2-3-and QM3-3-based developed nanocomposite materials with two different carbon spacers (C₆-41 and C₁₂-43) ranging from 0.389 to 0.400, 0.381 to 0.392 and 0.384 to 0.392 nmol/mg respectively, due to the high surface amine densities. While, hybridisation of QM4-3 and QM5-3 APTS surface functionalised materials were low with carbon spacers (C₆-41 and C₁₂-43), ranging from 0.142 to 0.167 and 0.138 to

0.171 nmol/mg respectively, due to the low amine densities. Furthermore, the hybrid capture efficiency route *via* APDS surface functionalised oligonucleotides-grafted nanocomposites of QM1-3, QM2-3-and QM3-3, QM4-3 and QM5-3 were less as compared to the APTS surface functionalised for both forward sequences modified with carbon spacers (C₆-41 and C₁₂-43) ranging from 0.278 to 0.281, 0.267 to 0.278, 0.191 to 0.196, 0.139 to 0.173 and 0.162 to 0.176 nmol/mg respectively.

For dehybridisation efficiency of the captured complementary sequence with carbon spacers (C₆-41 and C₁₂-43) for QM1-3, QM2-3, QM3-3, QM4-3 and QM5-3-based nanocomposites were ranging from 0.386 to 0.388, 0.377 to 0.388, 0.322 to 0.356, 0.143 to 0.164 and 0.143 to 0.165 nmol/mg respectively, *via* APTS route surface functionalisation data, while the dehybridisation efficiency *via* APDS surface functionalisation route on QM1-3, QM2-3, QM3-3, QM4-3 and QM5-3 nanocomposites were ranging from 0.266 to 0.279, 0.262 to 0.276, 0.184 to 0.191, 0.151 to 0.176 and 0.150 to 0.166 nmol/mg respectively. It was found that the oligonucleotide-conjugated nanocomposites were highly effective for the specific hybrid capture assay from the solution.

The EC-specific forward primer modified with (C₆-41and C₁₂-43) spacers nanocomposites grafted on QM1-3 QM2-3 and QM3-3 were successful at detecting EC in water samples, while oligonucleotide grafted QM4-3 and QM5-3 failed to detect *E. coli* DNA in water samples.

8.2 Future work

This work has focussed on the development of nanocomposite material by using several different commercial materials as host, while silver and iron oxide nanoparticles are used as guest nanoparticles. Furthermore, the developed nanocomposites were applied for the antimicrobial and DNA detection applications by grafting the oligonucleotide after surface-functionalisation. In future, it can be applied to the earthworm, and other bacteria causing several diseases and for bio-catalysts purposes by modifying with enzymes.

In this project, the developed composites were used to observe the antimicrobial potential against Gram-positive and Gram-negative specific bacteria *E. coli* and *S. aureus* respectively, and in future could be applied to capture from real food samples and bacteria, which develop the biofilm in the dental unit waterlines and causing severe diseases in the patients. On an industrial scale, this material can be used for water purification kits in water filtration appliances and could be used for the separation or extraction of heavy metals from water.

On the other hand, for DNA capturing applications, the composites were used only for specific sequence of *E. coli*, while in future the nanocomposite could be grafted with oligonucleotides of allergens in food and specific strains of other pathogenic bacteria. It could be utilised for the nonspecific oligonucleotides as negative control experiment with the oligonucleotide-grafted composites due to different surface properties of glutaraldehyde-functionalised nanocomposites and oligonucleotide-grafted nanocomposites which might help in non-specific capture. In addition to this, nanocomposites can be used for the bio-catalytic applications with the immobilisation of enzyme on the surface of the modified material. If these developed materials are

functionalised with the polymers, and liposomes, they can be used in drug delivery systems, because the polymer shows higher thermo sensitivity, better and more effective hyperthermia properties while liposomes permit a higher drug encapsulation response.

References

- Ahmad, A., Mukherjee, P., Senapati, S., Mandal, D., Khan, M.I., Kumar, R. & Sastry, M. 2003, "Extracellular biosynthesis of silver nanoparticles using the fungus *Fusarium oxysporum*", *Colloids and surfaces B: Biointerfaces*, vol. 28, no. 4, pp. 313-318.
- Ali, Q., Ahmed, W., Lal, S. & Sen, T. 2017, "Novel multifunctional carbon nanotube containing silver and iron oxide nanoparticles for antimicrobial applications in water treatment", *Materials Today: Proceedings*, vol. 4, no. 1, pp. 57-64.
- Alt, V., Bechert, T., Steinrücke, P., Wagener, M., Seidel, P., Dingeldein, E., Domann, E. & Schnettler, R. 2004, "An *in vitro* assessment of the antibacterial properties and cytotoxicity of nanoparticulate silver bone cement", *Biomaterials*, vol. 25, no. 18, pp. 4383-4391.
- Armbrust, E.V., Berges, J.A., Bowler, C., Green, B.R., Martinez, D., Putnam, N.H., Zhou, S., Allen, A.E., Apt, K.E., Bechner, M., Brzezinski, M.A., Chaal, B.K., Chiovitti, A., Davis, A.K., Demarest, M.S., Detter, J.C., Glavina, T., Goodstein, D., Hadi, M.Z., Hellsten, U., Hildebrand, M., Jenkins, B.D., Jurka, J., Kapitonov, V.V., Kroger, N., Lau, W.W., Lane, T.W., Larimer, F.W., Lippmeier, J.C., Lucas, S., Medina, M., Montsant, A., Obornik, M., Parker, M.S., Palenik, B., Pazour, G.J., Richardson, P.M., Rynearson, T.A., Saito, M.A., Schwartz, D.C., Thamtrakoln, K., Valentin, K., Vardi, A., Wilkerson, F.P. & Rokhsar, D.S. 2004, "The genome of the diatom *Thalassiosira pseudonana*: ecology, evolution, and metabolism", *Science (New York, N.Y.)*, vol. 306, no. 5693, pp. 79-86.
- Atlas, R.M., Williams, J.F. & Huntington, M.K. 1995, "*Legionella* contamination of dental-unit waters", *Applied and Environmental Microbiology*, vol. 61, no. 4, pp. 1208-1213.
- Bailey, S.E., Olin, T.J., Bricka, R.M. & Adrian, D.D. 1999, "A review of potentially low-cost sorbents for heavy metals", *Water research*, vol. 33, no. 11, pp. 2469-2479.
- Barbeau, J., Tanguay, R., Faucher, E., Avezard, C., Trudel, L., Cote, L. & Prevost, A.P. 1996, "Multiparametric analysis of waterline contamination in dental units", *Applied and Environmental Microbiology*, vol. 62, no. 11, pp. 3954-3959.
- Bell, B.P., Goldoft, M., Griffin, P.M., Davis, M.A., Gordon, D.C., Tarr, P.I., Bartleson, C.A., Lewis, J.H., Barrett, T.J. & Wells, J.G. 1994, "A multistate outbreak of *Escherichia coli* O157: H7—associated bloody diarrhea and hemolytic uremic syndrome from hamburgers: the Washington experience", *Journal of the American Medical Association (JAMA)*, vol. 272, no. 17, pp. 1349-1353.

- Bell, B.P., Griffin, P.M., Lozano, P., Christie, D.L., Kobayashi, J.M. & Tarr, P.I. 1997, "Predictors of hemolytic uremic syndrome in children during a large outbreak of *Escherichia coli* O157:H7 infections", *Pediatrics*, vol. 100, no. 1, pp. E12.
- Bhakdi, S. & Trandum-Jensen, J. 1991, "Alpha-toxin of *Staphylococcus aureus*", *Microbiological reviews*, vol. 55, no. 4, pp. 733-751.
- Brody, A., Strupinsky, E. & Kline, L. 2001, "Odor removers", *Active packaging for food applications*. Lancaster, Pa.: Technomic Publishing Company, Inc , pp. 107-117.
- Bruce, I.J. & Sen, T. 2005, "Surface modification of magnetic nanoparticles with alkoxysilanes and their application in magnetic bioseparations", *Langmuir*, vol. 21, no. 15, pp. 7029-7035.
- Bruce, I.J., Taylor, J., Todd, M., Davies, M.J., Borioni, E., Sangregorio, C. & Sen, T. 2004, "Synthesis, characterisation and application of silica-magnetite nanocomposites", *Journal of Magnetism and Magnetic Materials*, vol. 284, pp. 145-160.
- Chen, S., Xu, H., Xu, H., Yu, G., Gong, X., Fang, Q., Leung, K.C., Xuan, S. & Xiong, Q. 2015, "A facile ultrasonication assisted method for Fe₃O₄@SiO₂-Ag nanospheres with excellent antibacterial activity", *Dalton Transactions*, vol. 44, no. 19, pp. 9140-9148.
- Chen, S., Liu, J. & Zeng, H. 2005, "Structure and antibacterial activity of silver-supporting activated carbon fibers", *Journal of Materials Science*, vol. 40, no. 23, pp. 6223-6231.
- Chen, X. & Schluesener, H. 2008, "Nanosilver: a nanoparticle in medical application", *Toxicology Letters*, vol. 176, no. 1, pp. 1-12.
- Chou, W., Yu, D. & Yang, M. 2005, "The preparation and characterization of silver-loading cellulose acetate hollow fiber membrane for water treatment", *Polymers for Advanced Technologies*, vol. 16, no. 8, pp. 600-607.
- Chudasama, B., Vala, A.K., Andhariya, N., Upadhyay, R. & Mehta, R. 2009, "Enhanced antibacterial activity of bifunctional Fe₃O₄-Ag core-shell nanostructures", *Nano Research*, vol. 2, no. 12, pp. 955-965.
- Chyka, P.A. & Seger, D. 1997, "Position statement: single-dose activated charcoal. American academy of clinical toxicology; European association of poisons centres and clinical toxicologists", *Journal of toxicology. Clinical Toxicology*, vol. 35, no. 7, pp. 721-741.
- Chyka, P.A., Seger, D., Krenzelok, E.P., Vale, J.A., American Academy of Clinical Toxicology & European Association of Poisons Centres and Clinical Toxicologists 2005, "Position paper: Single-dose activated charcoal", *Clinical Toxicology (Philadelphia, Pa.)*, vol. 43, no. 2, pp. 61-87.

- Cornell, R.M. & Schwertmann, U. 2003, The iron oxides: structure, properties, reactions, occurrences and uses, *John Wiley & Sons*.
- Dastjerdi, R. & Montazer, M. 2010, "A review on the application of inorganic nano-structured materials in the modification of textiles: focus on anti-microbial properties", *Colloids and Surfaces B: Biointerfaces*, vol. 79, no. 1, pp. 5-18.
- Deitch, E.A., Marino, A.A., Malakanok, V. & Albright, J.A. 1987, "Silver nylon cloth: *in vitro* and *in vivo* evaluation of antimicrobial activity.", *Journal of Trauma*, vol. 27, no. 3, pp. 301-304.
- Del Campo, A., Sen, T., Lellouche, J. & Bruce, I.J. 2005, "Multifunctional magnetite and silica–magnetite nanoparticles: synthesis, surface activation and applications in life sciences", *Journal of Magnetism and Magnetic Materials*, vol. 293, no. 1, pp. 33-40.
- Deng, Y., Deng, C., Qi, D., Liu, C., Liu, J., Zhang, X. & Zhao, D. 2009, "Synthesis of core/shell colloidal magnetic zeolite microspheres for the immobilization of trypsin", *Advanced Materials*, vol. 21, no. 13, pp. 1377-1382.
- Devi, L.S. & Joshi, S. 2012, "Antimicrobial and synergistic effects of silver nanoparticles synthesized using soil fungi of high altitudes of eastern Himalaya", *Mycobiology*, vol. 40, no. 1, pp. 27-34.
- Dong, A., Sun, Y., Lan, S., Wang, Q., Cai, Q., Qi, X., Zhang, Y., Gao, G., Liu, F. & Harnood, C. 2013, "Barbituric acid-based magnetic N-halamine nanoparticles as recyclable antibacterial agents", *ACS Applied Materials & Interfaces*, vol. 5, no. 16, pp. 8125-8133.
- Dong, H., Huang, J., Koepsel, R.R., Ye, P., Russell, A.J. & Matyjaszewski, K. 2011, "Recyclable antibacterial magnetic nanoparticles grafted with quaternized poly (2-(dimethylamino) ethyl methacrylate) brushes", *Biomacromolecules*, vol. 12, no. 4, pp. 1305-1311.
- Dutil, S., Veillette, M., Mériaux, A., Lazure, L., Barbeau, J. & Duchaine, C. 2007, "Aerosolization of *mycobacteria* and *legionellae* during dental treatment: low exposure despite dental unit contamination", *Environmental Microbiology*, vol. 9, no. 11, pp. 2836-2843.
- Dzyaloshinsky, I. 1958, "A thermodynamic theory of "weak" ferromagnetism of antiferromagnetics", *Journal of Physics and Chemistry of Solids*, vol. 4, no. 4, pp. 241-255.
- Easmon, C.S. & Adlam, C. 1983, *Staphylococci and staphylococcal infections*. Volume 1. Clinical and epidemiological aspects. Volume 2. The organism *in vivo* and *in vitro*. *Academic Press*.
- Eby, D.M., Schaeublin, N.M., Farrington, K.E., Hussain, S.M. & Johnson, G.R. 2009, "Lysozyme catalyzes the formation of antimicrobial silver nanoparticles", *American Chemical Society*, vol. 3, no. 4, pp. 984-994.

- Eisenstein, B. & Zaleznik, D. 2000, "Enterobacteriaceae", *Principles and practice of infectious diseases*, vol. 2, pp. 1972-1973.
- Elder, R.O., Keen, J.E., Siragusa, G.R., Barkocy-Gallagher, G.A., Koohmaraie, M. & Laegreid, W.W. 2000, "Correlation of enterohemorrhagic *Escherichia coli* O157 prevalence in feces, hides, and carcasses of beef cattle during processing", *Proceedings of the National Academy of Sciences*, vol. 97, no. 7, pp. 2999-3003.
- Espinosa-Cristobal, L., Martinez-Castanon, G., Martínez-Martínez, R., Loyola-Rodriguez, J., Patino-Marin, N., Reyes-Macias, J. & Ruiz, F. 2009, "Antibacterial effect of silver nanoparticles against *Streptococcus mutans*", *Materials Letters*, vol. 63, no. 29, pp. 2603-2606.
- Falkenstein, D. 2018, What you need to know during Chicago carbon *E. coli* outbreak. Available: <http://www.foodpoisonjournal.com/?s=chicago> [2017, June 8th].
- Farokhzad, O.C. & Langer, R. 2009, "Impact of nanotechnology on drug delivery", *American Chemical Society*, vol. 3, no. 1, pp. 16-20.
- Feng, P., Weagant, S.D., Grant, M.A., Burkhardt, W., Shellfish, M. & Water, B. 2002, "BAM: Enumeration of *Escherichia coli* and the *Coliform* bacteria", *Bacteriological Analytical Manual*, pp. 13.
- Feng, Q., Wu, J., Chen, G., Cui, F., Kim, T. & Kim, J. 2000, "A mechanistic study of the antibacterial effect of silver ions on *Escherichia coli* and *Staphylococcus aureus*", *Journal of Biomedical Materials Research*, vol. 52, no. 4, pp. 662-668.
- Fields, B.S., Benson, R.F. & Besser, R.E. 2002, "*Legionella* and *Legionnaires'* disease: 25 years of investigation", *Clinical Microbiology Reviews*, vol. 15, no. 3, pp. 506-526.
- Foster, T. 1991, "Potential for vaccination against infections caused by *Staphylococcus aureus*", *Vaccine*, vol. 9, no. 4, pp. 221-227.
- Foster, T. & McDevitt, D. 1994, "Molecular basis of adherence of *Staphylococci* to biomaterials" in *Infections associated with indwelling medical devices* *American Society for Microbiology Washington, DC*, pp. 31-44.
- Frenzen, P.D., Drake, A., Angulo, F.J. & Emerging infections program food networking group 2005, "Economic cost of illness due to *Escherichia coli* O157 infections in the United States", *Journal of Food Protection*, vol. 68, no. 12, pp. 2623-2630.
- Garg, A.X., Suri, R.S., Barrowman, N., Rehman, F., Matsell, D., Rosas-Arellano, M.P., Salvadori, M., Haynes, R.B. & Clark, W.F. 2003, "Long-term renal prognosis of diarrhea-associated hemolytic uremic syndrome: a systematic review, meta-analysis, and meta-regression", *Journal of the American Medical Association (JAMA)*, vol. 290, no. 10, pp. 1360-1370.

- Göksay, D., Çotuk, A. & Zeybek, Z. 2008, "Microbial contamination of dental unit waterlines in Istanbul, Turkey", *Environmental Monitoring and Assessment*, vol. 147, no. 1-3, pp. 265-269.
- Gould, L.H., Bopp, C., Strockbine, N., Atkinson, R., Baselski, V., Body, B., Carey, R., Crandall, C., Hurd, S., Kaplan, R., Neill, M., Shea, S., Somsel, P., Tobin-D'Angelo, M., Griffin, P.M., Gerner-Smidt, P. & Centers for Disease Control and Prevention (CDC) 2009, "Recommendations for diagnosis of shiga toxin--producing *Escherichia coli* infections by clinical laboratories", *MMWR. Recommendations and reports : Morbidity and Mortality Weekly Report. Recommendations and reports*, vol. 58, no. RR-12, pp. 1-14.
- Gray, J., Norton, P., Alnouno, R., Marolda, C., Valvano, M. & Griffiths, K. 2003, "Biological efficacy of electroless-deposited silver on plasma activated polyurethane", *Biomaterials*, vol. 24, no. 16, pp. 2759-2765.
- Griffin, P., Bell, B., Cieslak, P., Tuttle, J., Barrett, T., Doyle, M., McNamara, A., Shefer, A. & Wells, J. 1994, "Large outbreak of *Escherichia coli* O157: H7 infections in the western United States: the big picture", *Recent advances in verocytotoxin producing Escherichia coli infections. Amsterdam: Elsevier*, , pp. 7-12.
- Griffin, P.M. & Tauxe, R.V. 1991, "The epidemiology of infections caused by *Escherichia coli* O157:H7, other enterohemorrhagic *E. coli*, and the associated hemolytic uremic syndrome", *Epidemiologic Reviews*, vol. 13, pp. 60-98.
- Hao, Y. & Teja, A.S. 2003, "Continuous hydrothermal crystallization of α -Fe₂O₃ and Co₃O₄ nanoparticles", *Journal of Materials Research*, vol. 18, no. 2, pp. 415-422.
- Harris, P.J.F. 2009, Carbon nanotube science: synthesis, properties and applications, *Cambridge university press*.
- Haul, R. 1982, "SJ Gregg, KSW Sing: adsorption, surface area and porosity. 2. auflage, academic press, London 1982. 303 Seiten, Preis: \$49.50", *Berichte Der Bunsengesellschaft für Physikalische Chemie*, vol. 86, no. 10, pp. 957-957.
- Hemraj-Benny, T., Bandoz, T.J. & Wong, S.S. 2008, "Effect of ozonolysis on the pore structure, surface chemistry, and bundling of single-walled carbon nanotubes", *Journal of Colloid and Interface Science*, vol. 317, no. 2, pp. 375-382.
- Herrera, M., Carrion, P., Baca, P., Liebana, J. & Castillo, A. 2001, "In vitro antibacterial activity of glass-ionomer cements", *Microbios*, vol. 104, no. 409, pp. 141-148.
- Hodgson B.J. 2013, Immobilisation of Bio-molecules on Magnetisable Solid Supports for Applications in Bio-catalysis and Bio-sensors, PhD, *University of Central Lancashire*, Preston.

- Howard, M., Sen Tapas 2011, Multifunctional nanocomposites with antimicrobial activity for the purification of contaminated water, *University of Central Lancashire*, Preston.
- Hugounenq, P., Levy, M., Alloyeau, D., Lartigue, L., Dubois, E., Cabuil, V., Ricolleau, C., Roux, S., Wilhelm, C. & Gazeau, F. 2012, "Iron oxide monocrystalline nanoflowers for highly efficient magnetic hyperthermia", *The Journal of Physical Chemistry*, vol. 116, no. 29, pp. 15702-15712.
- Hungin, A., Chang, L., Locke, G., Dennis, E. & Barghout, V. 2005, "Irritable bowel syndrome in the United States: prevalence, symptom patterns and impact", *Alimentary Pharmacology & Therapeutics*, vol. 21, no. 11, pp. 1365-1375.
- Hyeon, T., Lee, S.S., Park, J., Chung, Y. & Na, H.B. 2001, "Synthesis of highly crystalline and monodisperse maghemite nanocrystallites without a size-selection process", *Journal of the American Chemical Society*, vol. 123, no. 51, pp. 12798-12801.
- Iglesias-Silva, E., Rivas, J., Isidro, L.L. & Lopez-Quintela, M. 2007, "Synthesis of silver-coated magnetite nanoparticles", *Journal of Non-Crystalline Solids*, vol. 353, no. 8, pp. 829-831.
- Iijima, S. 1991, "Helical microtubules of graphitic carbon", *Nature*, vol. 354, no. 6348, pp. 56-58.
- Ioannidou, O. & Zabaniotou, A. 2007, "Agricultural residues as precursors for activated carbon production—a review", *Renewable and Sustainable Energy Reviews*, vol. 11, no. 9, pp. 1966-2005.
- Ishitani, T. 1995, "Active packaging for food quality preservation in Japan", *Special Publication, Royal Society of Chemistry*, vol. 162, no. 1, pp. 177-177.
- Jay, J.M. 2000, "Foodborne gastroenteritis caused by *Vibrio*, *Yersinia*, and *Campylobacter species*" in *Modern Food Microbiology* Springer, pp. 549-568.
- Jeong, S.H., Hwang, Y.H. & Yi, S.C. 2005, "Antibacterial properties of padded PP/PE nonwovens incorporating nano-sized silver colloids", *Journal of Materials Science*, vol. 40, no. 20, pp. 5413-5418.
- Juan, L., Zhimin, Z., Anchun, M., Lei, L. & Jingchao, Z. 2010, "Deposition of silver nanoparticles on titanium surface for antibacterial effect", *International Journal of Nanomedicine*, vol. 5, pp. 261-267.
- Jung, W.K., Koo, H.C., Kim, K.W., Shin, S., Kim, S.H. & Park, Y.H. 2008, "Antibacterial activity and mechanism of action of the silver ion in *Staphylococcus aureus* and *Escherichia coli*", *Applied and Environmental Microbiology*, vol. 74, no. 7, pp. 2171-2178.
- Kalishwaralal, K., Deepak, V., Ramkumarpandian, S., Nellaiah, H. & Sangiliyandi, G. 2008, "Extracellular biosynthesis of silver nanoparticles by the culture

- supernatant of *Bacillus licheniformis*", *Materials Letters*, vol. 62, no. 29, pp. 4411-4413.
- Kang, S., Pinault, M., Pfefferle, L.D. & Elimelech, M. 2007, "Single-walled carbon nanotubes exhibit strong antimicrobial activity", *Langmuir*, vol. 23, no. 17, pp. 8670-8673.
- Kanmani, P. & Lim, S.T. 2013, "Synthesis and structural characterization of silver nanoparticles using bacterial exopolysaccharide and its antimicrobial activity against food and multidrug resistant pathogens", *Process Biochemistry*, vol. 48, no. 7, pp. 1099-1106.
- Kasthuri, J., Veerapandian, S. & Rajendiran, N. 2009, "Biological synthesis of silver and gold nanoparticles using apiin as reducing agent", *Colloids and Surfaces B: Biointerfaces*, vol. 68, no. 1, pp. 55-60.
- Kawashita, M., Tsuneyama, S., Miyaji, F., Kokubo, T., Kozuka, H. & Yamamoto, K. 2000, "Antibacterial silver-containing silica glass prepared by sol-gel method", *Biomaterials*, vol. 21, no. 4, pp. 393-398.
- Kim, Y., Lee, B. & Yi, J. 2003, "Preparation of functionalized mesostructured silica containing magnetite (MSM) for the removal of copper ions in aqueous solutions and its magnetic separation", *Separation Science and Technology*, vol. 38, no. 11, pp. 2533-2548.
- Kiruba, A.V.S., Dakshinamurthy, A. & Selvakumar, P.M. 2013, "Eco-friendly biocidal silver-activated charcoal nanocomposite: antimicrobial application in water purification", *Synthesis & Reactivity in Inorganic, Metal-Organic, & Nano-Metal Chemistry*, vol. 43, no. 8, pp. 1068-1072.
- Klasen, H. 2000, "A historical review of the use of silver in the treatment of burns. II. Renewed interest for silver", *Burns*, vol. 26, no. 2, pp. 131-138.
- Knežević, N.Ž. & Lin, V.S. 2013, "A magnetic mesoporous silica nanoparticle-based drug delivery system for photosensitive cooperative treatment of cancer with a mesopore-capping agent and mesopore-loaded drug", *Nanoscale*, vol. 5, no. 4, pp. 1544-1551.
- Kong, H. & Jang, J. 2008, "Antibacterial properties of novel poly (methyl methacrylate) nanofiber containing silver nanoparticles", *Langmuir*, vol. 24, no. 5, pp. 2051-2056.
- Korunić, Z. & Mackay, A. 2000, "Grain surface-layer treatment of diatomaceous earth for insect control", *Arhiv za Higijenu Rada i Toksikologiju*, vol. 51, no. 1, pp. 1-11.
- Krishnan, K.M. 2016, *Fundamentals and applications of magnetic materials*, 1st edn, Oxford University Press, United Kingdom.

- Kumar, R. & Münstedt, H. 2005, "Polyamide/silver antimicrobials: effect of crystallinity on the silver ion release", *Polymer International*, vol. 54, no. 8, pp. 1180-1186.
- Kumar, V.S., Nagaraja, B., Shashikala, V., Padmasri, A., Madhavendra, S.S., Raju, B.D. & Rao, K. 2004, "Highly efficient Ag/C catalyst prepared by electrochemical deposition method in controlling microorganisms in water", *Journal of Molecular Catalysis A: Chemical*, vol. 223, no. 1, pp. 313-319.
- Kurland, H., Grabow, J., Staupendahl, G., Müller, F.A., Müller, E., Dutz, S. & Bellemann, M.E. 2009, "Magnetic iron oxide nanopowders produced by CO₂ laser evaporation—In situ coating and particle embedding in a ceramic matrix", *Journal of Magnetism and Magnetic Materials*, vol. 321, no. 10, pp. 1381-1385.
- Kvitek, L., Panáček, A., Soukupova, J., Kolar, M., Vecerova, R., Pucek, R., Holecová, M. & Zboril, R. 2008, "Effect of surfactants and polymers on stability and antibacterial activity of silver nanoparticles (NPs)", *The Journal of Physical Chemistry C*, vol. 112, no. 15, pp. 5825-5834.
- Lasota, T. 2014, Purification of human DNA of DNA profiling from body fluid contaminated soil using super paramagnetic iron oxide nanoparticles (SPIONS), PhD, *University of Central Lancashire*.
- Lechevallier, M.W., Hassenauer, T.S., Camper, A.K. & McFeters, G.A. 1984, "Disinfection of bacteria attached to granular activated carbon", *Applied and Environmental Microbiology*, vol. 48, no. 5, pp. 918-923.
- Lee, B.U. & Ji, J.H. 2008, "Inactivation of *S. epidermidis*, *B. subtilis*, and *E. coli* bacteria bioaerosols deposited on a filter utilizing airborne silver nanoparticles", *Journal of Microbiology and Biotechnology*, vol. 18, no. 1, pp. 176-182.
- Lee, J.E., Lee, N., Kim, H., Kim, J., Choi, S.H., Kim, J.H., Kim, T., Song, I.C., Park, S.P. & Moon, W.K. 2009, "Uniform mesoporous dye-doped silica nanoparticles decorated with multiple magnetite nanocrystals for simultaneous enhanced magnetic resonance imaging, fluorescence imaging, and drug delivery", *Journal of the American Chemical Society*, vol. 132, no. 2, pp. 552-557.
- Lee, J. 2004, Water, sanitation and hygiene links to health: facts and figures, *World Health Organization*, Geneva.
- Levinson, W. & Jawetz, E. 2000, Medical microbiology and immunology: examination and board review, Sixth edn, *Appleton & Lange*, USA.
- Lok, C., Ho, C., Chen, R., He, Q., Yu, W., Sun, H., Tam, P.K., Chiu, J. & Che, C. 2006, "Proteomic analysis of the mode of antibacterial action of silver nanoparticles", *Journal of Proteome research*, vol. 5, no. 4, pp. 916-924.
- Long, J.W., Logan, M.S., Rhodes, C.P., Carpenter, E.E., Stroud, R.M. & Rolison, D.R. 2004, "Nanocrystalline iron oxide aerogels as mesoporous magnetic

- architectures", *Journal of the American Chemical Society*, vol. 126, no. 51, pp. 16879-16889.
- Lu, C. & Chiu, H. 2006, "Adsorption of zinc (II) from water with purified carbon nanotubes", *Chemical Engineering Science*, vol. 61, no. 4, pp. 1138-1145.
- Luong, N.D., Lee, Y. & Nam, J. 2008, "Highly-loaded silver nanoparticles in ultrafine cellulose acetate nanofibrillar aerogel", *European Polymer Journal*, vol. 44, no. 10, pp. 3116-3121.
- Lyon, B.R. & Skurray, R. 1987, "Antimicrobial resistance of *Staphylococcus aureus*: genetic basis", *Microbiological Reviews*, vol. 51, no. 1, pp. 88-134.
- Mahmoudi, M., Milani, A.S. & Stroeve, P. 2010, "Synthesis, surface architecture and biological response of superparamagnetic iron oxide nanoparticles for application in drug delivery: a review", *International Journal of Biomedical Nanoscience and Nanotechnology*, vol. 1, no. 2, pp. 164-201.
- Mahmoudi, M., Sant, S., Wang, B., Laurent, S. & Sen, T. 2011, "Superparamagnetic iron oxide nanoparticles (SPIONs): development, surface modification and applications in chemotherapy", *Advanced Drug Delivery Reviews*, vol. 63, no. 1, pp. 24-46.
- Mahmoudi, M., Simchi, A., Imani, M., Milani, A.S. & Stroeve, P. 2008, "Optimal design and characterization of superparamagnetic iron oxide nanoparticles coated with polyvinyl alcohol for targeted delivery and imaging", *The Journal of Physical Chemistry B*, vol. 112, no. 46, pp. 14470-14481.
- Markarian, J. 2004, "Advances in PVC heat and light stabilization", *Plastics, Additives and Compounding*, vol. 6, no. 5, pp. 46-49.
- Marshall, J.K., Thabane, M., Garg, A.X., Clark, W.F., Salvadori, M., Collins, S.M. & Walkerton Health Study Investigators 2006, "Incidence and epidemiology of irritable bowel syndrome after a large waterborne outbreak of bacterial dysentery", *Gastroenterology*, vol. 131, no. 2, pp. 445-450.
- Mead, P.S., Slutsker, L., Dietz, V., McCaig, L.F., Bresee, J.S., Shapiro, C., Griffin, P.M. & Tauxe, R.V. 1999, "Food-related illness and death in the United States", *Emerging Infectious Diseases*, vol. 5, no. 5, pp. 607-625.
- Miles, A., Misra, S. & Irwin, J. 1938, "The estimation of the bactericidal power of the blood", *Journal of Hygiene*, vol. 38, no. 06, pp. 732-749.
- Mokhtari, N., Daneshpajouh, S., Seyedbagheri, S., Atashdehghan, R., Abdi, K., Sarkar, S., Minaian, S., Shahverdi, H.R. & Shahverdi, A.R. 2009, "Biological synthesis of very small silver nanoparticles by culture supernatant of *Klebsiella pneumoniae*: The effects of visible-light irradiation and the liquid mixing process", *Materials Research Bulletin*, vol. 44, no. 6, pp. 1415-1421.

- Montazer, M. & Maali Amiri, M. 2013, "ZnO nano reactor on textiles and polymers: Ex-situ and in-situ synthesis, application and characterization", *The Journal of Physical Chemistry B*, vol. 118, no.6, pp 1453–1470
- Moon, J.H., Kim, J.H., Kim, K., Kang, T., Kim, B., Kim, C., Hahn, J.H. & Park, J.W. 1997, "Absolute surface density of the amine group of the aminosilylated thin layers: ultraviolet-visible spectroscopy, second harmonic generation, and synchrotron-radiation photoelectron spectroscopy study", *Langmuir*, vol. 13, no. 16, pp. 4305-4310.
- Moon, J.H., Shin, J.W., Kim, S.Y. & Park, J.W. 1996, "Formation of uniform aminosilane thin layers: an imine formation to measure relative surface density of the amine group", *Langmuir*, vol. 12, no. 20, pp. 4621-4624.
- Mukha, I.P., Eremenko, A., Smirnova, N., Mikhienkova, A., Korchak, G., Gorchev, V. & Chunikhin, A.Y. 2013, "Antimicrobial activity of stable silver nanoparticles of a certain size", *Applied Biochemistry and Microbiology*, vol. 49, no. 2, pp. 199-206.
- Mürbe, J., Rechtenbach, A. & Töpfer, J. 2008, "Synthesis and physical characterization of magnetite nanoparticles for biomedical applications", *Materials Chemistry and Physics*, vol. 110, no. 2, pp. 426-433.
- Narita, A., Naka, K. & Chujo, Y. 2009, "Facile control of silica shell layer thickness on hydrophilic iron oxide nanoparticles via reverse micelle method", *Colloids and Surfaces A: Physicochemical and Engineering Aspects*, vol. 336, no. 1, pp. 46-56.
- Nersisyan, H., Lee, J., Son, H., Won, C. & Maeng, D. 2003, "A new and effective chemical reduction method for preparation of nanosized silver powder and colloid dispersion", *Materials Research Bulletin*, vol. 38, no. 6, pp. 949-956.
- O'donnell, M., Shore, A., Russell, R. & Coleman, D. 2007, "Optimisation of the long-term efficacy of dental chair waterline disinfection by the identification and rectification of factors associated with waterline disinfection failure", *Journal of Dentistry*, vol. 35, no. 5, pp. 438-451.
- Okoli, C., Sanchez-Dominguez, M., Boutonnet, M., Järås, S., Civera, C., Solans, C. & Kuttuva, G.R. 2012, "Comparison and functionalization study of microemulsion-prepared magnetic iron oxide nanoparticles", *Langmuir*, vol. 28, no. 22, pp. 8479-8485.
- Otake, T., Yoshinaga, J. & Yanagisawa, Y. 2001, "Analysis of organic esters of plasticizer in indoor air by GC-MS and GC-FPD", *Environmental Science & Technology*, vol. 35, no. 15, pp. 3099-3102.
- Pandey, S., Goswami, G.K. & Nanda, K.K. 2012, "Green synthesis of biopolymer–silver nanoparticle nanocomposite: An optical sensor for ammonia detection", *International Journal of Biological Macromolecules*, vol. 51, no. 4, pp. 583-589.

- Pankhurst, C.L. & Coulter, W.A. 2007, "Do contaminated dental unit waterlines pose a risk of infection?", *Journal of Dentistry*, vol. 35, no. 9, pp. 712-720.
- Park, J., An, K., Hwang, Y., Park, J., Noh, H., Kim, J., Park, J., Hwang, N. & Hyeon, T. 2004, "Ultra-large-scale syntheses of monodisperse nanocrystals", *Nature Materials*, vol. 3, no. 12, pp. 891-895.
- Park, J., Lee, E., Hwang, N., Kang, M., Kim, S.C., Hwang, Y., Park, J., Noh, H., Kim, J. & Park, J. 2005, "One-nanometer-scale size-controlled synthesis of monodisperse magnetic iron oxide nanoparticles", *Angewandte Chemie*, vol. 117, no. 19, pp. 2932-2937.
- Petcharoen, K. & Sirivat, A. 2012, "Synthesis and characterization of magnetite nanoparticles via the chemical co-precipitation method", *Materials Science and Engineering: B*, vol. 177, no. 5, pp. 421-427.
- Philipse, A.P., Van Bruggen, M.P. & Pathmamanoharan, C. 1994, "Magnetic silica dispersions: preparation and stability of surface-modified silica particles with a magnetic core", *Langmuir*, vol. 10, no. 1, pp. 92-99.
- Pramanik, A., Laha, D., Bhattacharya, D., Pramanik, P. & Karmakar, P. 2012, "A novel study of antibacterial activity of copper iodide nanoparticle mediated by DNA and membrane damage", *Colloids and Surfaces B: Biointerfaces*, vol. 96, pp. 50-55.
- Preoteasa, E., Ciortea, C., Constantinescu, B., Fluerașu, D., Enescu, S., Pantelica, D., Negoita, F. & Preoteasa, E. 2002, "Analysis of composites for restorative dentistry by PIXE, XRF and ERDA", *Nuclear Instruments and Methods in Physics Research Section B: Beam Interactions with Materials and Atoms*, vol. 189, no. 1, pp. 426-430.
- Prevost, G., Couppie, P., Prevost, P., Gayet, S., Petiau, P., Cribier, B., Monteil, H. & Piemont, Y. 1995, "Epidemiological data on *Staphylococcus aureus* strains producing synergohymenotropic toxins", *Journal of Medical Microbiology*, vol. 42, no. 4, pp. 237-245.
- Priester, J.H., Stoimenov, P.K., Mielke, R.E., Webb, S.M., Ehrhardt, C., Zhang, J.P., Stucky, G.D. & Holden, P.A. 2009, "Effects of soluble cadmium salts versus Cd Se quantum dots on the growth of planktonic *Pseudomonas aeruginosa*", *Environmental Science & Technology*, vol. 43, no. 7, pp. 2589-2594.
- Prucek, R., Tuček, J., Kilianová, M., Panáček, A., Kvítek, L., Filip, J., Kolář, M., Tománková, K. & Zbořil, R. 2011, "The targeted antibacterial and antifungal properties of magnetic nanocomposite of iron oxide and silver nanoparticles", *Biomaterials*, vol. 32, no. 21, pp. 4704-4713.
- Putnins, E.E., Giovanni, D.D. & Bhullar, A.S. 2001, "Dental unit waterline contamination and its possible implications during periodontal surgery", *Journal of Periodontology*, vol. 72, no. 3, pp. 393-400.

- Radheshkumar, C. & Münstedt, H. 2006, "Antimicrobial polymers from polypropylene/silver composites—Ag release measured by anode stripping voltammetry", *Reactive and Functional Polymers*, vol. 66, no. 7, pp. 780-788.
- Rai, M., Yadav, A. & Gade, A. 2009, "Silver nanoparticles as a new generation of antimicrobials", *Biotechnology Advances*, vol. 27, no. 1, pp. 76-83.
- Rangel, J.M., Sparling, P.H., Crowe, C., Griffin, P.M. & Swerdlow, D.L. 2005, "Epidemiology of *Escherichia coli* O157: H7 outbreaks, United States, 1982–2002",
- Ranjbar, Z.R. & Morsali, A. 2011, "Preparation of silver nanostructure from silver (I) coordination polymer and fabrication of nano silver (I) bromide by reverse micelles technique", *Synthetic Metals*, vol. 161, no. 15, pp. 1449-1455.
- Reisfeld, R., Saraidarov, T. & Levchenko, V. 2008, "Formation and structural characterization of silver nanoparticles in ormosil sol-gel films.", *Optica Applicata*, vol. 38, no. 1.
- Roberts, I.S. 1996, "The biochemistry and genetics of capsular polysaccharide production in bacteria", *Annual Reviews in Microbiology*, vol. 50, no. 1, pp. 285-315.
- Robitaille, P., Gonthier, M., Grignon, A. & Russo, P. 1997, "Pancreatic injury in the hemolytic-uremic syndrome", *Pediatric Nephrology*, vol. 11, no. 5, pp. 631-632.
- Rother, D., Sen, T., East, D. & Bruce, I.J. 2011, "Silicon, silica and its surface patterning/activation with alkoxy-and amino-silanes for nanomedical applications", *Nanomedicine*, vol. 6, no. 2, pp. 281-300.
- Rudge, S., Kurtz, T., Vessely, C., Catterall, L. & Williamson, D. 2000, "Preparation, characterization, and performance of magnetic iron–carbon composite microparticles for chemotherapy", *Biomaterials*, vol. 21, no. 14, pp. 1411-1420.
- Rusin, P.A., Rose, J.B., Haas, C.N. & Gerba, C.P. 1997, "Risk assessment of opportunistic bacterial pathogens in drinking water" in *Reviews of Environmental Contamination and Toxicology* Springer, vol. 152, pp. 57-83.
- Russell, A., Path, F., Si, F.P. & Hugo, W. 1994, "Antimicrobial activity and action of silver", *Progress in Medicinal Chemistry*, vol. 31, pp. 351.
- Safdar, N., Said, A., Gangnon, R.E. & Maki, D.G. 2002, "Risk of hemolytic uremic syndrome after antibiotic treatment of *Escherichia coli* O157: H7 enteritis: a meta-analysis", *Journal of the American Medical Association (JAMA)*, vol. 288, no. 8, pp. 996-1001.
- Santra, S., Tapeç, R., Theodoropoulou, N., Dobson, J., Hebard, A. & Tan, W. 2001, "Synthesis and characterization of silica-coated iron oxide nanoparticles in microemulsion: the effect of nonionic surfactants", *Langmuir*, vol. 17, no. 10, pp. 2900-2906.

- Sathishkumar, M., Sneha, K., Won, S., Cho, C., Kim, S. & Yun, Y. 2009, "Cinnamon zeylanicum bark extract and powder mediated green synthesis of nano-crystalline silver particles and its bactericidal activity", *Colloids and Surfaces Biointerfaces*, vol. 73, no. 2, pp. 332-338.
- Scallan, E., Hoekstra, R.M., Angulo, F.J., Tauxe, R.V., Widdowson, M., Roy, S.L., Jones, J.L. & Griffin, P.M. 2011, "Foodborne illness acquired in the United States—major pathogens", *Emerging Infectious Diseases*, vol. 17, no. 1.
- Schatzlein, D. 2015, XRF in the Lab: XRF Technology for the Non-Scientist, 1st edn, *Thermo Fisher Scientific Inc*, USA.
- Schneider, S., Halbig, P., Grau, H. & Nickel, U. 1994, "Reproducible preparation of silver sols with uniform particle size for application in surface-enhanced Raman spectroscopy", *Photochemistry and Photobiology*, vol. 60, no. 6, pp. 605-610.
- Scott, J.R. & Barnett, T.C. 2006, "Surface proteins of Gram-positive bacteria and how they get there", *Annual Review of Microbiology*, vol. 60, pp. 397-423.
- Sebastianelli, A., Sen, T. & Bruce, I.J. 2008, "Extraction of DNA from soil using nanoparticles by magnetic bioseparation", *Letters in Applied Microbiology*, vol. 46, no. 4, pp. 488-491.
- Seil, J.T. & Webster, T.J. 2012, "Antimicrobial applications of nanotechnology: methods and literature", *International Journal of Nanomedicine*, vol. 7, pp. 2767-2781.
- Sen, T. & Bruce, I.J. 2012, "Surface engineering of nanoparticles in suspension for particle based bio-sensing", *Scientific Reports*, vol. 2, p. 564-570
- Sen, T., Bruce, I.J. & Mercer, T. 2010, "Fabrication of novel hierarchically ordered porous magnetic nanocomposites for bio-catalysis", *Chemical Communications*, vol. 46, no. 36, pp. 6807-6809.
- Sen, T., Sebastianelli, A. & Bruce, I.J. 2006, "Mesoporous silica-magnetite nanocomposite: fabrication and applications in magnetic bioseparations", *Journal of the American Chemical Society*, vol. 128, no. 22, pp. 7130-7131.
- Sen, T., Sheppard, S.J., Mercer, T., Eizadi-Sharifabad, M., Mahmoudi, M. & Elhissi, A. 2012, "Simple one-pot fabrication of ultra-stable core-shell superparamagnetic nanoparticles for potential application in drug delivery", *Royal Society of Chemistry Advances*, vol. 2, no. 12, pp. 5221-5228.
- Setyawan, H., Fajaroh, F., Widiyastuti, W., Winardi, S., Lenggoro, I.W. & Mufti, N. 2012, "One-step synthesis of silica-coated magnetite nanoparticles by electrooxidation of iron in sodium silicate solution", *Journal of Nanoparticle Research*, vol. 14, no. 4, pp. 1-9.
- Shankar, S.S., Ahmad, A. & Sastry, M. 2003, "Geranium leaf assisted biosynthesis of silver nanoparticles", *Biotechnology Progress*, vol. 19, no. 6, pp. 1627-1631.

- Sharifabad, M., Mercer, T. & Sen, T. 2013, "Fabrication of stable bio-compatible mesoporous silica and core-shell silica-magnetite nanoparticles for potential application in drug delivery", *Nanotechnology: Bio Sensors, Instruments, Medical, Environment and Energy*, vol. 3, pp. 315-318.
- Sharma, V.K., Yngard, R.A. & Lin, Y. 2009, "Silver nanoparticles: green synthesis and their antimicrobial activities", *Advances in Colloid and Interface Science*, vol. 145, no. 1, pp. 83-96.
- Shirtcliffe, N., Nickel, U. & Schneider, S. 1999, "Reproducible preparation of silver sols with small particle size using borohydride reduction: for use as nuclei for preparation of larger particles", *Journal of Colloid and Interface Science*, vol. 211, no. 1, pp. 122-129.
- Siegler, R.L. 2003, "Postdiarrheal Shiga toxin-mediated hemolytic uremic syndrome", *Journal of the American Medical Association (JAMA)*, vol. 290, no. 10, pp. 1379-1381.
- Siegler, R.L. 1995, "The hemolytic uremic syndrome", *Pediatric clinics of North America*, vol. 42, no. 6, pp. 1505-1529.
- Simon-Deckers, A., Loo, S., Mayne-L'hermite, M., Herlin-Boime, N., Menguy, N., Reynaud, C., Gouget, B. & Carrière, M. 2009, "Size-, composition- and shape-dependent toxicological impact of metal oxide nanoparticles and carbon nanotubes toward bacteria", *Environmental Science & Technology*, vol. 43, no. 21, pp. 8423-8429.
- Singh, T. & Coogan, M. 2005, "Isolation of pathogenic *Legionella species* and *legionella-laden amoebae* in dental unit waterlines", *Journal of Hospital Infection*, vol. 61, no. 3, pp. 257-262.
- Singh, R., Stine, O.C., Smith, D.L., Spitznagel, J.K., Jr, Labib, M.E. & Williams, H.N. 2003, "Microbial diversity of biofilms in dental unit water systems", *Applied and Environmental Microbiology*, vol. 69, no. 6, pp. 3412-3420.
- Smetana, A.B., Klabunde, K.J., Marchin, G.R. & Sorensen, C.M. 2008, "Biocidal activity of nanocrystalline silver powders and particles", *Langmuir*, vol. 24, no. 14, pp. 7457-7464.
- Sondi, I. & Salopek-Sondi, B. 2004, "Silver nanoparticles as antimicrobial agent: a case study on *E. coli* as a model for Gram-negative bacteria", *Journal of Colloid and Interface Science*, vol. 275, no. 1, pp. 177-182.
- Song, K.C., Lee, S.M., Park, T.S. & Lee, B.S. 2009, "Preparation of colloidal silver nanoparticles by chemical reduction method", *Korean Journal of Chemical Engineering*, vol. 26, no. 1, pp. 153-155.
- Soroushian, B., Lampre, I., Belloni, J. & Mostafavi, M. 2005, "Radiolysis of silver ion solutions in ethylene glycol: solvated electron and radical scavenging yields", *Radiation Physics and Chemistry*, vol. 72, no. 2, pp. 111-118.

- Sotiriou, G.A. & Pratsinis, S.E. 2010, "Antibacterial activity of nanosilver ions and particles", *Environmental Science & Technology*, vol. 44, no. 14, pp. 5649-5654.
- Sreeprasad, T., Maliyekkal, S.M., Lisha, K. & Pradeep, T. 2011, "Reduced graphene oxide–metal/metal oxide composites: Facile synthesis and application in water purification", *Journal of Hazardous Materials*, vol. 186, no. 1, pp. 921-931.
- Stoeva, S., Klabunde, K.J., Sorensen, C.M. & Dragieva, I. 2002, "Gram-scale synthesis of monodisperse gold colloids by the solvated metal atom dispersion method and digestive ripening and their organization into two- and three-dimensional structures", *Journal of the American Chemical Society*, vol. 124, no. 10, pp. 2305-2311.
- Su, C. & Brandt, L.J. 1995, "*Escherichia coli* O157: H7 infection in humans", *Annals of Internal Medicine*, vol. 123, no. 9, pp. 698-707.
- Szymańska, J. 2005, "Microbiological risk factors in dentistry. Current status of knowledge", *Annals of Agricultural and Environmental Medicine*, vol. 12, no. 2, pp. 157-163.
- Tarleton, S. 2015, "Surface area: Brunauer-Emmett-Teller" in Progress in filtration and separation, ed. S. Tarleton, *Elsevier Ltd*, USA, pp. 585-608.
- Tauxe, R.V. 1997, "Emerging foodborne diseases: an evolving public health challenge", *Emerging Infectious Diseases*, vol. 3, no. 4, pp. 425-434.
- Thomas, V., Yallapu, M.M., Sreedhar, B. & Bajpai, S. 2007, "A versatile strategy to fabricate hydrogel–silver nanocomposites and investigation of their antimicrobial activity", *Journal of Colloid and Interface Science*, vol. 315, no. 1, pp. 389-395.
- Timko, M., Molcan, M., Hashim, A., Skumiel, A., Muller, M., Gojzewski, H., Jozefczak, A., Kovac, J., Rajnak, M. & Makowski, M. 2013, "Hyperthermic effect in suspension of magnetosomes prepared by various methods", *IEEE Transactions on Magnetics*, vol. 49, no. 1, pp. 250-254.
- Tiwari, D.K., Behari, J. & Sen, P. 2008, "Application of nanoparticles in waste water treatment", *World Applied Sciences Journal*, vol. 3, no. 3, pp. 417-433.
- Upadhyayula, V.K., Deng, S., Mitchell, M.C. & Smith, G.B. 2009, "Application of carbon nanotube technology for removal of contaminants in drinking water: a review", *Science of the Total Environment*, vol. 408, no. 1, pp. 1-13.
- Varlan, A.R., Sansen, W., Loey, A.V. & Hendrickx, M. 1996, "Covalent enzyme immobilization on paramagnetic polyacrolein beads", *Biosensors and Bioelectronics*, vol. 11, no. 4, pp. 443-448.
- Wadowsky, R.M., Wolford, R., McNamara, A.M. & Yee, R.B. 1985, "Effect of temperature, pH, and oxygen level on the multiplication of naturally occurring

Legionella pneumophila in potable water", *Applied and Environmental Microbiology*, vol. 49, no. 5, pp. 1197-1205.

- Wang, X., Dai, Y., Zou, J., Meng, L., Ishikawa, S., Li, S., Abuobeidah, M. & Fu, H. 2013, "Characteristics and antibacterial activity of Ag-embedded Fe₃O₄@SiO₂ magnetic composite as a reusable water disinfectant", *Royal Society of Chemistry Advances*, vol. 3, no. 29, pp. 11751-11758.
- Wang, X., Zhuang, J., Peng, Q. & Li, Y. 2005, "A general strategy for nanocrystal synthesis", *Nature*, vol. 437, no. 7055, pp. 121-124.
- Waterbeemd, D. & Van, M. 2009, Silane condensation to nanoparticles in suspension, PhD, *The University of Kent*, Kent.
- Wegscheider, W. 2012, "Modern methods of analysis in mineral raw materials industry", *BHM Berg-und Hüttenmännische Monatshefte*, pp. 1-6.
- Wu, P., Zhu, J. & Xu, Z. 2004, "Template-assisted synthesis of mesoporous magnetic nanocomposite particles", *Advanced Functional Materials*, vol. 14, no. 4, pp. 345-351.
- Yamamoto, O. 2001, "Influence of particle size on the antibacterial activity of zinc oxide", *International Journal of Inorganic Materials*, vol. 3, no. 7, pp. 643-646.
- Yamanaka, M., Hara, K. & Kudo, J. 2005, "Bactericidal actions of a silver ion solution on Escherichia coli, studied by energy-filtering transmission electron microscopy and proteomic analysis", *Applied and Environmental Microbiology*, vol. 71, no. 11, pp. 7589-7593.
- Yao, K. 2005, Higher performance polyurethane-organoclay nanocomposites, PhD edn, *Loughborough University Leicestershire, UK*, Leicestershire.
- Yeo, S.Y. & Jeong, S.H. 2003, "Preparation and characterization of polypropylene/silver nanocomposite fibers", *Polymer International*, vol. 52, no. 7, pp. 1053-1057.
- Yi, D.K., Selvan, S.T., Lee, S.S., Papaefthymiou, G.C., Kundaliya, D. & Ying, J.Y. 2005, "Silica-coated nanocomposites of magnetic nanoparticles and quantum dots", *Journal of the American Chemical Society*, vol. 127, no. 14, pp. 4990-4991.
- Zhang, D., Fakhrullin, R.F., Özmen, M., Wang, H., Wang, J., Paunov, V.N., Li, G. & Huang, W.E. 2011, "Functionalization of whole-cell bacterial reporters with magnetic nanoparticles", *Microbial Biotechnology*, vol. 4, no. 1, pp. 89-97.
- Zhang, L., Jiang, Y., Ding, Y., Povey, M. & York, D. 2007, "Investigation into the antibacterial behaviour of suspensions of ZnO nanoparticles (ZnO nanofluids)", *Journal of Nanoparticle Research*, vol. 9, no. 3, pp. 479-489.

- Zhao, W., Gu, J., Zhang, L., Chen, H. & Shi, J. 2005, "Fabrication of uniform magnetic nanocomposite spheres with a magnetic core/mesoporous silica shell structure", *Journal of the American Chemical Society*, vol. 127, no. 25, pp. 8916-8917.
- Zhou, Z., Wang, J., Liu, X. & Chan, H. 2001, "Synthesis of Fe₃O₄ nanoparticles from emulsions", *Journal of Materials Chemistry*, vol. 11, no. 6, pp. 1704-1709.
- Zou, J., Peng, Y. & Tang, Y. 2014, "A facile bi-phase synthesis of Fe₃O₄@SiO₂ core-shell nanoparticles with tunable film thicknesses", *Royal Society of Chemistry Advances*, vol. 4, no. 19, pp. 9693-9700.

Appendices

Appendix A-1

Preparation Method II

Bi-Phasic Magnetite Nanocomposite Mixture

1g MWCNT was introduced in 20 mL of FeCl₂ and FeCl₃ solution (1:2 molar solution) into a conical flask and stirred using a magnetic stirrer for an hour. After stirring, 50 mL of 1.6M solution of NH₄OH was added and stirred for further an hour, followed by centrifuge for 7-8 minutes at 4000 rpm. Upon completion of the centrifugation, the liquid was poured out carefully and the materials were washed in water before filtration.

Bi-Phasic Silver Nanocomposite Mixture

1g of solid commercial material (carbon nanotube) was introduced into 20 mL of 0.1M solution of silver nitrate and stirred with a magnetic stirrer for 1 hour.

After stirring, 50 mL of the 0.2M solution of the NaBH₄ was added and stirred for a further hour, followed by centrifuge for 7-8 minutes at 4000 rpm. The liquid was poured out carefully and the composite biphasic mixture was filtered and dried.

Bi-Phasic Magnetite Silver Nanocomposite Mixture

1g of solid biphasic magnetite nanocomposite was introduced into the 20 mL of 0.1M solution of silver nitrate and stirred for an hour.

After stirring, 50 mL of the 0.2M solution of NaBH₄ was added and stirred for a further hour, followed by centrifugation for 7-8 minutes at 4000 rpm; on completion of the centrifugation it was taken out from the centrifuge machine and the liquid was poured

out carefully; here 4 to 5 mL of water was introduced into the tube and then the biphasic mixture of magnetite silver nanocomposite was filtered and dried at room temperature.

Preparation Method III

Nanocomposite Materials by Wet Impregnation Process

This method was used for the preparation of silver-based nanocomposite materials by using different commercial materials (the list is given in section 2.1, such as MWCNT, AC, CPW-14, CPW-80 and DAE).

20 mL of 0.05M and 0.1M solutions of silver nitrate were introduced into the flask and 1g of each commercial material was added into the solution and gently stirred for 24 hours. After 24 hours, the suspension was centrifuged, washed, filtered and dried at RT for 24 hrs. After drying, the solid material was again soaked for 24 hours in 20 mL of 0.2M solution of the sodium borohydride then centrifuged, washed with deionised water ($\times 3$), filtered and dried.

Preparation Method IV

Magnetite Nanocomposite

0.5 g of commercially purchased solid materials (see section 2.1) was added into 20 mL of the solution of magnetite nanoparticles and was soaked in it for about one hour, followed by the addition of a few drops of 28% NH_4OH solution during the filtration of the soaked suspension on the filter paper. Furthermore, black colour was observed on the filter paper due to the addition of 28% NH_4OH in the mixture, which is the sign for the preparation of the iron oxide particles. Moreover, the filtered developed

material was dried at room temperature.

Silver Nanocomposites

0.5g of commercially purchased solid materials (see section 2.1) was added into 20 mL solution of silver nanoparticles. The concentration of silver nitrate solution was 0.001M and sodium borohydride was 0.002M. The solids were soaked in the solution for 30 minutes, which was followed by filtration on the filter paper along with the addition of a few drops of 0.002M NaBH₄ solution.

There was no change in the colour of the materials by the addition of the few drops of 0.002M NaBH₄ on the filtered silver composite.

Magnetite Silver Nanocomposites

One sample batch (0.5g) of developed magnetite nanocomposites was added into the 20 mL solution of silver nanoparticle. The solids were soaked in the solution for 30 minutes, which was followed by filtration on the filter paper along with the addition of a few drops of 0.002M NaBH₄ solution, and colour was observed finally, the developed material was dried at room temperature.

There was no change in the colour of the materials caused by the addition of a few drops of 0.002M NaBH₄ on the filtered magnetite silver nanocomposites but there was a tiny change in colour.

Appendix A-2

QM1-Based Composite

(a) Legionella

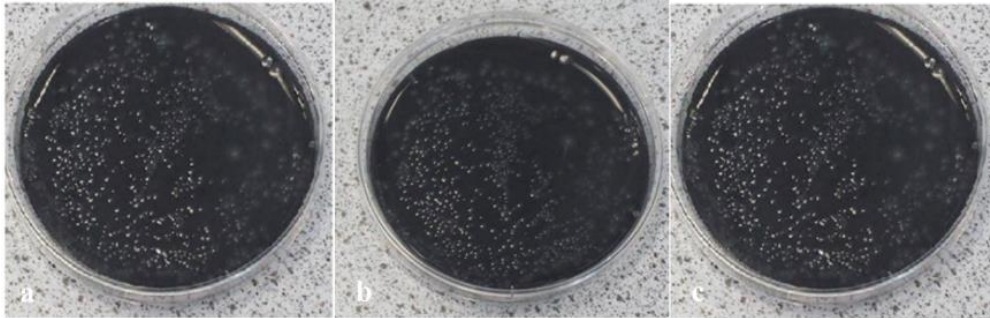


Figure A2-1 Control plates in DW with legionella (a) 10^{-8} Plate-1(b) 10^{-8} Plate-2 (c) 10^{-8} Plate-3

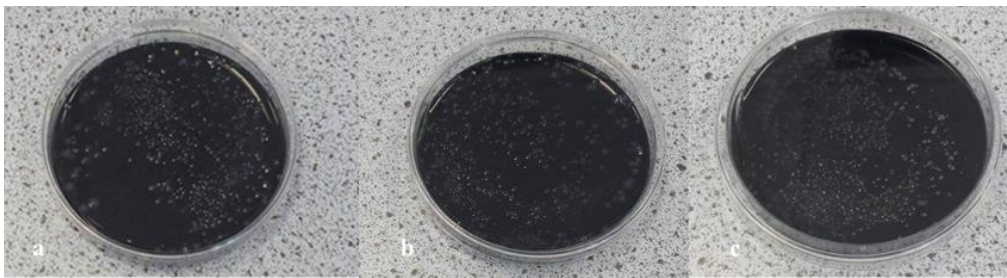


Figure A2- 2 QM1 against *Legionella* (a) 10^{-3} Plate-1(b) 10^{-3} Plate-2 (c) 10^{-3} Plate-3

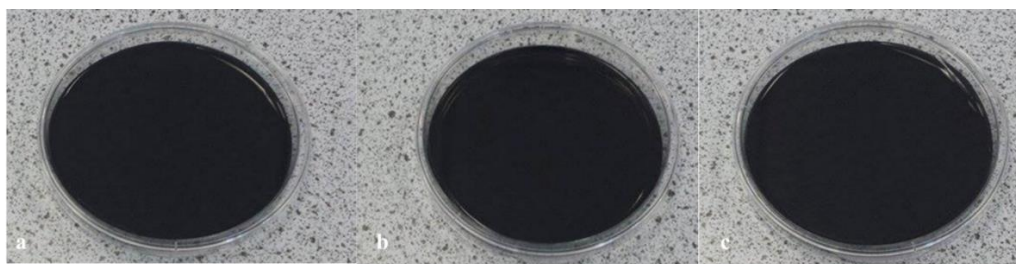


Figure A2-3 QM1-3 composite against *Legionella* (a) 10^{-0} Plate-1(b) 10^{-0} Plate-2 (c) 10^{-0} Plate-3

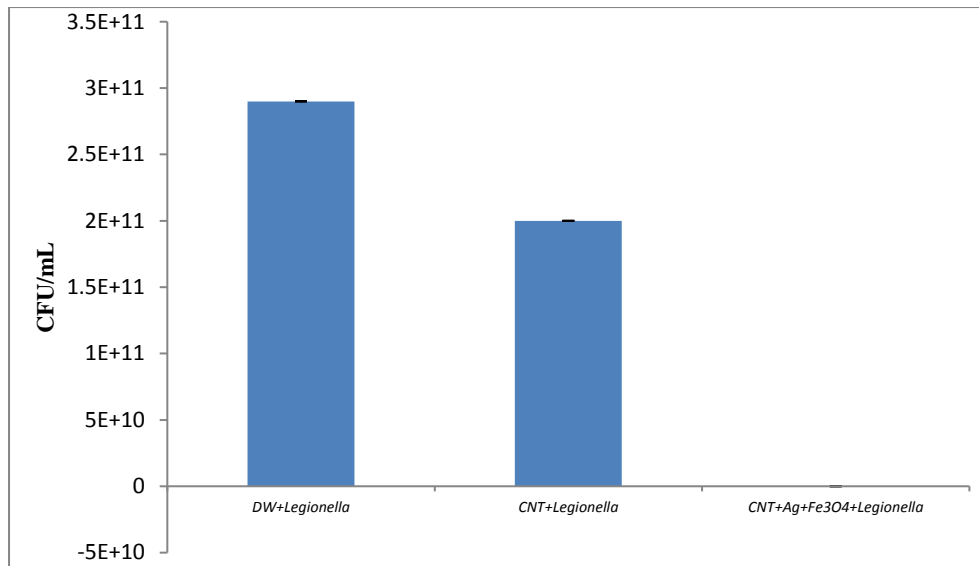


Figure A2-4 QM1 and QM1-3 against *Legionella* in sterilised water

QM2-Based Composite

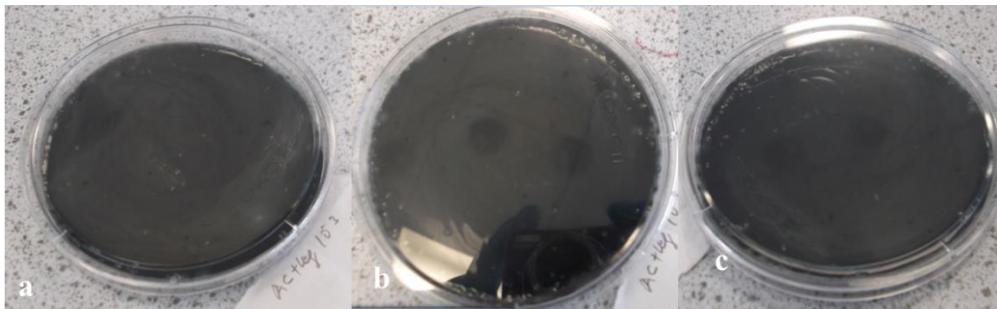


Figure A2- 5 (a and c) QM2 against *Legionella*

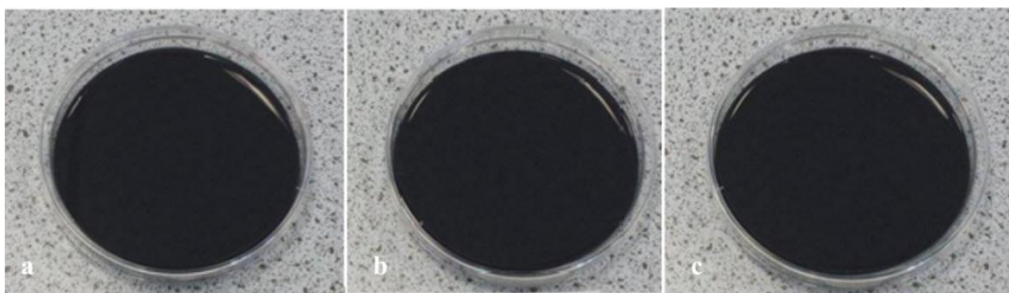


Figure A2-6 (a, b and c) QM2-3composite against *Legionella* in triplicate

QM3-Based Composite

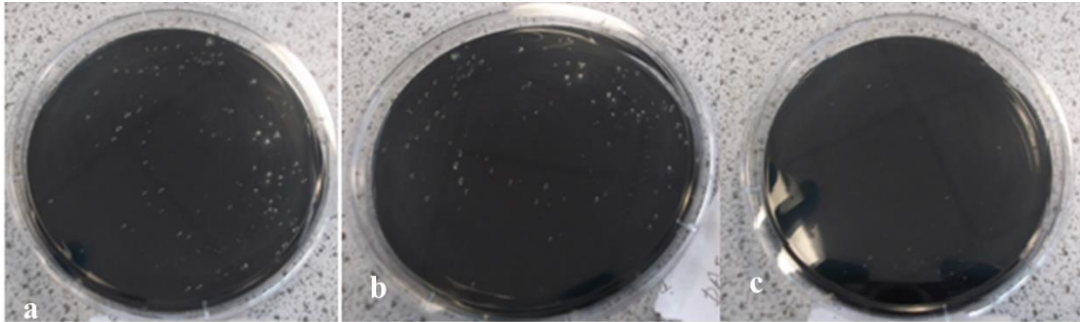


Figure A2-7 (a, b and c) QM3 against *Legionella*



Figure A2-8 (a, b and c) QM3-3 composite against *Legionella*

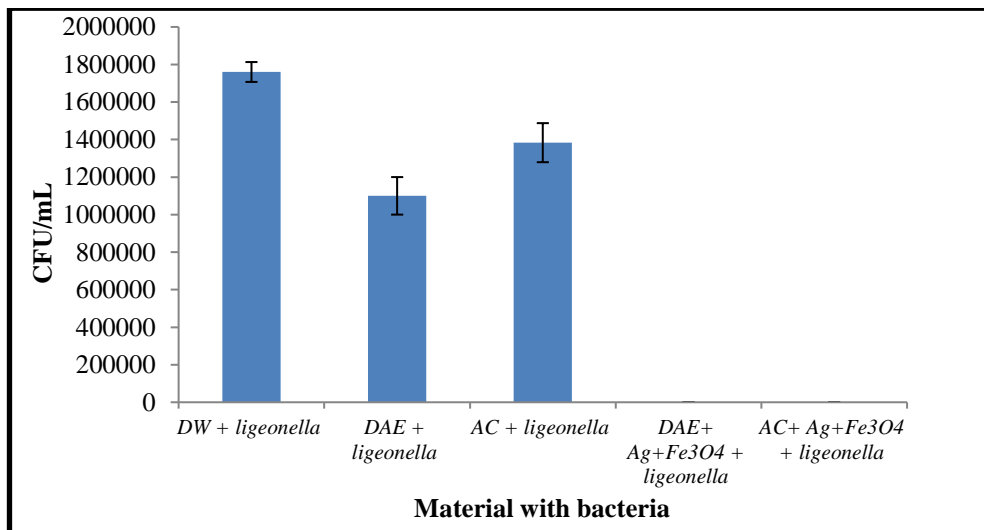


Figure A2-9 analysis of QM2, QM2-2, QM3, QM3-3 against *Legionella*

(b) Antimicrobial of Composites Against *E. coli* DH5- α



Figure A2-10 Control plates of *E. coli* in DW (distilled water)

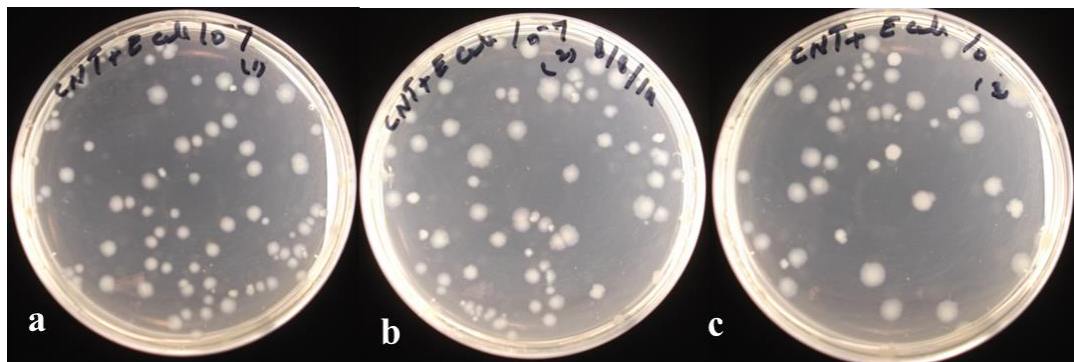


Figure A2-11 (a, b and c) QM1 against *E. coli*

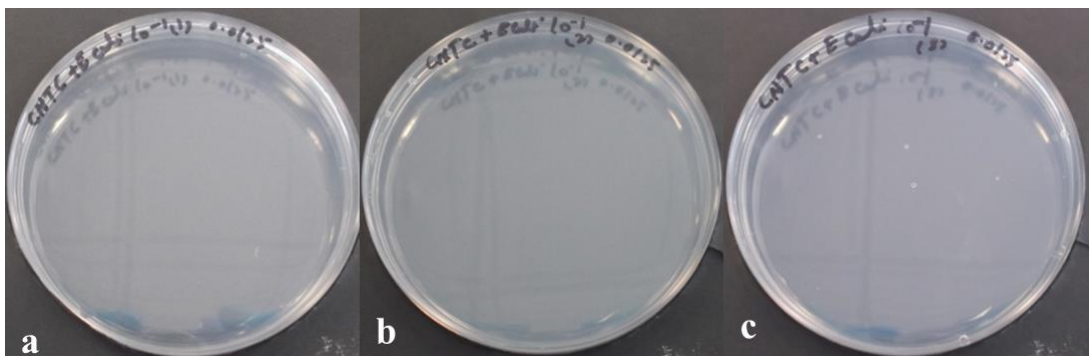


Figure A2-12 (a, b and c) QM1-3 against *E. coli*

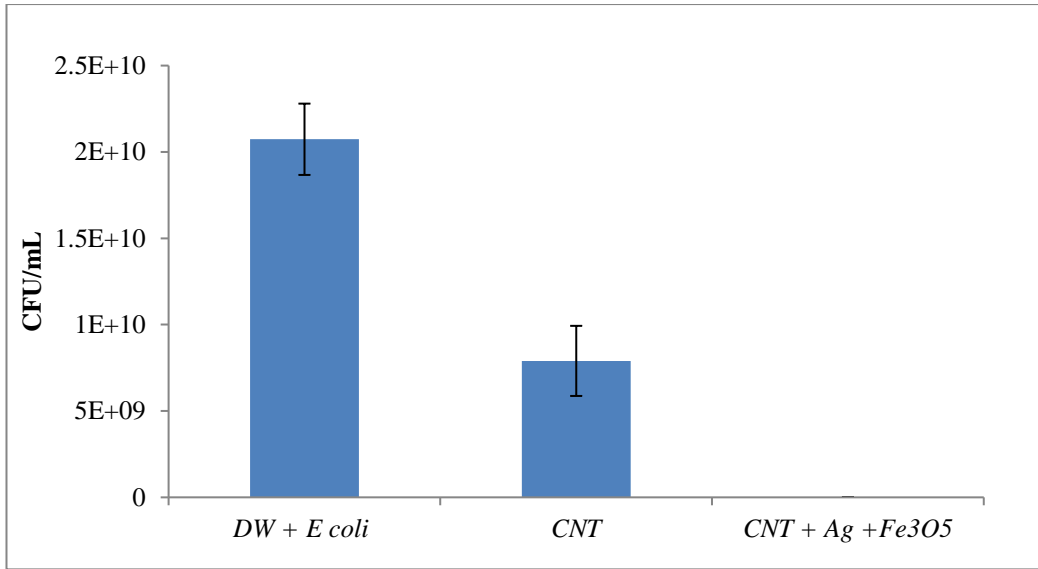


Figure A2-13 analysis of QM1, QM1-3 against *E. coli*

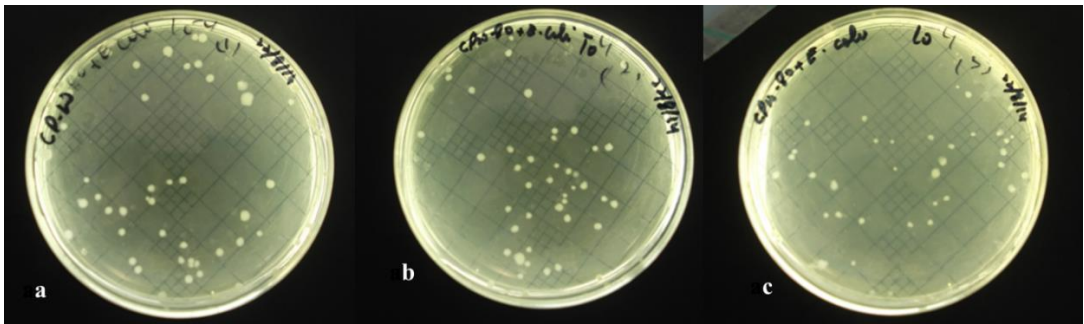


Figure A2-14 (a, b and c) QM5 with *E. coli*

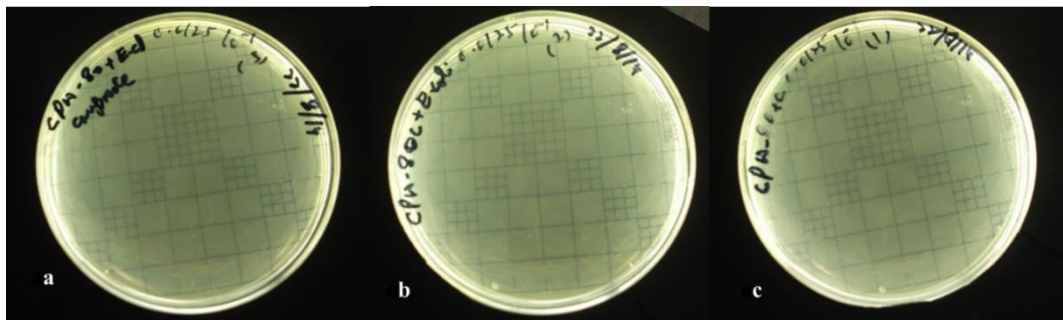


Figure A2-15 (a, b and c) QM4-3 against with *E. coli*

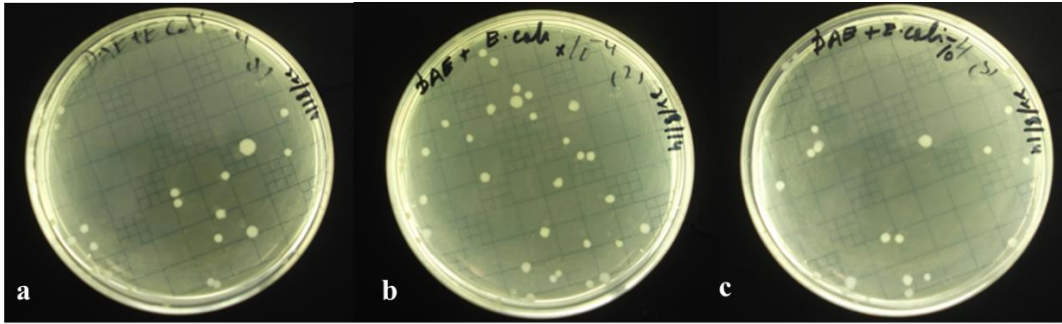


Figure A2-16 (a, b and c) QM3 against with *E. coli*

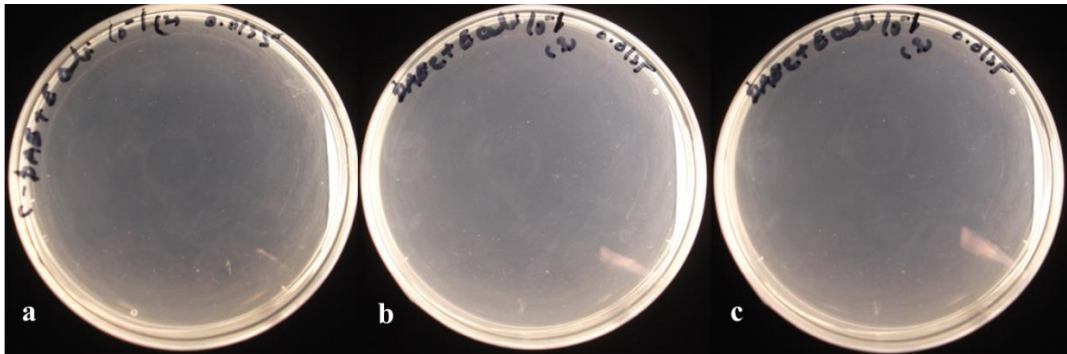


Figure A2-17 (a, b and c) QM3-3 against with *E. coli*

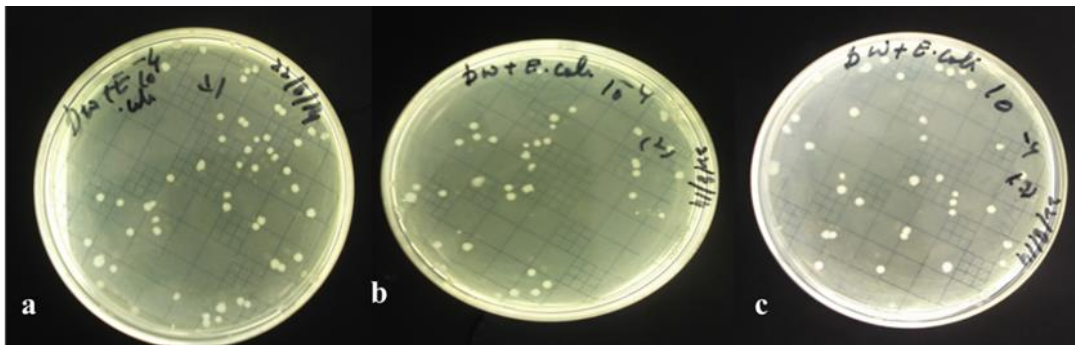


Figure A2-18 Control plates of *E. coli*

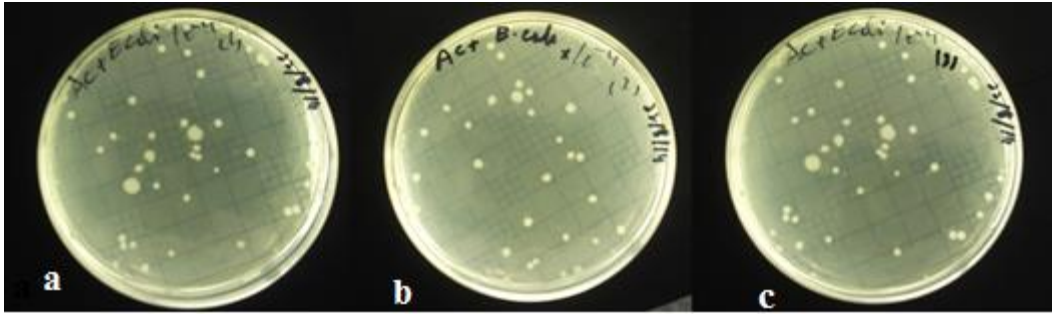


Figure A2-19 (a, b and c) QM2 against *E. coli*

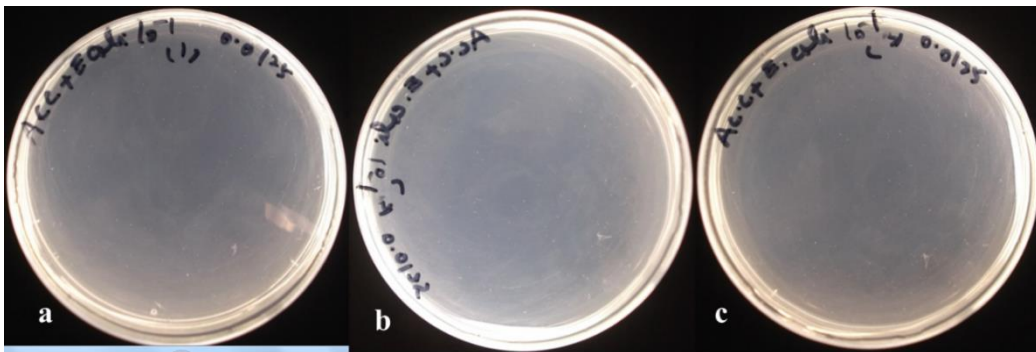


Figure A2-20 (a, b and c) QM2-3 against *E. coli*

Applications of the Composites on the *Pseudomonas aeruginosa*

QM2 and QM2-3-based composite (Activated charcoal and its composites)



Figure A2-22 Control plates of *Pseudomonas aeruginosa* in DW

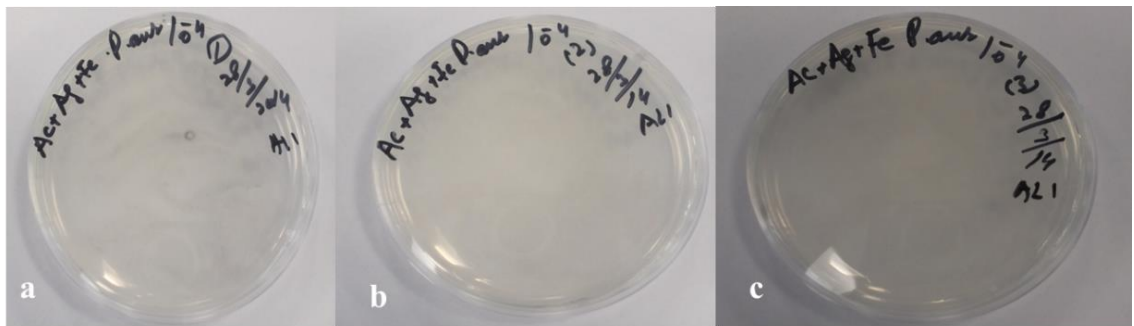


Figure A2-23 (a, b and c) QM2-3 against *Pseudomonas aeruginosa*

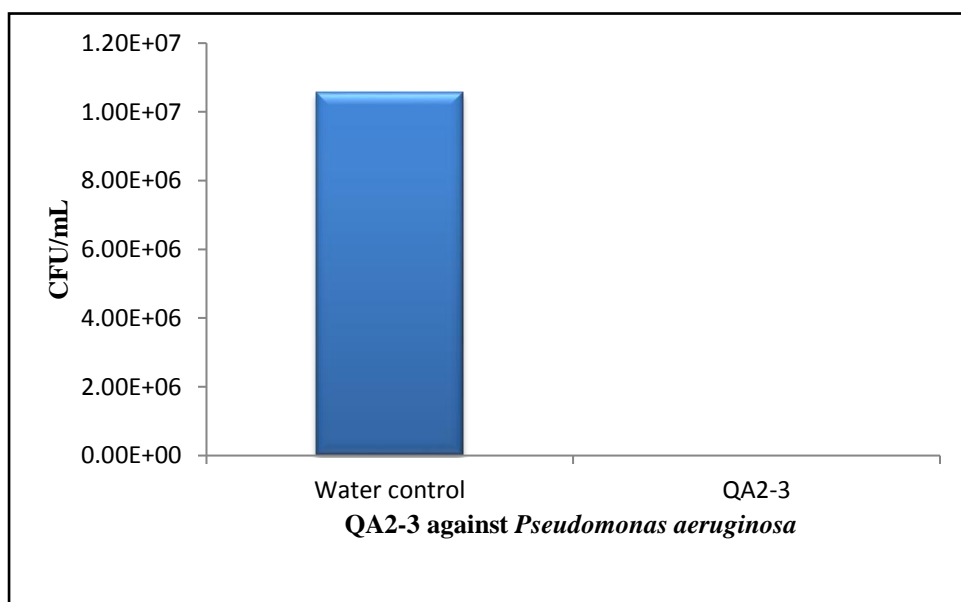


Figure A2-23 analysis of QM2-3 against *E. coli*

Applications of the Composites on the *Klebsiella pneumoniae*

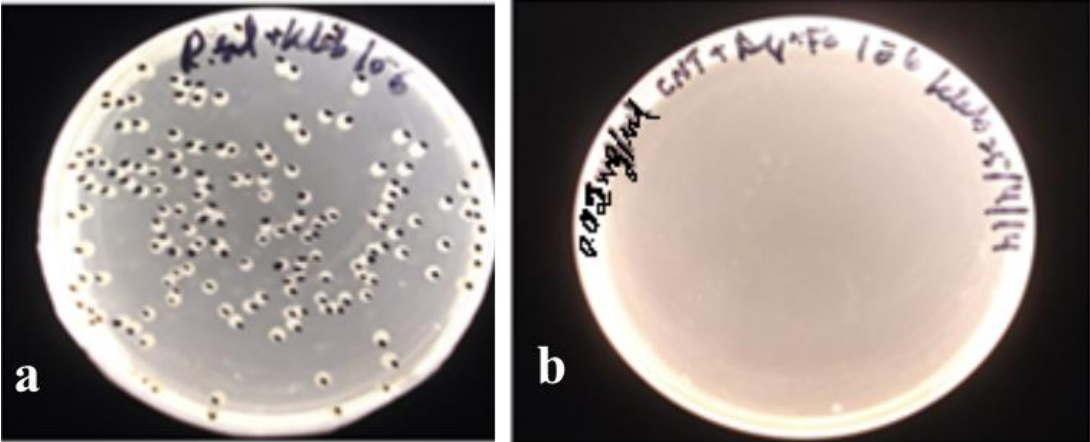


Figure A2-24 (a and b) Control of *K. pneumoniae* in ringer and QM1-3 against *K. pneumoniae*

Calculation for the Concentration of the Stock Solution of the Composite for Antimicrobial Applications.

The concentration of the stock solution was 2000 µg/mL; solution of 1000 µL was prepared which included the 100 µL of pure culture.

$$1. \frac{10 \times 1000}{2000} = 5 \mu g$$

So 5 µL of stock composite, 100 µL of culture and 895 µL of Ringer solution

$$5 + 100 + 895 = 1000 \mu L$$

Stock composite + Pure culture + Ringer solution = 1000 µL total sample

$$2. \frac{20 \times 1000}{2000} = 10 \mu g$$

So, 10 µL of stock composites, 100 µL of culture and 890 µL of ringer solution

$$10 + 100 + 890 = 1000 \mu L$$

Stock composite + Pure culture + Ringer solution = 1000 µL total sample

$$3. \frac{30 \times 1000}{2000} = 15 \mu g$$

So, 15 µL of stock composite, 100 µL of culture and 885 µL of ringer solution

$$15 + 100 + 885 = 1000 \mu L$$

Stock composite + Pure culture + Ringer solution = 1000 µL total sample

$$4. 50 \mu g/mL = 50 \times 1000 \frac{50 \times 1000}{2000} = 25 \mu g$$

So 25 µL of stock composites, 100 µL of culture and 875 µL of Ringer

solution

$$25+100+875= 1000 \mu\text{L}$$

Stock composite +Pure culture +Ringer solution= 1000 μL total sample

$$5. \quad \frac{100 \times 1000}{2000} = 50 \mu\text{g}$$

So, 50 μL of stock composite, 100 μL of culture and 850 μL of Ringer solution

$$50+100+850= 1000 \mu\text{L}$$

Stock composite +Pure culture +Ringer solution= 1000 μL total sample

$$6. \quad \frac{200 \times 1000}{2000} = 100 \mu\text{g}$$

So, 100 μL of stock composites, 100 μL of culture and 800 μL of Ringer solution

$$100+100+800= 1000 \mu\text{L}$$

Stock composite +Pure culture +Ringer solution= 1000 μL total sample

$$7. \quad \frac{300 \times 1000}{2000} = 150 \mu\text{g}$$

So, 150 μL of stock composites, 100 μL of culture and 750 μL of Ringer solution

$$150+100+750= 1000 \mu\text{L}$$

Stock composite +Pure culture +Ringer solution= 1000 μL total sample

Appendix-A-3

Antimicrobial applications of the Materials against *S. aureus*

MWCNTs-based composites (QM1, QM1-1, QM1-2 and QM1-3) against *S. aureus*

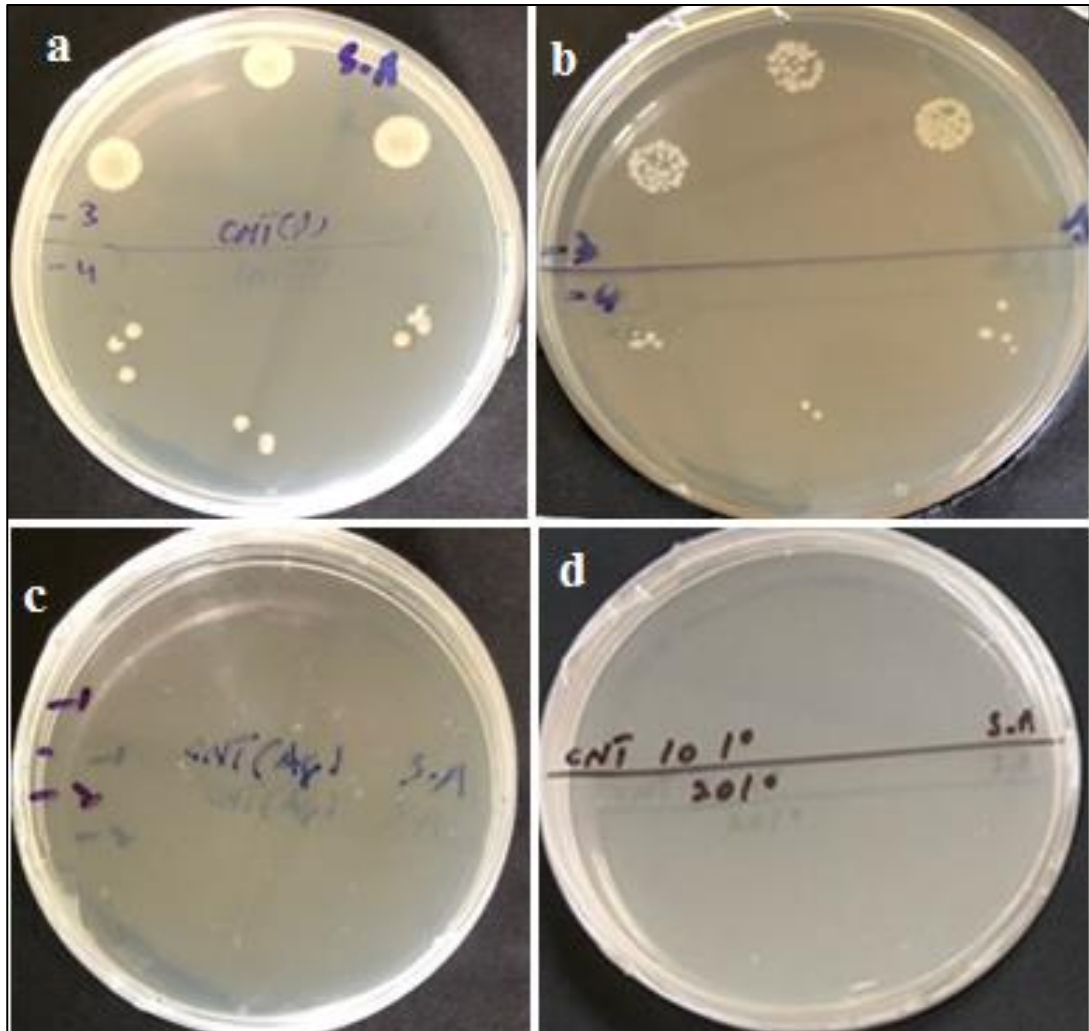


Figure A3-1 (a,b,c and d) MWCNTs-based composite (QM1) (a) QM1 (MWCNTs-unmodified) (b) QM1-1 (MWCNTs- modified with only iron oxide nanoparticles) (c) QM1-2 (MWCNTs - modified with only silver nanoparticles) and (d) QM1-3 (MWCNTs- modified with silver coating iron oxide against *S. aureus*)

AC-based composites (QM2, QM2-1, QM2-2 and QM2-3) against *S. aureus*

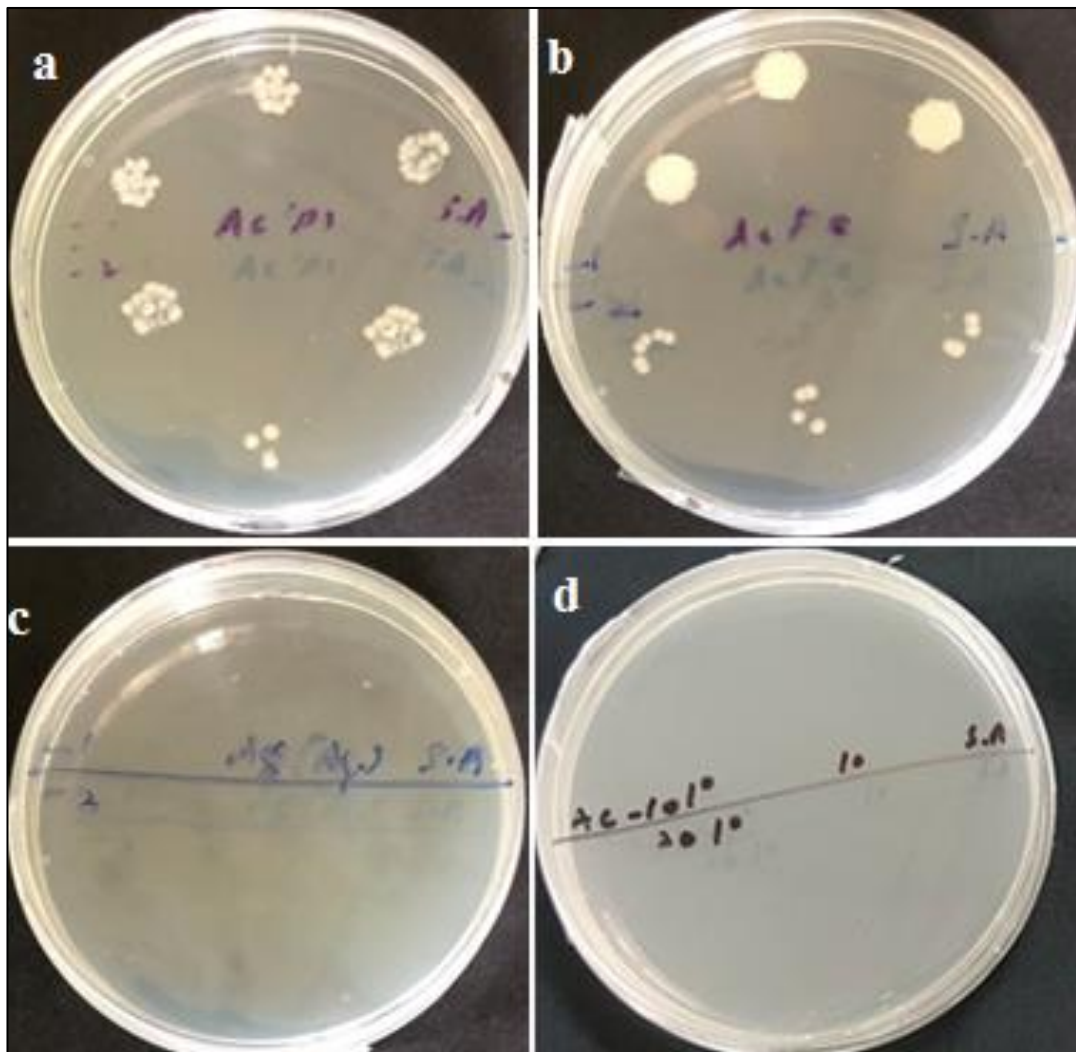


Figure A3-2 (a,b,c and d) AC-based composite (QM2) (a) QM2 (AC -unmodified) (b) QM2-1 (AC - modified with only iron oxide nanoparticles) (c) QM2-2 (AC - modified with only silver nanoparticles) and (d) QM2-3 (AC - modified with silver coating iron oxide against *S. aureus*

DAE composite) QM3, QM3-1, QM3-2 and QM3-3 against *S. aureus*

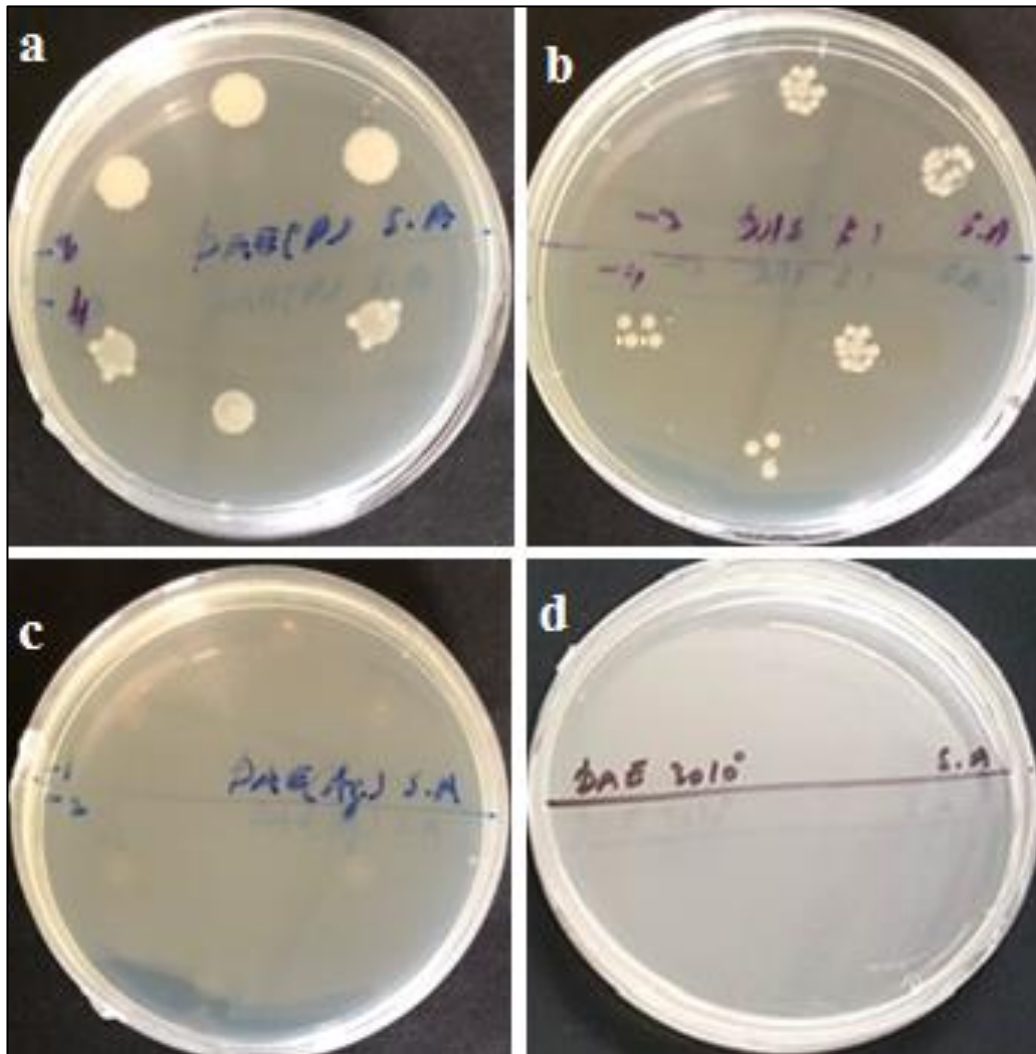


Figure A3-3 (a,b,c and d) DAE-based composite (QM3) (a) QM3 (DAE -unmodified) (b) QM3-1 (DAE - modified with only iron oxide nanoparticles) (c) QM3-2 (DAE - modified with only silver nanoparticles) and (d) QM3-3 (DAE - modified with silver coating iron oxide against *S. aureus*)

CPW-14 (QM4, QM4-1, QM4-2 and QM4-3) against *S. aureus*

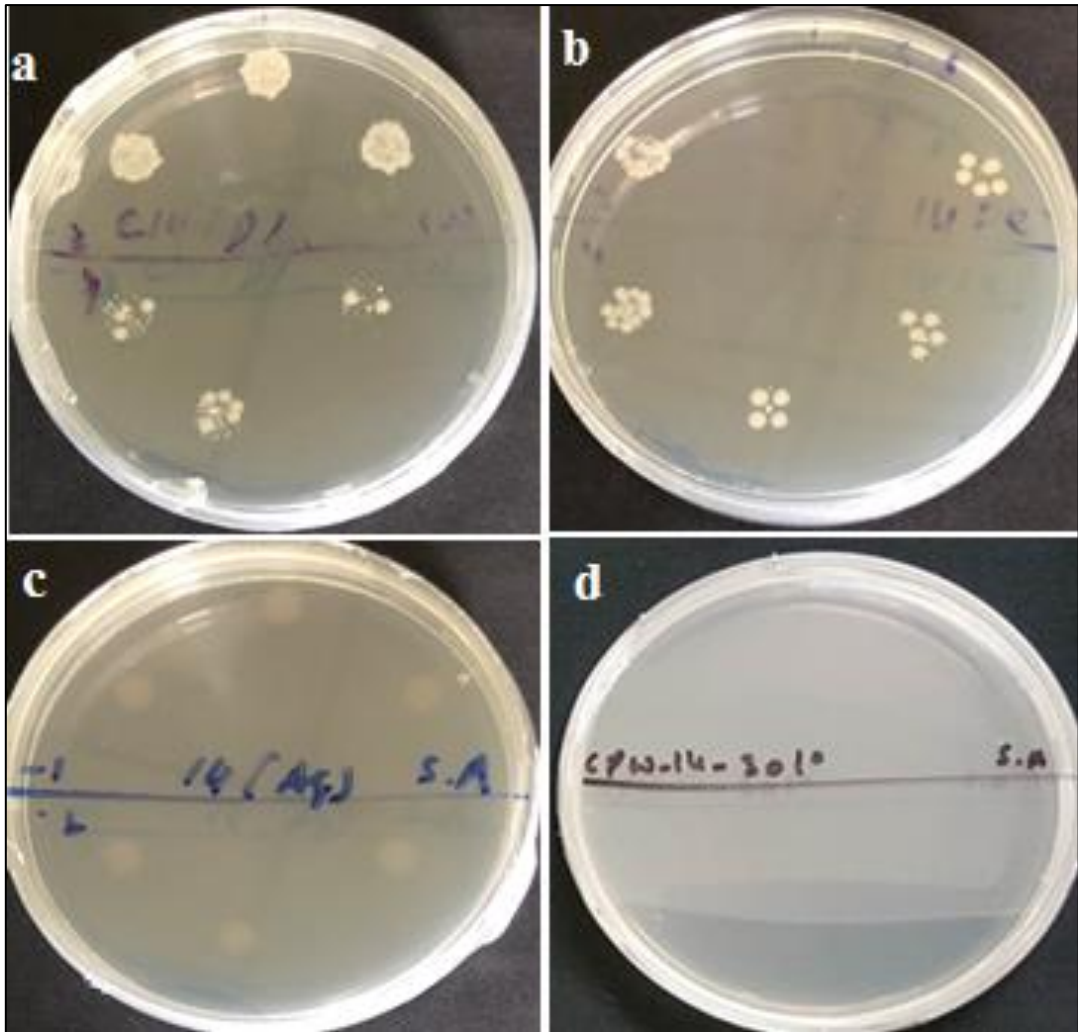


Figure A3-4 (a,b,c and d) CPW-14-based composite (QM4) (a) QM4 (CPW-14 -unmodified) (b) QM4-1 (CPW-14 - modified with only iron oxide nanoparticles) (c) QM4-2 (CPW-14 - modified with only silver nanoparticles) and (d) QM4-3 (CPW-14 - modified with silver coating iron oxide against *S. aureus*)

CPW-80 (QM5, QM5-1, QM5-2 and QM5-3) against *S. aureus*

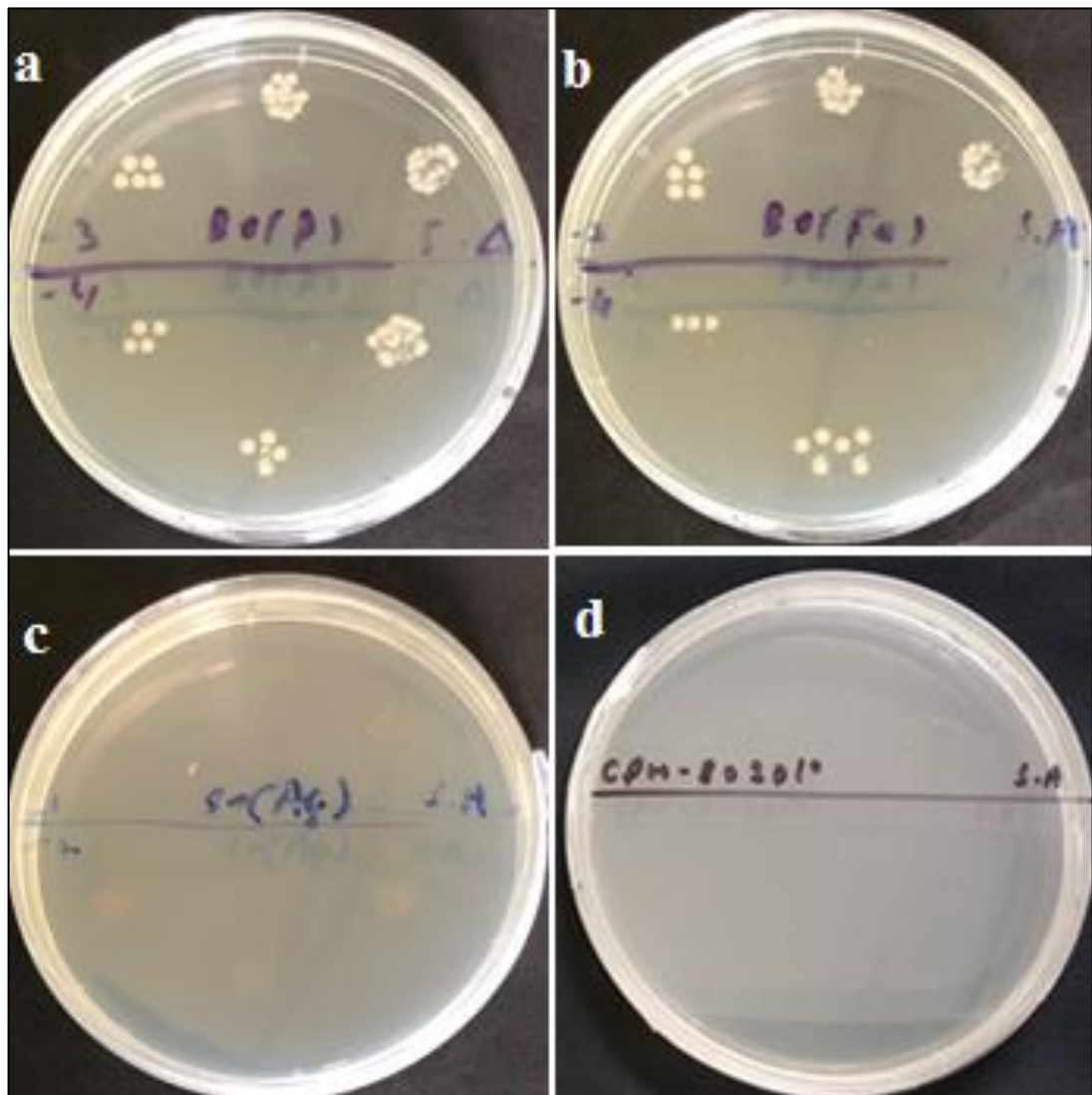


Figure A3-5 (a,b,c and d) CPW-80-based composite (QM5) (a) QM5 (CPW-80 - unmodified) (b) QM5-1 (CPW-80 - modified with only iron oxide nanoparticles) (c) QM5-2 (CPW-80 - modified with only silver nanoparticles) and (d) QM5-3 (CPW-80 - modified with silver coating iron oxide) against *S. aureus*

Antimicrobial applications of composites against *E. coli*

MWCNTs (QM1, QM1-1, QM1-2 and QM1-3) against *E. coli*

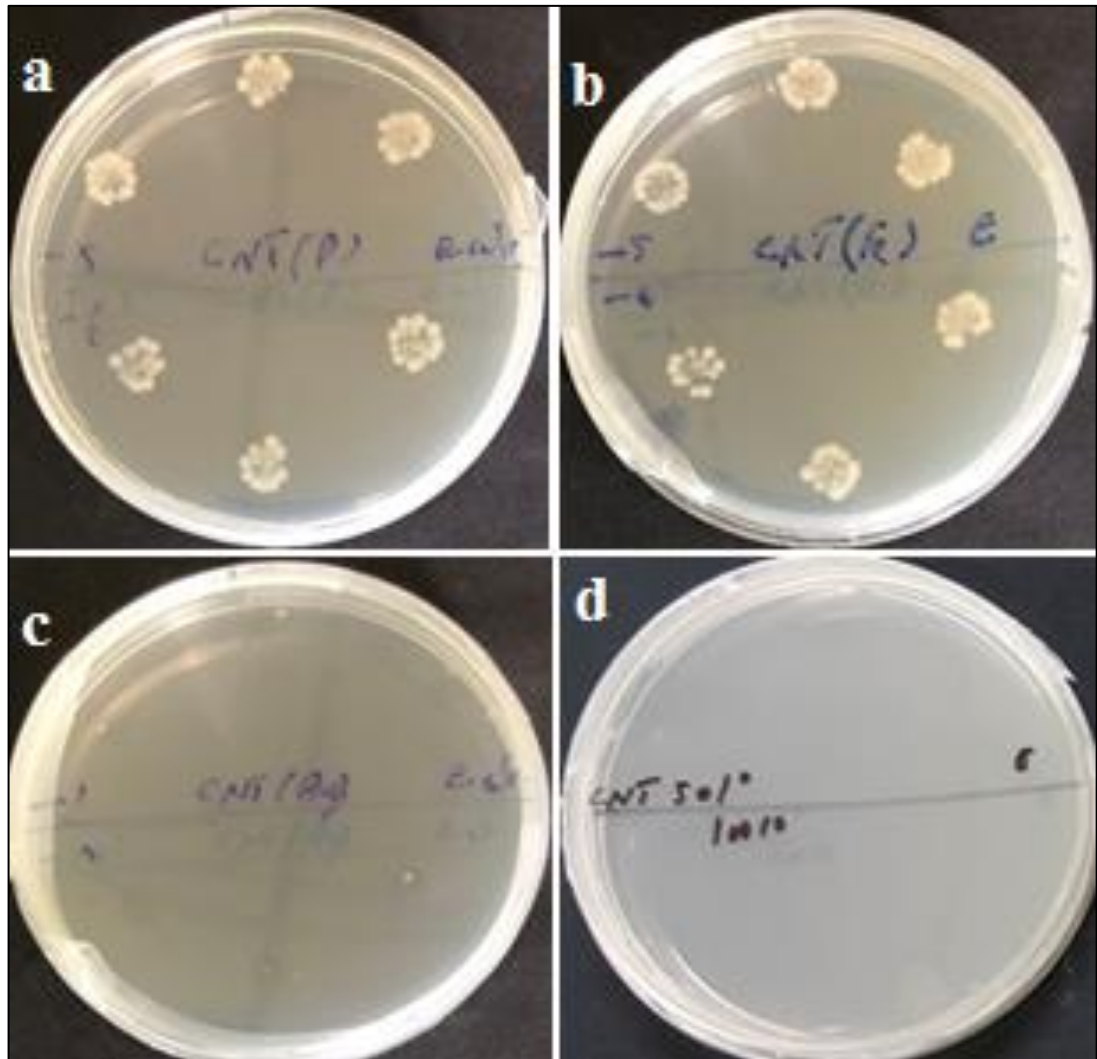


Figure A3-6 (a,b,c and d) MWCNTs-based composite (QM1) (a) QM1 (MWCNTs - unmodified) (b) QM1-1 (MWCNTs - modified with only iron oxide nanoparticles) (c) QM1-2 (MWCNTs - modified with only silver nanoparticles) and (d) QM1-3 (MWCNTs - modified with silver coating iron oxide against *E. coli*)

AC (QM2, QM2-1, QM2-2 and QM2-3) against *E. coli*

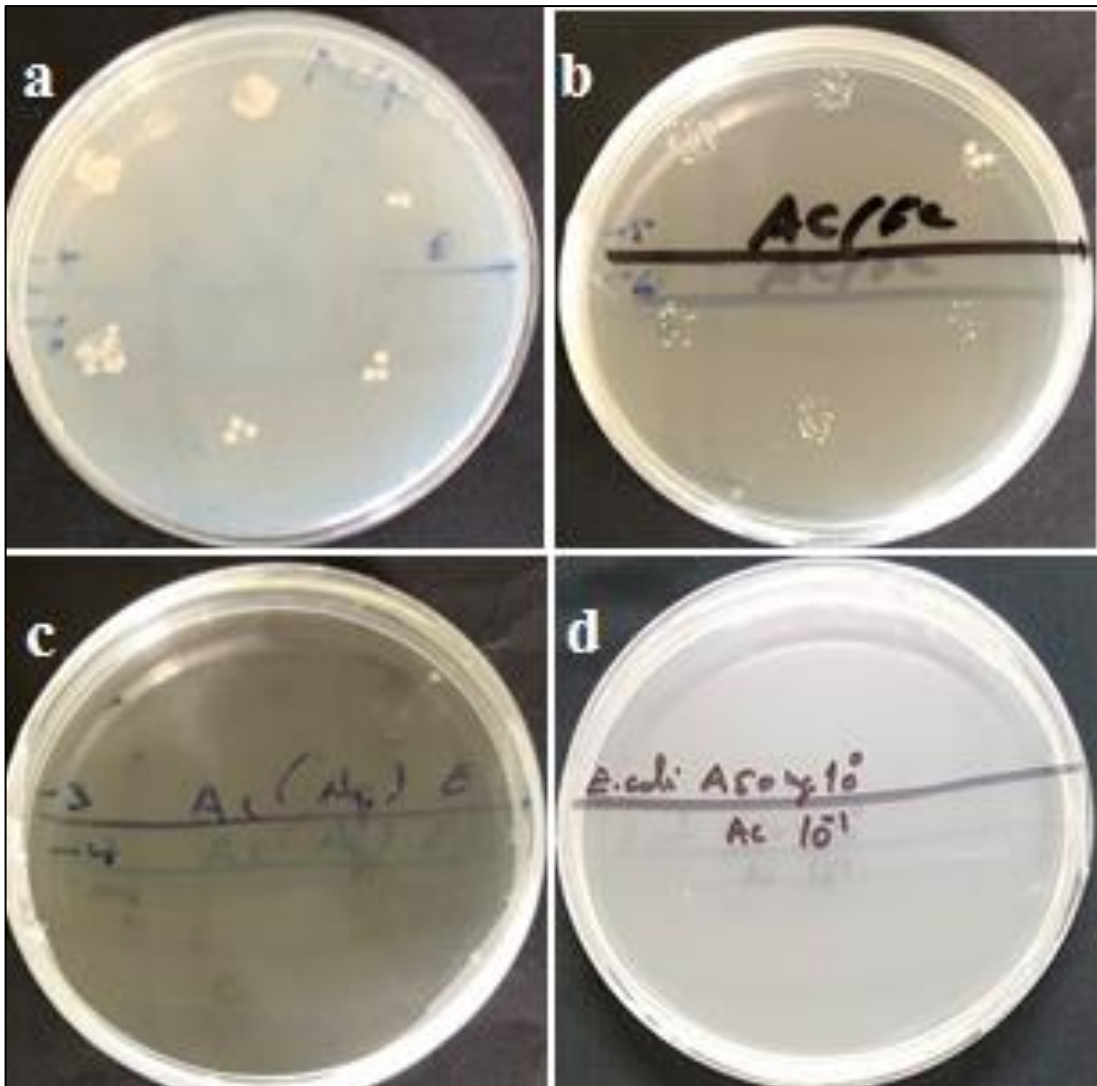


Figure A3-7 (a,b,c and d) AC-based composite (QM2) (a) QM2 (AC -unmodified) (b) QM2-1 (AC - modified with only iron oxide nanoparticles) (c) QM2-2 (AC - modified with only silver nanoparticles) and (d) QM2-3 (AC - modified with silver coating iron oxide against *E. coli*)

DAE (QM3, QM3-1, QM3-2 and QM3-3) against *E. coli*

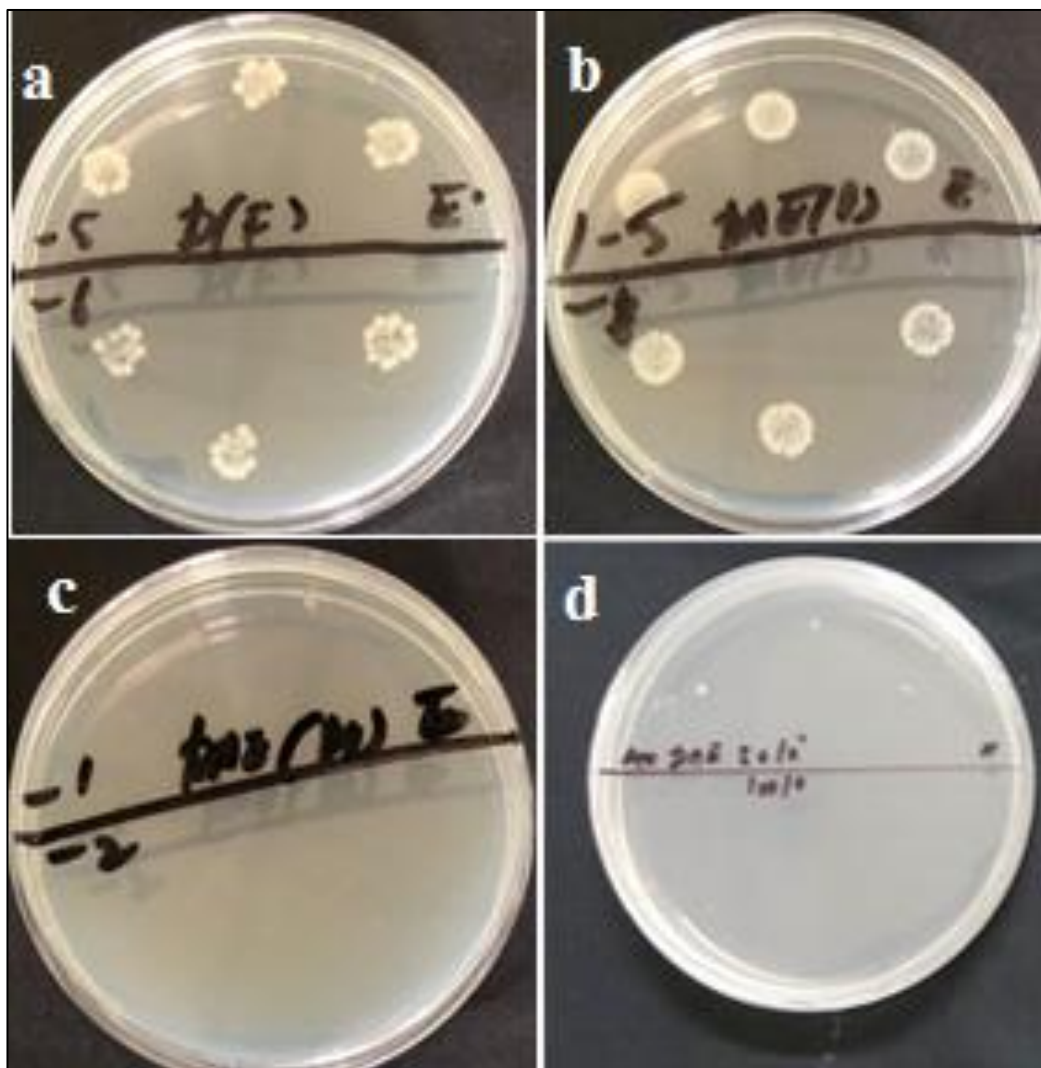


Figure A3-8 (a,b,c and d) DAE-based composite (QM3) (a) QM3 (DAE -unmodified) (b) QM3-1 (DAE - modified with only iron oxide nanoparticles) (c) QM3-2 (DAE - modified with only silver nanoparticles) and (d) QM3-3 (DAE - modified with silver coating iron oxide against *E. coli*

CPW-14 (QM4, QM4-1, QM4-2 and QM4-3) against *E. coli*

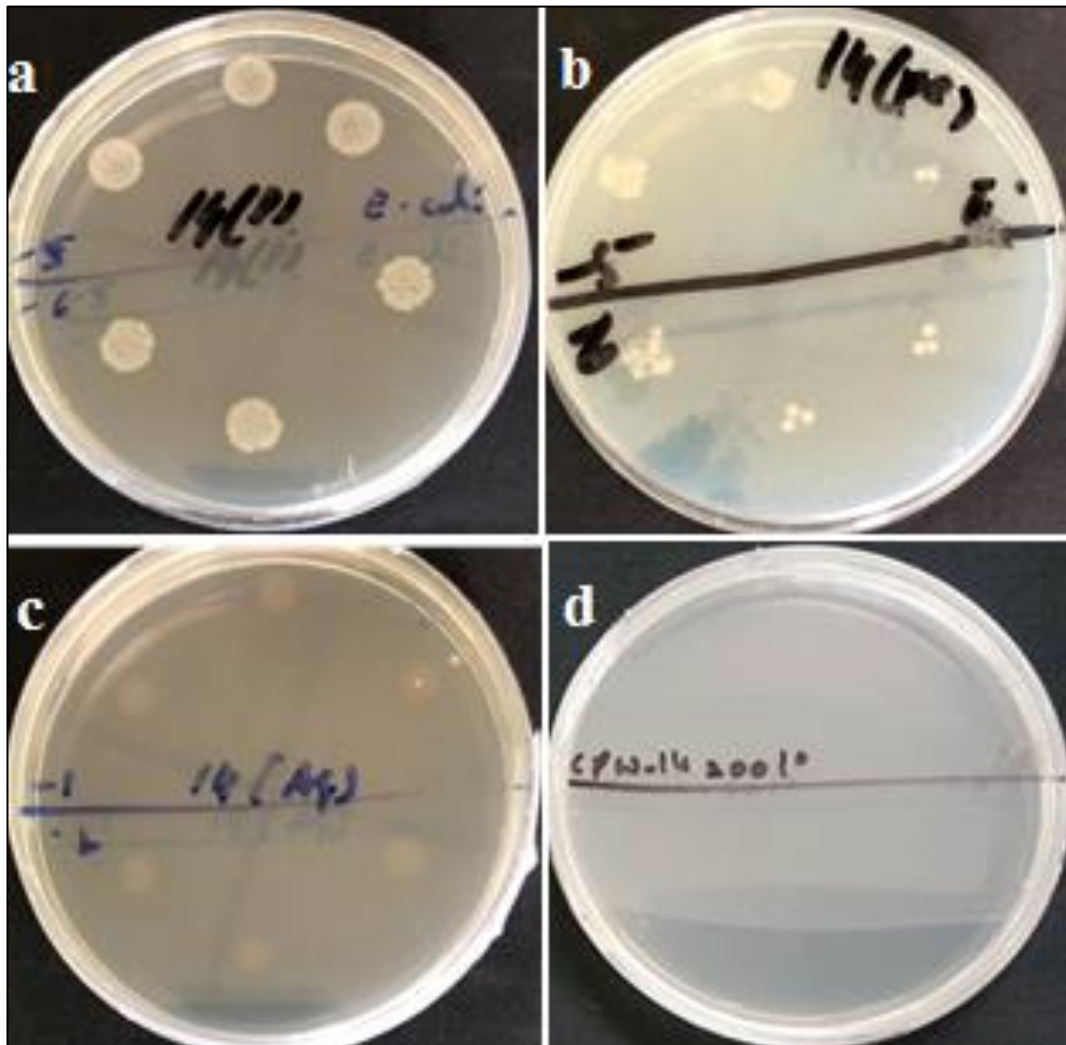


Figure A3-9 (a,b,c and d) CPW-14-based composite (QM4) (a) QM4 (CPW-14 -unmodified) (b) QM4-1 (CPW-14 - modified with only iron oxide nanoparticles) (c) QM4-2 (CPW-14 - modified with only silver nanoparticles) and (d) QM4-3 (CPW-14 - modified with silver coating iron oxide against *E. coli*)

QM5, QM5-1, QM5-2 and QM5-3 against *E. coli*

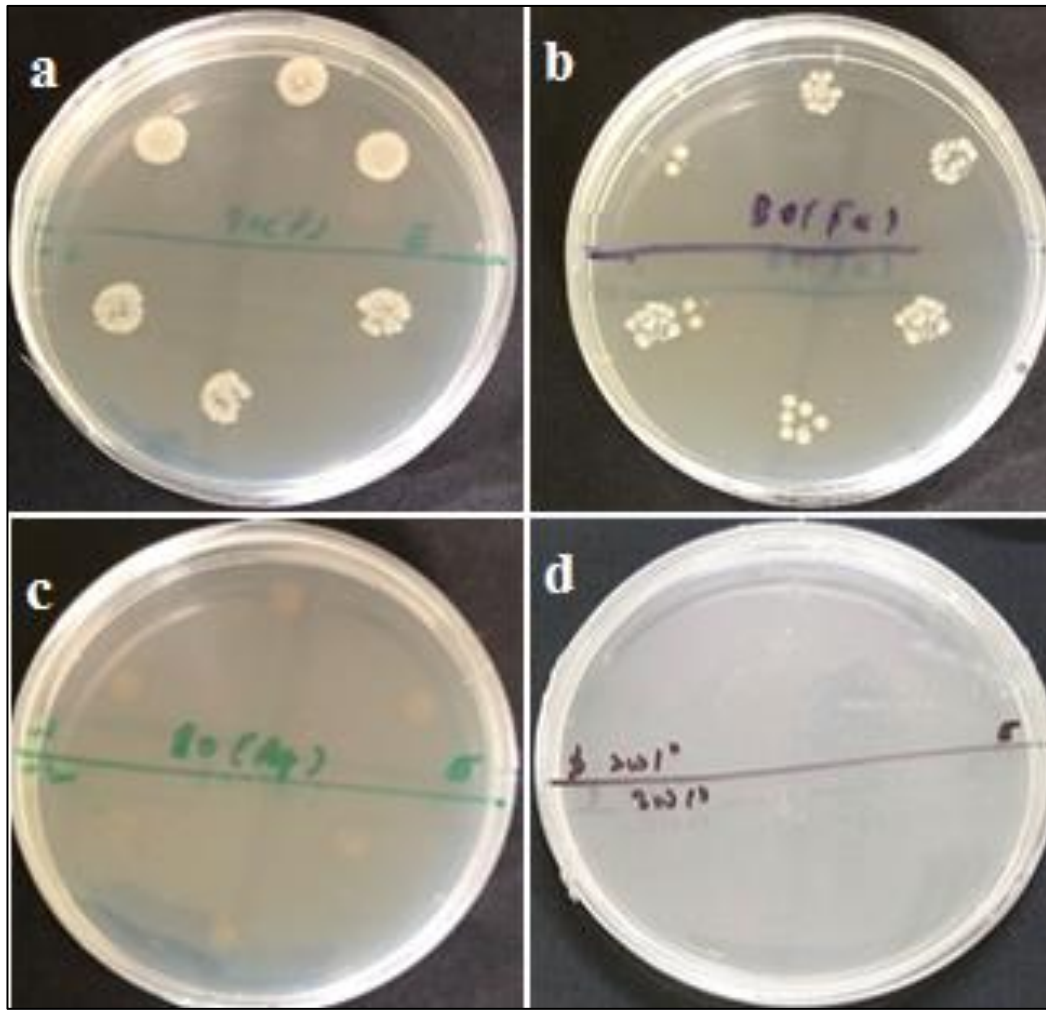


Figure A3-10 (a,b,c and d) CPW-80-based composite (QM5) (a) QM5 (CPW-80 - unmodified) (b) QM5-1 (CPW-80 - modified with only iron oxide nanoparticles) (c) QM5-2 (CPW-80 - modified with only silver nanoparticles) and (d) QM5-3 (CPW-80 - modified with silver coating iron oxide against *E. coli*)

Time kill assay against *S. aureus*

MWCNTs-based composite (QM1-3) against *S. aureus*

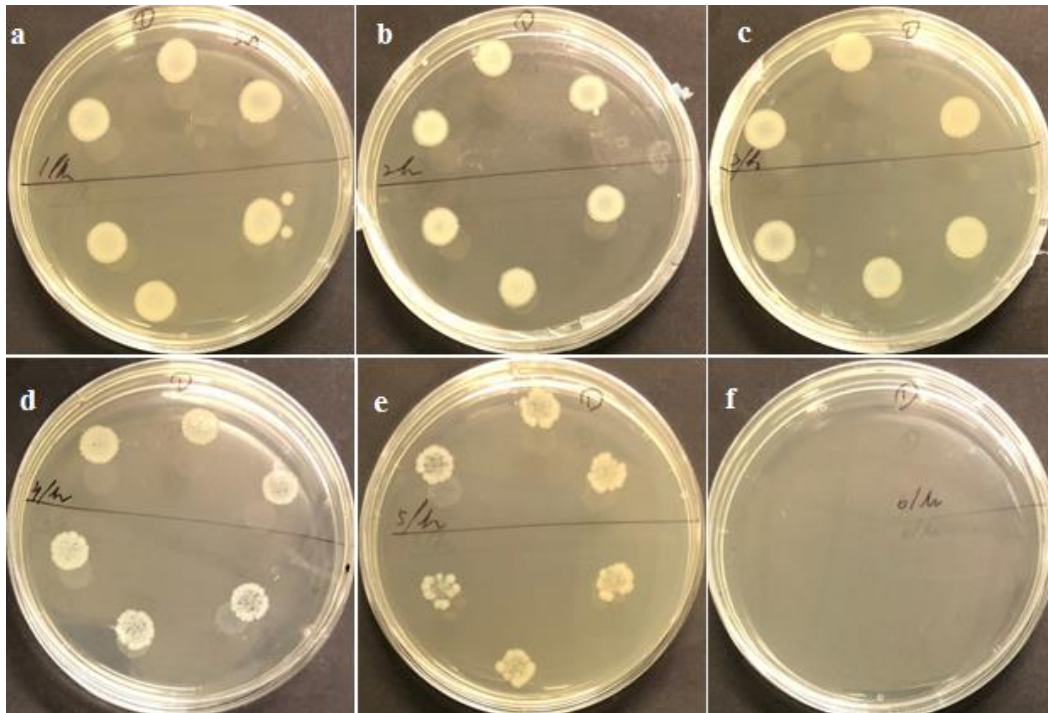


Figure A3-11 Time kill assay (a, b, c, d, e and f,) shows plates of each hours as 1 hour, 2 hours, 3 hours, 4 hours, 5 hours and 6 hours plates respectively

(AC) -based composite QM2-3 time-kill assay against *S. aureus*

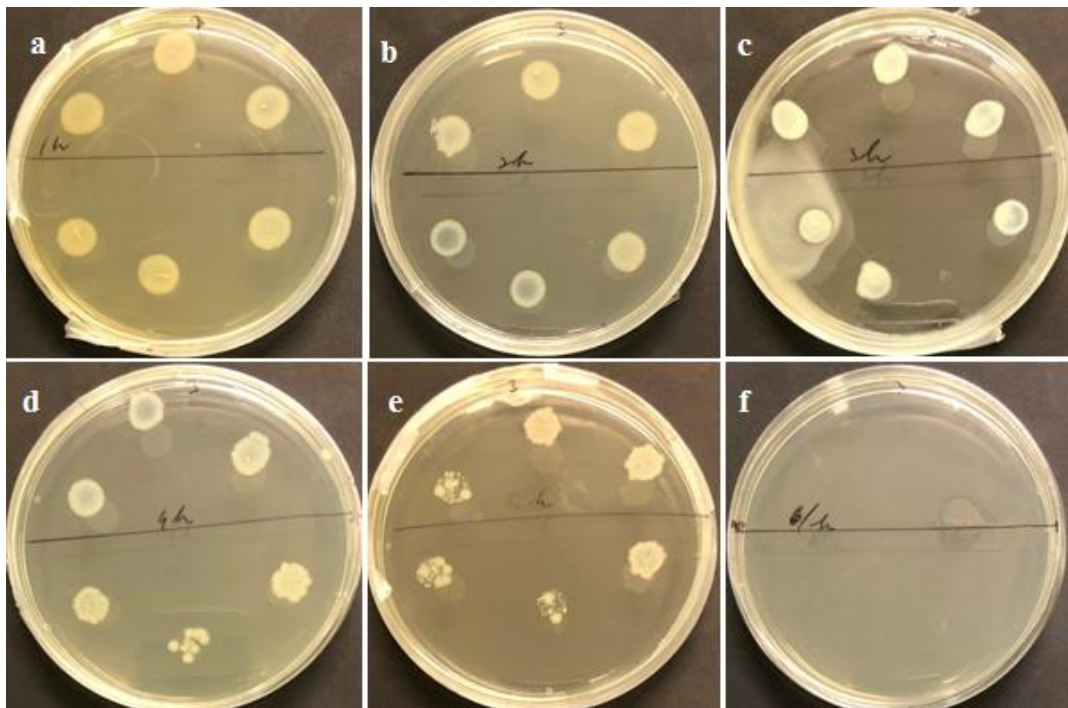


Figure A3-12 Time kill assay against *S. aureus* (a, b, c, d, e and f,) shows plates of each hours as 1 hour, 2 hours, 3 hours, 4 hours, 5 hours and 6 hours plates respectively

DAE-based composite (QM3-3) time-kill assay against *S. aureus*

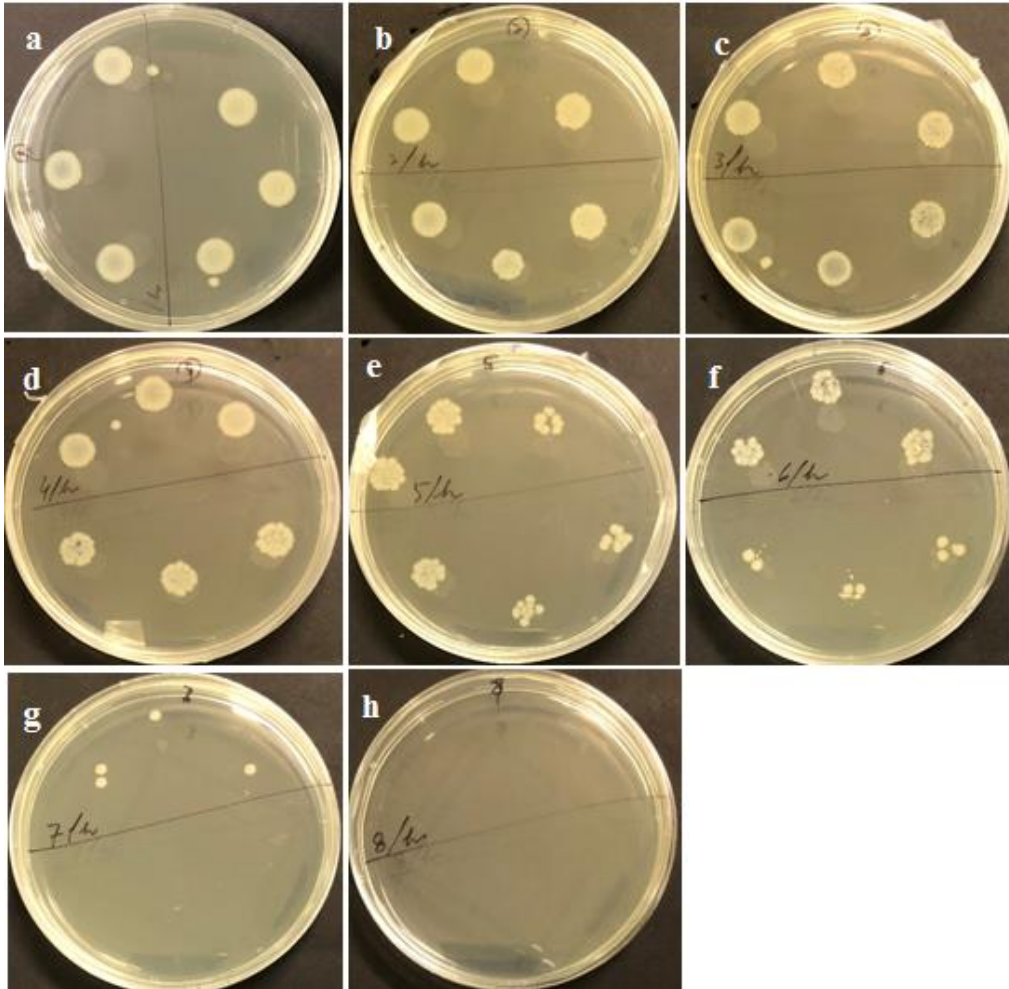


Figure A3-13 Time kill assay (a, b, c, d, e, f, g and h) shows plates of each hours as 1 hour, 2 hours, 3 hours, 4 hours, 5 hours, 6 hours, 7 hours and 8-hour plates respectively

CPW-14-based composite (QM4-3) time-kill assay against *S. aureus*

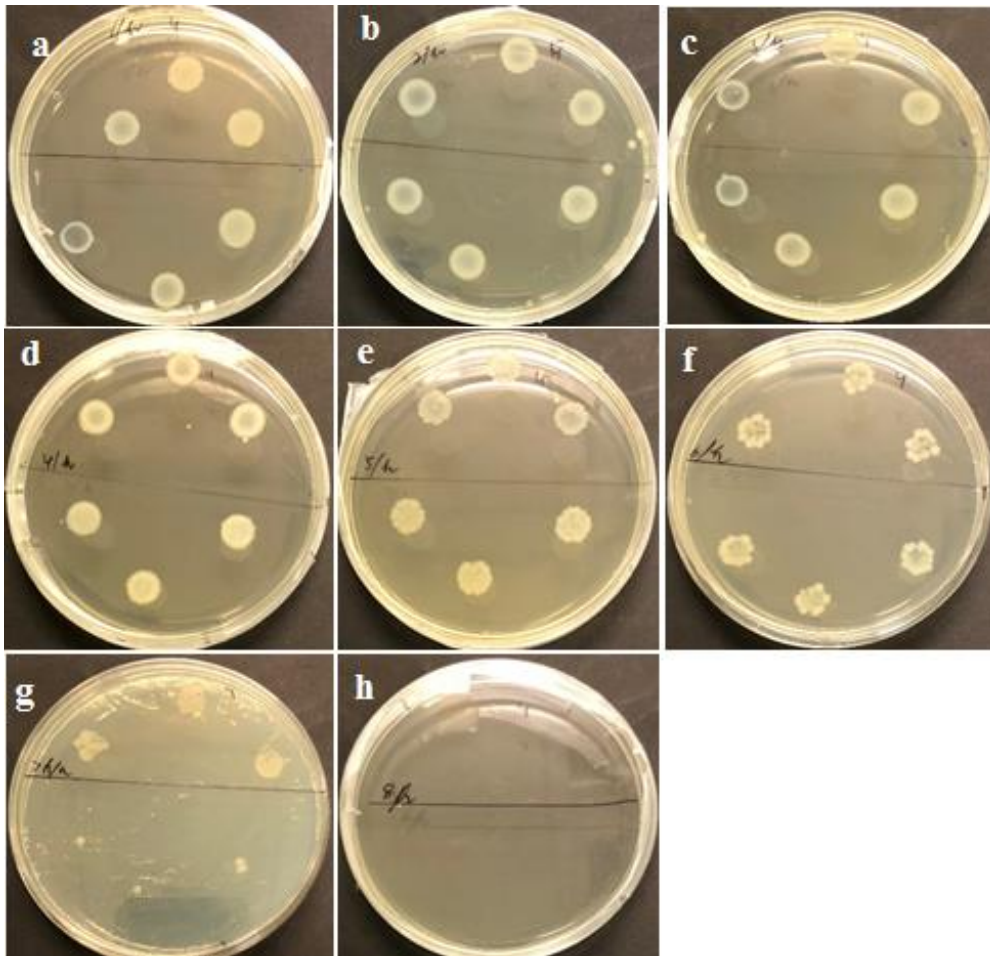


Figure A3-14 Time kill assay (a, b, c, d, e, f, g and h) shows plates of each hours as 1 hour, 2 hours, 3 hours, 4 hours, 5 hours ,6 hours, 7 hours and 8-hour plates respectively

CPW80-based composite (QM5-3) time-kill assay against *S. aureus*

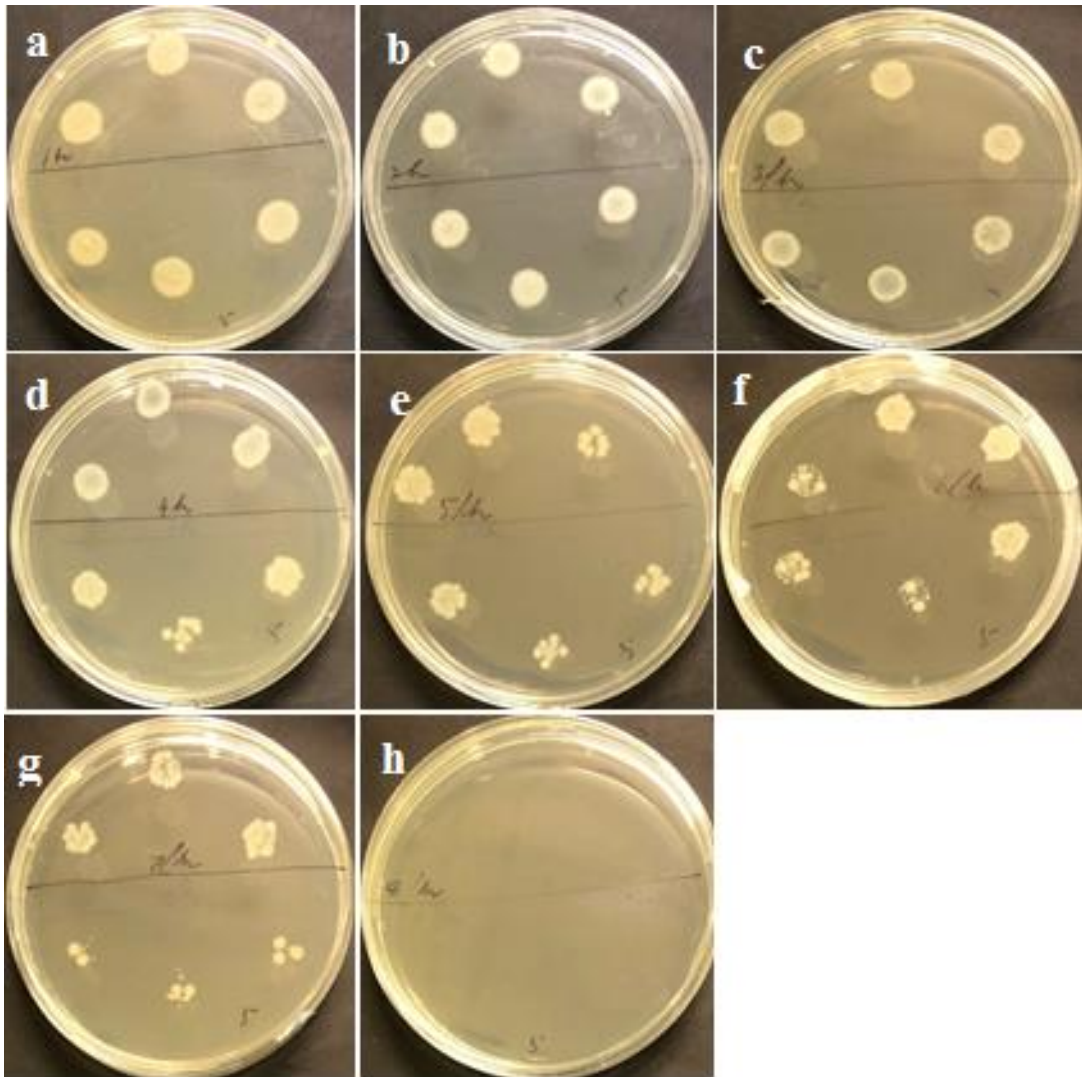


Figure A3-15 Time kill assay (a, b, c, d, e, f, g and h) shows plates of each hours as 1 hour, 2 hours, 3 hours, 4 hours, 5 hours ,6 hours, 7 hours and 8-hour plates respectively

Time kill experiment for *E. coli*

MWCNTs-based composite (QM1-3) time-kill assay against *E. coli*

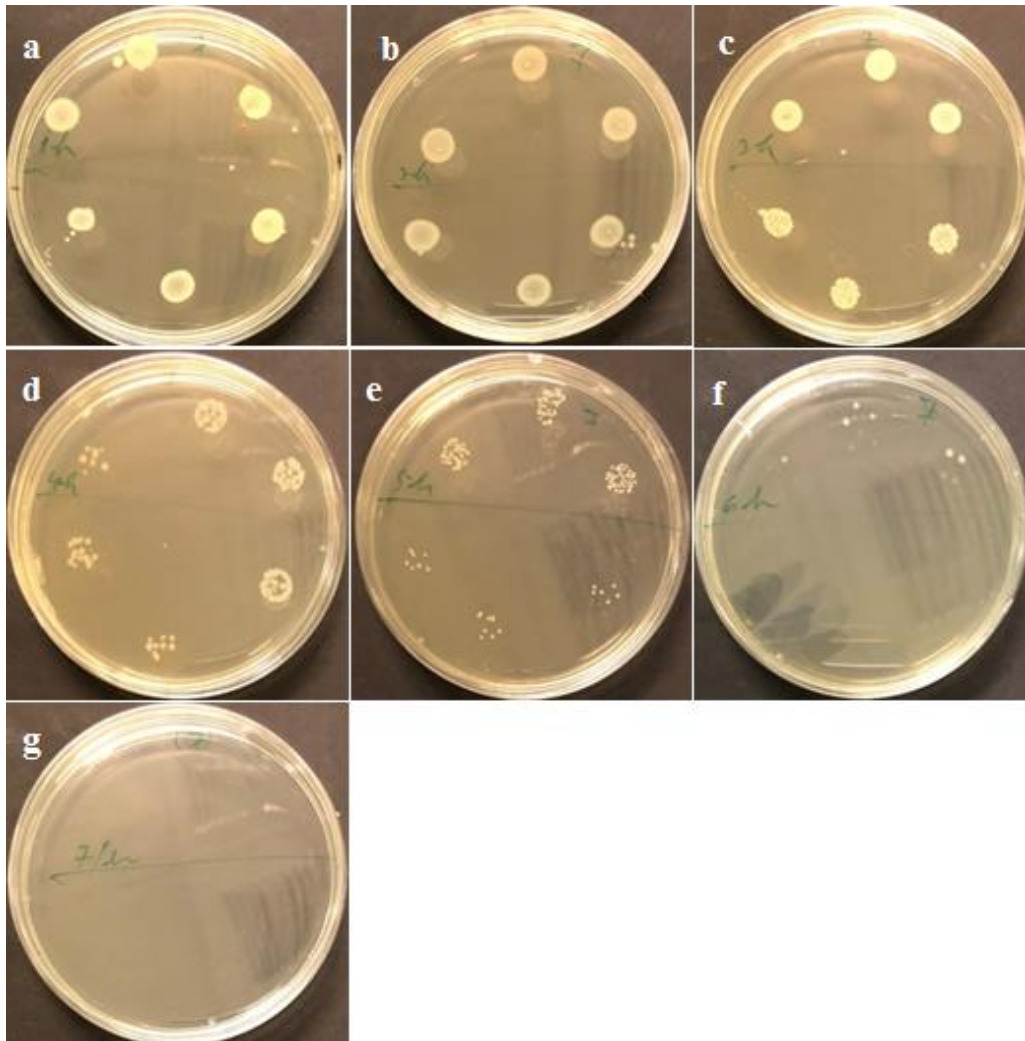


Figure A3-16 Time kill assay (a, b, c, d, e, f and g) shows plates of each hours as 1 hour, 2 hours, 3 hours, 4 hours, 5 hours ,6 hours and 7- hours plates respectively

AC-based composite (QM2-3) time-kill assay against *E. coli*

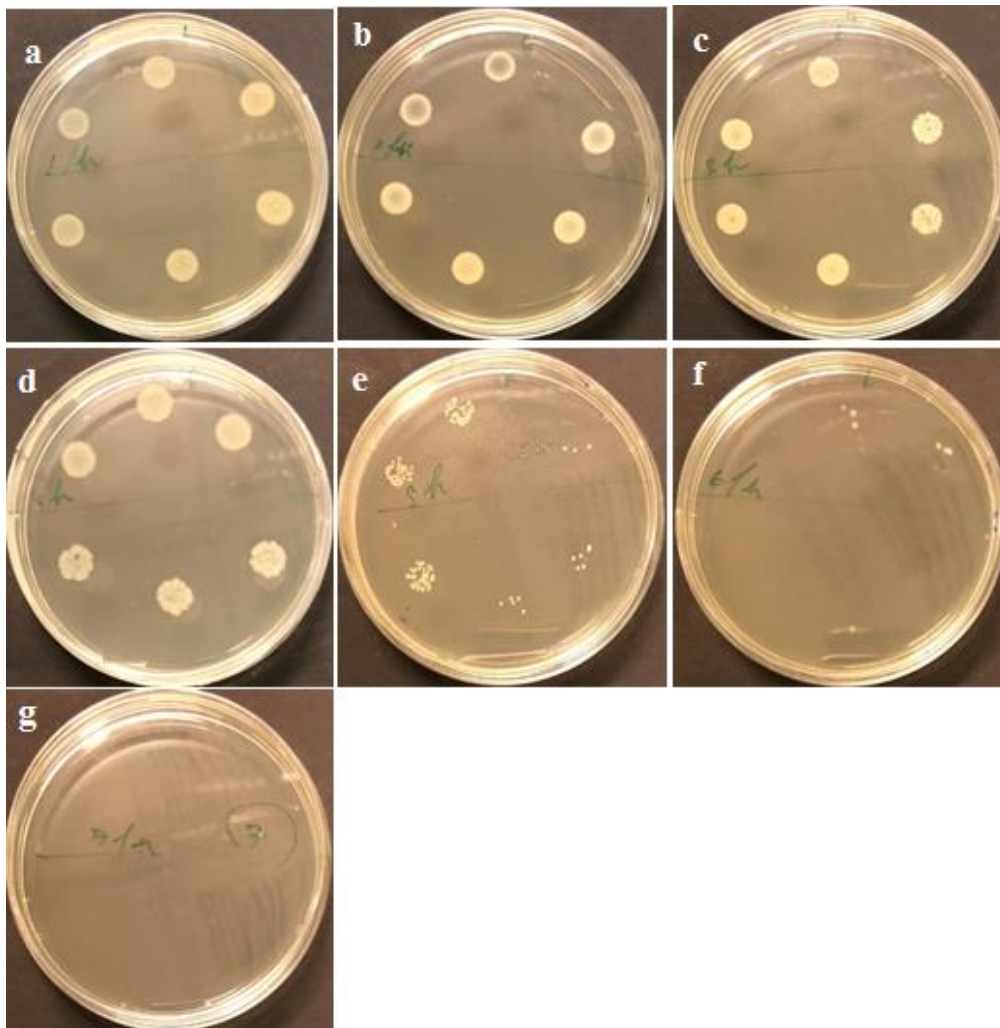


Figure A3-17 Time kill assay (a, b, c, d, e, f and g) shows plates of each hours as 1 hour, 2 hours, 3 hours, 4 hours, 5 hours ,6 hours and 7- hours plates respectively

DAE-based composite (QM3-3) time-kill assay against *E. coli*

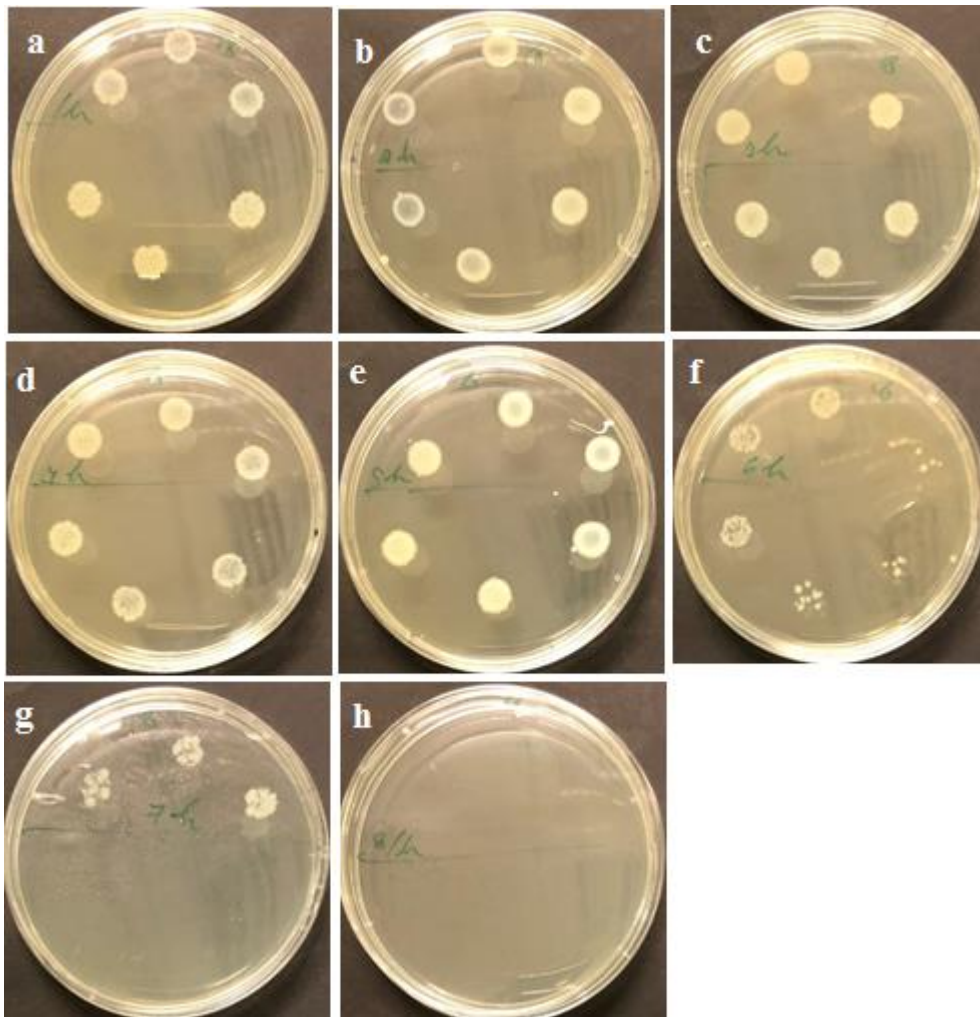


Figure A3-18 Time kill assay (a, b, c, d, e, f, g and h) shows plates of each hours as 1 hour, 2 hours, 3 hours, 4 hours, 5 hours ,6 hours, 7 hours and 8-hour plates respectively

CPW14-based composite (QM4-3) time-kill assay against *E. coli*

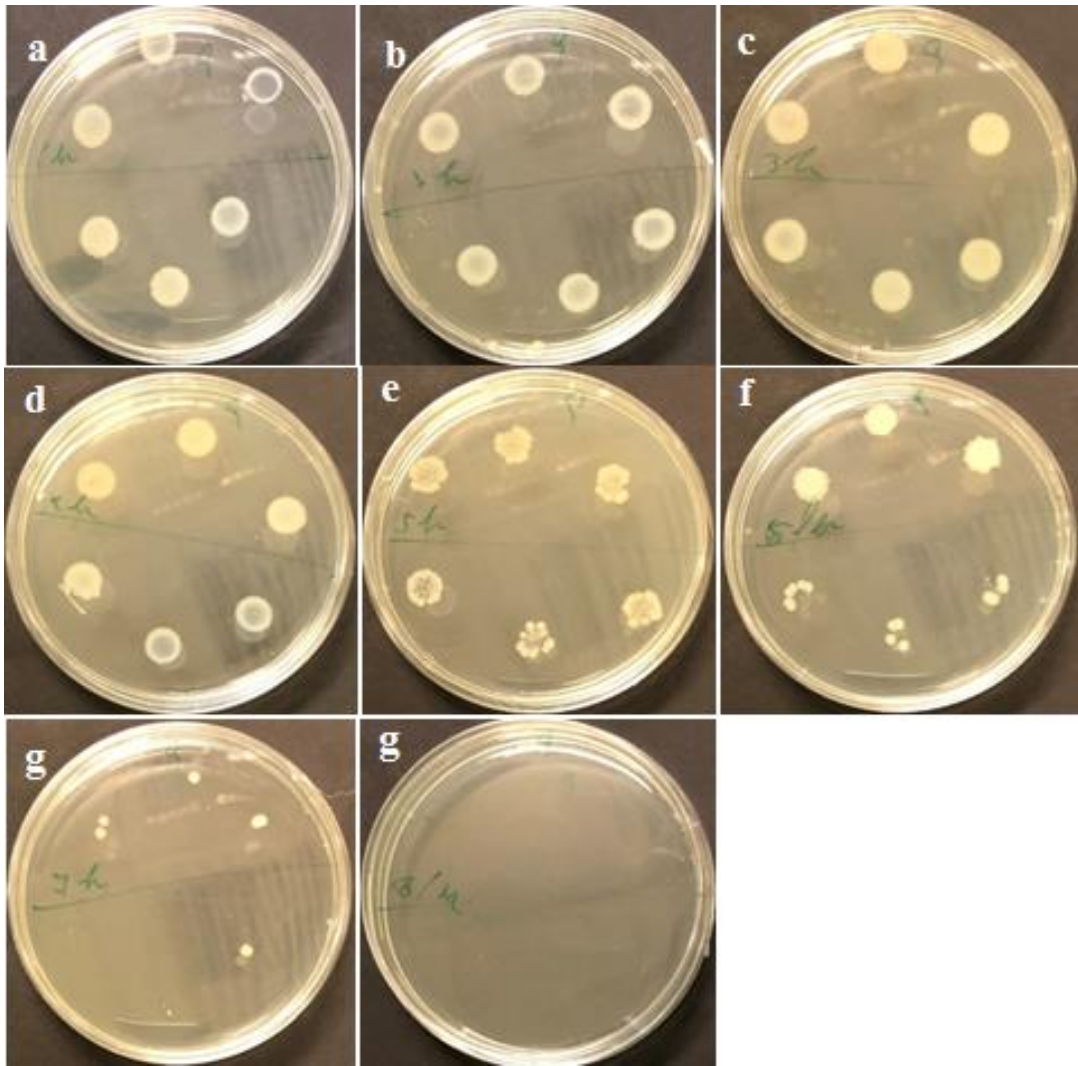


Figure A3-19 Time kill assay (a, b, c, d, e, f, g and h) shows plates of each hours as 1 hour, 2 hours, 3 hours, 4 hours, 5 hours ,6 hours, 7 hours and 8-hour plates respectively

CPW-80-based composite (QM5-3) time-kill assay against *E. coli*

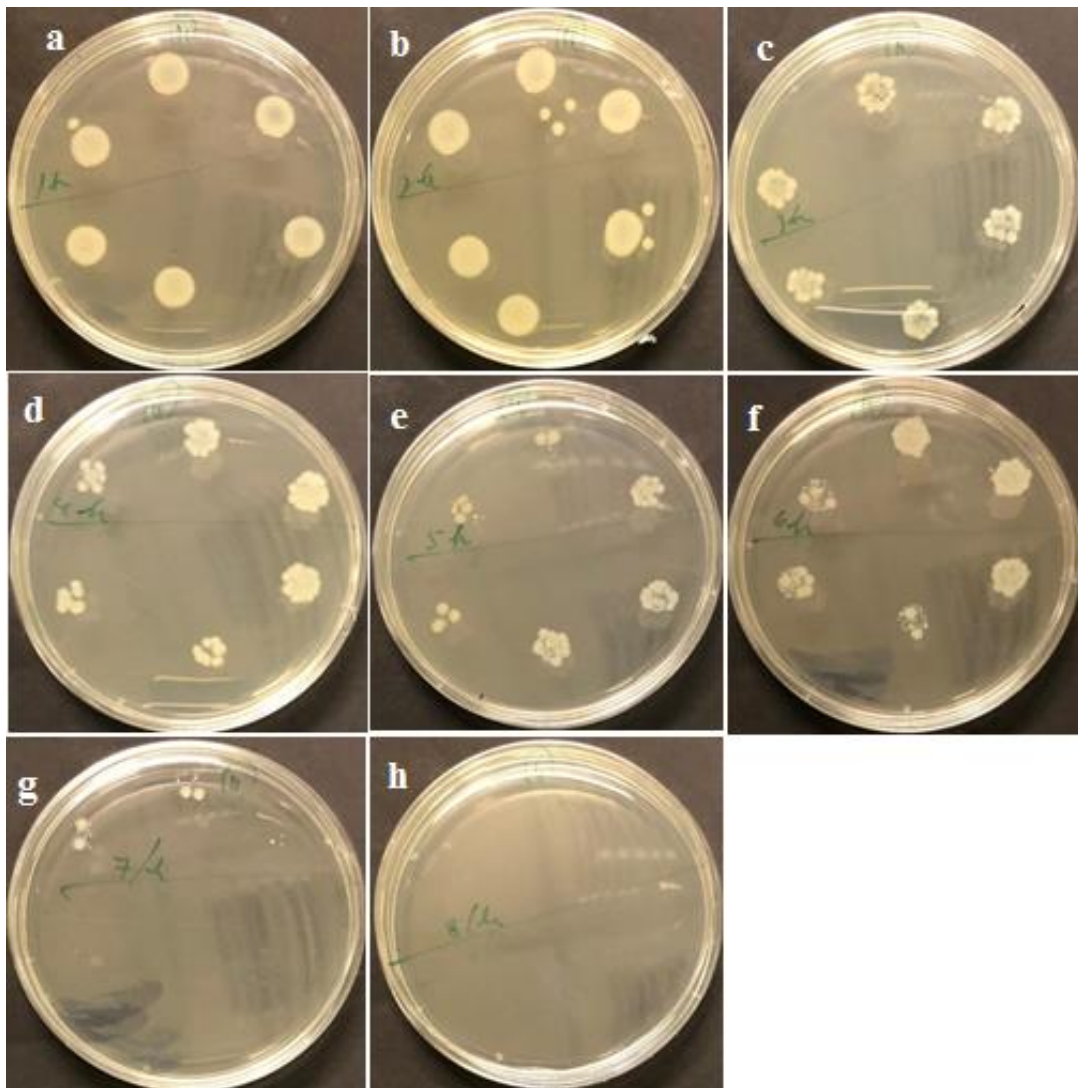


Figure A3-20 Time kill assay (a, b, c, d, e, f, g and h) shows plates of each hours as 1 hour, 2 hours, 3 hours, 4 hours, 5 hours ,6 hours, 7 hours and 8-hour plates respectively

Growth curve of *S. aureus*

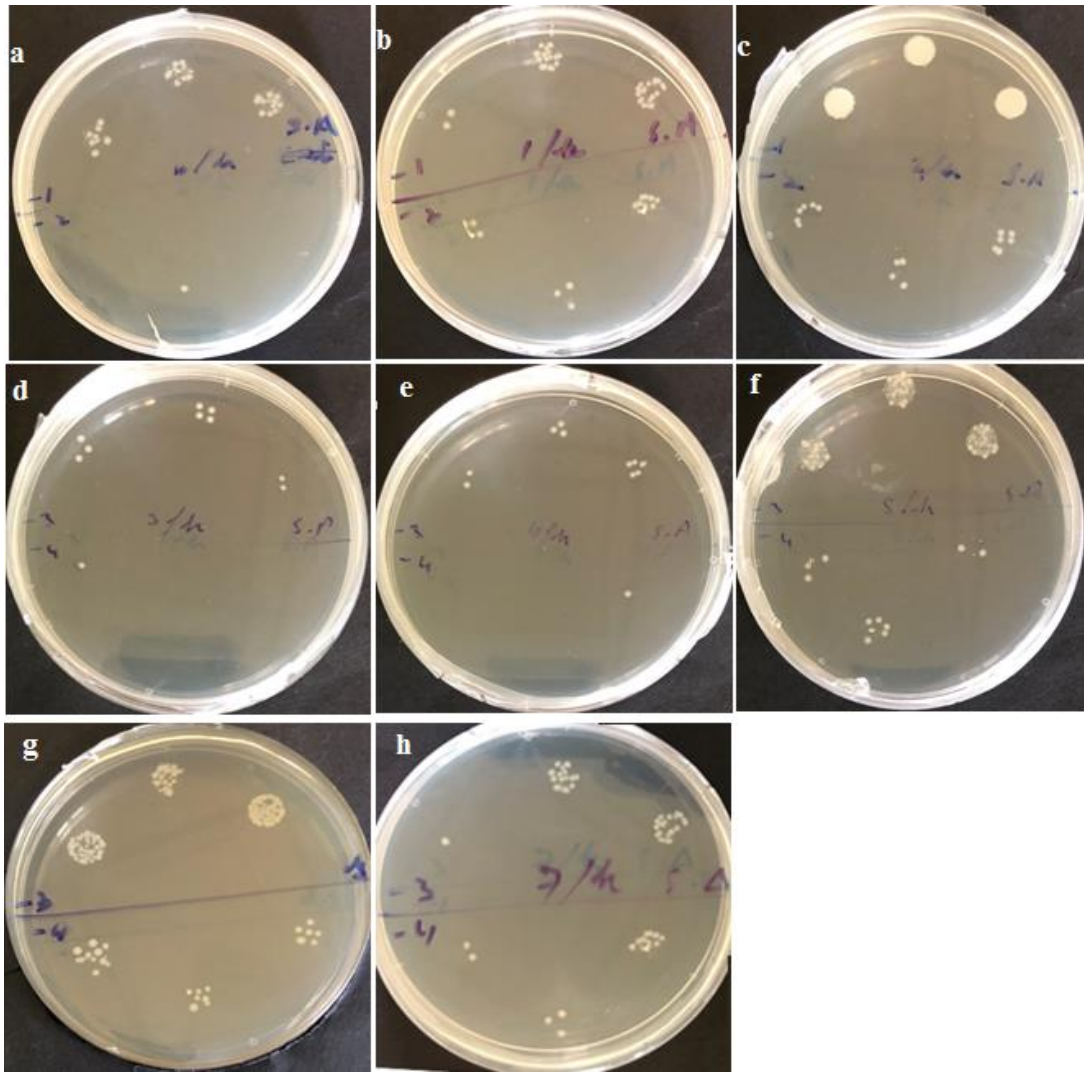


Figure A3-21 Growth curve assay of *S. aureus* (a, b, c, d, e, f, g and h) shows plates of each hours as 0 hour, 1 hour, 2 hours, 3 hours, 4 hours, 5 hours, 6 hours and 7-hour plates respectively

Growth curve of *E. coli*

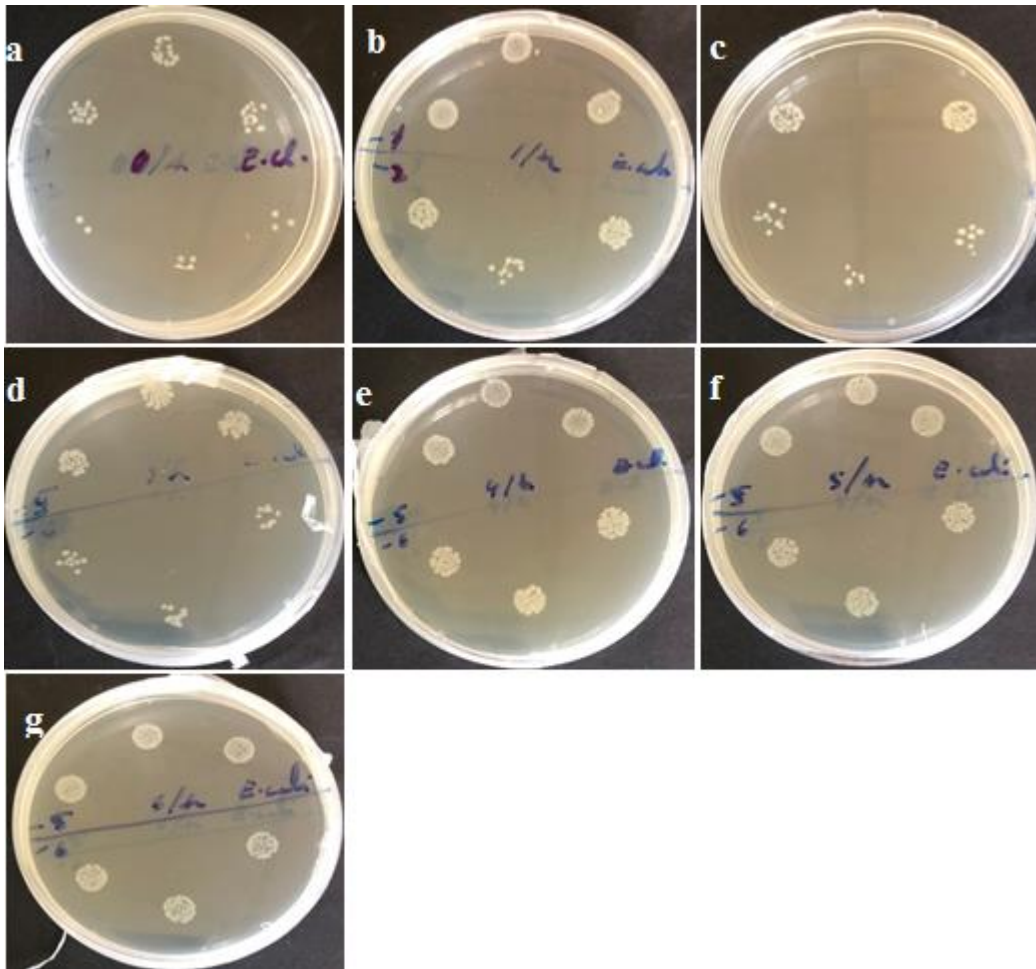


Figure A3-22 Growth curve assay of *S. aureus* (a, b, c, d, e, f, g and h) shows plates of each hours as 0 hour, 1 hour, 2 hours, 3 hours, 4 hours, 5 hours and 6-hours plates respectively